Mechanical behaviour of structured joints in 3D printed composite components: experimental, analytical and numerical study

Author: Lorenzo García Guzmán
Advisors: José Reinoso Cuevas
Luis Távara Mendoza

Continuum Mechanics and Theory of Structures
School of Engineering
University of Seville

Seville, 2020

GERM
GRUPO DE ELASTICIDAD Y RESISTENCIA DE MATERIALES

UNIVERSIDAD DE SEVILLA

PhD Thesis
Doctoral Program in Mechanical Engineering and Industrial Management

Mechanical behaviour of structured joints in 3D printed composite components: experimental, analytical and numerical study

Author:

Lorenzo García Guzmán

Advisors:

José Reinoso Cuevas

Assistant Professor

Luis Távara Mendoza

Associate Professor

Continuum Mechanics and Theory of Structures
School of Engineering
University of Seville

2020

A mi familia

Agradecimientos

Todo el trabajo que ha dado lugar a esta tesis no habría sido posible sin la colaboración de todas las personas que me han acompañado durante estos últimos años. Por tanto, me gustaría agradecer a todos aquellos que han contribuido de una forma u otra a conseguir este reto.

En primer lugar, me gustaría agradecer a mis directores de tesis José Reinoso y Luis Távara todo el tiempo que me han dedicado y su paciencia, ya que son responsables directos de gran parte de lo que he aprendido durante este tiempo. A Federico París, por confiar en mí y darme la oportunidad de conocer el mundo de la investigación.

También me gustaría agradecer al resto del Grupo de Elasticidad y Resistencia de Materiales, Israel García, Jesús Justo, Vlado Mantic, Mar Muñoz, Alejandro Estefani, Antonio Cañas, Isabel del Príncipe y Jose Ramón Rodríguez su ayuda durante este periodo. También a mis compañeros del programa de doctorado María Luisa Velasco, Teresa Guillén, Adelaida Macías, Teresa Aranda y Serafín Sánchez todo el tiempo compartido. En especial, a Patricia Zumaquero y Miguel Ángel Muñoz, por ser mi apoyo en el día a día del laboratorio.

Por último, a mi familia, por confiar en mí desde el primer momento y apoyarme en todas las decisiones que he tomado. A Ana, por sacarme una sonrisa cada día.

Lorenzo García Guzmán
Grupo de Elasticidad y Resistencia de Materiales

Sevilla, 2020

Abstract

Joining mechanisms become specially relevant in structures where multiple parts are involved, for instance in the automotive or the aerospace sectors. Hence, the efficiency of these connections, which generally correspond to the weakest component of the system in many problems, can determine the performance, the resistance and the integrity of the whole structure. The development of high strength-to-weight ratio materials such as the Fibre-Reinforced Polymers (FRPs) leaded to the extensive use of the adhesive joints at the expense of mechanical fasteners like rivets or bolts due to the some advantages such as a superior fatigue life, lightweight or multi-material assemblies, among others. Additionally, novel strategies regarding the fiber-reinforced composite manufacturing have emerged with the advent of 3D printing techniques, which allows complex geometries to be produced. This freedom of design can be skilfully exploited to create more efficient joints and to increase the overall structure performance.

This thesis encompasses a careful investigation of the potential routes to enhance the fracture resistance in adhesively bonded joints in 3D printed fiber-reinforced composite parts by means of patterned or structured interfaces. That is, improvements of the mechanical properties are achieved by geometrically modifying the bondline during the crack propagation. Three different perspectives were envisaged herein:

- Experimental: structured interfaces were manufactured in hybrid specimens, which include nylon and glass-fiber composite (GFC) laminates, employing Additive Layer Manufacturing (ALM). Specimens equipped with structured interfaces exhibiting different aspect ratios, i.e. the ratio between the amplitude and the wavelength of the geometrical pattern, were used in Double Cantilever Beam (DCB) tests in order to obtain empirical evidences of the fracture resistance improvement with respect to the baseline flat or straight configuration.
- Analytical: a simplified semi-analytical method was developed in order to understand the fracture toughness enhancement with the aspect ratio of the pattern, as was obtained in the experimental campaign.

- Numerical: Finite Element (FE) models were developed to simulate the crack onset and propagation in the Double Cantilever Beam specimens with structured interfaces through the employment of cohesive elements along the interface region. These simulations allowed the fracture conditions to be understood more accurately. Moreover, a novel variable based on J-Integral was proposed to calculate the energy release rate regardless the interface geometry for the purpose of comparing properly the different patterns. Finally, the Linear Elastic Brittle Interface Model (LEBIM), a constitutive model to represent abrupt failure for delamination and debonding processes, was adapted to the finite displacement and rotation formulation by means of a user-defined routine in the FE code ABAQUS®. This brittle model was employed in various FE tests experiencing mixed-mode fracture conditions such as Mixed Mode Bending (MMB), End Notch Flexure (ENF), Horizontal Drum Peel (HDP) or hierarchical-structured interface Double Cantilever Beam tests.

Resumen

Los sistemas de unión cobran especial relevancia en estructuras que involucran múltiples partes, por ejemplo en los sectores aeroespacial y automovilístico. Por tanto, la eficiencia de estas conexiones, que son la parte más débil de la estructura en muchos casos, pueden determinar el rendimiento, la resistencia y la integridad de toda la estructura. El desarrollo de materiales con un alto ratio resitencia-peso como los Polímeros Reforzados con Fibra (FRP, por sus siglas en inglés) ha conducido al uso extensivo de las uniones adhesivas a expensas de las uniones mecánicas, tales como remaches o pernos, debido a algunas ventajas como una mayor vida a fatiga, uniones más ligeras y multi-materiales, entre otras. Además, con la llegada de las técnicas de impresión 3D han surgido nuevas estrategias en relación con la fabricación de materiales compuestos reforzados con fibras, lo que permite producir geometrías complejas. Esta libertad de diseño puede ser explotada para crear uniones más eficientes y aumentar el rendimiento de toda la estructura.

Esta tesis constituye una investigación exhaustiva para mejorar la resistencia a la fractura en uniones adhesivas de piezas de material compuesto reforzadas con fibra fabricadas mediante impresión 3D a través de interfases estructuradas o con patrones. Esto es, las mejoras en las propiedades mecánicas se consiguen modificando geométricamente la línea de unión durante la propagación de la grieta. En este estudio se han contemplado tres perspectivas diferentes:

- Experimental: se fabricaron interfases estructuradas en especímenes híbridos, que incluyen nylon y material compuesto de fibra de vidrio (GFC, por sus siglas en inglés), mediante Fabricación Aditiva (ALM, por sus siglas en inglés). Los especímenes que incluyen interfases estructuradas con diferentes ratios de aspecto, esto es, la relación entre la amplitud y la longitud de onda del patrón geométrico, han sido utilizados en ensayos de Doble Viga en Voladizo (DCB, por su siglas en inglés) para obtener evidencias empíricas de la variación de la resistencia a la fractura respecto de la configuración básica plana.
- Analítica: se ha desarrollado un método simplificado para dar respuesta a la mejora de la resistencia a la fractura con la relación de aspecto de los patrones,

como se ha demostrado en la campaña experimental.

- Numérica: se han desarrollado modelos de Elementos Finitos (FE, por su siglas en inglés) para simular el inicio y la propagación de grieta en especímenes DCB con interfases estructuradas mediante la utilización de elementos cohesivos en la región de la interfase. Estas simulaciones permitieron un conocimiento más detallado de las condiciones de fractura. Además, se ha propuesto una nueva variable basada en la Integral J, apropiada para calcular la tasa de liberación de energía independientemente de la geometría de la interfase, para comparar adecuadamente diferentes patrones. Finalmente, el Modelo de Interfase Elástica Lineal Frágil (LEBIM, por sus siglas en inglés), un modelo constitutivo para representar fallos abruptos en delaminaciones y procesos de despegue, ha sido adaptado a la formulación de grandes desplazamientos y rotaciones mediante una subrutina de usuario en el código de elementos finitos ABAQUS®. Este modelo frágil ha sido empleado en varios modelos en los que se experimentan condiciones de fractura en modo mixto como los ensayos Mixed Mode Bending (MMB), End Notch Flexure (ENF), Horizontal Drum Peel (HDP) o DCB con interfases estructuradas jerarquizadas.

Contents

1 Introduction

1.1 Composite materials

Composite materials or composites can be defined as those materials derived from the combination of two or more constituents characterised by different chemical and mechanical properties, whose phases can be distinguished at macroscopical scale and they have an interface between them. The composite material, that arises from the corresponding combination of materials, has different properties than those associated with their secluded constituents. Generally, improvement of stiffness, strength, lightweight, cost, environmental resistance or fatigue life in structures are the reason of the production of such composites.

Composites can be seen in nature extensively, few such examples include, but not limited to muscles, wood or bamboo of strong fibers embedded in a soft matrix, among many others. Additionally, in different range of applications, bricks employed in building processes or the concrete, which combines different types of aggregates and lime based cement to efficiently support compressive loads are good examples of age old man-made materials.

Notwithstanding, the term "composite" is often related to high performance structures or the so-called Advanced Composite Materials (ACMs). The development of high strength and stiffness fibers and high-quality resins during the last century allowed ACMs to be employed in the most demanding engineering applications, specially in those where the lightweighting is absolutely imperative like the aerospace industry. These materials are characterised by: i) fiber-reinforcement (carbon, aramid and glass fibers) and, ii) ceramic, metal, or polymeric matrix with high strength and stiffness, low weight, and environmental resistance. The fiber-matrix combination relies on the specific application and requirements. Thus, the fiber is largely responsible for the ultimate strength of the composite, whereas the matrix provides the consistency and the deformation capacity needed in an engineering structure. It is worth mentioning that the role of the fiber-matrix interfaces is decisive in the damage onset and subsequent failure propagation. This fact is motivated by the generation of new surfaces, one of the main energy dissipative mechanisms in this type of composites.

As a comparison, Table 1.1 [1] reports some of the principal properties of the Fiber-Reinforced Plastics (FRP) constituents (fiber and matrix) and the properties of the actual composites and metals employed in the industry.

Table 1.1 Properties of representative composites, their constituents and structural metals in industry. CFRP, GFRP and KFRP stand for Carbon Fiber Reinforced Polymer, Glass Fiber Reinforced Polymer and Kevlar Fiber Reinforced Polymer [1].

Material	Young's modulus E [GPa]	Tensile strength σ_u [GPa]	Density ρ [g/cm^3]	Specific modulus E/ρ	Specific resistance σ_u/ρ
Carbon fiber	390	2.2	1.95	200	1.1
Glass fiber	76	1.4-2.5	2.56	29	5.4-9.7
Kevlar fiber	125	2.8-3.60	1.45	86	1.9-2.4
Epoxy matrix	3-6	0.035-0.100	1.1-1.4	2.3-4.6	0.026-0.076
Polyester matrix	2-4.5	0.040-.090	1.2-1.5	1.4-3.3	0.029-0.066
CFRP	83	0.38	1.54	53.5	0.24
GFRP	21.5	0.57	1.97	10.9	0.26
KFRP	40	0.65	1.40	29.0	0.46
Steel	210	0.45-0.83	7.8	26.9	0.058-0.106
Aluminium	73	0.41	2.7	25.5	0.096

It is worth remarking again the role of fiber-matrix interface, whose mechanical properties substantially influence the composite shear strength and fatigue strength. The selection of one constituent or another in a structure will depend upon the target application such as low-cost, high-performance, energy-absorbing, etc. It can be observed that fiber-reinforced composites lead the specific strength and modulus with respect to metals. These parameters are key in structures where the weight is a major design factor.

Another characteristic of the fiber-reinforced polymers is the control of the anisotropy, that is, the possibility of selecting the mechanical properties in different directions. Hence, on demand material can be made through the manufacturing process in order to optimise a certain structure, subjected to particular loads. This can be achieved by multi-directional plies, varying the volume fraction of fibers, etc.

These features made the aircraft manufacturers starting to move to composite material at 1950s and their use has significantly been increasing till date. In [2], Jones provides some interesting figures about the composite material use: composites can be made with the same strength and stiffness as high-strength steel but a 70% lighter, ACMs are as much three times as strong as aluminium and 40% lighter. However, not only the weight saving makes attractive composites over metals, but operation costs bolster its advantages. Despite its high initial costs (raw material and manufacturing), composites have lower life-cycle costs (initial, operation and maintenance cost) which serves as key element in the structural design. Hence, the use of composite material is specially

effective in weight-sensitive structures and are expected to spread progressively to other applications when extraction and manufacturing costs diminish. For example, it would save (data from 1999) around 900 dollars per kg in the commercial airplanes and around 2.000-22.000 dollars per kg in satellites.

In the aeronautical industry, the demand for composites rises due to its lightweight structures which in turn helps in fuel saving, and started to apply FRPs in parts such as wings, fuselage and landing gears. Within this context, it is estimated that, 6% of the total weight in the Airbus 300 (1974) comes from composites. This percentage was increased in the models Airbus 310-200 (1982) and Airbus 320 (1988), with a 8% and 20% of composite weight, respectively. Notwithstanding, the critical point in the large-scale employment of FRPs was the new generation of aircrafts carried out by Airbus and Boeing in the 21st century. On the one hand, the Boeing B787 reached the 50% in composite structural weight, being the 20% the percentage of aluminium alloys. On the other hand, the model Airbus A350 computes 53% of composite weight and 19% of aluminium alloys. So, the FRPs are established as the principal materials in the aerospace domain.

In addition to the benefits emanated from the lightweight capacities aforementioned, other properties of the fiber-reinforced polymer matrix can be exploited. Specific configurations of graphite-epoxy structures provide a thermal expansion coefficient close to zero, which is utilised in high-accuracy dimensional applications such as the antennas and signal systems placed in satellites, where the dimensions of the structures have to be unaltered under different thermal loads. The glass-fiber reinforced bodied Chevrolet Corvette in 1953 stands out in the automotive industry. Soon after, in 1981, their steel springs were replaced by composite spring, weighting from 19 kg to 3.6 kg [2]. However, the production rates are lower due to inevitably slow manufacturing process and much research is needed in this direction. Coming to the civil industry, the use of composites is widespread in bridge construction to effectively resist seismical loads. Lastly, glass-fiber reinforced products are employed in commercial applications such as boats, tennis rackets, skis, surf boards, while carbon fiber-reinforced plastics are used in high competitive sports like frame bicycles, golf clubs, hockey sticks or prosthesis.

Despite the numerous advantages of fiber reinforced composites over other materials, a great effort needs to be made to understand the mechanical behaviour and failure mechanisms that limit their use in a wide range of situations or affect in the design process. The marked anisotropic character, the presence of different constituents with highly distant properties of strength and stiffness, the relevance of the interface between such components, the freedom in the fiber orientation in laminates, number and thickness of the plies and adhesion properties between them and many other factors complicate the characterisation of composites and hence its failure prediction. Thus, simple rules as maximum stress or strain levels cannot be established as design factor. In other words, in comparison with metals, where researchers agree that the main damage process stems from the of plasticity, there is not a final agreement in composites as it involves complex failure mechanisms at both micro and macro scales. As a consequence, there is not an equivalent expression to the von Mises criterion in composites in order to predict damage onset or failure, but several criterion has been proposed in the last decades (Tsai-Wu [3],

Hashin [4], Tsai-Hill [5], Azzi [6], Hoffman [7], Chamis [8]). This lack of knowledge is reflected on the verification and validation schemes when composite materials takes effect in the industry. Compared to metal designs, more experimental, numerical and analytical resources are needed in the FRPs components. In the case of the aeronautical sector, a huge quantity of experimental tests at different scales must be performed to certify a component to be suitable to fly. For instance, to manufacture a wing, the material is tested by means of laboratory specimens (scale of cm), subcomponents and large components (scale of meters) are analysed experimentally, as well as the actual wing (tens of meters). This strategy arises from safety purposes due to the lack of confidence in the analytical models and computational simulations. Therefore, composite part validations and verifications require substantial economical resources and additional workloads that influence in the final cost of the assembly. Moreover, safety factors are applied to the ultimate design load, due to the presence of defects such as porosities, matrix cracks and fiber breakage, curing stresses, fiber misalignment, delaminations, cure and processing tolerances, among others, to allow a certain level of damage tolerance in the structure.

Nonetheless, in multi-layered composite, numerous factors make the prediction of the damage tolerance difficult and sometimes arduous. Mainly, these aspects are due to the variety of failure mechanisms, divided in intra-laminar (breaking of fibers, damage of matrix, fiber-matrix debonding) and inter-laminar (delamination), derived from the highly anisotropic nature of the composite materials. The intricate nature of the onset and the propagation of damage at different loading conditions make the current analytical and numerical models inadequate for its industrial standardisation and, consequently, the failures mechanisms need to be supported by experimental evidences.

1.2 Adhesive joints

Linking components within a structure is a major issue, either in a natural or in artificial parts, because these interface regions are comparatively weaker in comparison with the connected elements. Adhesive bondings constitute effective and powerful techniques that enable different elements to be connected, such techniques being used naturally for thousand of years through vegetable polymers such as starch [9], natural rubber adhesives like latex [10] or derived from animal proteins, principally from collagen present in tendons, bones and skin [11, 12]. In the last century, high-performance synthetic adhesives have been widespread in the industry applications, specially in those where strength-to-weight ratio and fatigue life are of great interest. In this line, epoxy, phenolic, or acrylic adhesives are extensively used in aeronautical structures [13–15] and space applications able to deal with temperature and space environment. Furthermore, bonding technologies allow lightweight assemblies of multi-material parts in the automotive industry to be produced or smooth surfaces in the carbody of high-speed trains for reduction of aerodynamic drag.

Due to their appealing performance, the adhesive bondings are gaining ground in most of very demanding applications at the expense of conventional mechanical joining systems. One of the benefits is the uniform stress distribution along the bondline.

In comparison with a bolted or a riveted joint, the portion of structure dedicated to transmit/support load is higher. Usually, this fact leads to more efficient, stiffer and lighter parts. The most extended use of structural adhesives is the bonding of thin plates, e.g. aircraft panels, whose stiffness and strength is higher than the adhesive. However, large wetting areas provide an effective load transmission and the capacities of every element in the joined system can be skilfully leveraged. The freedom in joint design permits the employment of adhesives in many components, regardless the geometry or the material, due to it can be applied in liquid state and its polymeric nature admits flexibility and deformations under thermal or mechanical loads. Thus, new configuration concepts can emerge for particular conditions. In addition, damping properties of polymers make them excellent candidates for long fatigue life applications. The variability of material combinations to be bonded is extensive such as metal-metal, composite-composite, metal-composite, sandwich panels (honeycomb core and composite skin), ceramics, plastics, etc.

Formally speaking, according to Kinloch definition [16], an adhesive is a material which, when applied to surface materials, can join them together and resist separation. The parts involved in the joining are called substrates, which are denominated adherents after the adhesion process. In this sense, adhesion refers to the attraction between substances consequence of intermolecular forces. According to da Silva [17], special attention is focused on the difference between interphase and interface. While the former term is referred to the region between the adhesive and the adherent, which has different mechanical and chemical properties than the bulk materials, the latter one, also called boundary layer, makes reference to the plane of contact between the two materials. Another substance, primer, is generally employed to enhance the adhesion phenomena between adhesive and adherents. A representation of a complete adhesive joint is illustrated in Fig. 1.1.

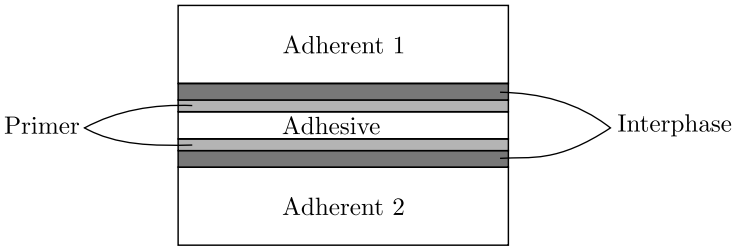

Figure 1.1 Principal elements in an adhesive joint.

Depending upon the substrate and adhesive properties, the surface treatment, manufacturing conditions, among other factors, the bonded joint will fail in different ways. Adhesive or interfacial failure refers to the separation of the adherent and the adhesive within the boundary layer. Otherwise, cohesive failure is obtained when a crack propagates within the adhesive. The main difference between previous failures is the involvement of the bulk material properties (adherent or adhesive) or the interphase properties. Other types of failure are derived from the combination of the adhesive

and cohesive failures, for instance an adhesive failure migrating from top to bottom surfaces. Some examples of failures are displayed in Fig. 1.2.

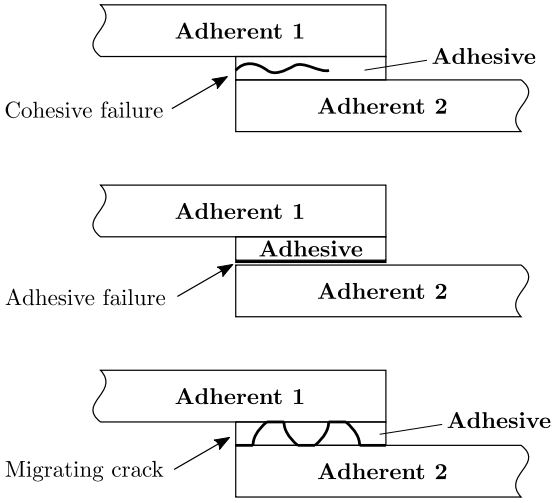

Figure 1.2 Failures in an adhesive joint.

There are scenarios in which, despite the low mechanical properties of adhesives in comparison with adherents, the joint strength is adequate for structural applications. The most common use is the thin plates bonding, where large bearing areas can be covered. Indeed, high-performance adhesives (for example those applied in aerospace structures) can make the joint tougher than adherents and cause the failure of its own adherents.

Notwithstanding, a deeper researching in adhesion technology is required to overcome some disadvantages with the aim to apply this method in a wider range of scenarios. The presence of multi-material corners prompt stress concentrators that may compromise the integrity of the joint. Some environmental conditions such as high temperatures or humidity degrade the adhesive properties. Furthermore, careful attention in fixture or tooling systems should be paid for accurate positions between components, due to there are no possibility to disassemble the joint after curing. For the same reason, quality controls cannot be carried out after the manufacturing process and the repair operations do not recover the original properties of strength and service life. Besides, to ensure a good adhesion between components, diverse surface treatments need to be conducted.

Considering the promising results attending to lightweight structures, improvement of fatigue life and protection provided against environmental factors like corrosion, among others, the comprehensive study of stress state, failure mechanisms and damage prediction is worth to be investigated.

In addition to the previous arguments, it is remarkable to mention that two different perspectives have coexisted during years to explain the adhesion phenomena: practical and fundamental adhesion. The former viewpoint involves the force or the energy required to separate an adhesive bond whereas the latter approach is focused upon the

mechanisms responsible for holding together the components of an adhesive bond at a molecular scale. This thesis is focused upon the practical adhesion but, for the sake of completeness, principal fundamental adhesion theories are summarised below:

- Adsorption theory gives priority to the existence of contact at molecular scale between substrates and adhesive to promote the forces of adhesion, such as primary covalent bonds or secondary van der Walls forces. In other words, the main idea is that when the contact at molecular level occurs, the adhesion is guaranteed. Unsuccessfully, if the energy of interaction between model molecules (even considering only weak or secondary forces) is compared with the corresponding practical adhesion, i.e. values obtained in laboratory, it can be observed a much higher strength.
- The mechanical theory attributes good adhesion to the interlocking between adhesive and a rough substrate surface. The adsorption theory is implicit in the contact between materials. Nevertheless, this approach allowed to explain the improved performance of rough surfaces over smooth surfaces in conditions where a good wetting is obtained. The plastic deformations in ductile adhesives because of stress concentrator leads to an increase of the energy released during the failure. This concept, apart from rough surfaces, is applied in microporous or microfibrous areas.

Both adsorption and mechanical theories were discussed in the work developed by McBain and Hopkins in the 1920s [18]. It is worth mentioning that, from the very beginning of the adhesive's study, the actual contact between adherent and adhesive were fundamental, as well as the relative disposition between them at the microscale.

An alternative interesting model to understand the appearance of weak bonds is the weak-boundary-layer theory introduced by Bikerman [19]. This model conceives a cohesively weak layer in the interfacial region (thin at the macroscopic level) in which the practical adhesion is taken into account to predict the stress failure. The aim was to investigate the influence of cohesively weak layers (water, lubricant, wet particles) that may be present onto the contact surface, where such a layer would be considered thick at a molecular scale.

As summary of the principal fundamentals to achieve a good adhesion process, contact between adhesive and substrate is crucial to promote molecular interfacial bonds and the surface roughness, porous, contaminants or other agents are decisive in the dissipative energy processes that distinguish the strong joints able to sustain high stress. So, wetting and spreading theory play an essential role, that is, the relation between surface energies and surface tensions by means of the contact angle and thermodynamic properties of the pair adhesive-substrate.

To this end, surface treatments prior to the adhesive application are an essential part for high-performance bonded structures. Certain methods can modify chemical and physical surface properties and, consequently, they can influence in the quality and durability of the adhesion. These pre-treatments rely upon the materials and the requirements involved in the joint design, that is, bond-promoting surfaces or environmental protection. With the purpose of accomplishing these aims, some categories

of treatments have been developed: (i) removing or preventing the weak layers and contaminants (oils, oxides, etc.) on the substrate surface, (ii) adding coupling agents to endorse molecular contact, (iii) texturing the substrate surface in order to produce specific arrangements that induce dissipative energy mechanisms and stress redistributions, (iv) passivating the substrate surface for corrosion resistance purposes.

One of the most-attracting pretreatments in high-efficient metals is anodizing. This electrochemical method forms a porous outer oxide with a honeycomb arrangement that increases the thickness of the natural oxide layer, as illustrated in Fig. 1.3.

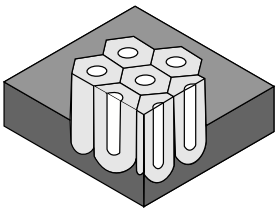

Figure 1.3 Cell structure after anodizing process.

Packham [20] investigated the role of the pores of an anodized aluminium. The polymer penetration into the pores helps mechanical interlocking between adhesive and adherent and, subsequently, to the energy dissipation [21]. The authors reported remarkable importance of the stress distribution at the joint: if the stresses are distributed along the bondline, avoiding stress concentration at the surfaces, more plastic energy will dissipate and hence better adhesion conditions will be achieved.

It is noteworthy that the effectiveness of the mechanical treatments, in which a preferable surface, through macro-roughness, is obtained after some degrease process. Again, these rough surfaces foster the appearance of high stress levels in the bulk materials. Hence, the production of such surfaces is well received. The grit-blasting, the slurry-blasting or the surface texturing using a power beam [22] take advantage of this fact. The industrialization of the latter approach were developed by the Surfi-Sculpt® and Comeld® processes. Regarding the texturing procedure, strength prediction models of the joints between fiber reinforced polymers and metals are studied in [23], a comparison between Finite Element method and meshless method to the multi-region problems were performed in [24], optimisation of the protrusion geometry using FE analysis is included in [25] and a micro-macro FE model was developed in [26] to investigate the failure modes in this attractive method to join composite-metal structures.

1.2.1 Adhesive joints in composite materials

Not only a proper material selection is necessary to get a system able to overcome all the requirements, even further in large structures involving many components. If the arguments of composite materials industrial employment are revised (high strength-to-weight ratio, high stiffness-to-weight ratio, high fracture toughness, fatigue life and environmental protection), one can examine other structural resources that may contribute to these goals. In the case of aerospace structures, multiple elements have to

be connected each other and this challenge represents an optimistic scenario in which striking developments may lead to more efficient designs. Unlike over conventional mechanical fasteners, adhesive bonding shares many of the composite material advantages such as high strength-to-weight ratio, design flexibility, damage tolerance, fatigue resistance. So, it is worth analysing the capabilities of this joining technology and determining the potential impact upon lightweight constructions.

Some aspects must be accounted for achieving a good performance of the adhesive joints. The manufacturing bonding process is essential to understand the subsequent failure mechanism and joint strength. Co-bonding method adhesively joins one cured substrate to an un-cured substrate whereas two un-cured substrates are linked in a co-curing technique. Other actions can be carried out, as a secondary bonding connecting two cured parts or multi-material bonding, where a composite cured part is bonded to metals, ceramics, etc. The strength of the joints vary according to the manufacturing bonding process [27, 28], however, not always the configuration can be chosen. This depends upon the function, complexity and scale of the parts, number of curing cycles, etc. Surface preparation is the key in every bonding procedure since favourable conditions are established in physical and chemical terms. Clean and active surfaces are desirables, so contaminant removals (dust, lubricants, corrosion layers), surface wettability and surface energy are present in most of surface treatments [29–31]. In this line, peel ply technique [32–34] represents an appealing method to protect the joint from environmental contamination (dust, moisture) and to create a high energy surface. Otherwise, some geometrical parameters of the adhesively bonded joints influence the quality and the durability such as the bondline thickness, the overlap length and the joint configuration. The effect of the adhesive thickness has been investigated for a wide range of mixed mode conditions [35–37]. Different trends are found relying on the ductile or brittle character of the adhesive [38], Mode I, Mode II, or mixed loading, the adherent mechanical properties, geometry of joints, etc. The joint configuration needs to avoid stress concentration and distribute the stresses correctly [39, 40]. Thus, general dimensions in adhesive joints (adherent and adhesive thickness, width, tapered thickness and length, stacking sequence, ply angle, fillet, etc) deserve to be studied.

Most common adhesives in structural applications are the epoxy polymeric materials (high strength and temperature resistance), cyanoacrylates (low resistance to moisture and temperature, fast bonding), anaerobics (suitable for cylindrical shapes), acrylics (fast curing in non-treated surfaces), polyurethanes (flexibility at low temperatures and fatigue life), silicones (used as sealant, flexibility, high-temperature resistance) and the phenolics, polyimides, and bismaleimides for high-temperature applications. Usually epoxy-based adhesives are employed in composite matrix bonding due to the compatibility between resin and adhesive.

With respect to an environmental perspective, there is a major concern regarding the reuse, the recycling and the recovery of bonded parts, therefore many researchers are developing some techniques to disbond the joint without damage [41, 42]. Apart from this ecological technique, high-performance renewable natural adhesives (bioadhesives) are currently investigated so as to substitute synthetic adhesive and to avoid any natural damages [43]. In addition, a new generation of adhesives with further capacities such as self-healing or easy recycle processes are in demand nowadays and some approaches

respecting material and particle addition were studied [44]. Further information about adhesively bonded joints in composite materials are available in [45, 46].

1.3 Biomimetics and bioinspired structures

The term biomimetics was coined by Otto Schmitt [47] in the 1950s to denominate "the study of the formation, structure, or function of biologically produced substances and materials (as enzymes or silk) and biological mechanisms and processes (as protein synthesis or photosynthesis) especially for the purpose of synthesizing similar products by artificial mechanisms which mimic natural ones". That is, investigating biological phenomenon with the aim of developing physical or engineering systems. There are numerous examples of bioinspiring designs such the chinese silk, that tried to imitate the spider silk; Leonardo's artefacts tried to mimic the bird flights or the Velcro® [48], that creates a novel zip fastener derived from the action of the hooked seeds of the burdock plant.

Outstanding results can be borrowed from nature, nonetheless a kind of translation or interpretation should be made to transfer the natural concept or mechanism to an artificial system or an engineering adaptation. In order to achieve a proper transition between nature and engineering fields, Vincent [49] proposed an interesting framework based upon a problem-solving system. It was originally developed in Russia [50] for general purposes and it was named TRIZ (Teorija Reshenija Izobretatel'skih Zadach), whose English translation can be "Theory of Inventive Problem Solving". The adaptation of this method to biology can be found in [51, 52]. This tool enables deconstructing the problem and getting a new solution from the features derived from other solved problems, with thousand of precedents in nature.

Hence, nature constitutes a vast source of information from which researchers can get inspired to develop new materials and structures. Additionally, hard biological materials, i.e. those characterised by their stiffness and strength (bones, teeth, seashell, wood), are made of a limited number of constituents (minerals like calcium, silica or hydroxyapatite and proteins such as cellulose, lignin, keratin, collagen) and they follow different strategies to perform many functionalities (mechanical support, environmental protection, cutting or crushing devices, etc) [53]. So, a combination of various properties, mainly stiffness, strength and fracture toughness [54], will be established as a function of the structural requirements. In fact, Wegst & Ashby [55] classified biological materials according to their stiffness, density, strength and fracture toughness, as depicted in Fig. 1.4. This study allows an overview of the natural material properties to be observed and shows the high level of efficiency of such elements. Unfortunately, the natural materials are optimised at each structural level (molecular, molecular assembly, micro-composite, cellular, macrocomposite, etc) and not always the man-made structures can deal with such a level of hierarchical organization. Consequently, despite of the technological controversies, many of the natural features responsible of the efficient designs can be exploited. From the mechanical point of view, the exceptional macroscopic properties can be achieved thanks to a wise load, stress and damage distribution, and an effective energy dissipation and resistance to crack propagation.

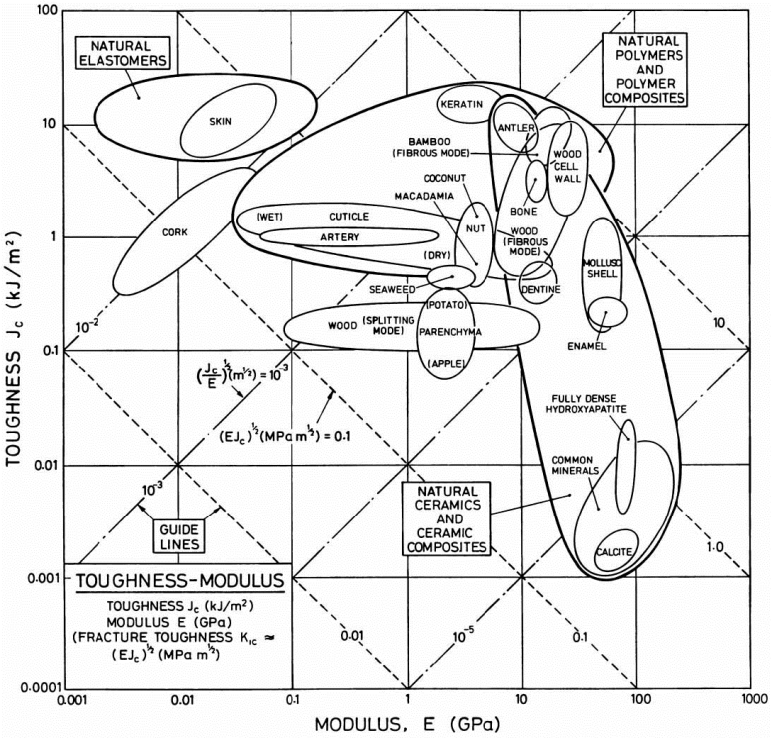

Figure 1.4 Toughness versus stiffness in biological materials. Reprinted from [55].

Naleway [56] arranged the most common structures in the biological materials on account of similar solutions for natural difficulties. In this respect, eight "structural design elements" were encountered as principal designs in the animal taxonomy (see Fig. 1.5 for a graphical representation):

1. Fibrous structures: taking advantage of high tensile strength of the fibers in a single direction. This technique is used when high stiffness in a certain diretion is required. It appears at nano- to micro-scale in nature and it presents high tension level but low or null compressive properties. Fibrous structures can be found in spider silk [57] or the hagfish slime threads [58].
2. Helical structures: offering increased strength and toughness via fibers, fibrils or reinforcements arranged in multiple directions and can be referred to as twisted-ply structures. This arrangement differs from fibrous structures in the in-plane isotropy, improvement of torsional stiffness and the appearance in the macroscopic level. Some examples are the crustacean exoskeletons [59] or the fish scales [60].
3. Gradient structures: progressive evolution of the material properties for the purpose of avoiding discontinuities in the stress distribution. The varying composition generates a gradient field to deal with dissimilar stress level between two materials

at the interface. Gradient strategies resides in the crab claws [61] or the fish scale [62].

4. Layered structures: multiple layers in a bottom-up ply able to increase the toughness due to increment of interfaces. These entities assume large changes in the mechanical properties and they are present in the mechanism responsible for the enhancement of fracture toughness. The abalone and conch, performing layered brick-and mortar architecture, present high fracture toughness due to the existence of interfaces [63, 64].

5. Tubular structures: arrays of aligned pores within the bulk material that enhance the energy absorption by arresting the crack growth and relaxing the stress concentration at the crack tip. Conversely, this micro-scale features decrease the stiffness of the structure and can be placed parallel or perpendicular to the loading direction. Horse hooves [65] and sheep horn [66] are representative examples of energy absorption in tubular systems.

6. Cellular structures: consist of high strength-to-weight ratio structures by means of cell arrangement, scaffold or highly porous materials. Generally, some soft material pattern creates empty spaces that endow structural capacities such as bending and increasing toughness. Usually, these arrangements are surrounded by dense walls or skins, like those employed in sandwich panels. The turtle shell [67] and the bird bones [68] are representative cases of sandwich structures in nature.

7. Suture structures: wavy, patterned or structured interfaces that join two rigid substrates through a compliant interface layer. This technique is required if strength and flexibility of the structure need to be controlled. This system appears in biological organisms such as the carapace of the red-eared slider [69] or the exoskeletal surfaces of diatoms [70].

8. Overlapping structures: are made of singular scales, able to slide each other, attached to a flexible substrate. This method enables a protective surface in an adjustable base and, therefore, it tends to be used as armour. Particular examples of overlapping structures are the shark skin [71] or the chiton exoskeleton [72].

Other material with a great deal of interest in the mechanical field is the nacreous shells, present in the mollusc group and responsible for the external loads protection (impacts, deformation, etc). Nacre is composed of 95% volume of aragonite (brittle) and 5% volume of proteins (compliant). The main feature of such material is the capacity of dissipating mechanical energy through inelastic deformations, which is achieved by means of the hierarchical arrangement at different length scales. In this material, aragonite tablets are stacked in a brick wall like structure, separated by a thin layer of organic material. Constitutive behaviour, damage tolerance, fracture toughness and failure of nacre have been extensively studied using Finite Element simulations [73–78].

Barthelat highlighted the role of the interfaces in the deformation level and energy released in the joined elements [54]. The size, shape and arrangement of the components of biological structures and, consequently, the interfaces between them, determine their main mechanical characteristics, that is, the stiffness, the strength and the fracture

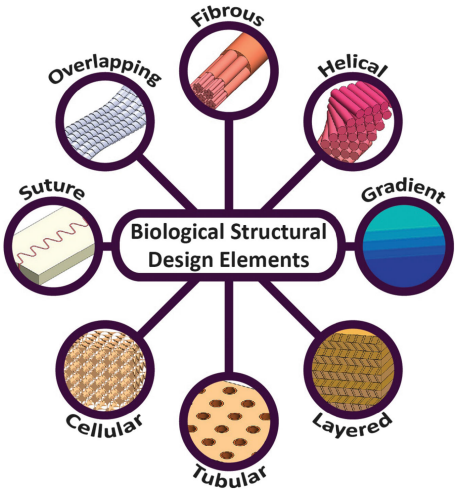

Figure 1.5 Biological structural design elements. Reprinted from [56].

toughness. Thus, the architecture, at different length scales (nano, micro and meso scales), is crucial for getting efficient materials, where deformation and fracture are principally governed by the interfaces [79,80]. Since interfaces are weaker than the bulk material, tortuous arrangements and crack paths can be formed for deformability and toughnening purposes, allowing large inelastic strain that redistribute stresses around defects and cracks. Other mechanisms to improve the toughness is the crack deflection and bridging.

From an engineering standpoint, some structures inspired by the biological materials were tested to modify or control the interface properties. The strain rate hardening were tested in tensile experiments on glass–polydimethylsiloxane (PDMS) nacre-like staggered composites [81]. A bioinspired laser-engraved suture technique was employed in glass bulk [82] in order to predefine the crack path and to create more intricate propagations. In this case, a jigsaw-like pattern describes the interface profile.

In this regard, the current capabilities and promising future advances in Additive Manufacturing (AM) represents a powerful alternative to generate bioinspired motifs so as to evaluate fundamental mechanics and its relation with the structure design via experimental testing. This manufacturing process is interesting due to its inherent ability to perform intricate geometries and to work with different materials. These observations, together with computational simulations and analytical models, will help us to comprehend the efficiency of biological structures. In the literature some successful cases of 3D printed bioinspired architectures can be found: interlocking suture materials including friction and contact in jigsaw-like geometries was investigated in [83,84], 3D printed bone-like specimen using a brick-and-mortar structure creates high-toughnening mechanisms [85], mechanics of suture joints connecting stiffer components (containing triangular, rectangular, trapezoidal, anti-trapezoidal shapes, etc), hierarchical and fractal-like interfaces, the influence of wave-form geometry and their length parameters (such as the amplitude and the wavelength, among others) were the subject matter in [86–90].

Stiffness, strength and toughness, as well as load transmission, tailored stress field and different kind of failure were deeply investigated.

It is remarkable the work developed by Zavattieri and colleagues, in which some of the biological structural design elements were tested in engineering structures: sinusoidal interfaces between different adherents under remote Mode I loading were studied using cohesive finite elements [91] and tested in metal coupons [92], the problem of the crack growth behaviour in Bouligand or helicoidal structures was treated theoretically using LEFM [93] and expiremental in glass fiber reinforced 3D printing helicoidal composites [94], analytical and finite-element models were correlated through the J-Integral to understand the role of the shape of geometrically patterned interfaces behind the crack tip [95].

Finally, Fig. 1.6-1.7 show the correlation between biological and bioinspired engineering suture or structured interfaces. In the subsequent chapters the advantages in the fracture properties of this structural design element is analysed.

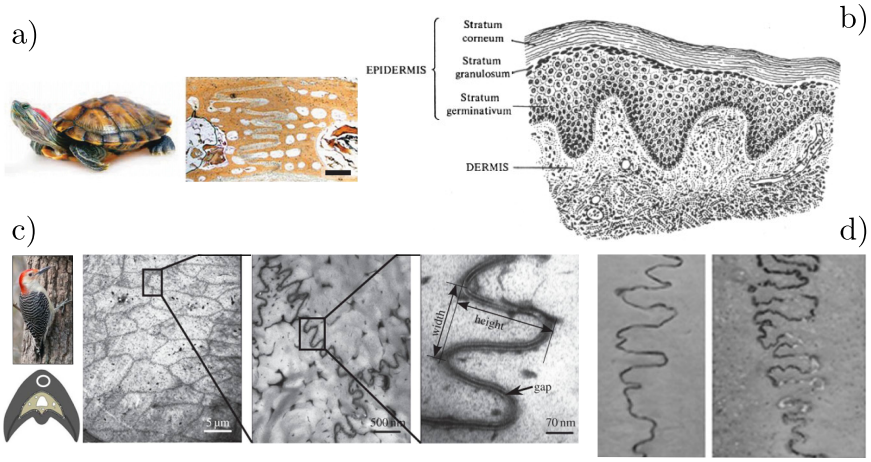

Figure 1.6 (a) Red-eared slider (Reptilia) with osteoderm sutures (adapted from [68] and [69]), (b) Structure of mammalian skin (adapted from [96]), (c) transmission electron microscope cross-section image of the woodpecker's beak at different length scales (adapted from [97]), (d) cranial sutures (adapted from [98]).

1.4 3D printing: state of art

As aforementioned in the previous section, the hierarchical level at various scales and the relevance of the arrangement of the different elements in a structural system lead to an extraordinarily complex and highly intricate designs. This is where 3D printing or Additive Manufacturing (AM) comes into play. This novel technology consists of reproducing 3D models from a Computer-Aided Design (CAD) by means of successively

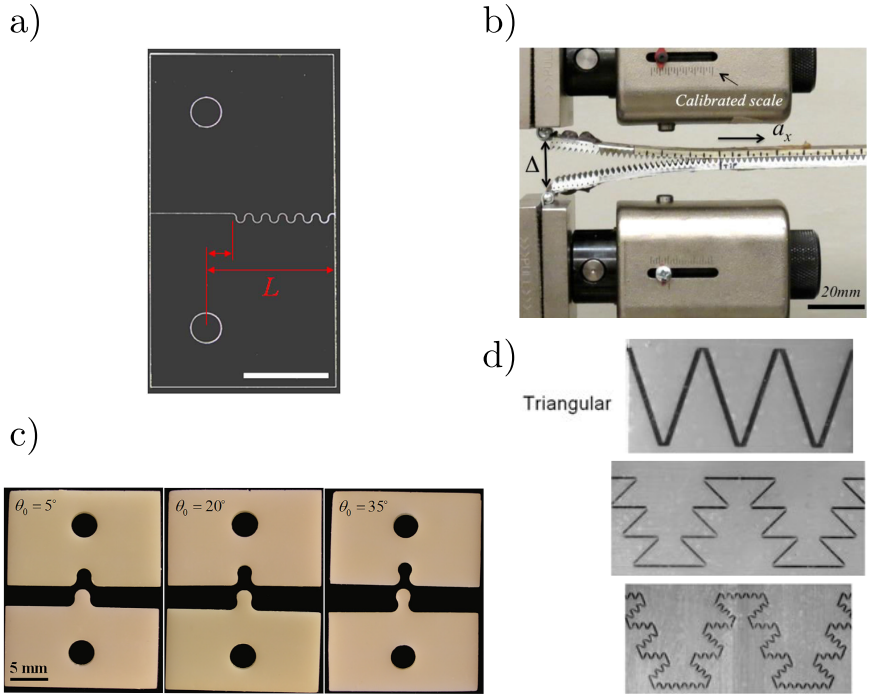

Figure 1.7 (a) A jig-saw-like interface laser engraved glass specimen (adapted from [82]), (b) sinusoidal DCB interface in a metal specimen (adapted from [92]), (c) 3D printed samples with interlocking suture (adapted from [84]), (d) ammonite inspired design of hierarchical suture interfaces with triangular patterns in 3D printed parts (adapted from [89]).

adding material layer on top of each other and it is characterised by the manufacturing of complicate structures and complex geometries. The first example of this method was the stereolithography (SLA) process developed by Hull in 1986 [99], although new processes emerged afterwards. In the first stage of this technology, AM was employed by architects and designers as a rapid prototyping tool thanks to the profitable, fast and high level of customisation of such prints. It was not until a few years ago when the employment of 3D printing in actual products in some industries like aerospace, construction or biomedical started. However, the mechanical properties, the anisotropic behaviour and the low production-rate of 3D printed parts in comparison with conventional industrial materials and processes restrict the large-scale products and mass-production. It is worth mentioning that the 3D printing advantages over conventional manufacturing such as material savings, flexibility in design, customisation and high-precision production of sophisticated shapes make that AM was deeply investigated and it was considered one of the fabrication processes of the future. Consequently, at present the 3D printed parts are confined to highly customised models (implants and devices for medical use, rapid prototyping, jewellery) and low-rate production elements (satellites, aircraft, robots,

etc).

Different AM methods, based on layer-by-layer deposition, were developed as a function of the material employed (polymer, metal, ceramic), the layer resolution, size of the part or the surface quality [100]. The main additive manufacturing methods are:

1. Fused Deposition Modelling (FDM) or Fused Filament Fabrication (FFF): a continuous filament of a thermoplastic material is heated in a nozzle up to reach a certain temperature and it is extruded on the printing bed or previous layers following a particular trajectory. Layer thickness, filament width, filament orientation, extrusion, print head speed and air gaps are the principal parameters in the printing process that influence the mechanical properties. Usually, thermoplastics offer weak mechanical properties but fiber-reinforced composites using FDM methods constitute an appealing alternative to enhance stiffness and strength [101].
2. Powder Bed Fusion (PBF): a heat source (laser beam or thermal print head) consolidate or fuse together the particles of metal powder layer previously spread and packed on a platform. Consecutive layers of melted powder will form the 3D metal printed part. The packing process, the powder size and distribution and the technique to fuse the metal (Selective Laser Sintering, SLS, and Selective Laser Melting, SLM) are crucial in the final mechanical properties [102, 103].
3. InkJet Printing (IJP) and contour crafting: small amount of material is drop-on-demand deposited, as an ink, through an injection nozzle onto specific location of the substrate. The droplets solidify tracking a continuous pattern and the solid is strong enough to hold the subsequent layers. This method is mainly used in ceramics for complex structures such as scaffolds for tissue engineering. The analogous process for large building structures is called contour crafting, which uses concrete paste or soil. The principal factor that determine the additive manufacturing performance are the ink viscosity and solid content, the particle size and distribution, the extrusion rate, nozzle size and speed of printing [104].
4. Stereolithography (SLA): a UV light or electron beam triggers photochemical processes in which the monomers transform to polymer chains. After polymerization, the layers are hold when the resin is solidified after the polymerization. Some post-process are employed to improve the mechanical properties of the parts. The monomers can be combined with other particles (ceramic, nanocomposites) for specific applications. The curing process and the kinetic of the reaction are the most critical points.
5. Direct Energy Deposition (DED): a laser or electron beam is applied into the powder or wire material just before the nozzle deposition, so that the melted material is deposited into the melted substrate and solidifies when the heat source no longer act in such region. Unlike the PBF process, the DED does not employ a powder layer, but the material feed is carried out similar to the FDM process using a high amount of energy for melting metals. In other words, it is similar to a welding process embedded in a FDM nozzle. This method is not as versatile to manufacture complex geometries as the PBF but it accepts multiple-axis deposition and multiple materials.

6. Laminated Object Manufacturing (LOM): sheets or rolls of materials are accurately cut (via laser or mechanically) and bonded together. This approach allows a wide range of materials to be exploited (polymer composites, ceramics, paper, metals) and post-processing (generally thermal treatments) is required to get satisfactory properties.

The principal materials employed in the AM processes can be divided in four groups:

1. Metals and its alloys: titanium and its alloys, steel alloys, a few aluminium alloys, nickel alloys, cobalt-based and magnesium alloys have been adapted for AM, mainly for PBF and DED procedures, although new techniques emerged in the last few years [105–107]. Each material presents individual advantages over the others, but the titanium alloys are the most common substance because of the high machining cost on the conventional manufacturing processes. With regard to aluminium, a material cheap for machining, it is interesting for AM due to high thermal conductivity that allow fast fabrications. AM metal parts can present similar performance to that of conventional manufacturing if the porosity and contaminants are controlled in the process. Finer microstructure and anisotropic behaviour in the printing direction are encountered in AM compared to traditional methods. Moreover, high surface roughness and poor layer bonding decrease the fatigue life of AM components. Nevertheless, post-manufacturing treatments, such as Hot Isostatic Pressing (HIP), polishing or chemical etching can reduce the surface roughness and enhance the fatigue behaviour. For these reasons, metal AM is suitable for the manufacturing of complex and lightweight elements, being optimised for lowering tooling costs and saving part assemblies in the biomedical and aerospace industries.
2. Polymer and composites: thermoplastic filaments, reactive monomers, resin and powder are the basic forms of polymer for additive manufacturing. The moulding and extrusion are the competing traditional methods, which are characterised by the cost-effective parts. The nature of these polymers lead to weak components and innovative methods are being developed to enhance the mechanical properties and performance [108, 109]. Polystyrene, polyamides and thermoplastic elastomers are used in Selective Laser Sintering (SLS), whereas thermoplastic polymers(e.g. acrylonitrile-butadiene-styrene copolymers (ABS), polycarbonate (PC) and polylactic acid (PLA)) could be processed by various 3D printing methods like SLA, FDM, or inkjet printing. In this regard, fiber-reinforced polymers were considered a forward movement to high-performance 3D printed composites [110]. Nanomaterials are also an AM alternative to improve the strength and the electrical properties of 3D printed parts [111, 112]. Further research resulted in the appearance of Nylon 6 in the FDM processes as an alternative to ABS [113]. These advancements in improved 3D printing materials show a great potential for their industrial manufacturing, however some drawbacks (limitation of printable materials, mechanical properties, speed and repeatability) should be overcome.
3. Ceramics: inkjet (suspension), powder bed fusion, paste extrusion and stereolithography are the main techniques and they are used in advanced lightweight

porous or lattice components for special applications, for example flexural strength [114] or high specific strength honeycomb structures [115]. Widening the materials for 3D printing of ceramics, dimensional accuracy and optimisation of the arrangement of material in the part are the current key challenges.

4. Concrete: is a recent material included in the AM methods, being the inkjet printing (with larger nozzles and high pressure, also called contour crafting) the most used in building structures [116]. Interlayer adhesion is considered one of the major issues in this process, but holds growing expectations in the automated construction.

Regarding the principal applications of industrial 3D printing manufacturing, it is the aerospace sector in which most AM parts are demanded. This fact is promoted by the mutual agreement between the requirements of aerospace industry and the advantages and characteristics of additive manufacturing:

- Complex geometry: the numerous parts with different functionalities involved in the manufacturing process may lead to intricate shapes.
- Waste of expensive materials: titanium, nickel-based or high-strength steel alloys require large amount of material that is not part of the final component due to the manufacturing method, for instance machining.
- Customised production: small batches are more profitable in AM.
- On-demand manufacturing: fabrication of AM components can reduce the storage of parts and the associated cost.
- Strength- and stiffness-to-weight ratio: the 3D printing allows lightweight elements to be produced.

Additive manufacturing has been employed using DED in titanium structural parts for the Boeing 787 Dreamliner or the first advanced Ariane 6 nozzle (SWAN) for the Vulcan 2.1 engine produced by ArianeGroup. PBF were exploited in the bracket of the Airbus A350 XWB, titanium fuselage and engine pylon components in Airbus A350 XWB and Airbus A320. FDM parts were used in the NASA's Mars rover and in the V-22 Osprey of Bell Helicopter. Other potential of 3D printing manufacturing in the aerospace industry is the repairing of components because of the inherent ability to adapt to different geometries and the possibility to produce on-demand parts in a short period of time.

With respect to fiber-reinforced composites in FFF additive manufacturing, such as Glass Fiber-Reinforced Polymers (GFRP), Carbon Fiber-Reinforced Polymers (CFRP) among others, the stage of development is lower than that associated with metal 3D printing. Because of the low mechanical properties compared to conventional metals, one of the most common applications of the current FFF materials is to serve as tooling or mould for traditional composite manufacturing and, therefore, it is somewhat restricted to small parts. Fiber-reinforced polymers for FFF have demonstrated dimensional stability for printed Vacuum Assisted Resin Transfer Molding (VARTM) tool [117] and autoclave tool [118] with negligible deviation with respect to the initial design.

Notwithstanding, the Big Area Additive Manufacturing (BAAM) (6m length × 2.5m width × 1.8 m height) [119] and the Large Scale Additive Manufacturing (30 m length × 3 m width × 1.5m height) [120] systems have been developed for large scale fiber-reinforced 3D printing, able to manufacture at material output rates up to 45 kg/h and 226 kg/h, respectively.

Several types of fiber reinforcements can be found in the related literature: short fibers [121, 122], nanofibers [123, 124] and continuous fibers [125–127]. Such reinforcements are embedded in thermoplastic matrix materials like Nylon, PLA, ABS, polyphenylene sulfide (PPS) and polyetherimide (PEI). With regard to short fiber-reinforced parts, the highest stiffness was found in carbon fiber reinforced PPS printed with the Composite Additive Manufacturing Research Instrument (CAMRI) system at Purdue University with 26.4 GPa for a 50 wt% (percentage by weight) in short fibers. However, this material cannot be compared to the mechanical capabilities of high-performance aluminium. Length of the fibers, damaging of the fibers during the extrusion process and the reduced aspect ratios [128], along with voids, are the main reason of the lessened stiffness and strength.

Otherwise, continuous fiber-reinforced materials and technology have been growing in the last few years. Markforged® was the first company in marketing continuous fiber-reinforced 3D filaments, providing Kevlar, glass and carbon fiber-reinforced composite filaments. Other companies such as Arevo® or Orbital Composite® offer different options of continuous fiber-reinforced printed parts. The former one supplies multi-axis printing using continuous fiber in customised products like bicycles or helmets whereas the former one patented a coaxial extrusion printing to produce continuous fiber composites onto curved surfaces and multifunctional composite structures made of wire and different types of elements. In contrast, Continuous Composites® is able to print parts with any continuous fibers including aramid, glass and carbon fiber, copper, nichrome wire and fiber optics using a high-speed UV-cure printing process with thermoset resins unsupported into space through the CF3D® process. So, the manufacturing is not limited to 2D slices, but fibers can be oriented in every direction and on the fly designs are produced thanks to advanced robotics. This company patented the CF3D® printing process, which enables around 50-60% fiber volume and layer compaction, achieving an insignificant value of porosity.

In conclusion, fiber volume fraction, limited kind of continuous fibers and the fiber wetting in the nozzle are the major concerns in continuous fiber-reinforced 3D printing. The improvement of such features will lead to stiffness and strength values comparable, even better, than aluminium.

Finally, the term 4D printing has emerged derived from the combination of 3D printing and the concept of the so-called smart materials. They are defined as materials able to change their shape or properties between different physical domains in a useful manner under the influence of certain stimuli from the environment [129]. Hence, 4D printing can be defined as an AM process which involves smart materials in the element fabrication and whose shape or mechanical behaviour can depend upon external stimuli. Some examples of 4D printing are the shape memory alloys (SMAs) [130, 131], 3D printing of shape memory polymers (SMPs) [132, 133], biomedical applications [134] or active origami and controlled sequential folding [135].

1.5 Interface damage modelling methods

As aforementioned in the previous Sections, the presence of interfaces in natural or man-made structures is remarkably widespread, either in the own internal material composition (composites) or the joining of the different parts of such structure. Therefore, the behaviour of interfaces has been addressed from different standpoints in order to understand its role within the system resistance. Basically, adhesively bonded joints can be analysed by means of analytical and numerical methods.

1.5.1 Analytical methods

The principal aim of these approaches is to provide a fast, easy and accurate explanation about adhesive bonding phenomenon, which yields to simplified assumption of such complex problems.

Firstly, in 1938 Volkersen analysed a single lap joint considering uniquely tension in the adherents, shear deformation in the adhesive and constant stress along the thickness [136]. This drastic simplification were improved taking into account the adherent bending and, consequently, the appearance of peeling stresses. Later, a simplified approach assuming perfect elastoplatic behaviour of the adhesive layer was proposed [137]. Over time more accurate and complex hypothesis were established, enabling the study of a wider range of materials and situations [138–140]. Alternatively, constant through-the-thickness adhesive shear stress and varying normal stress was considered to study the bonded joint in sandwich panels [141] and later work included mixed adhesive joints [142]. Adhesively composite bonded joints were studied in [143], where adherents were treated as bending beams, bending plates or general orthotropic laminates (through classical laminate theory) and the adhesive had a linear elastic behaviour. A very thin adhesive in an adhesively bonded single-lap composite joints [144] were investigated analytically via the laminated anisotropic plate theory in adherents, elastic-perfectly plastic behaviour in the adhesive and von Mises criterion. The approach developed in [143] was employed in [145, 146] to incorporate transverse in-plane strain and hygrothermal loads and to determine the in-plane and interlaminar stresses in the adherents.

Mainly, in the majority of the cases presented, both adherent and adhesives were modelled with a particular behaviour (linear elastic, elastoplastic, orthotropic laminates, nonlinear, etc) and employed a relatively easy theory (beam theory, plates theory, laminate theory) to calculate the stress and strain fields to predict the joint failure.

1.5.2 Numerical methods

The Finite Element Method (FEM) became the most valued technique for mechanics simulations during the last decades thanks to its ability to deal with complex geometries and loads and the lack of necessity to assume simplifying hypothesis. Nevertheless, mechanical and fracture characterisation of adhesively bonded joints is not straightforward due to many factors, such as adhesive type, adherent type, cure cycle or bondline thickness, are involved in the definitive properties. Thus, the lack of appropriate fracture criterion is balanced by a large amount of experimental tests.

In this framework, the most relevant approaches are categorized as the continuum mechanics, fracture mechanics and damage mechanics techniques. In the sequel, a short description of such methods is presented, being a comprehensive discussion beyond the scope of the current work.

1.5.2.1 Continuum mechanics

This scheme has been applied in "perfect" joints, that is, the adhesion between adhesive and adherent is complete, and both parts are modelled by continuum elements. Generally, simple criterion like maximum stress [147], strain [148] or energy density [149] are applied. However, the presence of bi-material singularities make this method mesh-dependent.

1.5.2.2 Fracture mechanics

In this approach the fracture toughness of the adhesive is the parameter that controls the failure in an adhesive joint. The fracture properties can be determine by normal and shear deformation taking place at the crack tip, so the concept of mixed mode is extensively used in this field [150]. In the case of Linear Elastic Fracture Mechanics (LEFM), the method employs linear elastic behaviour and the existence of a crack. Nonetheless, the adhesive defects considered herein are not supposed to be cracks and plasticity may appear in the adherents. Consequently, many scenarios would not be eligible for this technique. Alternatively, stress singularity approach (fracture mechanics without initial crack) [151–155] proposes an onset criterion based on the generalised stress-intensity factor at the interface corners.

1.5.2.3 Damage mechanics based on the cohesive-like crack method

Damage modelling consists of monitoring the complete response of the material, from the damage onset to the failure propagation in the same analysis. Local approach (zero-thickness elements) and continuum approach (finite-thickness elements) are used to model damage in the so-called Cohesive Zone Models (CZMs). These areas predefine the crack path and progressive damage and failure are defined by a Traction Separation Law (TSL). That is, tractions are function of the displacements between the nodes of the cohesive elements. These features can be easily implemented in finite-element software by means of user-subroutines, allowing different materials, mechanical and fracture responses to be modelled. Notwithstanding, determining the parameters that characterise such materials is cumbersome and there is not a consensus about the physical meaning of such parameters. Moreover, the meshing procedure and convergence analysis is a challenging task if the cohesive elements come into play, specially in complex geometries. Basically, these parameter are the fracture toughness, i.e. the area under the TSL, and the maximum stress or displacement that delimit the damage onset. Definitely, other features can be conveniently added for more accurate predictions. Hence, these factors will condition the shape of the TSLs [156].

Despite these obstacles, many authors have developed inverse methods in order to acquire cohesive parameter from experiments [157–161]. Double Cantilever Beam (DCB), Mixed Mode Flexure (MMF) or End Notch Flexure (ENF) tests, among others, were employed in the correlation procedures.

On the one hand, the original CZM standpoint interpreted the adhesive layer as zero thickness (appropriate for delamination events) and, consequently, only adhesive or cohesive failure (separately) can be modelled. On the other hand, the current tendency tends towards the combination of more comprehensive scenarios, so that adhesive failure, cohesive failure, and mixed failures in bonded joints can be analysed regardless the geometry of the interface or the loads. In this way, an Adhesive Process Zone Model (APZM) was proposed in [162], which combines cohesive zones with cohesive approach to model interfacial and bulk damage [163]. Another controversy geometrical parameter critical in the joint strength is the bondline thickness and the use of single rows of cohesive elements [164] or solid/continuum elements [165].

Advantages of CZM approach related to adaptability to multiple adhesive behaviour and easy implementation in finite-element commercial softwares can be exploited through different cohesive law shapes (triangular, trapezoidal, exponential, linear, etc). Broadly speaking, there is a general agreement for brittle and ductile adhesive, modelled by means of triangular and trapezoidal shapes respectively [164, 166]. Other events can be included in the cohesive law, e.g. moisture and temperature [167, 168].

Regarding the industrial application, the use of CZM in adhesive joints of large structures is restricted to simple cases due to the models need a great level of refinement in the meshing step and the convergence of the analysis is not guaranteed [169–171]. Some alternatives have emerged to overcome these difficulties such as hierarchical superimposed Finite Element Method [172] or meshless methods [171].

Conclusively, damage modelling exploiting cohesive-like concepts is a relatively recent technique whose advantages and enhanced developments are yet to be arrived in the next years. Major drawbacks, such as cohesive parameters identification, accuracy, or robustness in the convergence computational analysis, have to be overwhelmed in order to extend this field to a wide range of applications.

1.6 Objectives

This study constitutes the first approach of the Elasticity and Strength of Materials Group (GERM in its Spanish acronym) in the bio-inspired design of adhesive joints in composite materials. Previous studies about adhesively bonded joints have been developed in the framework of Fracture Mechanics by means of the investigation of singular stress state at multi-material corners [153–155] or the Damage Mechanics using Cohesive Zone Model for debonding event simulations [173–175]. Therein, fundamental aspects about the adhesive joint performance, most unfavourable area in the joint configuration, accurate characterisation of adhesive properties or the development of new computational tools are the major aims. Notwithstanding, the investigation of improvement techniques within the adhesive joint performance was not carried out so far. Hence, for the sake of clarity, the main goals of this thesis are divided in general and particular objectives.

Concisely, the general purpose of the present thesis is to introduce bio-inspired designs for improvement of fracture properties of adhesively bonded joints and to

address introductory approaches from the experimental, analytical and computational standpoints.

Specifically, the general objectives of this research are:

- Introduce the concept of "bio-inspired" designs and show the potential of this alternative approach as a mechanism to solve engineering problems. Pointedly, adhesion and joining mechanisms present in biological systems have been reviewed in order to identify a suitable method for enhanced engineering adhesively bonded joints.
- Explore the viability of suture or structured interfaces in composite materials by accounting for current manufacturing capabilities such as continuous fiber-reinforced 3D printing.
- Establish a framework for the theoretical and computational investigation of structured interfaces. Simplified analytical models for comparison purposes and elemental considerations in Finite Element Method for damage onset and crack propagation simulations were employed to clearly understand the physics of patterned interface cohesive-like cracks.

The particular objectives are summarised in the following list. The most relevant aspects and achievements reached during the thesis are pinpointed.

- Analyse the feasibility of structured interface manufacturing using composite materials, such as Carbon or Glass Fiber Reinforced Plastics, and propose geometries, shapes and dimensions able to be 3D printed. This constitutes a starting point for experiment configurations, although the parameters will change in the future due to the advancement in manufacturing techniques.
- Experimentally prove the efficiency of wavy interfaces in adhesives joints, in particular through the performance of fracture tests.
- Develop analytical and numerical models for the comprehension of the damage and fracture phenomenon in this kind of structures. Simplified theoretical models considering principal geometrical parameters of the pattern and adhesive properties allow fast approximations to be made. Finite Element models give accurate information about the fracture process zone and satisfactory agreements with experiments can be reached.
- Develop novel computational tools so as to apply concepts of damage mechanics under large displacement scenarios. Expressly, a new procedure to determine cohesive traction-separation jumps or displacements in the Cohesive Zone Model under large displacement conditions was implemented by means of a material user-subroutine.

The manufacturing and design process in any engineering structure requires an extensively investigation about every component and technique that play a role in the structural application. Regarding the materials, special attention is devoted to the microstructure in metals or the distribution/arrangement of the constituents in composites,

as well as their mechanical properties. With respect to manufacturing processes, the surface treatments, where the surface geometry is carefully sculpt at the micro-scale to favour energy dissipation (anodizing, Comeld®, peel ply), are highly appreciated in adhesively bonded joints. In this concern, the joint configuration or, in other words, the geometry at the macro-scale of the substrates and adhesive, is established in the simplest way, that is, considering flat interfaces. Straightforward analysis and easier fabrication methods are the reasons of the extensive employment of such plain geometry. Therefore, with the advent of powerful and innovative manufacturing process and computational resources the optimisation of adhesive joint designs at different length scales can be accomplished.

1.7 Outline

The present thesis is organised in eight chapters. In each chapter some of the aforementioned objectives are deepened in order to specify and show the details needed to properly understand the manufacturing and the mechanics of the structured interfaces. In general terms, this document can be divided into four distinct parts: introduction, first part, second part and conclusions:

The introduction presents the basic terminology and science/technological fields involved in the subsequent sections. The first part serves as a technical introduction in which the fundamentals of the modelling and analysis framework employed in the theoretical and numerical models are introduced. Second part displays the experimental, theoretical and numerical results of the structured interfaces from a fracture and damage mechanics points of view. Finally, the conclusion section points out the principal outcomes of the investigation and future work and developments.

- The introduction chapter shows a review and the state of art of the different aspects that come into play in this research such as composite materials, adhesive bonding of composite materials, biomimetics and bioinspired structures, 3D printing and interface modelling.
- The first part involves Chapters 2 and 3. The basic introduction of Continuum Mechanics and a brief summary of the Finite Element Method is discussed in Chapter 2 and Chapter 3 outlines the main aspects of Fracture Mechanics and interface damage modelling as well as the elemental tools for the nonlinear computational mechanics. Particularly, Linear Elastic Fracture Mechanics (LEFM) is outlined, an overview of the path-independent contour integral J-Integral is presented and fundamental aspects of the Cohesive Zone Models are summarised. Special attention is devoted to the bilinear and the Linear Elastic-Brittle Interface Modelling (LEBIM), the two TSLs employed in the numerical models. Kinematics of nonlinear computational mechanics are introduced for the calculation of posterior cohesive displacements under large rotations and displacements.
- The second part, Chapters 4-7, shows the experimental, theoretical and numerical studies carried out on patterned interfaces. The experimental section, Chapter 4, shows the manufacturing and testing procedures in order to produce the specimens

suitable for the evaluation of the fracture properties in Double Cantilever Beam (DCB) tests. The theoretical section, Chapter 5, provides a model to interpret the experimental results under several simplifying hypothesis and using two different mixed mode criteria, as well as the experimental-theoretical correlation. Chapter 6 details the Finite Element simulations of the patterned interface DCB tests carried out in the experimental campaign (Chapter 4) employing a Cohesive Zone Model with a bilinear cohesive law to characterise the crack path. A numerical-experimental correlation of the load-displacement curves was performed and the corresponding fracture properties were obtained. In addition, a novel J-Integral formulation was developed so as to determine the effective fracture toughness in structured interfaces, regardless the geometry of the crack path. Chapter 7 presents the Finite Element implementation of a novel procedure to determine the displacement in a cohesive element in the context of finite strain or large displacement theory. This innovative formulation is assessed by means of the correlation with experimental data collected from literature and the simulation of hierarchical structured interfaces conducted herein.

- Principal conclusions about the employment of structured interfaces in enhanced-performance adhesive joints are drawn in Chapter 8, whereby future challenges in this field are posed.

2 Basis of Continuum Mechanics and Finite Element Method

Continuum Mechanics is the theory that explains those phenomena related to continuum materials, that is, domains in which the space is totally filled and no voids nor separation within the substance are considered [176]. Some physical scenarios in solids and fluids can be elucidated using this theory.

Despite many scenarios in the structural analysis can be studied by assuming linear elastic behaviour, such an approach is no longer valid in systems where some source of nonlinearity is developed during the deformation process. These nonlinearities emerge from different perspectives: (i) material nonlinearity, in which the constitutive equation that governs the stress-strain relation is explicitly nonlinear, (ii) geometrical nonlinearity, in which the geometrical variations affect to the load transmission, and (iii) nonlinear boundary conditions. So, material nonlinearities are an intrinsic material characteristic, whereas geometrical nonlinearity relies on how the loads and boundary conditions change due to the structure deformation. Hence, this theory can address the study of different materials, such as elastomers, biological soft tissues or elastic-plastic materials and, generally speaking, scenarios where the deformed and undeformed shapes are significantly different.

Both linear and nonlinear continuum mechanics solve an structural analysis by means of the kinematics, stress, equilibrium and constitutive behaviour. Nonetheless, linear mechanics is restricted to small deformations, where the geometrical changes are considered negligible, whilst the nonlinear approach allows large deformations to be examined.

Regarding Solid Mechanics, the fundamental behaviour is ruled by the laws of conservation of mass, equilibrium equations and balance of momentum, the boundary conditions as well as the constitutive relations. Firstly, the material particles $\mathbf{X}$, referred to the initial position of an arbitrary material point, are described by using a Cartesian system $\mathbf{E}_I$ at time $t = 0$. If motion occurs, the current position of such particles $\mathbf{x} = \mathbf{x}(\mathbf{X}, t)$ are defined by the base vector $\mathbf{e}_i$ at a generic time t. $\mathbf{E}_I$ and $\mathbf{e}_i$ are allowed to be different, nonetheless, it is considered initial and current Cartesian basis to be

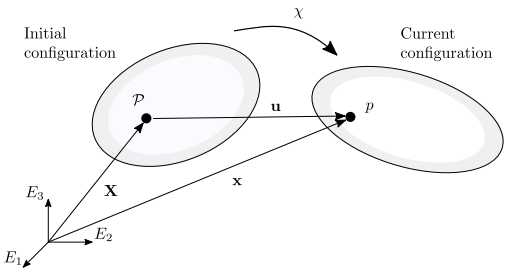

Figure 2.1 Motion of a deformable body and description of the mapping function χ [177].

coincident. The relation between initial and current point configurations, as depicted in Fig. 2.1 is determined by the mapping function χ as

$$\mathbf{x} = \chi(\mathbf{X}, t), \tag{2.1}$$

where the displacement field $\mathbf{u}$ can be inferred as the difference between the current and reference vector positions, according to the expression

$$\mathbf{u} = \mathbf{x}(\mathbf{X}, t) - \mathbf{X}. \tag{2.2}$$

In a deformable body, the position of the material particles is as important as the variation of the relative spatial position between neighbouring points, that is, the change of the vector during deformation. Such variation is described by the deformation gradient tensor $\mathbf{F}$, defined as

$$\mathbf{F} := \frac{\partial \chi(\mathbf{X}, t)}{\partial \mathbf{X}} = \nabla \chi(\mathbf{X}, t). \tag{2.3}$$

In the following, two different descriptions can be adopted in order to describe the behaviour of a system: *material langrangian description* where the variables are referred to the reference configuration prior to the deformation and *spatial eulerian description* where the quantities are referred to the actual or current state during the deformation. Hence, this two-point tensor relates vectors in the material or reference configuration into spatial or deformed vectors according to

$$d\mathbf{x} = \mathbf{F} d\mathbf{X}. \tag{2.4}$$

Likewise, the material or initial vector configuration can be obtained by pulling back the current vector, which is performed using the inverse operator $\mathbf{F}^{-1}$ as follows

$$d\mathbf{X} = \mathbf{F}^{-1} d\mathbf{x}. \tag{2.5}$$

The deformation gradient tensor $\mathbf{F}$ is an adequate tool to describe the motion of the particles and the relative distance between points in a deformable body. So, it represents a valid variable to measure strains in the body and, consequently, to describe the mechanical behaviour of a deformable domain. Principal aspects derived from the

deformation gradient tensor $\mathbf{F}$ associated with strain measures, as well as its physical meaning, is detailed in Section 2.1.

2.1 Strain measures

The description of the motion is fundamental, even further if large deformations or rotations take place in the problem. The differences between initial and current position of a certain particle allows alternative coordinate systems to be defined, which are referred to the material or langrangian and spatial or eulerian description.

The operator $\mathbf{F}$ relates vectors between spatial (deformed) and material (undeformed) configurations, see Fig. 2.2 for a graphical example of simple line transformation).

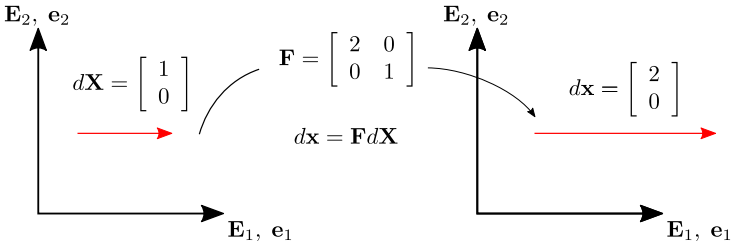

Figure 2.2 Role of the deformation gradient tensor.

Accordingly, different strain measures can be derived from deformation gradient tensor. For a physical interpretation of deformation, let the initial and current square lengths be defined as

$$dS^2 = d\mathbf{X} \cdot d\mathbf{X}; \qquad ds^2 = d\mathbf{x} \cdot d\mathbf{x}. \tag{2.6}$$

The strain will be determined by means of the difference of the material and spatial square length, dS^2 and ds^2 respectively, in terms of material vector $d\mathbf{X}$ as

$$\frac{1}{2}\left(ds^2 - dS^2\right) = \frac{1}{2}\left(d\mathbf{X}^{\mathrm{T}}\mathbf{F}^{\mathrm{T}}\mathbf{F}d\mathbf{X} - d\mathbf{X}^{\mathrm{T}}d\mathbf{X}\right) = \frac{1}{2}d\mathbf{X}^{\mathrm{T}}\left(\mathbf{F}^{\mathrm{T}}\mathbf{F} - \mathbf{I}\right)d\mathbf{X}, \tag{2.7}$$

where $\mathbf{I}$ stands for the second-order identity matrix and the right Cauchy-Green deformation tensor is

$$\mathbf{C} = \mathbf{F}^{\mathrm{T}}\mathbf{F}, \tag{2.8}$$

whereas the Green-Lagrange strain tensor renders

$$\mathbf{E} = \frac{1}{2}\left(\mathbf{C} - \mathbf{I}\right). \tag{2.9}$$

Expressing such difference in square lengths in terms of the spatial vectors $d\mathbf{x}$, one finds

$$\frac{1}{2}\left(ds^2 - dS^2\right) = \frac{1}{2}\left(d\mathbf{x}^{\mathrm{T}} d\mathbf{x} - d\mathbf{x}^{\mathrm{T}}\mathbf{F}^{-\mathrm{T}}\mathbf{F}^{-1} d\mathbf{x}\right) = \frac{1}{2} d\mathbf{x}^{\mathrm{T}}\left(\mathbf{I} - \mathbf{F}^{-\mathrm{T}}\mathbf{F}^{-1}\right) d\mathbf{x}, \tag{2.10}$$

where the left Cauchy-Green tensor is given by

$$\mathbf{b} = \mathbf{F}\mathbf{F}^{\mathrm{T}}, \tag{2.11}$$

and the Euler-Almansi strain tensor is defined as

$$\mathbf{e} = \frac{1}{2}\left(\mathbf{I} - \mathbf{b}^{-1}\right). \tag{2.12}$$

To obtain a strain measure, the difference in length $\left(ds^2 - dS^2\right)$ should be divided by another square length quantity. Referring Eq. (2.7) to dS, the Green's strain according to the initial vector direction is obtained as

$$\varepsilon_G = \frac{1}{2}\left(\frac{ds^2 - dS^2}{dS^2}\right) = \frac{d\mathbf{X}^{\mathrm{T}}}{dS}\mathbf{E}\frac{d\mathbf{X}}{dS} = \mathbf{N}^{\mathrm{T}}\mathbf{E}\mathbf{N}, \tag{2.13}$$

where $\mathbf{N}$ is a unit material vector in the direction of $d\mathbf{X}$. Thus, the material tensor $\mathbf{E}$ characterizes the strain state with respect to the initial configuration according to material directions.

Alternatively, if the Eq. (2.10) is divided by ds^2, one obtains

$$\varepsilon_A = \frac{1}{2}\left(\frac{ds^2 - dS^2}{ds^2}\right) = \frac{d\mathbf{x}^{\mathrm{T}}}{ds}\mathbf{e}\frac{d\mathbf{x}}{ds} = \mathbf{n}^{\mathrm{T}}\mathbf{e}\mathbf{n}, \tag{2.14}$$

where $\mathbf{n}$ is a unit vector in the direction of $d\mathbf{x}$. So, the spatial tensor $\mathbf{e}$ determines the strains state with respect to the current configuration.

Considering the example of Fig. 2.2, which indicates an uniaxial stretch, the previous strain measures are equal to: $\varepsilon_G = 1$ and $\varepsilon_A = \frac{1}{2}$ for the vector $d\mathbf{X}$ due to the fact that initial and current lengths are different to each other ($dS = 1$ and $ds = 2$).

In order to understand the shear components of the deformation gradient, let consider the tensor $\mathbf{F}_2$, responsible of the deformation illustrated in Fig. 2.3. Then, let consider two dissimilar vectors in the material configuration. Herein, $d\mathbf{X}_1 = [1,\ 0]^{\mathrm{T}}$ and $d\mathbf{X}_2 = [0,\ 1]^{\mathrm{T}}$ are considered for the sake of clarity, although others vector can be used without loss of generality.

Following a similar procedure employed to get normal strains, shear strain is obtained through the difference of the scalar product of vectors $d\mathbf{X}_1$ and $d\mathbf{X}_2$ in material and spatial configurations. If such difference is expressed in the material coordinate system, one obtains

$$\frac{1}{2}\left(d\mathbf{x}_1 \cdot d\mathbf{x}_2 - d\mathbf{X}_1 \cdot d\mathbf{X}_2\right) = \frac{1}{2} d\mathbf{X}_1^{\mathrm{T}}\left(\mathbf{C} - \mathbf{I}\right) d\mathbf{X}_2 = d\mathbf{X}_1^{\mathrm{T}}\mathbf{E} d\mathbf{X}_2, \tag{2.15}$$

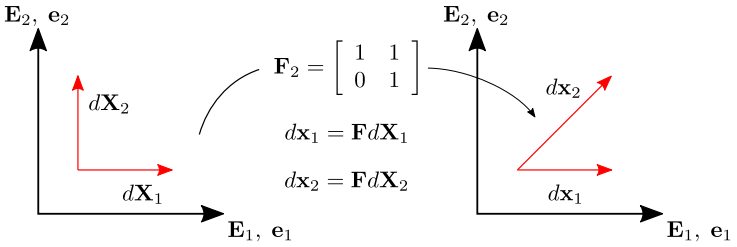

Figure 2.3 Deformation gradient tensor under simple shear motion.

whereas the next expression is computed for the spatial reference system

$$\frac{1}{2}\left(d\mathbf{x}_1 \cdot d\mathbf{x}_2 - d\mathbf{X}_1 \cdot d\mathbf{X}_2\right) = \frac{1}{2} d\mathbf{x}_1^{\mathrm{T}} \left(\mathbf{I} - \mathbf{b}^{-1}\right) d\mathbf{x}_2 = d\mathbf{x}_1^{\mathrm{T}} \mathbf{e} d\mathbf{x}_2. \tag{2.16}$$

If $d\mathbf{X}_1$ and $d\mathbf{X}_2$ and, correspondingly $d\mathbf{x}_1$ and $d\mathbf{x}_2$ presented in Fig. 2.3 are employed in Eqs. (2.15)-(2.16) and dividing such expressions by the corresponding material and spatial norms ($dS_{d\mathbf{X}_1} = |d\mathbf{X}_1|$ and $dS_{d\mathbf{X}_2} = |d\mathbf{X}_2|$ for material configuration and $ds_{d\mathbf{x}_1} = |d\mathbf{x}_1|$ and $ds_{d\mathbf{x}_2} = |d\mathbf{x}_2|$ for spatial configuration) to operate with unit vectors, one obtains

$$\varepsilon_{12,G} = \frac{1}{2} \frac{d\mathbf{x}_1}{dS_{d\mathbf{X}_1}} \cdot \frac{d\mathbf{x}_2}{dS_{d\mathbf{X}_2}} = \mathbf{N}_{d\mathbf{X}_1}^{\mathrm{T}} \mathbf{E} \mathbf{N}_{d\mathbf{X}_2}, \tag{2.17}$$

$$\varepsilon_{12,A} = \frac{1}{2} \frac{d\mathbf{x}_1}{ds_{d\mathbf{x}_1}} \cdot \frac{d\mathbf{x}_2}{ds_{d\mathbf{x}_2}} = \mathbf{n}_{d\mathbf{x}_1}^{\mathrm{T}} \mathbf{e} \mathbf{n}_{d\mathbf{x}_2}, \tag{2.18}$$

where $\mathbf{N}_{d\mathbf{X}_1}$ and $\mathbf{N}_{d\mathbf{X}_2}$ are unit vectors along the material directions $d\mathbf{X}_1$ and $d\mathbf{X}_2$, respectively, and $\mathbf{n}_{d\mathbf{x}_1}$ and $\mathbf{n}_{d\mathbf{x}_2}$ are unit vectors along the spatial directions $d\mathbf{x}_1$ and $d\mathbf{x}_2$, respectively.

Hence, the geometrical interpretation of the shear components in the strain tensor, $\varepsilon_{12,G}$ and $\varepsilon_{12,A}$, can be conceived as the change in the direction between two perpendicular material vectors.

2.2 Polar decomposition and evaluation of strain and stress fields in the conventional continuum element formulation

In this Section, the role of the deformation gradient $\mathbf{F}$, its physical interpretation and the different strain measures $\mathbf{E}$ and $\mathbf{e}$ are succinctly reviewed. This development is essential to understand the calculation of the strain and stress measures in regular solid finite elements and to identify the key variables that change with respect to the novel interface element established in Section 7.1.1.2. Special attention is devoted to the role of the spectral or polar decomposition of the deformation gradient tensor (Fig. 2.4) according to

$$\mathbf{F} = \mathbf{R}\mathbf{U}, \tag{2.19}$$

$$\mathbf{F} = \mathbf{VR}, \tag{2.20}$$

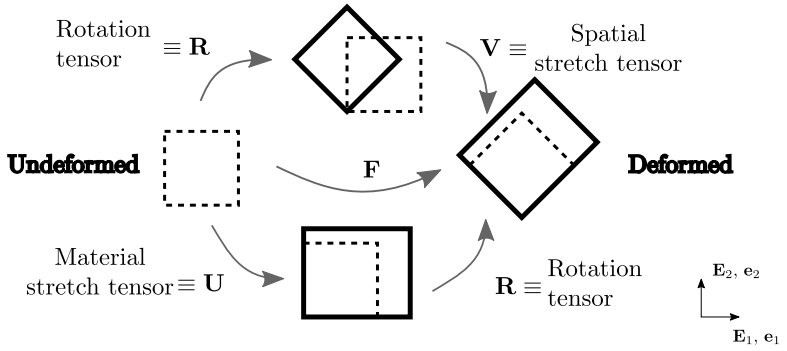

Figure 2.4 Two-dimensional representation of polar decomposition. Deformation gradient **F** is divided into the stretch component, through material stretch tensor **U** or spatial stretch tensor **V**, and rotation component, by the rotation tensor **R**.

where former expression corresponds to the material or lagrangian description and the latter one corresponds to the spatial or eulerian description. In the material description the variables are referred to original or initial coordinates **E**, as long as the spatial description describe magnitudes in the current position in space **e**. Hence, on the one hand, for a material description the solid is deformed in first place and rotated afterwards. On the other hand, the solid is first rotated and then stretched in the spatial description. Further details about nonlinear continuum mechanics can be found in [177].

In this way, different descriptions of the deformation can be perceived as a function of the rotation or stretch tensor definitions.

The formulation employed to calculate strain and stress quantities under large displacement conditions is summarised in this Section. To this end, let the right Cauchy–Green deformation tensor be defined by the polar decomposition as

$$\mathbf{C} = \mathbf{F}^T\mathbf{F} = \mathbf{U}^T\mathbf{R}^T\mathbf{RU}. \tag{2.21}$$

Due to rotation tensor **R** is orthogonal, that is, $\mathbf{R}^T\mathbf{R} = \mathbf{I}$, the right Cauchy-Green tensor can be described by the stretch tensor **U** as

$$\mathbf{C} = \mathbf{U}^T\mathbf{U}. \tag{2.22}$$

In the general-purpose continuum elements the reference system is chosen in such a way that the material stretch tensor is symmetric or, in other words, is expressed in the principal directions of the tensor **C** as follows

$$\mathbf{C} = \sum_{\alpha=1}^{3} \lambda_\alpha^2 \mathbf{N}_\alpha \otimes \mathbf{N}_\alpha, \tag{2.23}$$

where λ_α^2 are the eigenvalues of $\mathbf{C}$ and $\{\mathbf{N}_1\,\mathbf{N}_2\,\mathbf{N}_3\}$ are the corresponding orthogonal unit eigenvectors. Considering the symmetry of the material stretch tensor, Eq. (2.22), and the principal directions of right Cauchy-Green tensor, Eq. (2.23), the tensor $\mathbf{U}$ can be formulated as

$$\mathbf{U} = \sum_{\alpha=1}^{3} \lambda_\alpha \mathbf{N}_\alpha \otimes \mathbf{N}_\alpha. \tag{2.24}$$

In the same way, the left Cauchy-Green tensor or Finger tensor $\mathbf{b}$ can be written in terms of polar decomposition as follows

$$\mathbf{b} = \mathbf{F}\mathbf{F}^{\mathrm{T}} = \mathbf{V}\mathbf{R}\mathbf{R}^{\mathrm{T}}\mathbf{V} = \mathbf{V}\mathbf{V}^{\mathrm{T}}. \tag{2.25}$$

Considering the corresponding eigenvector and eigenvalues of $\mathbf{b}$, the spatial stretch tensor is given by

$$\mathbf{V} = \sum_{\alpha=1}^{3} \bar{\lambda}_\alpha \mathbf{n}_\alpha \otimes \mathbf{n}_\alpha. \tag{2.26}$$

Taking into account the relation between $\mathbf{U}$ and $\mathbf{V}$ through Eqs. (2.19)-(2.20), the former expression can be written by means of the material coordinate system according to

$$\mathbf{V} = \sum_{\alpha=1}^{3} \lambda_\alpha \left(\mathbf{R}\mathbf{N}_\alpha\right) \otimes \left(\mathbf{R}\mathbf{N}_\alpha\right). \tag{2.27}$$

Hence, the tensor $\mathbf{R}$ rotates the material eigenvectors $\{\mathbf{N}_1, \mathbf{N}_2, \mathbf{N}_3\}$ into the spatial triad $\{\mathbf{n}_1, \mathbf{n}_2, \mathbf{n}_3\}$:

$$\mathbf{n}_\alpha = \mathbf{R}\mathbf{N}_\alpha, \tag{2.28}$$

whereas the eigenvalues remain constant $\bar{\lambda}_\alpha = \lambda_\alpha$. Fig. 2.5 shows the material triad $\{\mathbf{N}_1, \mathbf{N}_2\}$ and spatial triad $\{\mathbf{n}_1, \mathbf{n}_2\}$ in a 2D analysis, displaying the rotation between initial and current axis under different strain conditions: superimposed rigid body rotation, deformation in principal directions of strain and simple shear. Shaded region indicates the area under consideration in langrangian and eulerian configurations, respectively. Thus, the system $\{\mathbf{N}_1, \mathbf{N}_2\}$ points out the principal direction of strains and the basis $\{\mathbf{n}_1, \mathbf{n}_2\}$ displays the current position of such vectors.

The tensor $\mathbf{R}$ rotates initial axis $\{\mathbf{N}_1, \mathbf{N}_2\}$ to the corresponding current position $\{\mathbf{n}_1, \mathbf{n}_2\}$ and it accounts for rigid body rotations as well as rotations due to the actual deformation. In the case of rigid body rotations along with the rotation of the principal directions caused by strains, the tensor $\mathbf{R}$ is the sum of both mechanisms.

Hence, the tensor $\mathbf{R}$ in regular solid elements is prescribed by the symmetry of tensor $\mathbf{U}$. That is, first the material stretch tensor $\mathbf{U}$ is defined by imposing symmetry and then the rotation tensor is calculated via the polar decomposition $\mathbf{R} = \mathbf{F}\mathbf{U}^{-1}$. In other words, among all the combinations of stretching and rotation to describe the motion between

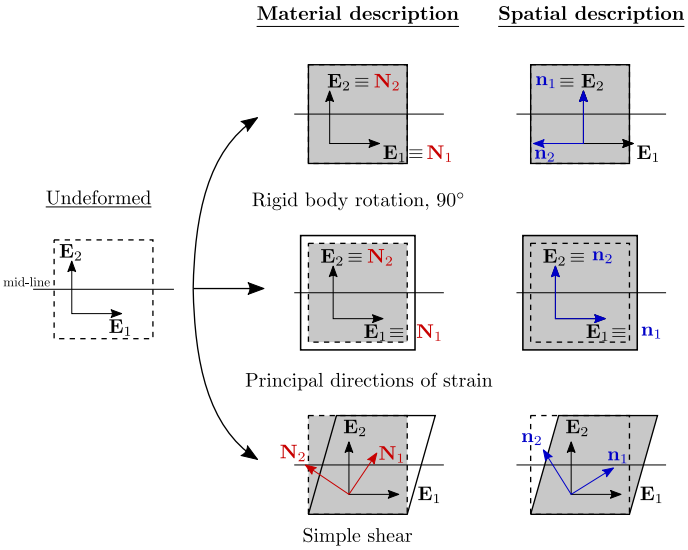

Figure 2.5 Material and spatial coordinate systems under rigid body rotations, deformation in principal directions of strain and simple shear.

initial and current configurations, it is selected the one that undergoes symmetrical deformation followed by the rotation needed to get the final position.

If alternative definitions of rotation and material stretch tensors are assumed, different pairs of $\mathbf{R}$ and $\mathbf{U}$ will be obtained. Fig. 2.6 outlines the consequence of defining different tensors for the same deformation in material and spatial configurations.

2.3 The concept of stress: the Cauchy stress tensor

Let introduce the concept of stress by analysing the action of one region of the body $\mathscr{R}_1$ over a second region $\mathscr{R}_2$ in contact in the deformed configuration, as shown in Fig. 2.7. Considering an spatial or eulerian area Δa with normal vector $\mathbf{n}$ and the resultant forces on such area Δp, the traction vector is defined as

$$\mathbf{t}(\mathbf{n}) = \lim_{\Delta a \to 0} \frac{\Delta p}{\Delta a}. \tag{2.29}$$

Then, studying the translational equilibrium in a reference tetrahedron, the components of traction can be expressed as a function of the components of the stress tensor σ, according to the expression

$$\mathbf{t}(\mathbf{x}, \mathbf{n}) = \sigma(\mathbf{x})\mathbf{n}. \tag{2.30}$$

It is worth mentioning that both area and resultant force are referred to the current configuration, so spatial tensor σ is related to true stress. In Section 2.4.3 we will

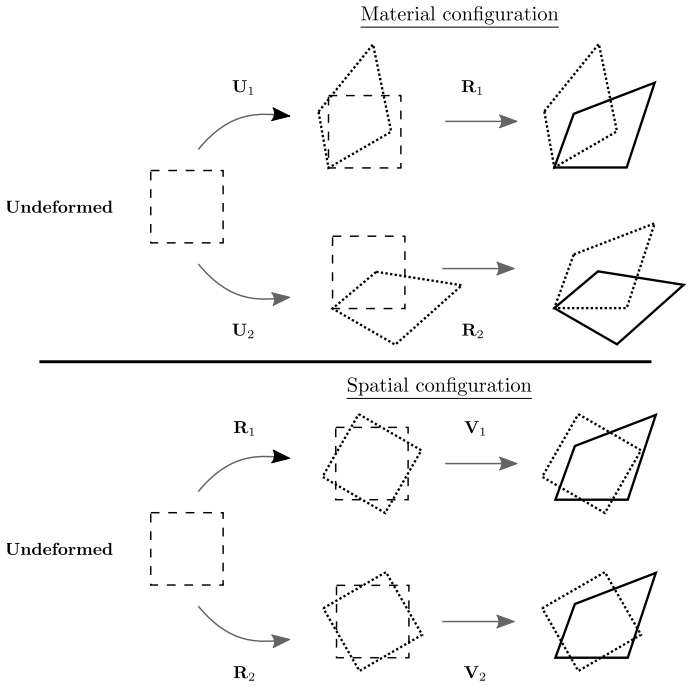

Figure 2.6 Stretch tensor $\mathbf{U}_1$, $\mathbf{U}_2$, $\mathbf{V}_1$ and $\mathbf{V}_2$ as a consequence of different rotation tensor definition $\mathbf{R}$.

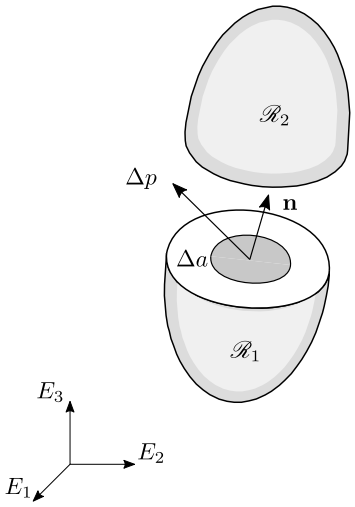

Figure 2.7 Resultant forces Δp over an area Δa in a deformable body.

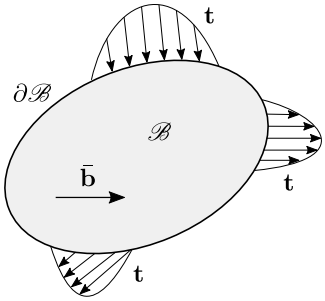

Figure 2.8 Equilibrium of a body $\mathscr{B}$ under the action tractions $\mathbf{t}$ on the boundary $\partial\mathscr{B}$ and body forces $\bar{\mathbf{b}}$ in the volume.

see alternative stress variables that are not associated with the current spatial area. Otherwise, the rotational equilibrium led to the symmetry of the Cauchy stress tensor as

$$\boldsymbol{\sigma} = \boldsymbol{\sigma}^{\mathrm{T}}. \tag{2.31}$$

2.4 Equilibrium and variational principles

2.4.1 Equilibrium

A body subjected to body forces $\bar{\mathbf{b}}$ per unit of volume and traction $\mathbf{t}$ applied on the boundary of the domain, as depicted in Fig. 2.8, is considered to establish the translational equilibrium. For equilibrium under quasi-static conditions, the sum of forces acting in the domain must be null as

$$\int_{\partial\mathscr{B}} \mathbf{t}\,ds + \int_{\mathscr{B}} \bar{\mathbf{b}}\,dv = 0, \tag{2.32}$$

where ds and dv represents the surface and volume differential in the spatial configuration, $\mathscr{B}$ and $\partial\mathscr{B}$ symbolises the body in the current configuration and its corresponding contour. The body and its contour in the initial configuration stand for $\mathscr{B}_{(0)}$ and $\partial\mathscr{B}_{(0)}$, respectively.

If the traction $\mathbf{t}$ is expressed in terms of the Cauchy stress tensor $\boldsymbol{\sigma}$ and the Gauss theorem is applied to the surface integral, the Eq. (2.32) can be calculated by means of the variables of the domain as

$$\int_{\mathscr{B}} \left(\nabla\cdot\boldsymbol{\sigma} + \bar{\mathbf{b}}\right) dv = 0, \tag{2.33}$$

where the operator $\nabla\cdot$ stands for the divergence.

Equalling the integrand of Eq. (2.33), the infinitesimal equilibrium leads to

$$\mathbf{r} = \nabla\cdot\boldsymbol{\sigma} + \bar{\mathbf{b}} = 0 \text{ in } \mathscr{B}. \tag{2.34}$$

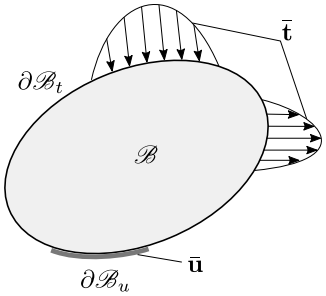

Figure 2.9 Domain $\mathscr{B}$, body contour $\partial\mathscr{B}$ and boundary conditions (prescribed tractions $\bar{\mathbf{t}}$ and displacements $\bar{\mathbf{u}}$ over the contour $\partial\mathscr{B}_t$ and $\partial\mathscr{B}_u$ respectively).

2.4.2 Principle of Virtual Work particularized for the deformed configuration

Generally, Continuum Mechanics governing relations are solved using the *weak form* of the partial differential equations (PDE) or variational principles due to the inconveniences to find an analytical solution of the problem in most of the scenarios.

In this context, let $\mathscr{B}$ to be a solid with a boundary $\partial\mathscr{B}$ in the deformed configuration under static equilibrium in which the displacement field is symbolised by $\mathbf{u}$. Moreover, the domain is subjected to the body forces $\bar{\mathbf{b}}$, tractions $\bar{\mathbf{t}}$ are imposed on the contour $\partial\mathscr{B}_t \in \partial\mathscr{B}$ and displacements $\bar{\mathbf{u}}$ are imposed on the contour $\partial\mathscr{B}_u \in \partial\mathscr{B}$. That is, Neumann bondary conditions are applied on $\partial\mathscr{B}_t$ and Dirichlet boundary conditions are imposed on $\partial\mathscr{B}_u$, so that $\partial\mathscr{B}_t \cup \partial\mathscr{B}_u = \partial\mathscr{B}$ and $\partial\mathscr{B}_t \cap \partial\mathscr{B}_u = \oslash$. A graphical representation of the domain along with boundary conditions is depicted in Fig. 2.9.

The strong form of the boundary value problem is outlined as follows:

- Equilibrium equation: $\nabla \cdot \boldsymbol{\sigma} + \bar{\mathbf{b}} = 0$, where $\boldsymbol{\sigma} = \boldsymbol{\sigma}^{\mathrm{T}}$ because of the balance of the angular momentum.
- Strain-displacement relation: $\boldsymbol{\varepsilon} := \nabla^s \mathbf{u}$.
- Constitutive relations: $\boldsymbol{\sigma} = \mathbb{C} : \boldsymbol{\varepsilon}$.
- Neumann boundary conditions: $\boldsymbol{\sigma}\,\mathbf{n} = \bar{\mathbf{t}}$ on $\partial\mathscr{B}_t$.
- Dirichlet boundary conditions: $\mathbf{u} = \bar{\mathbf{u}}$ on $\partial\mathscr{B}_u$,

where $\boldsymbol{\sigma}$ is the Cauchy stress tensor, $\boldsymbol{\varepsilon}$ is the deformation tensor and $\mathbb{C}$ stands for the tangent stiffness operator or the elasticity tensor. Further information about the constitutive law is included in Section 2.5.

This set of partial differential equations constitute the *strong form* of the elastic problem. Such PDEs are analytically solvable for simple scenarios, including domain, constitutive behaviour and boundary conditions. More complex situations need to be approximated by a *weak form* of the boundary value problem (BVP).

The so-called *weak form* of the problem allows to solve a BVP by employing algebraic equations, which is more convenient and efficient from the computational perspective.

In the field of Solid Mechanics, the *weak form* of the equilibrium equations is performed by the *principle of virtual work*.

In fact, the *weak form* of equilibrium equations can be addressed via variational formulation by using weighting function vectors or minimising a certain functional.

To begin with, let the virtual work per unit of volume δw be defined as

$$\delta w = \mathbf{r} \cdot \delta \mathbf{u} = 0. \tag{2.35}$$

where $\delta \mathbf{u}$ is the arbitrary virtual displacement or the vector-valued test function. Such vector must fulfil the Dirichlet conditions on the boundary $\partial \mathscr{B}_u$. This equivalent expression of the translational equilibrium can be integrated over the body domain as

$$\delta W(\mathbf{u}, \delta \mathbf{u}) = \int_{\mathscr{B}} \left(\nabla \cdot \sigma + \bar{\mathbf{b}}\right) \cdot \delta \mathbf{u} = 0. \tag{2.36}$$

The divergence of the vector $(\sigma \delta \mathbf{u})$ can be expressed as

$$\nabla \cdot (\sigma \delta \mathbf{u}) = \nabla \cdot (\sigma) \cdot \delta \mathbf{u} + \sigma : \nabla \delta \mathbf{u}, \tag{2.37}$$

where the operator : stands for the double product or double contraction operator.

Introducing Eq. (2.37) into the *weak form* of the translational equilibrium and applying the Gauss theorem, the *principle of virtual work* reads

$$\delta W(\mathbf{u}, \delta \mathbf{u}) = \int_{\mathscr{B}} \sigma : \delta \varepsilon dv - \int_{\partial \mathscr{B}} \mathbf{t} \cdot \delta \mathbf{u} da - \int_{\mathscr{B}} \bar{\mathbf{b}} \cdot \delta \mathbf{u} dv = 0. \tag{2.38}$$

The *weak form* of the equilibrium equations in Solid Mechanics can be addressed from an energetic standpoint, where the *principle of virtual work* is retrieved from the minimization of the functional Π. The functional $\Pi = \Pi_{\text{int}} + \Pi_{\text{ext}}$ can be derived from the displacement field $\mathbf{u}$ as long as the material constitutive law and the kinematics are known. The displacement field will be the one that satisfies the minimization conditions and fulfils equilibrium, which involves that the first variation of the potential energy becomes null: $\delta \Pi_{VW}(\mathbf{u}) = 0$. Introducing the internal and external potential energy terms in the functional, the *principle of virtual work* reads

$$\begin{aligned} \delta \Pi_{VW} &= \delta \Pi_{\text{int}}(\mathbf{u}, \delta \mathbf{u}) + \delta \Pi_{\text{ext}}(\mathbf{u}, \delta \mathbf{u}) \\ &= \int_{\mathscr{B}} \sigma : \nabla \delta \mathbf{u} dv - \int_{\partial \mathscr{B}} \mathbf{t} \cdot \delta \mathbf{u} da - \int_{\mathscr{B}} \bar{\mathbf{b}} \cdot \delta \mathbf{u} dv = 0. \end{aligned} \tag{2.39}$$

On the one hand, the displacement field $\mathbf{u}$ should have square integrable first derivatives and satisfy the Dirichlet boundary conditions

$$\mathscr{U} = \{\mathbf{u} \in \mathscr{H}^1,\ \mathbf{u} = \bar{\mathbf{u}} \text{ on } \partial \mathscr{B}_u\}, \tag{2.40}$$

where $\mathscr{H}^1$ is the Sobolev space of order 1. On the other hand, the virtual displacement $\delta \mathbf{u}$ satisfies

$$\mathscr{U}^0 = \{\delta \mathbf{u} \in \mathscr{H}_0^1,\ \delta \mathbf{u} = 0 \text{ on } \partial \mathscr{B}_u\}. \tag{2.41}$$

2.4.3 Work conjugacy

The first term of Equation (2.38) represents internal virtual the work according to

$$\delta\Pi_{\text{int}} = \int_{\mathscr{B}} \boldsymbol{\sigma} : \delta\boldsymbol{\varepsilon} dv. \tag{2.42}$$

The pair $\boldsymbol{\sigma} - \delta\boldsymbol{\varepsilon}$ constitutes a *work conjugate* and is responsible of the virtual work done by internal forces expressed in spatial or eulerian variables, that is, considering the deformed domain.

Other *work conjugate* pairs can be defined relying on the configuration considered in the internal virtual work calculation:

- *Kirchhoff stress tensor* $\boldsymbol{\tau}$:

$$\delta\Pi_{\text{int}} = \int_{\mathscr{B}_{(0)}} \boldsymbol{\tau} : \delta\boldsymbol{\varepsilon} dV; \qquad \boldsymbol{\tau} = J\boldsymbol{\sigma}. \tag{2.43}$$

- *First Piola-Kirchhoff stress tensor* (PK1) $\mathbf{P}$:

$$\delta\Pi_{\text{int}} = \int_{\mathscr{B}_{(0)}} \mathbf{P} : \delta\mathbf{F} dV; \qquad \mathbf{P} = J\boldsymbol{\sigma}\mathbf{F}^{-\text{T}}. \tag{2.44}$$

- *Second Piola-Kirchhoff stress tensor* (PK2) $\mathbf{S}$:

$$\delta\Pi_{\text{int}} = \int_{\mathscr{B}_{(0)}} \mathbf{S} : \delta\mathbf{E} dV; \qquad \mathbf{S} = J\mathbf{F}^{-1}\boldsymbol{\sigma}\mathbf{F}^{-\text{T}}, \tag{2.45}$$

where dV symbolises the volume differential in the undeformed configuration ($\mathscr{B}_{(0)}$).

2.5 Constitutive laws

A description of the kinematics and the strain measures in a deformable body were addressed previously, as well as the concept of stress. Nonetheless, these two physical variables, strain and stress, are related to each other by means of the constitutive equations, that characterise the behaviour of a particular materials, for instance, elastic, viscoelastic, elastoplastic, etc.

The elastic materials represent the simplest constitutive law in Solid Mechanics because the relationship between stress and strain only depends on the deformations of the current configuration. The St. Venant–Kirchhoff model relates stresses and strains of homogeneous, elastic and isotropic materials in the undeformed configuration, so the second Piola-Kirchhoff and the material stress tensor $\mathbf{E}$ are associated under large displacement hypothesis through the general form

$$\mathbf{S} = \mathbb{C} : \mathbf{E}, \tag{2.46}$$

where $\mathbb{C}$ is the fourth order material or langrangian elasticity tensor. Nonetheless, this expression can be written in terms of material properties as

$$\mathbf{S} = \tilde{\lambda}\,(\mathrm{tr}\mathbf{E})\,\mathbf{I} + 2\tilde{\mu}\mathbf{E}, \tag{2.47}$$

where $\mathbb{C} = \tilde{\lambda}\mathbf{I}\otimes\mathbf{I} + 2\tilde{\mu}\mathbb{I}$, being $\mathbf{I}$ and $\mathbb{I}$ are the second and fourth order identity matrix and $\tilde{\lambda}$ and $\tilde{\mu}$ symbolise the Lamé constants. This expression is equivalent to the Hooke's law under small displacements assumptions.

In order to determine the spatial or eulerian elasticity tensor $\tilde{\mathbb{C}}$, the Piola push forward operator $\left(J^{-1}\phi_*[]\right)$ is applied to $\mathbb{C}$ so that the Cauchy stress tensor σ can be associated with spatial symmetrical strain ε by

$$\sigma = \tilde{\mathbb{C}} : \varepsilon, \tag{2.48}$$

where the relationship between material and spatial elasticity tensors in indicial form is

$$\tilde{\mathbb{C}} = \sum_{\substack{i,j,k,l=1\\I,J,K,L=1}}^{3} J^{-1}F_{iI}F_{jJ}F_{kK}F_{lL}\mathbb{C}_{IJKL}. \tag{2.49}$$

2.6 Finite Element Method approximation

Using the Finite Element discretization concept, Eq. (2.39) can be calculated by means of the sum of the integral of individual elements as

$$\sum_e \int_{v^e} \sigma : \delta\varepsilon dv - \sum_e \int_{v^e} \bar{\mathbf{b}}\cdot\delta\mathbf{u} dv - \sum_e \int_{\partial v^e} \mathbf{t}\cdot\delta\mathbf{u} d\partial v = 0, \tag{2.50}$$

where v^e is the element domain, ∂v^e is the element boundary and e the number of elements. To perform such calculation, the domain geometry $\mathbf{x}$ and the displacement field $\mathbf{u}$ need to be approximated by using the nodal positions $\mathbf{x}^a$, the nodal displacements $\mathbf{u}^a$ and the shape functions N^a following an isoparametric standpoint as

$$\mathbf{x} \approx \hat{\mathbf{x}} = \left\{ \begin{array}{c} \hat{x}_1 \\ \hat{x}_2 \\ \hat{x}_3 \end{array} \right\} = \sum_a N^a \left\{ \begin{array}{c} \hat{x}_1^a \\ \hat{x}_2^a \\ \hat{x}_3^a \end{array} \right\} = \sum_a N^a \hat{\mathbf{x}}^a, \tag{2.51}$$

$$\mathbf{u} \approx \hat{\mathbf{u}} = \left\{ \begin{array}{c} \hat{u} \\ \hat{v} \\ \hat{w} \end{array} \right\} = \sum_a N^a \left\{ \begin{array}{c} \hat{u}^a \\ \hat{v}^a \\ \hat{w}^a \end{array} \right\} = \sum_a N^a \hat{\mathbf{u}}^a, \tag{2.52}$$

where index a indicates nodal values. Additionally, through the operator $\mathbf{B}^a$, which contains the derivatives of the shape functions, the strain field can be approximated as

$$\varepsilon \approx \hat{\varepsilon} = \sum_a \mathbf{B}^a \hat{\mathbf{u}}^a, \tag{2.53}$$

whereas the virtual strain field $\delta\varepsilon$ presents an equivalent expression.

Introducing the strain and displacement approximations in the discretized *principle of virtual work*, Equation (2.50), one obtains

$$\left[\sum_e \int_{v^e} \mathbf{B}^a \sigma dv\right] \delta \mathbf{u}^a - \left[\sum_e \int_{v^e} \bar{\mathbf{b}} dv\right] \delta \mathbf{u}^a - \left[\sum_e \int_{\partial v^e} \bar{\mathbf{t}} ds\right] \cdot \delta \mathbf{u}^a = 0. \tag{2.54}$$

Assuming that the constitutive relationship is defined by the operator $\mathbf{D}$, which represents the fourth order tensor $\mathbb{C}$ in Voigt notation, so that $\sigma = \mathbf{D}\varepsilon$ and rearranging the terms, the *weak form* approach, expressed in an algebraic equation system, reads

$$\mathbf{K}_{ab} \hat{u}_a + \mathbf{f}_a = 0, \tag{2.55}$$

where

$$\mathbf{K}_{ab} = \sum_e \int_{v^e} \mathbf{B}^a \mathbf{D} \mathbf{B}^b dv, \tag{2.56}$$

$$\mathbf{f}_a = -\sum_e \int_{v^e} N^a \bar{\mathbf{b}} - \sum_e \int_{\partial v^e} N^a \bar{\mathbf{t}} ds. \tag{2.57}$$

Further information about Finite Element Method is detailed in [177, 178].

3 Fundamentals aspects of Fracture Mechanics

This Chapter constitutes a succinct review about the main concepts employed within the fracture phenomena of materials. Herein, the origin of the discipline denominated Fracture Mechanics and the pioneer works are outlined, as well as the cutting edge models used in advanced Finite Element simulations. In this Section, the different techniques used to measure the fracture properties are explained, and the concepts involved in it. The validity of the assumptions made in this framework along with the advantages and limitations of such theory are also discussed.

The foundational theory of Fracture Mechanics was laid out during World War II, motivated by the catastrophic failure of planes and ships due to the presence of cracks in the material. This is the case of the Liberty Ships in 1942, that had undergone brittle fracture in their hulls while travelling in the cold North Atlantic sea. Such failure was attributed to the decrease of toughness and embrittlement of the steel. Other example of failure induced by cracks are the Havilland Comet in the 1950s, where cracks growing from corners of the square fuselage windows. But, it is only during the beginning of 21st century when Fracture Mechanics becomes popularized by the mathematical sophistication and increased computational power [179].

The basic fundamentals of Fracture Mechanics established before the 1960s were developed for linear elastic materials or globally linear elastic behaviour, that is, small-scale plasticity is confined at the crack tip and it is considered negligible. This approach is called Linear Elastic Fracture Mechanics (LEFM) and it represents the starting point for more sophisticated models. After the solid background provided by Griffith [180] and Irwin [181], among other authors, some assumptions were made in order to characterise the behaviour of nonlinear materials. Elastic-plastic considerations were accounted for techniques like Crack Tip Opening Displacement (CTOD) and the J-Integral so as to enable plastic deformations to be analysed in this framework.

3.1 Linear Elastic Fracture Mechanics

One of the essential concept in Fracture Mechanics, which studies the growth of cracks, is the surface energy or the energy needed to create a new surface. This idea can be addressed from an atomistic standpoint by considering the attractive forces between atoms. The attraction forces between individual atoms are modelled as nonlinear springs and the bond energy can be computed as

$$E_b = \int_{x_0}^{\infty} P dx, \tag{3.1}$$

where x_0 is the equilibrium distance and P the applied force, whose distribution can be approximated by a sinusoidal law as follows

$$P = P_c \sin\left(\frac{\pi x}{\lambda_a}\right), \tag{3.2}$$

where λ_a is the semi-period of the sine wave of the Fig. 3.1.

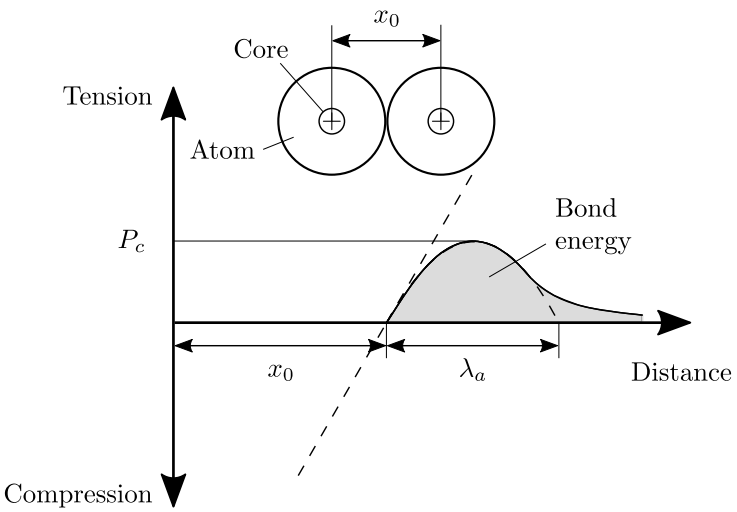

Figure 3.1 Force-displacement curve at atomic scale.

If the attraction distribution is linearized and expressed in terms of force per unit of area, consequently one obtains

$$\sigma = \sigma_c \left(\frac{\pi x}{\lambda_a}\right). \tag{3.3}$$

Subsequently, if stress is expressed by the Young modulus E, the critical stress for the rupture of the bond can be written as

$$\sigma_c = \frac{E\lambda_a}{\pi x_0}. \tag{3.4}$$

So, establishing that two surfaces are created during the crack advance, the surface energy can be estimated as

$$\gamma_s = \frac{1}{2}\int_0^{\lambda_a} \sigma_c \sin\left(\frac{\pi x}{\lambda_a}\right) dx = \sigma_c \frac{\lambda_a}{\pi}. \tag{3.5}$$

Thus, critical stress σ_c can be obtained in terms of surface energy γ_s and material young modulus E as

$$\sigma_c = \sqrt{\frac{E\gamma_s}{x_0}}. \tag{3.6}$$

These simple calculations bring to light that the stress level needed to develop a crack growth is related to material properties such as the stiffness and surface energy. Nonetheless, these approximations do not occur in real structures, where additional factors have to be taken into account, as the rest of the Sections points out.

The disagreement between former calculations and experiments, where the strength were much lower than atomistic predictions in brittle materials, led to consider flaws in the microstructure of the specimen. It was thought that these defects increased the stress locally, compromising the global strength of the structure.

The first study in linear elasticity of flaws was developed by Kirsch in 1898 [182], in which the stress concentrations in holes were analysed. This approach were extended by Inglis [183], who investigated elliptical holes in flat plates. In particular, linear elastic solutions were analysed in elliptical holes of axis $2a$ and $2b$ in an infinite plate loaded perpendicular to the major axis (see Fig. 3.2). This method allows a wide range of scenarios to be included into the analysis, where the stress at the crack tip is determined to be

$$\sigma_{\mathrm{A}} = \sigma\left(1 + \frac{2a}{b}\right). \tag{3.7}$$

The stress concentrator is defined by the relationship $\sigma_{\mathrm{A}}/\sigma$, where σ is the remote applied stress, as displayed in Fig. 3.2. This parameter is 3 at circular holes ($a = b$), as predicted by Kirsch, and it becomes infinity for flattened ellipses ($b = 0$). A more convenient form of Eq. 3.7 to study large aspect ratio scenarios, i.e. $a >> b$, including the radius of curvature ρ as

$$\sigma_{\mathrm{A}} = 2\sigma\sqrt{\frac{a}{\rho}}, \tag{3.8}$$

where $\rho = b^2/a$. This equation enables stress concentration to be calculated in non-elliptical notches except at the crack tip. Moreover, an infinite stress at the crack

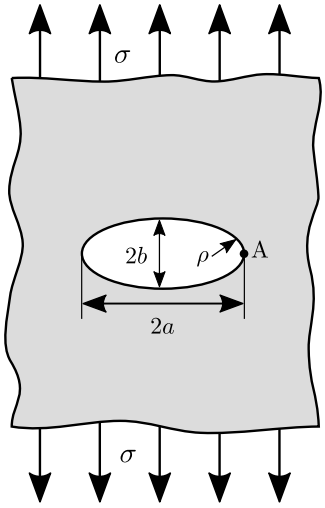

Figure 3.2 Elliptical hole in an infinite plate.

is obtained for sharp cracks ($\rho = 0$), regardless the applied stress. Meaning that, for a small infinitesimal load, the structure would break.

Hence, this contradiction laid the foundation for the development of energy-based criterion, despite there are no evidences of the Linear Elastic Fracture Mechanics (LEFM) in real materials. The First Law of Thermodynamics and the conservation of energy principle state that a crack growth is possible only if the total energy in the system decreases or remains constant. So, the critical condition for fracture propagation is

$$\frac{dE}{dA} = \frac{d\Pi}{dA} + \frac{dW_s}{dA} = 0, \tag{3.9}$$

where E is the total energy, Π the potential energy related to internal strain energy and external forces, and W_s is the work necessary to create a new surface. In other words, the system has two mechanisms in which the energy is stored (potential energy) and released (surface energy). While the plate is being loaded, the system has two alternatives: (i) store the energy in the system, or (ii) create new surfaces by means of a crack advancement. So, in each load step the structure has to answer the next question: would the total energy of the system E decrease (or remain constant) if a crack growth occurs? If yes, the crack propagates in order to achieve new equilibrium conditions. If not, the energy will be stored without crack propagation. In conclusion, the system will attain such states where total energy is minimized.

The Inglis' limiting case ($\rho = 0$) was employed by Griffith to set the energy balance for an increase of the crack area in an infinite plate under tension, that is, the plate width B is much higher than the crack length a and $a << b$ (see Fig. 3.2). Under such assumptions, the strain energy of the plate can be expressed as a function of the crack

length as in

$$\Pi = \Pi_0 - \frac{\sigma^2}{E} B\pi a^2, \tag{3.10}$$

where Π_0 is the uncracked potential energy. The energy required to create a new surface is

$$W_s = 4aB\gamma_s. \tag{3.11}$$

Thus, the critical stress for crack advance can be expressed as

$$-\frac{d\Pi}{dA} = \frac{W_s}{dA} \Longrightarrow \frac{\pi\sigma_f^2 a}{E} = 2\gamma_s \Longrightarrow \sigma_f = \left(\frac{2E\gamma_s}{\pi a}\right)^{1/2}. \tag{3.12}$$

So, as long as the crack advance produces a decrease in the total energy of the system, the propagation will occur. This concept is extremely important in Fracture Mechanics due to the fact that it allows the physical understanding of the material behaviour.

An alternative energy-based approach proposed by Irwin [181] became more suitable for engineering applications, since the energy release rate was defined by

$$G := -\frac{d\Pi}{dA}. \tag{3.13}$$

This quantity represents the change of potential energy with respect to an infinitesimal increment of crack area. According to Equation 3.10, the energy release rate G for a wide plate in plane stress conditions with a $2a$ crack length is

$$G = \frac{\pi\sigma^2 a}{E}, \tag{3.14}$$

and the corresponding critical energy release rate G_c is defined by

$$G_c = \frac{dW_s}{dA} = 2\gamma_s, \tag{3.15}$$

where G_c is a material property called fracture toughness.

The potential energy can be determined from the test procedures, for instance, the cross head displacement and the load applied by the machine as follows

$$\Pi = U - F. \tag{3.16}$$

This approach is also appropriate to asses fracture properties by an experimental setup, where U is the strain energy stored in the body and F is the work done by external forces.

In this concern, beam theories and Strength of Material models can be used to easily obtain strain energy values and the work developed by the external forces, according to load controlled or displacement controlled tests. Most of standards employed to measure fracture properties, in general G_c values, are based on this linear elastic approach and some corrections to account for geometrical nonlinearities [184, 185] are considered.

Emanating from the previous discussion, it can be concluded that, crack propagation is fundamentally determined by two factors: (i) the driving forces or the energy release rate during the test G, and (ii) the resistance to crack propagation or the critical energy release rate G_c. The former feature relies on the configuration of the test and the latter one is a material characteristic. In this way, the crack advance occurs when the energy release rate $d\Pi/dA$ is sufficient to create new areas dW_s and the energy of the system decreases or remain constant, i.e. $G \geq G_c$.

Another interesting approach applicable to certain crack configurations is the stress analysis of cracks developed by Westergaard [186], Irwin [181], Sneddon [187] and Williams [188], in which the stress state is defined by a constant dimensionless functions

$$\sigma_{ij} = \left(\frac{k}{\sqrt{r}}\right) f_{ij}(\theta) + \sum_{m=0}^{\infty} A_m r^{m/2} g_{ij}^{(m)}(\theta), \tag{3.17}$$

where σ_{ij} is the stress tensor, r and θ are the polar coordinates respect to the crack tip and f_{ij} and $g_{ij}^{(m)}$ are dimensionless functions. Higher-order terms are defined by the amplitude A_m and dimensionless functions $g_{ij}^{(m)}$. This means that the vicinity of the crack tip is governed by a singularity that varies according to $r^{-1/2}$ and the proportionality constant k. Nevertheless, the rest of the terms, the amplitude and the dimensionless functions depend upon the loading mode and boundary conditions. The loading modes are: Mode I, load is applied normal to the crack plane; Mode II, in-plane shear where crack surfaces slides along the crack plane or along the initial crack direction; Mode III, out-of-plane shear where crack surfaces slide perpendicular to the initial crack direction. A graphical representation of the modes of fracture is included in Fig. 3.3.

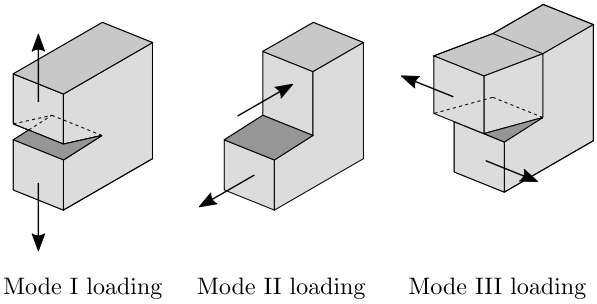

Figure 3.3 Modes of fracture.

Following Westergaard's and Irwin's procedures of an infinite plate with a crack for Mode I loading, the stress state in the area immediately surrounding the crack tip is characterised by

$$\sigma_{xx} = \frac{\sigma_\infty \sqrt{a}}{\sqrt{2r}} \cos\frac{\theta}{2}\left(1 - \sin\frac{\theta}{2}\sin\frac{3\theta}{2}\right), \tag{3.18}$$

$$\sigma_{yy} = \frac{\sigma_\infty \sqrt{a}}{\sqrt{2r}} \cos\frac{\theta}{2}\left(1 + \sin\frac{\theta}{2}\sin\frac{3\theta}{2}\right), \tag{3.19}$$

$$\tau_{xy} = \frac{\sigma_\infty \sqrt{a}}{\sqrt{2r}} \cos\frac{\theta}{2}\sin\frac{\theta}{2}\cos\frac{3\theta}{2}. \tag{3.20}$$

In summary, the stress field under the condition $r << a$ is defined by an asymptote in $r \to 0$ proportional to $r^{-1/2}$ and the factor $\sigma_\infty \sqrt{a}$ for normal and shear directions. So, a single parameter, K_I for Mode I loading, can be used to describe the stress state in linear elastic material in presence of a crack. Equivalent expressions and parameters, K_{II} and K_{III}, can be derived for Mode II and Mode III loading.

Perfectly linear elastic materials with ideal cracks presents a singularity responsible for infinity stresses at the crack tip $r = 0$, regardless the remote load. In general, the fracture is not controlled by the stress of a single point, even though singular stresses are developed in an infinitesimal area, sufficient energy is required to create new surfaces and to break the bonds at the atomic level. Hence, only Stress Intensity Factor (SIF) is meaningful from the Fracture Mechanics standpoint if it is associated with the system energy.

Recalling the infinite plate with crack length $2a$ in Equation 3.9, the SIF can be defined as a function of the failure stress according to the energy criterion as

$$\sigma_f^2 = \frac{GE}{\pi a} \Longrightarrow G = \frac{\sigma_f^2 \pi a}{E}. \tag{3.21}$$

Moreover, if the Stress Intensity Factor, K, is defined in order to get a direct relationship with the energy release rate G, one yields to

$$K^2 = \sigma_f^2 \pi a \Longrightarrow K = \sigma_f \sqrt{\pi a}. \tag{3.22}$$

In this way, the global and local behaviour of the cracked plate are related: the stress, strain and displacement field close to the crack tip is connected to the global energy release rate in a crack growth.

3.2 Nonlinear Fracture Mechanics: J-Integral

The validity of the LEFM is limited by the fulfilment of the initial hypothesis, that is, linear elastic behaviour or, at least, nonlinear behaviour is confined at the crack tip and the global response of the domain can be considered as linear elastic. Nevertheless, numerous engineering materials do not exhibit such performance so that this model needs to be extended in order to cover a wider range of structures. Specifically, elastic-plastic fracture mechanics was introduced in 1960s with the aim of investigating the role of larger plastic areas surrounding the crack tip.

The contour integral developed by Rice [189] allows nonlinear materials to be characterised from the fracture standpoint by considering elastic-plastic laws as nonlinear elastic behaviour.

Rice proved that the energy release rate in nonlinear materials can be characterised by means of the so-called J-Integral and, additionally, the J value characterises stress and strain fields at the crack tip, as stress intensity factor K did in linear elastic scenarios. In order to liken this section to LEFM, the concept of energy release rate for nonlinear elastic laws is presented firstly. As stated in the previous section, let J to be the change of nonlinear potential energy with respect to an infinitesimal increment of crack area

$$J = -\frac{d\Pi}{dA}, \tag{3.23}$$

where Π is the potential energy and A is the crack area. Consequently, the potential energy can be expressed as the difference between the strain energy stored U and the work developed by the external forces F as

$$\Pi = U - F. \tag{3.24}$$

In order to understand J integral in detail, consider a certain portion of the cracked body in 2D, in which A' represents the area bounded by the curve Γ' as depicted in Fig. 3.4, where the potential energy in the absence of body forces is

$$\Pi = \int_{A'} \omega dA - \int_{\Gamma'} T_i u_i ds, \tag{3.25}$$

where $\omega = \int_0^{\varepsilon_{ij}} \sigma_{ij} d\varepsilon_{ij}$ is the strain energy density, $T_i = \sigma_{ij} n_j$ and u_i are the tractions and displacements at the contour Γ' and n_j is the vector normal to the contour.

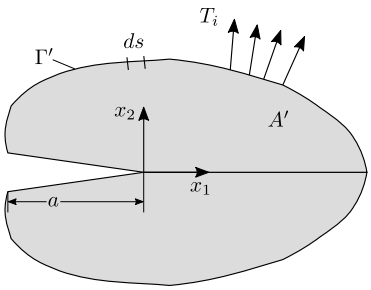

Figure 3.4 General contour in a J-Integral calculation. A' stands for the area within the curve Γ' and T_i represents the tractions along the contour.

The rate of change in potential energy with respect to an increment of crack length a is

$$\frac{d\Pi}{da} = \int_{A'} \frac{d\omega}{da} dA - \int_{\Gamma'} T_i \frac{du_i}{da} ds. \tag{3.26}$$

In regions where displacements or tractions are prescribed, this line integral can be calculated by $du_i/da = 0$ and $dT_i/da = 0$, respectively. The reference system is located

at the crack tip regardless of the crack length, so that the coordinate axis is moving with the crack growth. In this way, the material derivative d/da renders

$$\frac{d}{da} = \frac{\partial}{\partial a} + \frac{\partial x}{\partial a}\frac{\partial}{\partial x} = \frac{\partial}{\partial a} - \frac{\partial}{\partial x}, \tag{3.27}$$

as it is assumed that crack advancement follows the x direction of the coordinate system making $\partial x/\partial a = -1$. Thus, Equation 3.26 is given as

$$\frac{d\Pi}{dA} = \int_{A'} \left(\frac{\partial \omega}{\partial a} - \frac{\partial \omega}{\partial x} \right) dA - \int_{\Gamma'} T_i \left(\frac{\partial u_i}{\partial a} - \frac{\partial u_i}{\partial x} \right) ds. \tag{3.28}$$

Accounting for the definition of strain energy density, the first term of the equation's right hand side can be evaluated as

$$\frac{\partial \omega}{\partial a} = \frac{\partial \omega}{\partial \varepsilon_{ij}} \frac{\partial \varepsilon_{ij}}{\partial a} = \sigma_{ij} \frac{\partial}{\partial x_j} \left(\frac{\partial u_i}{\partial a} \right). \tag{3.29}$$

Using the Principle of Virtual Work, the former equation can be expressed in terms of tractions on boundaries as

$$\int_{A'} \sigma_{ij} \frac{\partial}{\partial x_j} \left(\frac{\partial u_i}{\partial a} \right) dA = \int_{\Gamma'} T_i \frac{\partial u_i}{\partial a} ds. \tag{3.30}$$

Applying Eq. 3.29 and Eq. 3.30 in Eq. 3.28 leads to

$$\begin{aligned} \frac{d\Pi}{dA} &= \int_{\Gamma'} T_i \frac{\partial u_i}{\partial a} ds - \int_{A'} \frac{\partial \omega}{\partial x} dA - \int_{\Gamma'} T_i \left(\frac{\partial u_i}{\partial a} - \frac{\partial u_i}{\partial x} \right) ds \\ &= - \int_{A'} \frac{\partial \omega}{\partial x} dA + \int_{\Gamma'} T_i \frac{\partial u_i}{\partial x} ds. \end{aligned} \tag{3.31}$$

The exploitation of the Green's theorem in the last expression yields

$$-\frac{d\Pi}{dA} = \int_{\Gamma'} \left(\omega n_x - T_i \frac{\partial u_i}{\partial x} \right) ds = \int_{\Gamma'} \left(\omega dy - T_i \frac{\partial u_i}{\partial x} ds \right), \tag{3.32}$$

since $n_x ds = dy$. Hence, the J-Integral can be seen as an energy parameter, specifically the energy release rate in nonlinear elastic material under quasi-static conditions.

The ability to determine the energy release rate together with the path-independent character of the J-Integral made this technique a powerful tool from the experimental and computational standpoint.

The path independence of J can be proved by evaluating the J-Integral in a generic closed contour Γ^* and by making use of the Green's theorem as

$$J^* = \int_{\Gamma^*} \left(\omega dy - T_i \frac{\partial u_i}{\partial x} \right) ds = \int_{A^*} \left[\frac{\partial \omega}{\partial x} - \frac{\partial}{\partial x_j} \left(\sigma_{ij} \frac{\partial u_i}{\partial x} \right) \right] dx dy. \tag{3.33}$$

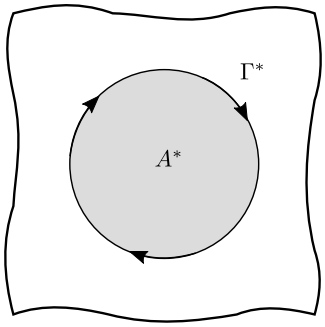

Figure 3.5 Generic closed J-Integral contour..

If the integral value is zero, the path-independence is guaranteed. To this end, the definition of the strain energy density is employed as

$$\frac{\partial \omega}{\partial x} = \frac{\partial \omega}{\partial \varepsilon_{ij}} \frac{\partial \varepsilon_{ij}}{\partial x}, \tag{3.34}$$

and the definition of small-strain tensor in Eq. 3.34 leads to

$$\frac{\partial \omega}{\partial x} = \frac{1}{2}\sigma_{ij}\left[\frac{\partial}{\partial x}\left(\frac{\partial u_i}{\partial x_j}\right) + \frac{\partial}{\partial x}\left(\frac{\partial u_j}{\partial x_i}\right)\right] = \sigma_{ij}\frac{\partial}{\partial x_j}\left(\frac{\partial u_i}{\partial x}\right), \tag{3.35}$$

with $\sigma_{ij} = \sigma_{ji}$. Applying the equilibrium condition in abscense of body forces

$$\frac{\partial \sigma_{ij}}{\partial x_j} = 0, \tag{3.36}$$

one obtains

$$\sigma_{ij}\frac{\partial}{\partial x_j}\left(\frac{\partial u_i}{\partial x}\right) = \frac{\partial}{\partial x_j}\left(\sigma_{ij}\frac{\partial u_i}{\partial x}\right). \tag{3.37}$$

This result leads to the second term of the Eq. 3.33 so that the J^* is null in any closed contour. So, the J-Integral can be applied to calculate the energy release rate in the whole solid performing the line integral over an arbitrary curve surrounding the crack tip. For instance, setting the contour around the crack lips as shown in Fig. 3.6, divided in $\Gamma_1, \Gamma_2, \Gamma_3, \Gamma_4$, the closed contour J-Integral could be expressed as the sum of each part i.e.

$$J = J_1 + J_2 + J_3 + J_4 = 0. \tag{3.38}$$

Since crack lips are traction free, i.e. $T_i = 0$, and are located in a horizontal plane $dy = 0$, the associated J values are null, that is, $J_2 = J_4 = 0$. Consequently, $J_1 = -J_3$ and any curve around the crack tip leads to the same value of J.

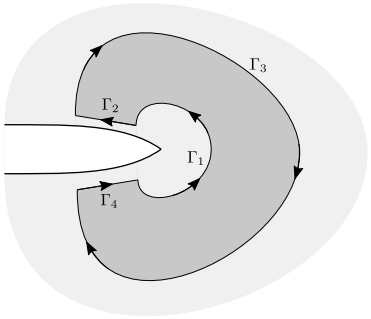

Figure 3.6 Closed J-Integral contour divided into $\Gamma_1, \Gamma_2, \Gamma_3, \Gamma_4$ sections.

Moreover, for the sake of completeness of the J-Integral and its capabilities, J can be considered as a stress intensity parameter, as the factor K characterised the stress and strain field in linear elastic solid in presence of cracks. Hutchinson [150] and Rice and Rosengren [190] proved that J plays the role of stress intensity factor in nonlinear elastic materials within the plastic zone. Then, two singularity-dominated areas can be found in small-scale yielding structures: one in the elastic zone and other in the plastic zone. This plastic singularity also predicts infinite stress as $r \to 0$, so this theory does not describe the behaviour in real parts, where this singularity is not present. The principal reason is the development of large strains at the crack tip that invalidate the plasticity analysis. Such strains create a blunted crack tip that is not considered in the small-strain approach and the J-controlled singularity is not appropriate for strains greater than 10%. Therefore, J-Integral technique is useful to characterise structures undergoing small-scale yielding.

However, it can be stated that the J-Integral allows the energy release rate to be computed in nonlinear elastic materials by means of a path-independent contour integral. That is, the change of potential energy in the entire solid can be calculated through a contour integral surrounding the crack tip, thanks to its path-independent character. Nonetheless, the energy release concept in elastic-plastic materials is slightly different from the perfectly elastic ones.

On the one hand, the change of potential energy in elastic materials is associated exclusively with the energy released due to a crack growth, that is, the energy needed to break the atomic bonds γ_s. On the other hand, such variation in the elastic-plastic solids is related to the energy absorbed (both elastic and plastic), necessary to generate a crack advance ($\gamma_s + \gamma_p$, bond breaking and plastic work respectively). During the deformation of the specimen, a plastic zone is developed around the crack tip prior to fracture and, consequently, a plastic wake remains when the crack grows. In this way, the plastic wake in the specimen as well as the actual fracture process, see Fig. 3.7, are accounted for the analysis. In this scenario, the contour integral can be conceived as the energy flow of the specimen to the plastic zone and the plastic wake. Unfortunately, there are some limitations regarding the application of this technique in elastic-plastic materials.

Thus, if the J-Integral is examined from a more general standpoint (Generalized Energy Release Rate) [179], in which a general energy balance law is applied to derive

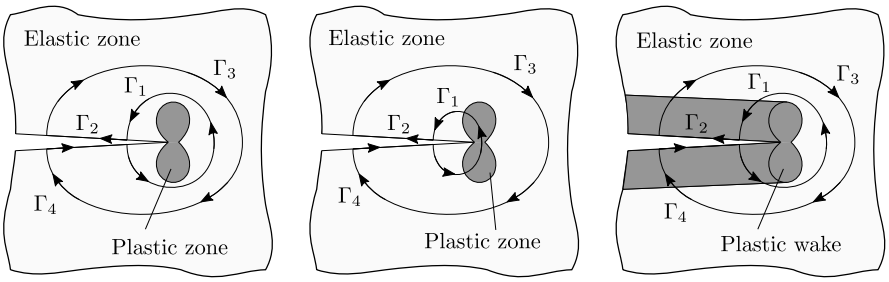

(a) Path-independent J-Integral contour in presence of a plastic zone.

(b) Path-dependent J-Integral contour in presence of a plastic zone.

(c) Path-dependent J-Integral contour in presence of a plastic wake in a growing crack.

Figure 3.7 Path dependence of the J-Integral under plastic dissipation.

the energy release rate and other contour integrals regardless of the material response, it can be stated that the J-Integral is path independent if Γ is defined in the elastic zone. This nature is lost when the contour integral is evaluated inside the plastic zone. In cases where Γ fits the crack tip, that is, the contour radius tend to zero, the energy release rate does not take into account the work dissipated in the plastic wake. Hence, in elastic-plastic materials such as metals in which most of the energy required to create new surfaces is dedicated to form the plastic wake, the energy release rate approaches to zero and subsequently the contour integral becomes path-dependent.

Therefore the energy release rate is unequivocally defined in materials where the plastic zone is surrounded by an elastic region (such as brittle or small-scale yielding materials). Otherwise, in fully-plastic conditions or crack growing scenarios in elastic-plastic materials the path-dependent character varies the meaning of J.

3.3 Interface fracture modelling

Interfaces are very thin regions between two different well-defined domains involved in the mechanical properties of the global body, including stiffness, strength and fracture resistance. They are responsible for the load and stress transmission between the two solids and therefore, the mechanical and fracture performance strongly rely on the interface properties.

The original approach to deal with interface fracture mechanics was based on the LEFM, where a crack along a perfectly bonded interfaces between two different linear-elastic, homogeneous and isotropic materials was investigated [191]. In the William's work, two stress singularities were found in the plates considered in the study: a square-root singularity and an oscillatory singularity. Then, the stresses are proportional to the inverse square root of the distance from the point of the crack and the oscillatory character preserves this tendency. Otherwise, the same features were encountered by Sih and Rice [192] in the resolution of a bending of a plate composed of two plates of materials (isotropic and homogeneous) having dissimilar elastic properties, bonded

together along a straight line which sustains a crack. Despite the presence of oscillatory stresses and interpenetration in a certain region of the interface, this problem attracted attention of some researchers [193–195].

The unrealistic oscillatory behaviour and the interpenetration led to the assumption of a contact zone along the interface [196, 197]. However, for many materials and conditions under study, the contact zone was negligible in comparison with the crack length and the oscillatory solution was accepted as long as the interpenetration were small [150, 198].

Being the theoretical framework established, some experimental campaigns were accomplished in order to study a crack between dissimilar adherents connected by different adhesives, like epoxy, copper or alumina [199–201]. In addition, interface behaviour between only two materials were investigated: aluminium and epoxy [202], glass and epoxy [203] or two ceramic clays [204]. These experiments revealed that the critical interface energy release rate G_c was function of the mixed mode. Moreover, the interface crack between two anisotropic material was studied in [205].

3.3.1 Cohesive Zone Model

In this Section the transition transition between the interface modelling by means of Continuum Mechanics, which involves singularities at the interface, and Cohesive Zone Model, where such singularities are removed, is addressed. Consider a domain with two bodies Ω_1 and Ω_2, where the surface S represents the interface between the solids, as shown in Fig. 3.8. At this point, in the undeformed configuration, the surface S belongs to both bodies Ω_1 and Ω_2, that is, $S_1 = S_2 = S$. Then, the material points located at the interface $\mathbf{X}_{\text{int}}$ moves to its corresponding deformed position $\mathbf{x}_{\text{int}}$ in a unequivocally relation, that is, one undeformed point becomes one point in the deformed or spatial configuration. So, it is not possible to create new free surfaces from the continuum standpoint due to the fact that it violates the fundamental law of continuity. Hence, the current configuration (including crack extension and new surfaces) cannot be mapped from the initial configuration using the Continuum Mechanics standpoint $\mathbf{x}_{\text{int}} = \chi(\mathbf{X}_{\text{int}}, t)$.

To overwhelm the generation of new surfaces between domains keeping the continuum perspective, consider a supplementary domain Ω^* bounded by the surfaces S_1 and S_2. That is, an infinitesimal thin body (embedded in a surface) which enables to develop deformations to become a 3D solid. In this way, the surfaces S_1 and S_2 belongs to domain Ω_1 and Ω_2 prior to separation , whereas S_1 is associated with Ω_1 and Ω^*, S_2 corresponds to Ω_2 and Ω^*. Material normal vector $\mathbf{N}$ is branched into normal spatial vectors $\mathbf{n}_1$ and $\mathbf{n}_2$, according to surfaces S_1 and S_2 respectively. Additionally, both surfaces will be separated by a certain distance δ and the constitutive law will relates such distance and directions with normal and shear tractions, as illustrates in Fig. 3.8. Usually, the behaviour of the domain Ω^* is defined by a traction-separation law (TSL) $t - \delta$, calculating the tractions through the displacement jumps across the interface.

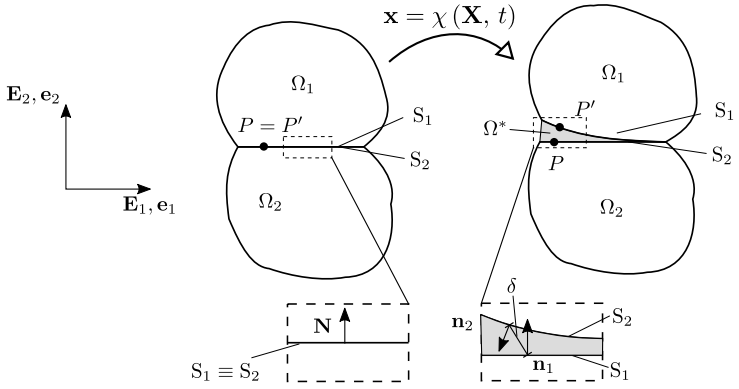

Figure 3.8 Conceptual scheme of the cohesive zone model.

Therefore the tractions becomes null after a critical distance δ_c as follows

$$t = \begin{cases} t(\delta) & \text{if} \quad \delta < \delta_c \\ 0 & \text{if} \quad \delta \geq \delta_c. \end{cases} \tag{3.39}$$

In this approach the traction-displacement relationship can be established so that the fracture properties of the interface are considered in the analysis and the crack extension can be modelled by setting null tractions at certain regions of the cohesive process zone. These TSLs can be divided into potential-based and non-potential based:

- Potential-based: the traction-displacement relationship is derived from a potential function Ψ_{int} that characterises the fracture performance. The first potential derivative allows the traction to be calculated and the second derivative provides the material tangent stiffness. This approach ensures a proper treatment of the energy regardless the path separation and a non-negative work for closed path.
- Nonpotential-based: the constitutive law does not depend on a potential and the model may not be consistent regarding the energy dissipated for arbitrary separation paths and consequently, the fracture performance under general mixed mode conditions is not guaranteed.

Furthermore, the constitutive equation in a cohesive zone model must be independent of any superimposed rigid body movement. The energy dissipated during the fracture process is equal to the work of separation or the area under the traction-separation curve and characterise the Mode I, Mode II and mixe mode fracture conditions. Usually, these equations present a softening part in which the material undergoes a stiffness decreasing controlled by a damage parameter.

In addition, the cohesive traction-separation laws can be classified according to the modelling of the damage initiation:

Intrinsic: the cohesive law considers tractions from zero to the maximum stress (initiation part) as well as the stiffness decreasing (softening part). Therefore, both

damage onset and failure criterion is contemplated in the cohesive model. Moreover, cohesive elements should be inserted from the beginning of the analysis.

Extrinsic: the cohesive TSL is active where the nodes that are placed on the interface, but belong to the bulk material, reach a critical value. In this way, the damage initiation is not included in the cohesive formulation, but just the softening behaviour is implemented along the interface.

In the following, the predominant CZMs that have been extensively used in the literature and the principal characteristics of the phenomena of decohesion are listed. A graphical representation of each model is included in Fig. 3.9:

- Barenblatt introduced the concept of the cohesive process zone. His pioneer work [206, 207] proposed a model for investigating cracks in brittle materials, in which the cohesion force varies according to a molecular model.
- Dugdale [208] suggested a criterion to study the yielding of an elastic-plastic steel sheet, where a constant cohesive force was developed in the plastic zone.
- Needleman [209] applied the cohesive zone model for describing the process of void nucleation from initial debonding through complete decohesion of rigid inclusions in elastic-viscoplastic materials. A polynomial curve was employed in the latter analysis while exponential-based laws were employed in subsequent studies [210, 211].
- Rice [212] analysed the interfacial embrittlement by solute segregation theoretically using an exponential cohesive law that fit to the energy of the universal bonding correlation. Rice stated that the area under the traction-separation curve could be calculated for elastic-brittle materials by the well-know application of the J-Integral

$$G = \int_0^{\infty} \sigma(\delta) d\delta = 2\gamma_{\text{int}}, \tag{3.40}$$

  where G is the strain energy release rate. Nonetheless, in circumstances for small-scale plastic zone, the energy release rate can be defined as

$$G = \omega_p + 2\gamma_{\text{int}}, \tag{3.41}$$

  where ω_p is the plastic work ahead of the crack tip.
- Tvergaard and Hutchinson [213] proposed a trapezoidal-like traction-separation law for the analysis of crack growth initiation and fracture resistance computation in elastic-plastic solids. Thus, the area under the curve Γ_0 is delimited by the displacements δ_1, δ_2 and δ_c and the maximum stress $\sigma_{\max}$.
- Camacho and Ortiz [214] employed a CZM in order to study multiple cracks along arbitrary paths in the fragmentation of brittle materials. The cohesive law models a gradual loss of strength with increasing separation and establishes the fracture energy needed to create a new free surface. In this case, the authors separate between tensile and compressive conditions and the normal and tangential stresses, σ and τ respectively, ramped down linearly with the separation δ.

- Geubelle and Baylor [215] analysed the delamination of composite plates under low-velocity impacts by means of 2D cohesive elements. This scheme allows spontaneous initiation and propagation of delamination and matrix crack events. The cohesive elements were conceived as nonlinear springs linking standard finite elements according to a traction-separation law accounting for any possible mixity mode. To this end, bilinear relations between traction and displacement under normal and shear directions were considered, in which the area under the curve in pure normal and shear loading corresponds to G_{Ic} and G_{IIc} values.

3.3.2 Bilinear Interface formulation

As a consequence of the rapid evolution of the simulations capacities, a wide range of numerical tools have been used for the understanding of failure mechanisms in bonded joints or composite delamination, in which an inelastic behaviour governs the system. This is the case of CZMs in the context of FE analysis [216–219], which offer an efficient and versatile simulation tool for triggering fracture events in solids. In particular, CZMs allow simulating crack propagation events under mixed mode conditions [220, 221] and have been proven as an appropriate tool to analyse interfacial fracture events in patterned specimens, see Chapter 6. Particularly, a finite thickness element interpretation for adhesive joints can be considered in line with [222, 223] and obeying a bilinear TSL response. In the following aspect we briefly summarizes the basic aspects of this CZ profile.

In the bilinear CZM behaviour considered in this study, traction t is governed by a damage initiation criterion and a damage variable D which is responsible for the degradation of the material properties (Fig. 3.10). This model shows an initial linear elastic behaviour up to reaching the onset damage criterion at traction t^0 and, afterwards, a linear stiffness degradation up to the critical displacement δ^f or complete failure. Note that δ^f and the mixed mode ratio based on displacement is $\beta = \frac{\delta_s}{\delta_s+\delta_n}$ are function of the normal and shear jump displacements δ_n and δ_s, respectively. On the other hand, critical fracture energy associated with pure Mode I, pure Mode II and a general mixed mode loading respectively are G_{Ic}, G_{IIc} and G_c.

The beginning of the degradation at the maximum normal and shear tractions, t_n^0 and t_s^0, according to a quadratic stress onset criterion [224], is determined as

$$\left\{\frac{\langle \tilde{t}_n \rangle_+}{t_n^0}\right\}^2 + \left\{\frac{\tilde{t}_s}{t_s^0}\right\}^2 = 1, \tag{3.42}$$

where $\tilde{t}_n$ and $\tilde{t}_s$ are normal and shear tractions along the initial linear-elastic evolution and $\langle\rangle_+$ is the Macaulay bracket, that excludes compressive tractions in the current criterion. In this line, $\tilde{t}_n = k_n\delta_n$ and $\tilde{t}_s = k_s\delta_s$, with k_n and k_s being the penalty stiffness respectively in normal and shear direction.

Eqs. (3.43)-(3.44) show the normal and shear traction evolution, t_n and t_s respectively, and Eqs. (3.45)-(3.46) show the definition of the damage variable D, ranging from

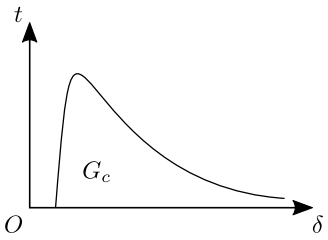

(a) Barenblatt: molecular law.

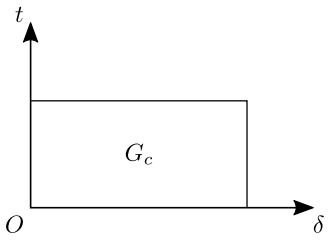

(b) Dugdale: constant law.

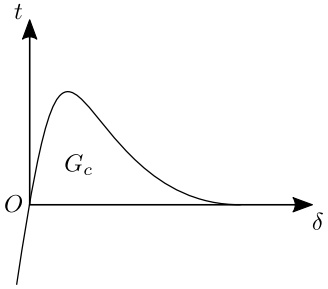

(c) Needleman: polynomial law.

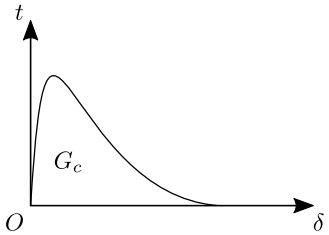

(d) Rice-Wang: exponential law.

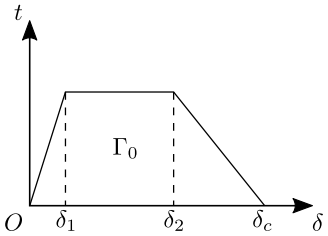

(e) Tvergaard-Hutchinson: trapezoidal law.

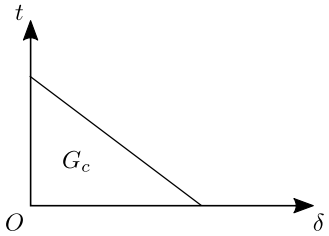

(f) Camacho-Ortiz: linear law.

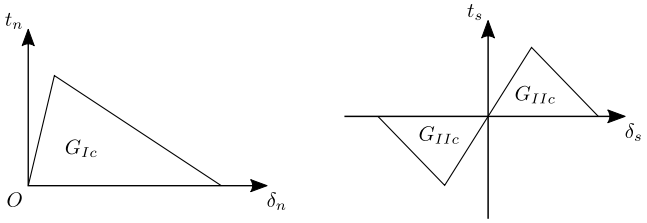

(g) Geubelle-Baylor: bilinear law.

Figure 3.9 Principal cohesive laws used in decohesion problems.

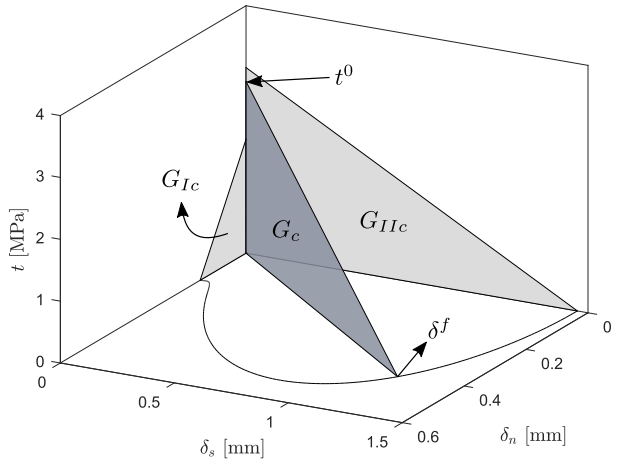

Figure 3.10 Traction-separation law under pure Mode I, pure Mode II and general mixed mode conditions, where G_{Ic}, G_{IIc} and G_c are the corresponding critical energy release rates, respectively. t^0 represents the traction at the onset criterion and δ^f symbolises the displacement corresponding to the total stiffness loss.

$D = 0$ (pristine material) to $D = 1$ (complete failure or total degradation), i.e.

$$t_n = \begin{cases} (1-D)\,\tilde{t}_n, & \text{if } \tilde{t}_n \geq t_n^0 \\ \tilde{t}_n, & \text{otherwise,} \end{cases} \tag{3.43}$$

$$t_s = \begin{cases} (1-D)\,\tilde{t}_s, & \text{if } |\tilde{t}_s| \geq |t_s^0| \\ \tilde{t}_s, & \text{otherwise,} \end{cases} \tag{3.44}$$

$$D = \frac{\delta^f\left(\delta - \delta^0\right)}{\delta\left(\delta^f - \delta^0\right)}, \tag{3.45}$$

with

$$\delta = \sqrt{\langle \delta_n \rangle_+^2 + \delta_s^2}, \tag{3.46}$$

where δ is the equivalent displacement used under mixed mode fracture conditions, δ^0 and δ^f correspond to the equivalent displacement when the onset criterion is fulfilled and when complete degradation occurs, respectively. Finally, fracture energy under mixed mode conditions are ruled by the Benzeggah-Kenane criterion [225] as

$$G_c = \left(1 - \left(\frac{G_{II}}{G_T}\right)^{\eta}\right) G_{Ic} + \left(\frac{G_{II}}{G_T}\right)^{\eta} G_{IIc}, \tag{3.47}$$

where $G_T = G_I + G_{II}$.

In the present CZM formulation, material stiffness decreases linearly, after the onset criterion is reached. Similarly, tractions decrease linearly on the softening zone from $t_n = t_n^0$ and $t_s = t_s^0$ up to $t_n = 0$ and $t_s = 0$ (representing complete failure) as long as a fixed fracture mixed mode ratio ($\beta = \text{constant}$) occurs. The evaluation of the normal and shear tractions and jump displacements allows the energy release rate associated with fracture Mode I and Mode II, G_I and G_{II} to be computed.

3.3.3 Linear Elastic-Brittle Interface Modelling (LEBIM)

A special case of Traction-Separation Law for the purpose of investigating the interface damage and failure propagation is the Linear Elastic-Brittle Interface Modelling (LEBIM). This approach is adequate to model the behaviour of adhesively bonded joints when a thin elastic adhesive layer links both solids or the debonding process of a bimaterial system where no third phase appears between such materials, as occurs in the delamination between plies and fiber-matrix debonding within a composite [226]. This kind of interfaces, where the average stiffness of the adherents is higher than the layer stiffness, is generally classified as *spring type interface*, *linear-elastic interface* or *weak interface* and they can be modelled as a continuous elastic spring foundation using suitable continuum properties [227, 228].

A powerful tool to describe fracture or debonding events is to endow such elastic spring with fracture properties, obeying a certain failure criterion according to the maximum strength or critical energy release rate [229, 230]. LEBIM was succinctly proposed by Prandtl [231] and Mott [232] and later enhanced by Távara [230, 233] so as to include shear and additional mixed mode conditions and to provide a frictionless elastic contact behaviour in the broken interface to prevent interpenetration after fracture process.

Moreover, the LEBIM enables the combination of the stress and energy based failure criterion in the same formulation. Thus, on the one hand, the former criterion deals with stress concentrators and delimits a maximum value, whereas on the other hand, the latter approach studies the propagation of existing cracks by means of the critical stress intensity factor or the critical energy release rate. The linear elastic-brittle interface formulation merges these two standpoints in a single criterion. Notwithstanding, the principal difference between classical stress or energy based criterion and LEBIM is the presence of stress singularities. As occurs in the laws presented in Section 3.3.1, such singularity is removed due to the stress at the crack tip is limited by a finite value. Likewise, it was stated that the energy release rate can be obtained through the interface tractions at the crack tip (in presence of a previous crack) or even in undamaged zones of the interface in the instant prior to the failure [227, 229].

The constitutive equations prescribe tractions and displacements for intact interfaces using a linear elastic law and are given by the following expressions

$$t_n = \begin{cases} k_n \delta_{\mathrm{n}}, & \text{if } \delta_{\mathrm{n}} \leq \delta_{\mathrm{n}}^c \\ 0, & \text{otherwise,} \end{cases} \tag{3.48}$$

$$t_s = \begin{cases} k_s \delta_{\mathrm{s}}, & \text{if } |\delta_{\mathrm{s}}| \leq |\delta_{\mathrm{s}}^c| \\ 0, & \text{otherwise,} \end{cases} \tag{3.49}$$

where t_n and t_s are normal and shear tractions, δ_{n} and δ_{s} are normal and shear relative displacements and k_n and k_s are normal and shear stiffnesses, respectively, as shown in Fig. 3.11

After interface failure, the following nonlinear behaviour is assumed to avoid interpenetration between adherents, as depicted in Fig.3.12 via a contact penalty condition, which can be written as

$$t_n = \begin{cases} k_n \delta_{\mathrm{n}}, & \text{if } \delta_{\mathrm{n}} < 0 \\ 0, & \text{otherwise,} \end{cases} \tag{3.50}$$

$$t_s = 0. \tag{3.51}$$

Note that tractions are limited by a fracture energy criterion, i.e. $G \leq G_c$, as shown in Fig. 3.11. Thus, energy release rate stored G and critical fracture toughness G_c are needed to describe the behaviour of the linear-elastic perfectly brittle model. Hence, for mixed mode conditions, fracture Mode I and Mode II are determined by normal and shear tractions as

$$G = G_I + G_{II}, \tag{3.52}$$

$$G_I = \frac{\langle t_n \rangle_+ \langle \delta_{\mathrm{n}} \rangle_+}{2} = \frac{\langle t_n \rangle_+^2}{2k_n}, \tag{3.53}$$

$$G_{II} = \frac{t_s \delta_{\mathrm{s}}}{2} = \frac{t_s^2}{2k_s}, \tag{3.54}$$

where G_I, G_{II} and G are the Mode I, Mode II and total energy stored, respectively. The symbol $\langle \rangle_+$ stands for the Macauly brackets and therefore only positive values of normal tractions and displacements are used in the G_I calculation.

In the right part of the inequation $G \leq G_c$, G_c corresponds to a material property that can be defined by the Mode I and Mode II counterparts (G_{Ic} and G_{IIc}) according to a fracture mixed mode criterion. In the present investigation the Benzeggah-Kenane criterion is used, see Eq. (3.47).

3.3.4 Comparison between linear and nonlinear Fracture Mechanics in the Cohesive Zone Model

An illustrative example of the nonlinear Fracture Mechanics is examined in [234], where the difference between the critical energy release rate G_c (corresponding to the LEFM analysis) and the work or separation Ω (the area under the traction-separation curve in a CZM) were studied in the Mode I quasi-static crack propagation in adhesive joints. In this work, it is clearly described the role of the inelastic and elastic counterparts in

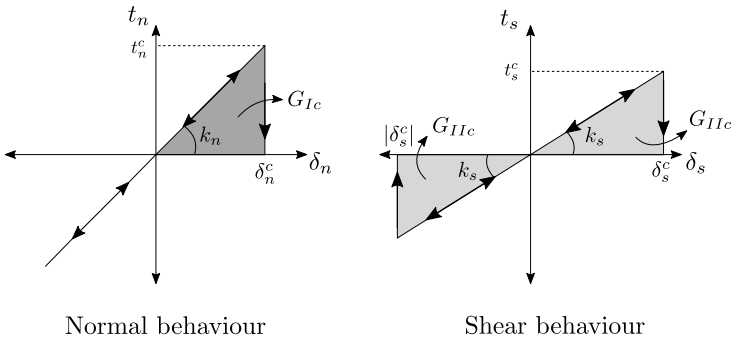

Figure 3.11 Linear Elastic Brittle Interface Model along intact interfaces: traction-separation law in normal ($t_n - \delta_n$) and shear ($t_s - \delta_s$) directions.

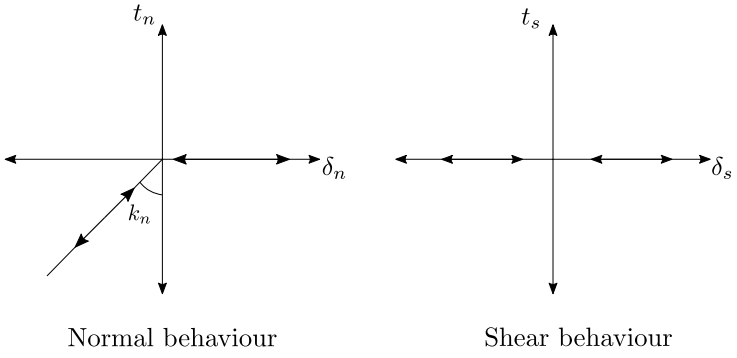

Figure 3.12 Linear Elastic Brittle Interface Model in broken interfaces: traction-separation law in normal ($t_n - \delta_n$) and shear ($t_s - \delta_s$) directions.

the variation of the nonlinear potential energy Π_{NL} with the crack advance a. In this regard, the energy dissipated ahead of the crack tip before crack propagation Π_D is the key magnitude to understand the nonlinear energy release rate concept. Thus, the total potential energy in a nonlinear system Π_{NL} can be divided into recoverable and dissipated energy, Π and Π_D respectively as

$$\Pi_{NL} = \Pi + \Pi_D. \tag{3.55}$$

Let consider a DCB test with monotonically increasing prescribed displacements, where the adherents are linear elastic and the interface is modelled using linear or bilinear traction-separation laws in order to investigate the behaviour of linear and nonlinear energy release rate. Fig. 3.13.a and Fig. 3.13.b show the linear and nonlinear TSLs employed at the interface, where the stored and dissipated energy are indicated for active and broken points. The principal difference between linear and nonlinear laws is the energy dissipation during the loading process prior to crack propagation or plastic energy. On the one hand, the linear law stores all the energy and releases

it instantaneously when reaching the critical value δ_c, exhibiting a perfectly-brittle performance. On the other hand, the work done in the nonlinear law is divided into dissipated and stored energy as a consequence of the stiffness decreasing in the softening part. When the corresponding critical value δ_c is reached, the crack grows and the work of separation Ω is released. Such behaviours provoke different responses in the load-displacement curve, as depicted in Fig. 3.14.

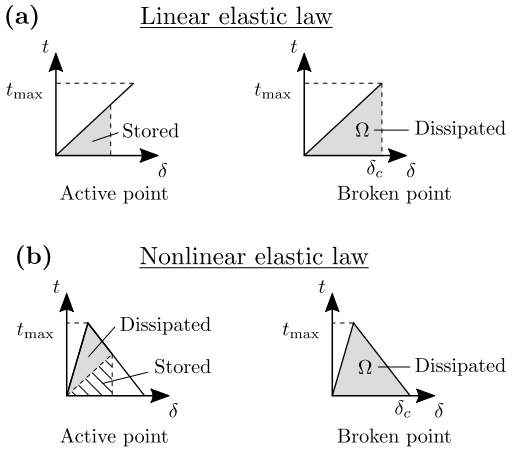

Figure 3.13 (a) Linear-elastic traction-separation law in an active and a broken point. (b) Bilinear-elastic traction-separation law in an active and a broken point. Ω symbolises the work of separation.

Recalling the expression (3.24) and according to the potential energy decomposition established in Eq. (3.55), different interpretations emerge for the energy release rate:

- Linear energy release rate $\dfrac{d\Pi}{da}$: the potential energy is obtained from linear elastic interfaces (Fig. 3.13.a). The system increases the force linearly up to a non-equilibrium state A (see Fig. 3.14.a). At this point, the crack grows from a_0 to $a_0 + \Delta a$ and the system progresses to the next equilibrium state B. Then, applying the energy balance $\Delta\Pi = \Delta W - \Delta D$, the dissipated energy in the fracture process ΔD can be easily obtained (see Fig. 3.14.b) as:
  - Potential energy: $\Pi_A = \overline{\text{OAA'O}}$, $\Pi_B = \overline{\text{OBB'O}}$,
  - Work done by external forces: $\Delta W = \overline{\text{ABB'A'A}}$
  - Dissipated or released energy due to the crack advance: $\Delta D = \overline{\text{OABO}}$.
- Nonlinear energy release rate $\dfrac{d\Pi_{NL}}{da}$: the potential energy is obtained from nonlinear elastic interfaces (Fig. 3.13.b). Consider specimens with two different crack lengths a_0 and $a_0 + \Delta a$ and no previous damage or loading in the analysis. According to Fig. 3.14.c, the load-displacement curves will travel along the curved lines $\overline{OA}$ and $\overline{OB}$, respectively. To get the forces and displacements prior

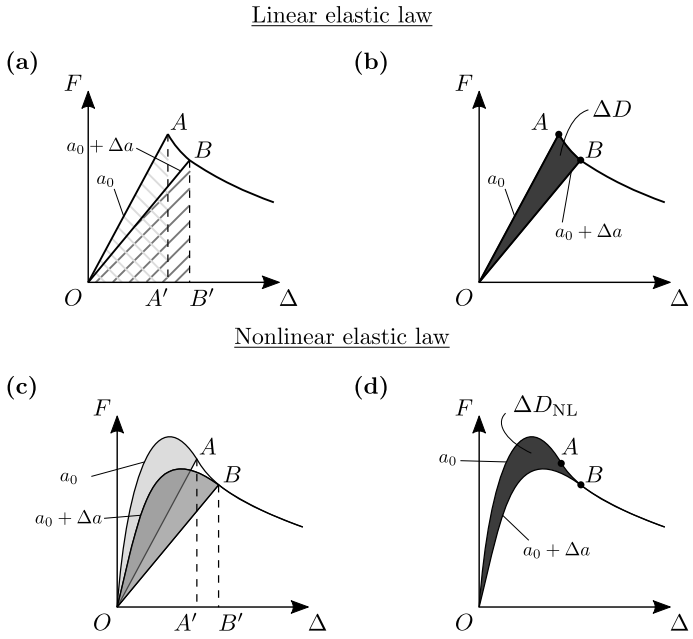

Figure 3.14 Scheme of a load-displacement curves in a DCB test with monotonically increasing prescribed displacements at crack length a_0 and $a_0 + \delta a$. (a) Load-displacement curve with stored energy (cross-hatched area) and (b) released energy (dark shaded area) in a linear elastic interface. (c) Load-displacement curve with plastic energy prior to fracture (light shaded area) and (d) released energy (dark shaded area) in a nonlinear elastic interface.

to the crack propagation $(F_{\mathrm{A}}, \Delta_{\mathrm{A}})$ and $(F_{\mathrm{B}}, \Delta_{\mathrm{B}})$, the external work W_{A} and W_{A} has to be done. Part of this work is stored in the system (Π_{A} and Π_{B}) and the rest is dissipated before crack propagation (shaded areas: $\Pi_{D,\mathrm{A}}$ and $\Pi_{D,\mathrm{B}}$). Hence, the nonlinear energy release rate account for both elastic energy stored and energy dissipated ahead of the crack tip prior to the crack advance, that is, the sum of cross-hatched (Fig. 3.14.a) and shaded (Fig. 3.14.c) regions. As the linear case, the work done by external forces between adjacent crack lengths is ΔW and the energy balance $\Delta\Pi = \Delta W - \Delta D$ can be applied, where the energy released due to the crack propagation is depicted in Fig. 3.14.d as

- Nonlinear potential energy: $\Pi_{\mathrm{NL,A}} = \overline{\mathrm{OAA'O}}$, $\Pi_{\mathrm{NL,B}} = \overline{\mathrm{OBB'O}}$ (segments $\overline{\mathrm{OA}}$ and $\overline{\mathrm{OB}}$ are curves),
- Linear potential energy: $\Pi_{\mathrm{A}} = \overline{\mathrm{OAA'O}}$, $\Pi_{\mathrm{B}} = \overline{\mathrm{OBB'O}}$,
- Dissipated energy prior to fracture: $\Pi_{D,\mathrm{A}} = \overline{\mathrm{OAO}}$, $\Pi_{D,\mathrm{B}} = \overline{\mathrm{OBO}}$ (segments $\overline{\mathrm{OA}}$ and $\overline{\mathrm{OB}}$ are curves),
- Work done by external forces: $W_{\mathrm{A}} = \overline{\mathrm{OAA'O}}$, $W_{\mathrm{A}} = \overline{\mathrm{OBB'O}}$, $\Delta W = \overline{\mathrm{ABB'A'A}}$ (segments $\overline{\mathrm{OA}}$ and $\overline{\mathrm{OB}}$ are curves)

– Dissipated or released energy due to the crack advance: $\Delta D = \overline{\text{OABO}}$ (segments $\overline{\text{OA}}$, $\overline{\text{AB}}$ and $\overline{\text{BO}}$ are curved).

Thus, in the case of G_c is defined as the change of linear elastic potential energy with respect to the crack length $G_c = \frac{d\Pi}{da}$ in presence of a nonlinear TSL, the energy dissipated ahead of the crack tip (shaded area in Fig.3.14.c) may play an important role in the energy computation. Otherwise, if J is defined as the change of nonlinear potential energy $J_c = \frac{d\Pi_{\text{NL}}}{da}$, the next expression is obtained as

$$J_c = G_c + \frac{d\Pi_{\text{D}}}{da}. \tag{3.56}$$

Therefore, for the linear elastic case, always $J_c = G_c$ due to the absence of plastic energy. Moreover, this relationship is valid for nonlinear behaviour if: (i) the plastic Π_{D} energy is negligible respect to the linear elastic energy, (ii) the difference of such dissipated energy prior to fracture $\frac{d\Pi_{\text{D}}}{da}$ respect to the crack length is small, that is, the area enclosed in both shaded regions of Fig. 3.14.c is the same. In that case, the energy dissipated due to the increase of crack length is the same as that of the linear elastic case: $\Delta D_{\text{NL}} = \Delta D$.

4 Experimental analysis of patterned interfaces in Double Cantilever Beam tests

At present, a recurrent objective concerns the achievement of a superior fracture resistance behaviour of adhesive joints under general loading conditions. This improved response can be attained through increasing the corresponding strength and toughness properties, and therefore making them comparable to alternative joining methodologies (e.g bolted or riveted joints). One of the potential strategies to improve the strength and fracture properties of adhesive joints is to alter their geometrical definition via the introduction of biomimetic concepts.

Structured interfaces can be defined as those whose contact surfaces (between adherents) are not defined by flat profiles. The concept of structured interfaces has been extensively assessed in different applications, whereby it has been shown that the interface definition plays a crucial role on the fracture response through governing the tortuosity of the corresponding crack paths [235–239]. Furthermore, patterned interfaces can also comply with suture waveforms, which stem from intricate interface geometries including the presence of re-entrant features, see [84, 90] for the experimental analysis of suture interfaces using 3D printing capabilities based on polymeric materials.

The exploitation of these extraordinary capabilities have attracted the attention of many researchers in the last few years, who aim to provide plausible interpretations for the complex mechanical aspects taking place in different interface configurations. One of the driving forces for such investigations has been the advent of novel Additive Layer Manufacturing (ALM) techniques, i.e. 3D printing procedures, which has promoted the production of very complex interface designs such as triangular, trapezoidal, rectangular or “jigsaw”-like shapes. Several number of studies deeply investigated such behaviour through the combination of computational [240] and experimental [241] techniques, recognizing the relevant improvement of fracture behaviour of structured interfaces

over flat configurations.

At present, the development of novel ALM techniques that enable printing fiber-reinforced composite materials [242] fosters a new paradigm for the design of 3D printed composite specimens. Specifically, the fused deposition modelling (FDM) processes allow Fiber Reinforced Polymers (FRP) deposition to be performed. Benefits of FRP and improvements over properties of plastics were studied in [243, 244], while the influence of process parameters (fiber content, temperature or pressure, among others) in the mechanical properties of the produced parts were recently presented in [245–247]. However, the production and mechanical analysis of 3D printed composite specimens with structured interface definitions has received a very limited attention.

In view of the previous arguments, the objective of the present Chapter is the experimental investigation of the fracture resistance of 3D printed adhesively bonded Double Cantilever Beam (DCB) composite specimens containing structured interfaces. In particular, without loss of generality, the current study is focused on the analysis of trapezoidal interface patterns, paying special attention to:

1. The definition of a reliable manufacturing procedure to fiber-reinforced composite DCB specimens with structured interfaces for their posterior experimental tests.
2. The identification of most beneficial interface definition which endows the best response of the coupon in terms of fracture resistance.

The chapter is organized as follows. Section 4.1 assesses the current ALM production techniques for composite materials using the 3D printer MarkOne®. The experimental program concerning the composite DCB specimens with structured interfaces is described in Section 4.2, whereby the corresponding results are analyzed. Finally, Section 4.3 summarizes the main conclusions obtained.

4.1 Coupons definition: evaluation of current 3D printing capabilities for structured interfaces

This Section outlines the main stages regarding the production of composite DCB specimens with structured interfaces. Section 4.1.1 describes the assessment of the 3D printing capabilities available at the present moment in the Elasticity and Strength of Materials Laboratoy at the University de Seville (Spain), whereas Section 4.1.2 details the manufacturing process of composite DCB coupons with flat and trapezoidal interface profiles.

4.1.1 Manufacturing of structured interfaces: evaluation of 3D printing capabilities

This section briefly presents the assessment of the 3D printing capabilities of the ALM kit MarkOne® for the production of composite specimens with non-conventional interfaces, which includes the CAD software Eiger® for the definition of the solid model. A particular attention is devoted to the evaluation of the printing results in terms of geometrical tolerances and surface finishing in order to guarantee the coherence of the subsequent experimental program. To facilitate the identification of the production phases, a reference system on the printing bed is defined, see Fig. 4.1.

One fundamental limitation of the current printing capabilities is that structured interfaces could not be produced using fiber reinforced (carbon or glass) materials up to the delimiting outer surfaces of the specimen (those that feature the structured profile of the interface). Therefore, the present analysis is restricted to the production of nylon-based interfaces.

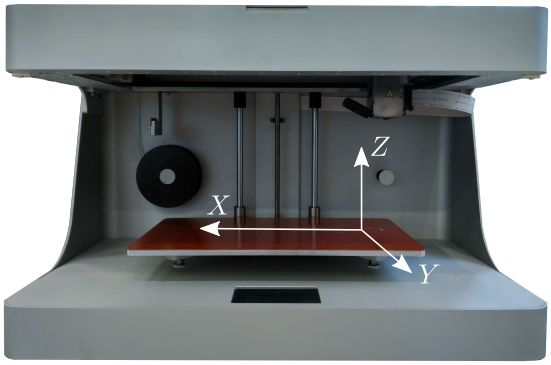

Figure 4.1 Overview of MarkOne® 3D printer and reference axes in the printing process.

With regard to the geometrical definition of structured interfaces, a preliminary test coupon which included triangular, trapezoidal, sinusoidal and rectangular typologies with different dimensions and aspect ratios was produced (Fig. 4.2.a). This specimen was manufactured from nylon, whose Young's modulus is $E = 0.38$ GPa. The geometrical characteristics were: 11.5 cm in-plane length (X-direction), 1 cm in-plane height (y-direction), without considering the interface dimensions, and 2 cm out-of-plane depth (Z-direction), see Fig. 4.2.b and Fig. 4.2.c.

The specific dimensions of the interfaces in this first assessment stage were designed following the guidelines discussed in [92]. In that investigation, the authors claimed that a significant increase in fracture resistance of DCB specimens with respect to flat interface configurations can be achieved by setting a high value for the ratio A/λ, where A denotes the amplitude of the patterns and λ identifies the wavelength. Relying on these considerations, the wavelength values were initially equal to 0.5, 1 and 2 mm, whereas the corresponding amplitudes corresponded to 1, 1.5 and 2 mm. These dimensions complied with the geometrical resolution tolerances specified by the 3D printer supplier ($100\,\mu m$ in z-axis, $6.25\,\mu m$ in x-axis and y-axis). Note also that for a complete definition of trapezoidal profiles, the parameter r is introduced, which is defined as the ratio between the horizontal length of a trapezium and the wavelength. Thus, a trapezium with $r = 0$ identifies a triangle, whereas the case with $r = 1$ corresponds to a rectangle (see Fig. 4.2.a).

The resulting preliminary coupon for evaluation purposes is shown in Fig. 4.2.c. Analyzing this figure, it is interesting to observe that the printed specimen considerably deviated from the nominal definition using the geometrical software model, see Fig. 4.2.b. These poor definitions were associated with dilatation effects of nylon during the printing production process.

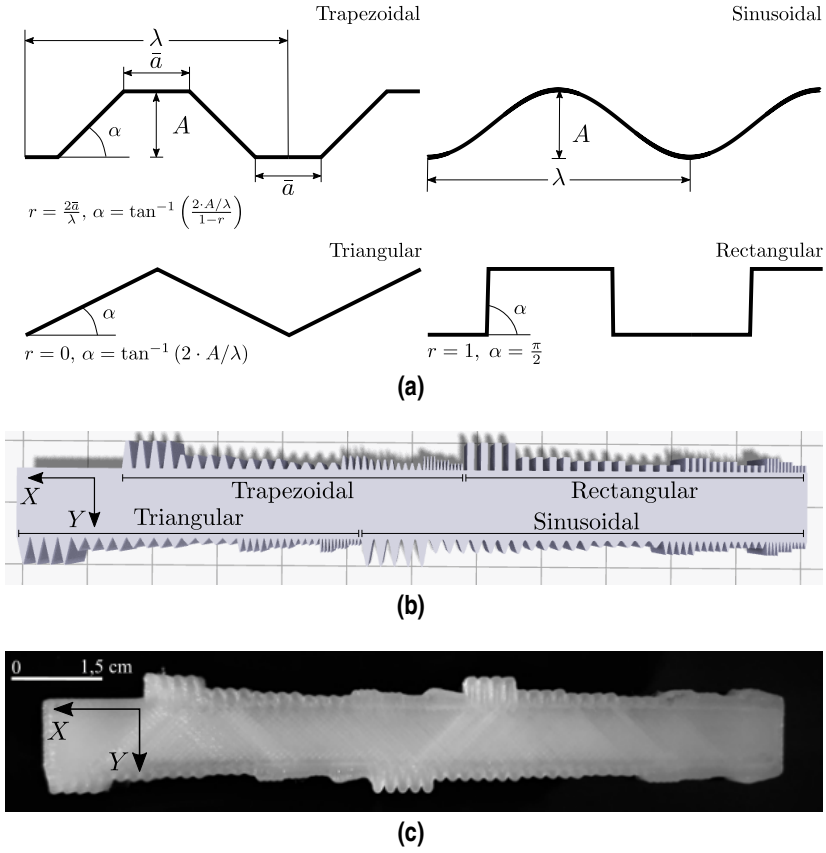

Figure 4.2 (a) Trapezoidal, rectangular, triangular and sinusoidal interfaces definition. (b) 3D view by Eiger software and (c) printing result of the structured interface specimen with trapezoidal ($r = 1/2$), rectangular, triangular and sinusoidal shape and parameters $A = 1, 1.5, 2$ mm and $\lambda = 0.5, 1, 2$ mm.

Focusing our attention on trapezoidal interface profiles, a particular geometrical range for the interface dimensions, which ensured the appropriate geometrical termination, was identified. Fig. 4.3 depicts a nylon specimen definition whose in-plane characteristics were: 7 cm in-plane length (X-direction), 1 cm in-plane width (y-direction), which integrated different trapezoidal interface profiles with the following parameters: $A = 2$, mm and $\lambda = 6$,8,12 mm, setting $r = 1/2$. In this graph, it can be observed that the upper in-plane edge of the coupon included trapezoidal interfaces with wavelengths equal to 6 (left-extreme) and 8 (right-extreme) mm, whereas the lower edge exclusively involved trapeziums with wavelength equal to 12 mm in length.

Amplitude and wavelength measurements of the latter interface definitions ($A = 2$ mm and $\lambda = 6, 8, 12$ mm) were done in order to verify the improvements in the geometrical accuracy through the use of an optical lens system and a measuring software

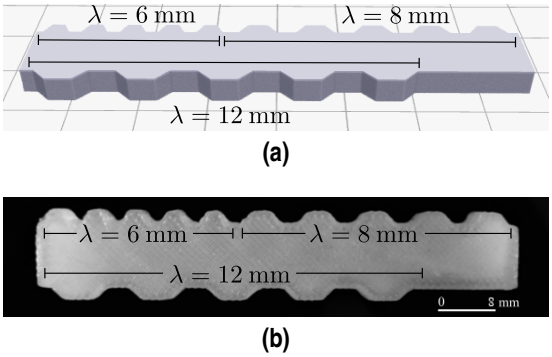

Figure 4.3 Trapezoidal interface with $A = 2\,\text{mm}$ and $\lambda = 6, 8, 12\,\text{mm}$: (a) 3D view by Eiger software and (b) printing result.

(Fig. 4.4). Analyzing the data shown in this figure, it can be observed that amplitude and wavelength dimensions were produced satisfactorily with respect to the nominal dimensions (solid model produced in the CAD software). Wavelength errors were around 1% for $\lambda = 6\,\text{mm}$, 11.11% for $\lambda = 8\,\text{mm}$ and 9.46% for $\lambda = 12\,\text{mm}$, whereas amplitude deviations corresponded to 10.85%, 7.55% y 12.75%, respectively, see Fig 4.4. This level of inaccuracy with respect to the nominal values was considered as acceptable. Correspondingly, the posterior experimental program involving DCB coupons with trapezoidal interfaces were defined obeying these geometrical dimensions.

4.1.2 Manufacturing of composite DCB specimens using 3D printing techniques

In this Section, the steps required to manufacture nylon and mixed nylon–glass-fiber composite DCB coupons for the effective fracture toughness tests (Section 4.2) are described. Nylon coupons were used as a first approach in order to detect potential inaccuracies and irregularities during the printing process. The geometrical characteristics of the DCB specimens under analysis (Fig. 4.5) were: length L = 250 mm, width $W = 25$ mm, thickness h = 5 mm.

A remarkable aspect of the ALM technique used by the 3D printer MarkOne® was the way through which the designed parts were produced. This printing system accomplished a layer-wise material deposition perpendicular to the printing bed, i.e. along the Z-axis (Fig. 4.6). Based on it, three potential productions options can be defined (Fig. 4.6). The first option regards the material deposition along the thickness direction of the specimen (referred as *printing in horizontal direction*), which locates the longitudinal axis (L) and the width axis (W) on the printing bed. In contrast to this, the second production option locates the longitudinal axis (L) and the thickness axis h of the specimen on the printing bed, whereas the third option locates the width axis (W) and the thickness axis h of the specimen on the printing bed. The two latter options are identified as *printing in vertical direction*.

In addition to the previous considerations, recalling [248], identical conditions along the printing procedure were followed for the production of the current DCB coupons in

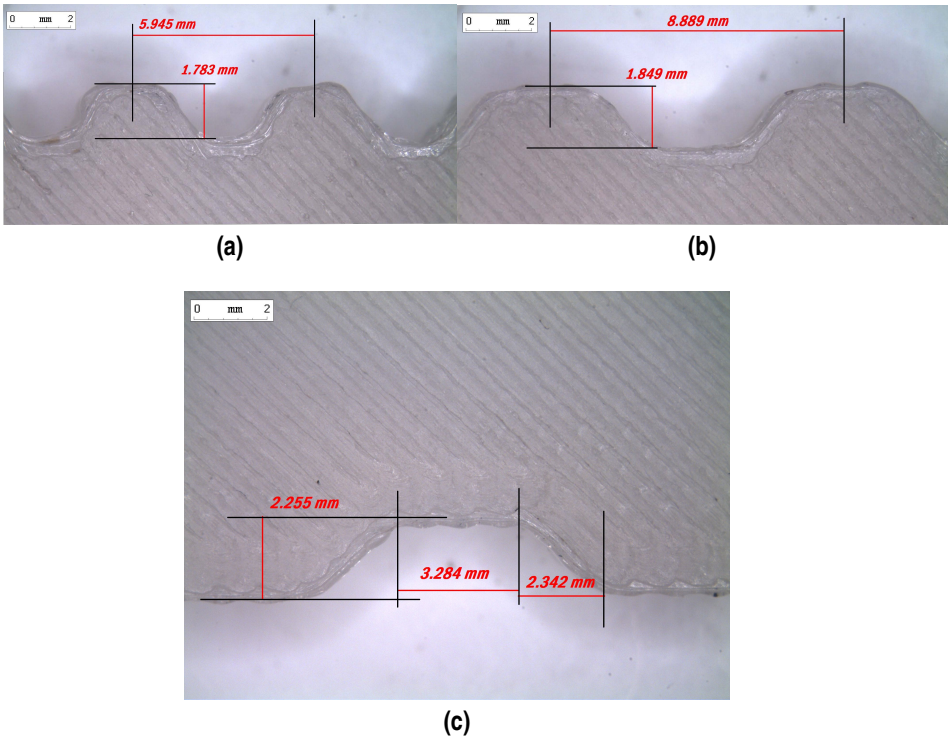

Figure 4.4 Amplitude and wavelength errors in Fig. 4.3 for (a) $A = 2\,\text{mm}, \lambda = 6\,\text{mm}$, (b) $A = 2\,\text{mm}, \lambda = 8\,\text{mm}$ and (c) $A = 2\,\text{mm}, \lambda = 12\,\text{mm}$.

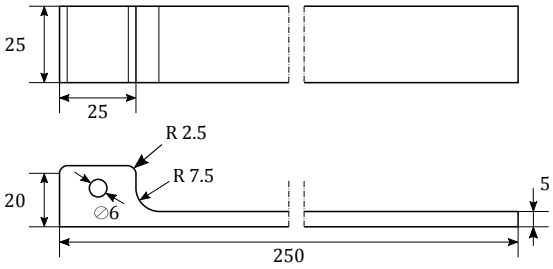

Figure 4.5 Sketch of the first specimen for G_{Ic} test.

order to prevent the potential influence of extrude temperature, printing speed, among others, on the corresponding mechanical response.

4.1.2.1 ALM manufacturing of DCB specimens with flat interfaces

For the case of the nylon coupons, the first printing position under investigation corresponded to the material deposition layer-wise along the specimen thickness direction (printing in *horizontal direction*), see Fig. 4.7. In this graph, a residual deformation at

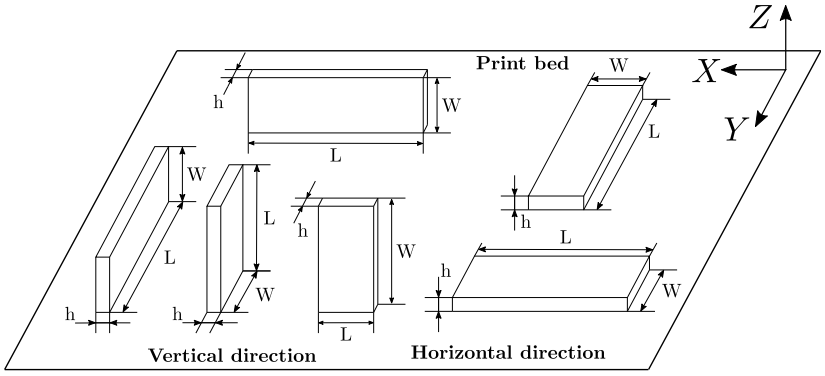

Figure 4.6 Identification of *horizontal* and *vertical printing directions* of DCB coupons.

the corners of the part was identified during the printing process due to the occurrence of the so-called warping effects, which stemmed from the existing thermal cycle. These effects led to undesirable specimen definition, and therefore this printing option was discarded. Fig. 4.8 shows the details of the warping effects and the thickness of the specimen when the printing procedure was concluded.

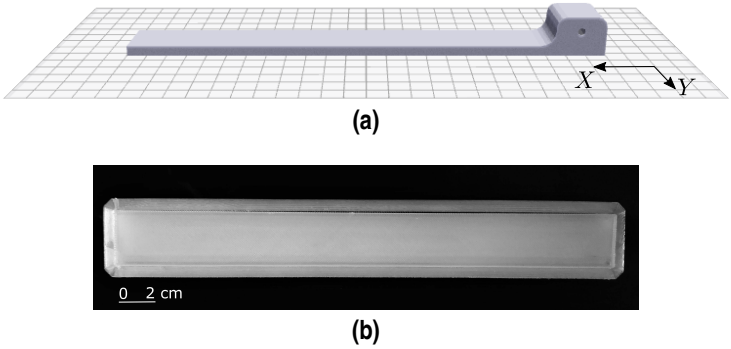

Figure 4.7 Nylon DCB specimen according to Fig. 4.5 printed in *horizontal direction*: (a) 3D view by Eiger software and (b) in-plane view ($X-Y$ plane) of the printing result.

Since the warping effects did not allow the manufacturing of the specimens to be performed according to the previous orientation, the subsequent coupons were printed along the width direction of the specimen (printing in *vertical direction*), as shown in Fig. 4.9. Unfortunately, in line with the previous printing option, the part started to warp when it reached a thickness value of around 5 mm, and therefore the printing procedure was once again interrupted (see Fig. 4.10).

Relying on the previous arguments, it can be concluded that warping effects occurred for very slender parts. In order to achieve a precise specimen production, the consideration of auxiliary supporting systems or alternative printing techniques for warping

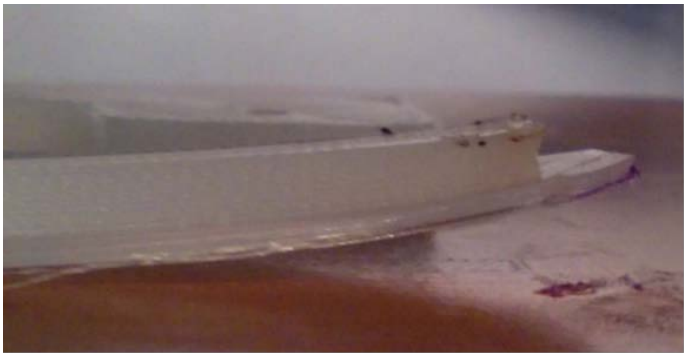

Figure 4.8 Detail of the specimen's corner of a nylon DCB specimen printed in *horizontal direction* according to Fig. 4.5.

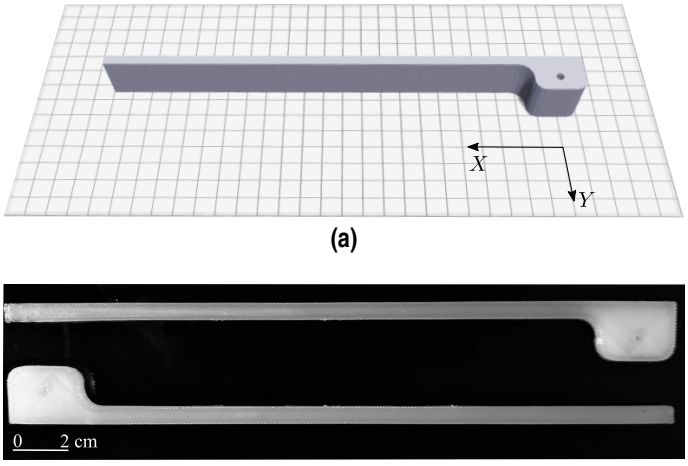

Figure 4.9 Nylon DCB specimen printed in *vertical direction* according to Fig. 4.5: (a) 3D view by Eiger software and (b) printing result.

prevention would be required [244].

Due to the fact that none of nylon specimens succeeded with the required geometrical characteristics, the specifications of the materials used for the posterior coupons were modified. In this sense, the production of hybrid nylon–glass-fiber specimens was considered. The mechanical properties of the glass-fiber reinforced material herein employed were: $E_{11} = 25.84$ GPa, $E_{22} = 1.13$ GPa, $\nu_{12} = 0.37$, $G_{12} = 0.88$ GPa [244]. The objective with regard to the use of glass-fiber for the current prototypes were twofold: (i) taking advantage of the superior strength and stiffness properties of glass-fiber over nylon from a mechanical point of view, (ii) the idealization of a robust design and printing process that allowed the production of DCB coupons incorporating structured interfaces to be carried out within acceptable geometrical tolerances. In this context,

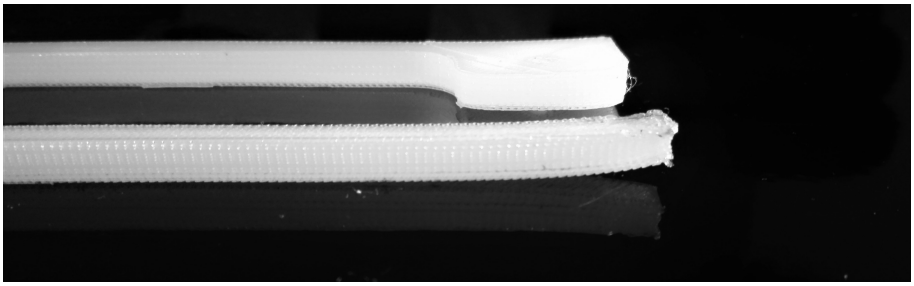

Figure 4.10 Detail of the specimen corner of a nylon DCB specimen printed in *vertical direction* according to Fig. 4.5.

theoretically, the differences in stiffness and thermal expansion coefficient between nylon and glass-fiber ($60 \times 10^{-6\circ}C^{-1}$ and $4.9 \times 10^{-6\circ}C^{-1}$, respectively) may mitigate the development of the previous warping effects during the manufacturing process. These characteristics allow the conditions according to the AITM standard [249] to be fulfilled.

Fig. 4.11 shows the layout of the material in the CAD solid model (glass fiber-reinforced material is identified by solid yellow lines) and the actual specimen, which was printed along its width direction (printing in *vertical direction*). Note that the specimen definition depicted in Fig. 4.11 initially included the deposition of glass-fiber reinforced material at the gripping system, which substantially increased the printing times (from about 7 hours to 14 hours). Each coupon part of length $L = 180$ mm, width $W = 25$ mm, thickness $h = 5$ mm consisted of 248 glass fiber reinforced layers of 0.1 mm in thickness, with 4 groups of composite filaments, that were orientated along the longitudinal direction of the specimen, and 2 nylon layers which corresponded to the topmost and bottommost layers.

The obtained specimens were characterized by a notable higher stiffness in comparison with the conventional DCB coupons made from nylon. However, the accuracy of the printed gripping system presented significant deficiencies. Thus, its production for each coupon was discarded in subsequent stages, being replaced by the use of an auxiliary carbon reinforced plate that connected the DCB specimen to the testing machine.

Three flat interface coupons, compatible with the available tooling (described in the AITM standard [249]) and fitting with the recommended dimensions in the ISO specification [184], were produced with the following dimensions: length $L = 169$ mm, width $W = 20$ mm, thickness $h = 4$ mm. These coupons were printed along the thickness direction (printing in *horizontal direction*). Each of two flat beams of the system consisted of 25 layers with 0.1 mm in thickness of glass-fiber reinforced composite, h_1, and 15 nylon layers with 0.1 mm in thickness, $(h - h_1)$, which were bonded using an adhesive layer, see Section 4.2. The pre-visualization of the specimen and the fiber layout, as well as the resulting specimen after the printing process are shown in Fig. 4.12, whereas a sketch depicting the specimen dimensions is available in Fig. 4.13.a.

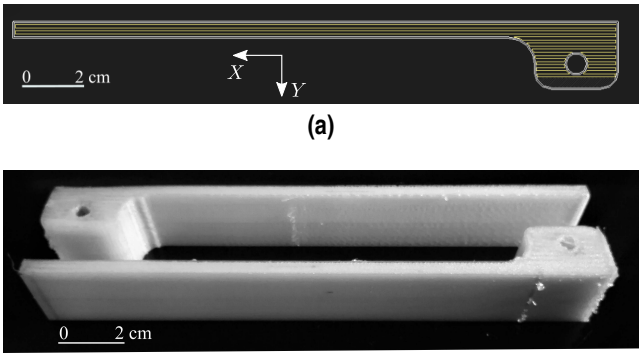

Figure 4.11 Glass-fiber DCB specimen according to Fig. 4.5 printed in *vertical direction*: (a) 2D view by Eiger software of a glass-fiber layer and (b) printing result.

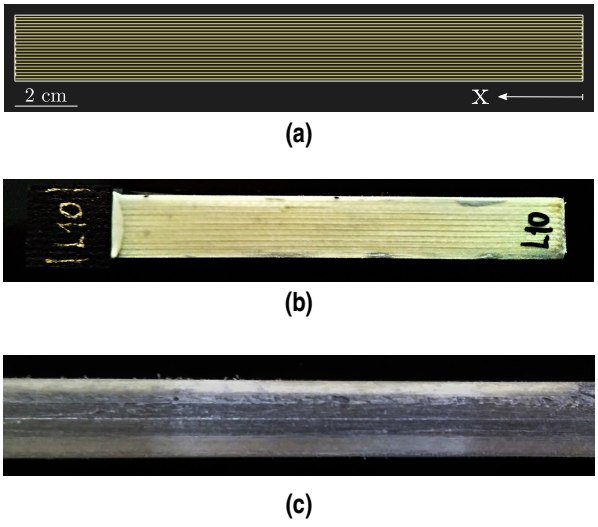

Figure 4.12 (a) 2D view by Eiger software of a glass-fiber composite layer. (b) Printing result of a glass-fiber DCB specimen according to Fig. 4.5 printed in *horizontal direction*. (c) Detail of the flat interface.

4.1.2.2 ALM manufacturing of DCB specimens with trapezoidal interfaces

Following the basic aspects of the printing procedure described above for flat interfaces, several DCB specimens with trapezoidal interfaces using three different wavelengths ($\lambda = 4, 6, 8$ mm) and two different amplitudes ($A = 1.5, 2$ mm) were printed along their thickness direction (printing in *horizontal direction*). $r = 1/2$ was considered for all printed specimens. In order to create an existing pre-crack, in line with standard

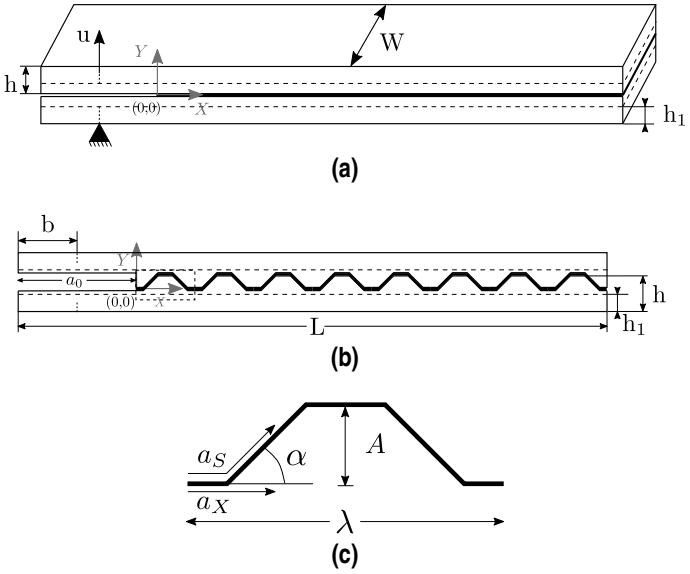

Figure 4.13 (a) Double cantilever beam (DCB) with a flat interface of length L, total thickness h, glass-fiber thickness h_1, nylon thickness $h - h_1$, width W and pre-crack length a_0. (b) DCB with trapezoidal interface of parameters A, amplitude, and λ, wavelength. Distance between the left end of the beam and the applied displacement point is represented by b. (c) Magnified view of trapezoidal interface. The actual crack length measured from the initial point $(0,0)$ is a_S. The projection of the crack length a_S along the X axis is a_X and the angle of the leaning section is $\alpha = \tan^{-1}\left(\frac{4A}{\lambda}\right)$ for $r = 1/2$.

DCB specimens, the printing procedure does not include a bonded interface on the side around the gripping system. Fig. 4.13.b depicts a sketch of a trapezoidal DCB specimen, including its overall dimensions and the position of the initial crack tip. Fig. 4.14 shows the graphical specimen designs and the produced specimen. In order to assembly the two beams of DCB system with structured interface profiles, a male-female design was required (Fig. 4.14). These parts were bonded using an adhesive (see details in Section 4.2), replicating the flat configurations.

Each of the beam halves that composed the DCB system consisted of 25 layers with 0.1 mm in thickness of glass-fiber composite, (h_1). Trapezoidal interfaces were manufactured from nylon using 25 layers with 0.1 mm in thickness for $A = 2\,\text{mm}$ $(h - h_1)$, and 20 layers with 0.1 mm in thickness for $A = 1.5\,\text{mm}$ $(h - h_1)$). Note that 5 nylon layers were part of the bulk material (beams), while the rest of nylon layers composed the interface region (Fig. 4.14.c). See Appendix A for further details. As was described above, the structured profile was produced using nylon, because of the impossibility of using fiber at this region of the specimen. This limitation arises from the specifications of the 3D printing system, which requires a minimal area equals to $6.45\,\text{cm}^2$ to use fiber-reinforced material within a layer during the manufacturing

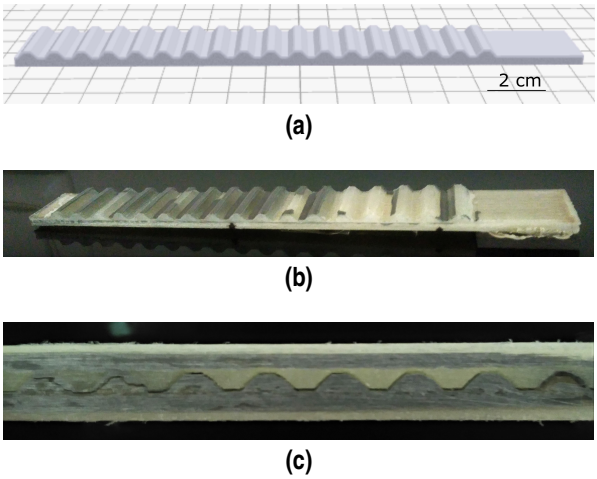

Figure 4.14 (a) 2D view by Eiger software of a glass-fiber layer and (b) printing result of a glass-fiber DCB specimen printed in *horizontal direction* according to Fig. 4.5. (c) Detail of the trapezoidal interface with $A = 2$ mm and $\lambda = 8$ mm.

process. The layers of the trapezoidal interface consisted of small rectangles whose areas were smaller than this threshold value.

Three samples of each configuration combining $\lambda = 4{,}6{,}8$ mm and $A = 1.5$, 2 mm were produced, which were identified as: (i) Tz1: $A = 2$ mm, $\lambda = 8$ mm; (ii) Tz2: $A = 2$ mm, $\lambda = 6$ mm; (iii) Tz3: $A = 2$ mm, $\lambda = 4$ mm; (iv) Tz4: $A = 1.5$ mm, $\lambda = 8$ mm; (v) Tz5: $A = 1.5$ mm, $\lambda = 6$ mm; (vi) Tz6: $A = 1.5$ mm, $\lambda = 4$ mm. However, some DCB samples (Tz3-Tz6) led to invalid results due to the fact that the crack growth was not confined to the interface, migrating to adjacent regions of the specimen. This undesirable response was attributed to the presence of defects during the printing process, and therefore the corresponding results are not included.

Table 4.1 summarizes the amplitude and wavelength values of the trapezoidal interface for three different "teeth" in each coupon configurations, as well as mean and standard deviation values of these parameters. In this way, we can determine the level of accordance and repeatability of each specimen used in the test program. Analyzing these data, with regard to the amplitude values, all measurements were slightly smaller than the nominal value, but this difference was repeated along the interface with an acceptable variance. Referring to the wavelength, a close agreement between the actual and nominal values was achieved. The average dimensions of each configuration included in Section 4.2.2 are detailed in Table A.2.

Table 4.1 Measurements of amplitude and wavelength for the produced DCB specimens with trapezoidal interface profiles employed in the experimental campaign.

Theoretical [mm]			Tooth 1 [mm]		Tooth 2 [mm]		Tooth 3 [mm]		Mean values [mm]	
	A	λ	A	λ	A	λ	A	λ	A	λ
Tz1-1	2	8	1.87	7.99	1.58	8.01	1.74	7.96	1.73 ± 0.14	7.99 ± 0.02
Tz1-2	2	8	1.73	8.02	1.54	7.97	1.63	8.05	1.63 ± 0.09	8.01 ± 0.04
Tz1-3	2	8	1.68	7.95	1.74	8.00	1.79	8.05	1.74 ± 0.05	8.00 ± 0.05
Tz2-1	2	6	1.69	6.08	1.58	6.14	1.63	5.90	1.63 ± 0.05	6.04 ± 0.12
Tz2-2	2	6	1.87	6.04	1.83	6.05	1.86	5.90	1.85 ± 0.02	5.99 ± 0.08
Tz2-3	2	6	1.86	6.09	1.72	5.83	1.82	6.12	1.80 ± 0.07	6.01 ± 0.16
Tz3-1	2	4	1.63	4.12	1.69	4.03	1.63	4.14	1.65 ± 0.03	4.09 ± 0.05
Tz5-1	1.5	6	1.16	5.92	1.29	6.28	1.32	5.97	1.25 ± 0.08	6.05 ± 0.19
Tz6-1	1.5	4	1.37	4.02	1.42	3.99	1.42	4.04	1.40 ± 0.03	4.02 ± 0.03

4.2 Experimental program: tests and results

4.2.1 Test description

In this section, the set-up of the experimental campaign and a detailed description of the performed test are given. The principal objective of the proposed DCB tests concerns with the characterization of the fracture resistance of bonded 3D printed hybrid nylon–glass-fiber reinforced coupons with trapezoidal interfaces (Section 4.1).

After the two sides of the DCB coupons for each configuration (flat or structured) were manufactured, the final system was assembled according to the following steps:

1. The brim region, which corresponded to an additional surrounding layer to decrease the warping effect, and remainder of nylon were removed from the specimen.
2. The specimens were cleaned with acetone to eliminate any additional debris and contaminants.
3. They were dried to eliminate the existing humidity that could deteriorate the test data.
4. The two halves of each DCB coupon were bonded with the adhesive EA 9394 at room temperature. The mechanical properties of the adhesive are: ultimate strength $\sigma_{rup} = 31.5\,\text{MPa}$, rupture strain $\varepsilon_{rupt} = 1.76\%$, Young's modulus $E = 4.1\,\text{GPa}$. These properties were obtained when the adhesive was strained at $0.1\,\text{min}^{-1}$ and cured for 45 min at $75°C$ [250].
5. In order to guarantee an initial crack length, a teflon film was inserted along the first 25 mm of each beam during the joining process.
6. Once the two beams were assembled, the DCB specimen, together with the pliers and the aluminium plates used to apply a uniform pressure between the two beams, was inserted into a convection oven for 90 min at $66°C$ for the adhesive curing process.

7. Finally, two auxiliary square carbon fiber plates of 25.5 mm side and 3 mm thickness were bonded to the outer surfaces of the beams around the pre-cracked end. These plates connect the specimen to the gripping system of the testing machine. The plates were bonded to the beams with the 2-component fast curing adhesive X60. The distance between the point where the displacement (Δ) was applied and the end of the DCB specimen was equal to $b = 12.75$ mm (see Fig. 4.13).

Fig. 4.15 shows a representative bonded DCB specimen with the load block connected. Tests were conducted using a universal testing machine INSTRON 4482, with a load cell of 5 kN under displacement control conditions. The loading rate corresponded to $\dot{\Delta} = 0.5$ mm/min, so that the experimental campaign was performed under quasi-static conditions.

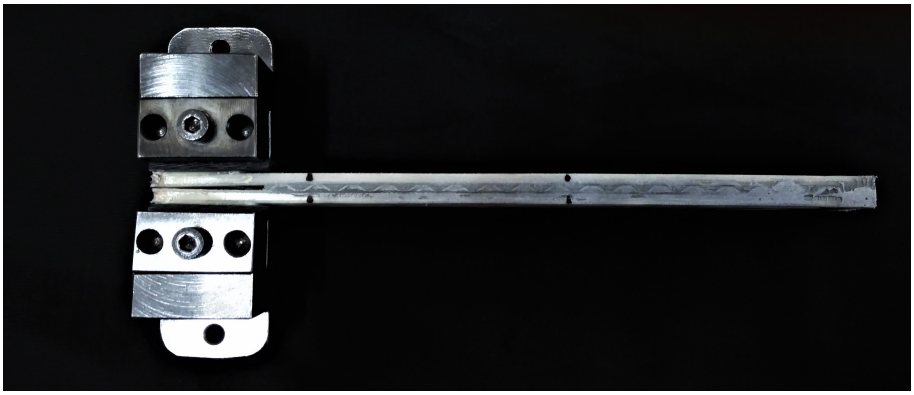

Figure 4.15 Trapezoidal interface specimen with parameters $A = 2$ mm and $\lambda = 8$ mm with load blocks. Black marks in the specimen indicate the projection of the actual crack length along the X axis in the position $a_{X1} = 10$ mm and $a_{X2} = 70$ mm.

In line with the standards mentioned above, the following supporting conditions were prescribed: a vertical cross-head displacement Δ (along the Y-axis), was applied close to the left-side border of the beam (at $X = -a_0 + b$ in Fig. 4.13), while the right-side border of the specimen (at $X = \mathrm{L} - a_0$ in Fig. 4.13) was free. The cross-head displacement along the Y-direction in Fig. 4.13, perpendicular to the crack plane, was recorded during the test.

The specimens herein considered were tested without any previous loading history. Crack growth was monitored during data recording. It is worth mentioning that the auxiliary carbon fiber plates of the system exhibited very low deformation, ensuring the correct transmission of the load from the machine gripping to the coupons and avoiding extra energy release sources. Finally, the experiments were carried out in an environmentally controlled room with the following conditions: temperature 22°C, 50 % moisture, and pressure 1 atm.

4.2.2 Experimental results

The experimental results corresponding to 3D printed nylon–glass-fiber reinforced DCB specimens with flat and trapezoidal interface profiles are comprehensively discussed in this section. Special attention is devoted to the qualitative and quantitative description of the experimental data, pinpointing the benefits of using structured interfaces for the achievement of an increase in the crack resistance in comparison with current flat interface designs.

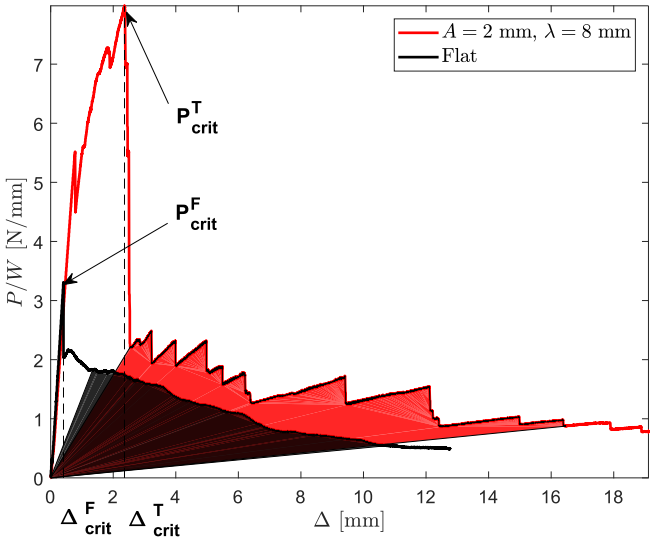

Figure 4.16 Load-displacement curves of flat and trapezoidal interface with parameters $A = 2\,\text{mm}$ and $\lambda = 8\,\text{mm}$. Filled areas represent the energy released during the DCB tests between effective crack length $a_{X1} = 10\,\text{mm}$ and $a_{X2} = 70\,\text{mm}$.

Fig. 4.16 depicts a representative load vs displacement evolution curve, where a direct comparison between flat and trapezoidal interface ($A = 2$ mm, $\lambda = 8$ mm) configurations is performed. As discussed previously, qualitative similar evolutions were obtained for the rest of structured DCB coupons herein considered, whose results are not depicted in Fig. 4.16 for the sake of clarity. The first observation is that the peak load for structured DCB specimen P^T_{crit} is notable higher than that corresponding to flat interface definition P^F_{crit}. Furthermore, both curves can be divided in two different regions. The initial part of the curve was characterized by a proportional load-displacement evolution up to reaching their corresponding peak value (P^T_{crit} for structured DCB and P^F_{crit} for flat DCB), whose respective critical displacements are identified by Δ^T_{crit} and Δ^F_{crit}. We note that this initial phase of both diagrams are very close to each other, indicating a similar bending stiffness for such configurations. However, the critical loading and

displacement values for crack initiation are significantly higher for the structured DCB coupon than that referred to the flat DCB specimen.

Continuing the analysis of Fig. 4.16, the second stage of the $P-\Delta$ diagram is characterized by a decreasing evolution of the load-displacement curve ($\Delta > \Delta_{crit}$), which clearly indicated the development of crack events along the interface. Throughout this second phase, the flat DCB coupon featured a soft evolution till the residual strength value. Conversely, the evolution of the DCB specimen with trapezoidal interface definition was characterized by a saw-tooth profile, this behavior being associated with the crack evolution path between adjacent trapeziums along the interface. Note that within this degrading stage, any unloading would endow a linear decrease of the $P-\Delta$ curve back to the origin. Therefore, the marked area in red represents the energy released during the test including the structured interface.

Additionally, it is worth mentioning that, in some specimens, very localized crack growth started in the rising part of the load–displacement evolution curve (Fig. 4.16). This phenomenon can be identified in such evolution with a small kink along the initial phase with a subsequent increase till reaching P_{crit}. The occurrence of this kink was mainly attributed to the presence of small imperfections at the adhesive layer, in particular around the pre-crack region. Due to the potential presence of such imperfections, the peak load might have slightly different quantitative values for the identical DCB specimens.

Fig. 4.17 depicts the load vs. displacement evolution curves for the structured DCB specimens, with valid performance, in comparison with flat DCB cases. This graph shows very similar stiffness values for $A = 2$ mm (Fig. 4.17.a), see the zoomed region in Fig. 4.17.b, whilst small deviations for $A = 1.5$ mm (Fig. 4.17.c) with respect to flat DCB coupons along the pre-peak evolution are observed. The slight discrepancies for $A = 1.5$ mm cases were derived from the presence of larger pre-crack regions than those previously mentioned but the corresponding fracture resistance performances are worth to be analyzed.

In addition, the positive slope regions in these jumps during the evolution are attributed to the crack growth along the inclined sections of the trapezoidal pattern. The load increments or the peaks which appear in the softening part of the curve may be explained due to the occurrence of mixed-mode fracture conditions along the inclined sections of the trapezoidal pattern. Note that as general trend, in line with [92], force values increase with higher values for the ratio A/λ and correspondingly the critical opening displacement for crack initiation.

With regard to the energy released for each coupon, its quantification was carried out by processing the data of the load-(cross-head) displacement curve. In this regard, we assumed that this determination can be conducted based on standard methods, which have been extensively used for flat DCBs [249]. In this concern, mixed mode fracture conditions at the interface were prone to occur for DCB samples with structured interfaces. Accordingly, complying with the hypothesis stating that the energy is exclusively dissipated along the interface and for elastic deformation of the DCB beams, it is important to distinguish between two possible critical energy release rate values [92]:

- The first option is denominated as effective or apparent critical energy release rate

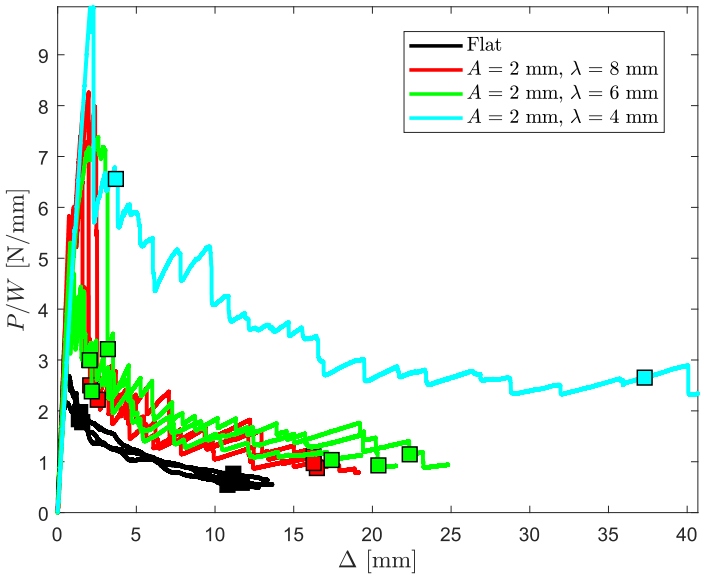

(a) Load-displacement curves of flat (black) and structured interfaces with parameters $A = 2\,\text{mm}$, $\lambda = 8\,\text{mm}$ (red), $A = 2\,\text{mm}$, $\lambda = 6\,\text{mm}$ (green), $A = 2\,\text{mm}$, $\lambda = 4\,\text{mm}$ (cyan).

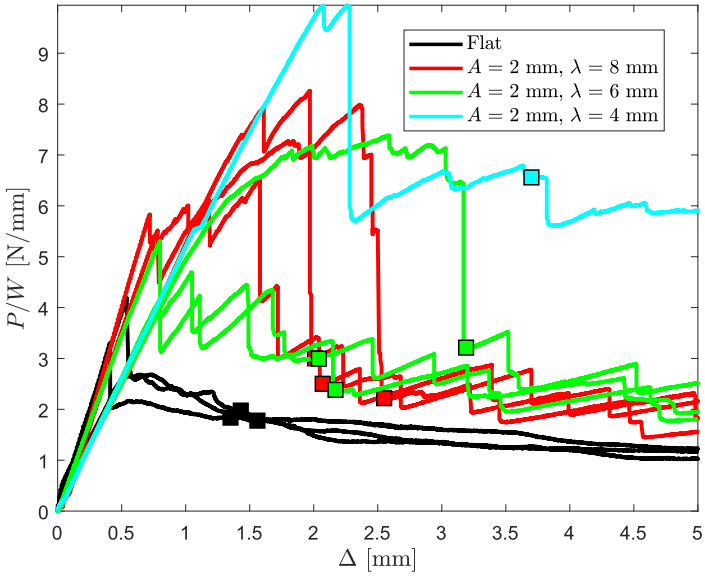

(b) Zoom-up of plot given in (a) in the range $\Delta = (0 - 5)$ mm .

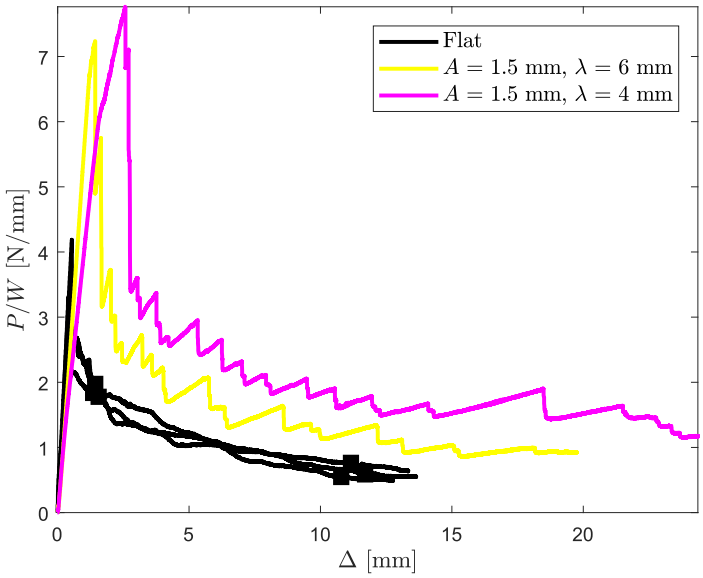

(c) Load-displacement curves of flat (black) and structured interfaces with parameters $A = 1.5\,\text{mm}$, $\lambda = 6\,\text{mm}$ (yellow) and $A = 1.5\,\text{mm}$, $\lambda = 4\,\text{mm}$ (magenta).

Figure 4.17 Load-displacement curves of flat (black) and structured interfaces. Square markers in the curves represent the load-displacement value when the crack reaches $a_{X1} = 10\,\text{mm}$ and $a_{X2} = 70\,\text{mm}$.

G_c^X, which considers the energy dissipated during the crack propagation when the crack is extended along the X-direction (Fig. 4.13). Then, the crack length is identified by a_X (as shown in Fig. 4.13), and the computation of the critical energy release rate reads

$$G_c^X = -\frac{\partial \Pi_f(a_X)}{\partial (W \cdot a_X)}, \tag{4.1}$$

where $\Pi_f(a_X)$ is the energy dissipated during the crack propagation when the crack grows an area $\mathrm{d}A_f = W\mathrm{d}a_X$.

- Alternatively, the actual critical energy release rate G_c^S can be defined as the energy dissipated during the crack propagation, when the crack is extended along the S-direction (defined by a_S in Fig. 4.13) as

$$G_c^S = -\frac{\partial \Pi_f(a_S)}{\partial (W \cdot a_S)}, \tag{4.2}$$

$\Pi_f(a_S)$ being the energy dissipated during the crack propagation when the crack grows an area $\mathrm{d}A_f = W\mathrm{d}a_S$ and S-direction identifying the curvilinear pattern

following the crack.

Specifically, in order to quantify such properties, the actual area created by the crack advance ($W \cdot a_S$) and its projection on the horizontal plane ($W \cdot a_X$), between two different effective crack lengths (a_{X1} and a_{X2}), was employed. At this point, it is worth mentioning that for flat interfaces, this distance can be determined by directly taking measurements on the test specimen ($a_X = a_S$). Conversely, for specimens with trapezoidal interfaces, the crack advance (a_S) can be described as a function of geometrical parameters of the interface and the distance along the horizontal axis (X-axis): $a_S = a_S(a_X, A, \lambda)$.

According to [249], the computation of the fracture energy for a DCB tests requires the load and displacement values when the crack reaches $a_{X1} = 10\,\text{mm}$ and $a_{X2} = 70\,\text{mm}$. A digital microscope camera was used to monitor the crack propagation, and therefore the corresponding displacement and loading values at a_{X1} and a_{X2} (which were previously marked in the specimen as shown in Fig. 4.15), were recorded.

Analyzing the experimental evolutions shown in Fig. 4.17, square markers correspond to the load and displacement values at which the crack length reaches the locations $a_{X1} = 10\,\text{mm}$ and $a_{X2} = 70\,\text{mm}$, in both flat and structured interfaces following trapezoidal patterns. The enclosed area between the experimental curve and straight lines that connect the origin with each marker represents the energy released in each configuration (Fig. 4.16).

Table 4.2 reports the effective (G_c^X) and actual (G_c^S) critical energy release rates for the DCBs with trapezoidal and flat interfaces under investigation. Relying on these data, it can be observed that, as expected, the higher A/λ ratio was defined, the higher improvements on the fracture resistance values G_c^S and G_c^X with respect to the flat configuration were obtained. Indeed, the ratio between effective and actual interfacial fracture toughness complied within the range 20-60%, featuring an increasing evolution with the aspect ratio A/λ. This fact indicates that the contribution of the fracture Mode II at the local crack tip becomes more significant for higher values of A/λ. In fact, since the results of G_c^X can be interpreted as the critical energy release rate that is required to propagate a crack along the X-direction, higher values of A/λ lead to the creation of larger areas during the crack propagation of the interface.

Performing a direct comparison of the critical energy release rates for structured interface configurations with those referred to flat DCBs, which correspond to the reference scenario in current practical applications, a significant improvement of the crack resistance performance can be appreciated.

This beneficial effect can be directly appreciated in Fig. 4.18 with the corresponding average values being summarized in Table 4.3. The most unfavourable configuration with $A/\lambda = 1/4$ experienced an increment of the corresponding effective critical energy release rate around 99% in comparison to the reference flat value, whereas the actual critical energy release rate was increased of around 65%. Although these improvements in the fracture resistance values are of considerable magnitude, the best configuration in these terms showed an increment of the effective and actual critical release rates around 803% and 459%, respectively. These impressive data clearly reveal the potential crack resistance improvements that can be achieved by means of the production of specimens with structured interfaces. Consequently, the conception of new prototypes through the

Table 4.2 Effective fracture toughness G_c^X, actual fracture toughness G_c^S, effective and actual fracture toughness ratio $\frac{G_c^X}{G_c^S}$ and projected area in horizontal plane and actual area created $\frac{A_S}{A_X}$ in each specimen tested.

Configuration	Sample	A [mm]	λ [mm]	A/λ [−]	$G_c^X \left[\frac{\text{J}}{\text{m}^2}\right]$	$G_c^S \left[\frac{\text{J}}{\text{m}^2}\right]$	$\frac{G_c^X}{G_c^S}$ [−]	$\frac{A_S}{A_X}$ [−]
Flat	L1	-	-	0	144.8	144.8	1	1
	L2	-	-	0	139.9	139.9	1	1
	L3	-	-	0	124.3	124.3	1	1
Tz1	Tz1-1	2	8	0.25	260.4	215.7	1.20	1.20
	Tz1-2	2	8	0.25	237.0	196.3	1.20	1.20
	Tz1-3	2	8	0.25	324.5	268.9	1.20	1.20
Tz5	Tz5-1	1.5	6	0.25	262.1	217.1	1.20	1.20
Tz2	Tz2-1	2	6	0.333	291.0	218.3	1.33	1.33
	Tz2-2	2	6	0.333	400.0	300.0	1.33	1.33
	Tz2-3	2	6	0.333	422.4	316.8	1.33	1.33
Tz6	Tz6-1	1.5	4	0.375	484.0	345.4	1.40	1.40
Tz3	Tz3-1	2	4	0.5	1231.2	760.9	1.62	1.62

use of novel ALM techniques can certainly mitigate the onset and development of crack events in bonded composite joints. In this way, such manufacturing capabilities can contribute to foster innovative design scenarios for the future generation of composite structural components in practical applications.

Table 4.3 Average G_c^X and G_c^S and comparison of structured specimens regard to flat case $\frac{G_c^X}{G_c^X|_{Flat}}$ and $\frac{G_c^S}{G_c^S|_{Flat}}$.

A/λ [−]	$G_c^X \left[\frac{\text{J}}{\text{m}^2}\right]$	$G_c^S \left[\frac{\text{J}}{\text{m}^2}\right]$	$\frac{G_c^X}{G_c^X\|_{Flat}}$ [−]	$\frac{G_c^S}{G_c^S\|_{Flat}}$ [−]
0 (Flat)	136.3 ± 10.7	136.3 ± 10.7	1	1
2/8	271.0 ± 37.5	224.5 ± 31.1	1.99	1.65
2/6	371.2 ± 70.3	278.4 ± 52.7	2.72	2.04
1.5/4	484.0 ± 0	345.4 ± 0	3.55	2.53
2/4	1231.2 ± 0	760.9 ± 0	9.03	5.58

4.3 Concluding remarks

An experimental campaign to determine the fracture properties of patterned-interface fiber-reinforced 3D printed adhesively bonded joints has been developed. This empirical analysis allowed a comparison of the structured interfaces with the baseline configuration (flat interface) to be performed. Moreover, the limitations and the potential of this technique have been examined for long fiber- reinforced 3D printed specimens. In particular, a dimensional analysis provided an initial estimation for geometrical parameters of the interface, mainly the amplitude A and wavelength λ of the pattern, of the desktop continuous fiber 3D printer MarkOne®.

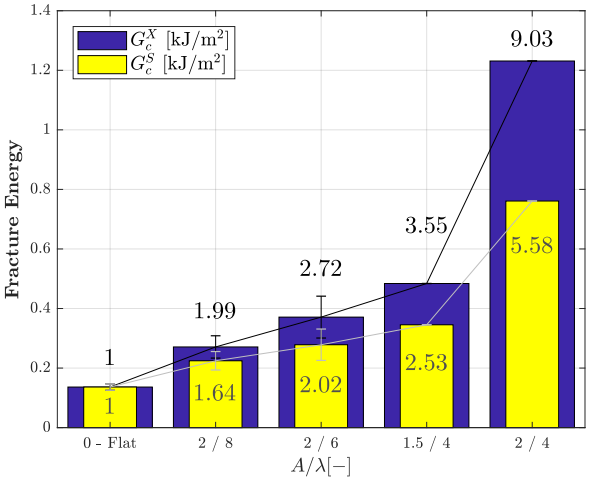

Figure 4.18 Average G_c^X and G_c^S and comparison of structured specimens regard to flat case $\frac{G_c^X}{G_c^X|_{Flat}}$ and $\frac{G_c^S}{G_c^S|_{Flat}}$.

Regarding the experimental tests, nylon–glass-fiber composite hybrid specimens for Double Cantilever Beam tests with different interface configurations were tested including flat interfaces and trapezoidal patterns with dimensions $A = 2$, 1.5 mm and $\lambda = 4$, 6, 8 mm. The concept of effective or apparent critical energy release rate G_c^X were introduced so as to compare properly different profiles at the interface in a DCB test, regardless the size and shape of the pattern.

Promising perspectives emanate from the experimental results, where every structured configuration increases the fracture energy with respect to the reference straight interface in the debonding process. Such enhancement of the effective critical fracture toughness increase with the ratio A/λ and ranges from twice to nine times higher for the specimens considered in the study ($A/\lambda = [0.25 - 0.5]$).

5 Analytical study of patterned interfaces in Double Cantilever Beam tests

Structured patterns have shown experimentally substantial improvements of the interfacial adhesion properties in terms of damage tolerance and energy dissipation in Chapter 4 and by other authors [251, 252].

This fact motivated to establish a simplified analytical cohesive-based model, which enables the achievement of a more profound understanding with regard to such considerable improvements in terms of fracture resistance properties. This model provides a simple, robust and rapid prototyping tool for the design of structured interfaces for its application under general mixed-mode fracture conditions, taking into account the influence of the different parameters of the cohesive law in the patterned interface energy release rate. These results are compared with the experimental data, being the theoretical predictions in close agreement.

The present Chapter is organized as follows. Section 5.1 addresses the development of the analytical method herein proposed and the corresponding assessment of the theoretical predictions with respect to the experimental data. Finally, Section 5.2 summarizes the advantages and limitations of the proposed analytical model.

5.1 A Simplified Analytical Approach (SAA) to predict the properties of a structured interface

The aim of this Section is to provide a simplified explanation of the effective fracture toughness increment when trapezoidal interfaces are used.

This analytical model stems from the necessity of providing a plausible mechanical explanation with regard to the significant increase in fracture toughness values for structured interface specimens with trapezoidal patterns with respect to those corresponding to coupons with flat interface profiles. Therefore, through the definition

of the geometrical parameters of the interface and the adhesive properties, possible estimations of the fracture toughness in future designs might be accomplished by means of simple calculations. These predictions could significantly contribute to reduce the costs associated with the design and execution times of the corresponding experimental program.

For the development of the present model, it is interesting to note also that different interface geometries (different types of profiles) are compared with respect to the flat case and it would be convenient to consider the analysis of each region of the interface for its individual analysis, i.e. the fracture conditions at the interface horizontal edges are different from those corresponding to the inclined edges for the current loading conditions. Moreover, due to the repetitive pattern, it is assumed that the particular analysis of these regions can be extrapolated to what occurs at the complete interface. In such a way, the problem is locally analyzed, the model becoming valid for any crack length (provided that it is of the order of the parameters that define the interface A, λ) and any dimension of the non-conventional configuration.

To this end, the construction of the current analytical model relies on the hypothesis stating that the strain state at the interface is assumed to be uniform along each of the regions of the trapezium, i.e. the horizontal and the inclined edges of the interface, during the fracture process. Furthermore, it is additionally supposed that the external imposed displacement at each trapezium, that is transferred from the testing machine, coincides with the vertical direction (Y-axis) according to the framework given in Fig. 5.1.

Based on the previous considerations, the adhesive layer experiments mixed mode fracture conditions at the inclined edges of the interface, which are function of the angle α (Fig. 5.1.b and Fig. 5.1.c), whereas Mode I fracture conditions can be envisaged at the horizontal sections of each trapezium (Fig. 5.1.a and Fig. 5.1.c).

A standard bilinear cohesive model in plane strain conditions is considered, see Section 3.3.2.

Stiffness in normal and tangential direction are allowed to have different values, i.e. $k_n \neq k_s$. These parameters of the cohesive law, k_n and k_s, can be associated with the elastic adhesive properties through Young's modulus and Poisson's ratio [226]. Thus, for a correct characterisation of the elastic behaviour in an adhesive joint, dissimilar values for penalty stiffness in normal and shear direction are required. In this way, energy released rates in Mode I and Mode II can be calculated by

$$G_I = \frac{1}{2} k_n \left(\delta_n^0(\beta) \delta_n^f(\beta) - \delta_n \delta_n^f(\beta) \right), \tag{5.1}$$

$$G_{II} = \frac{1}{2} k_s \left(\delta_s^0(\beta) \delta_s^f(\beta) - \delta_s \delta_s^f(\beta) \right), \tag{5.2}$$

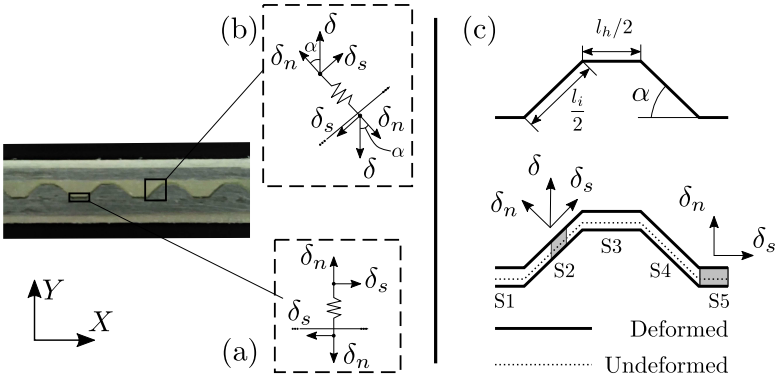

Figure 5.1 Sketch of displacements at the interface in the SAA: (a) flat interface edge, and (b) inclined interface edge. (c) Undeformed and deformed scenario assumed in SAA. δ, δ_n, δ_s represent the total, normal and tangential displacements, respectively, and α represents the angle of the inclined section along the interface. l_i and l_h represent the length of the inclined and horizontal sections in the trapezium, respectively.

where β identifies the displacement-based mixed-mode ratio. Assuming that damage evolution is based on energetic aspects, the mixed mode can be expressed as

$$B = \frac{G_{II}}{G_T} = \frac{\frac{k_s}{k_n}\beta^2}{1-2\beta+(1+\frac{k_s}{k_n})\beta^2}, \quad \text{with} \quad \beta = \frac{\delta_s}{\delta_s+\delta_n} = \frac{\sin\alpha}{\sin\alpha+\cos\alpha}, \tag{5.3}$$

where α is the angle of the sloped region of the joint section and $G_T = G_I + G_{II}$ is the total energy released, i.e., the sum of energies in Mode I, G_I, and Mode II, G_{II}.

5.1.1 Linear evolution of the mixed mode and stiffness relationship $k_s/k_n = 1$

At this point, a linear evolution between fracture Mode I and Mode II and a stiffness relationship between normal as well as shear direction equal to $\frac{k_s}{k_n} = 1$ is assumed. These hypothesis constitute the simplest case for the theoretical approach to study patterned interfaces.

Given a particular interface definition, the portion of the horizontal edges m_1 with respect to the total interface length $l_t = l_i + l_h$ reads: $m_1 = l_h/l_t$, where l_h represents the length of the horizontal edges for a given interface profile. In a similar way, the ratio between the inclined and total interface lengths take the form: $m_2 = l_i/l_t$, where l_i stands for the length for the inclined edges of each trapezium. Then, the fracture energy that is dissipated along an inclined edge for a given mode mixity B can be computed through the Benzeggah-Kenane criteria particularized by a fitting exponent $\eta = 1$.

In addition, note that an extreme case implies a vertical interface edge, whereby pure Mode II fracture conditions take place.

With these ingredients at hand, for the current study, the fracture energy released at the trapezoidal interface can be estimated by taking into consideration the energy dissipated at each region, i.e. the horizontal and inclined edges, with respect to the their corresponding length ratios m_1 and m_2, respectively. In such a way, the critical energy release rate for each interface configuration with respect to the actual interface length, G_c^S, or to the interface wavelength, G_c^X, can be approximated as

$$G_c^S = m_1^S G_{Ic} + m_2^S \left[B G_{IIc} + (1-B) G_{Ic} \right], \tag{5.4}$$

$$G_c^X = m_1^X G_{Ic} + m_2^X \left[B G_{IIc} + (1-B) G_{Ic} \right], \tag{5.5}$$

where

$$m_1^S = l_h / l_t, \quad m_2^S = l_i / l_t, \tag{5.6}$$

$$m_1^X = l_h / \lambda, \quad m_2^X = l_i / \lambda. \tag{5.7}$$

The previous formulation could be also generalized for the case for interface profiles with several inclined edges, whose respective length ratios would be denoted as m_i. Thus, Eq.(5.4) would take the form

$$G_c^S = \sum_{i=1}^{n_i} m_i \left[B_i G_{IIc} + (1-B_i) G_{Ic} \right] \tag{5.8}$$

where n_i is the number of inclined edges along the particular interface pattern, and B_i is the corresponding mode mixity.

In the following, the accuracy of the current analytical model for the estimation of the critical energy release rate for structured interfaces is assessed using the experimental data presented in Section 4.2.2.

Fig. 5.2 shows the correlation between the experimental results and the estimations of the critical energy release rate using the developed analytical method for different G_{IIc}/G_{Ic} ratios (assuming $G_{Ic} = 136.3$ J/m^2) as a function of the aspect ratio A/λ and the angle α. As can be seen in the graphs, there is a wide range of values of the ratio A/λ within the interval [0 - 0.30] where a very good agreement between the analytical model and the experimental results was achieved for appropriate values of G_{IIc}/G_{Ic}. This latter ratio had a significant influence on the evolution of the curve within the considered range, especially for very high A/λ values for which the role of the parameters affected by G_{IIc} become more relevant.

Moreover, as can be observed in Fig. 5.2, the evolution trends for G_c^X and G_c^S are different from each other. On the one hand, the slope of the evolution corresponding to the apparent fracture toughness G_c^X is increasing for high A/λ values. This increasing slope reveals the increase of area which is produced with the variable A/λ to travel a similar distance along the X-direction. On the other hand, the slope of the G_c^S presents an asymptotic evolution, which would correspond to G_{IIc}.

Recalling the previous discussion, due to the good agreement between the analytical model and the experimental values, the proposed model can be considered a valuable

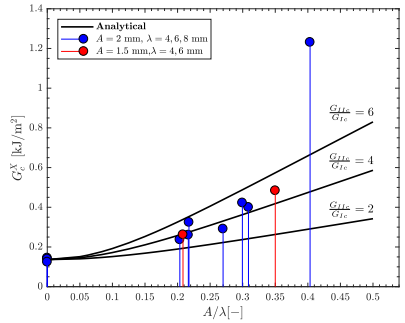

(a) Effective fracture toughness G_c^X versus aspect ratio $\frac{A}{\lambda}$.

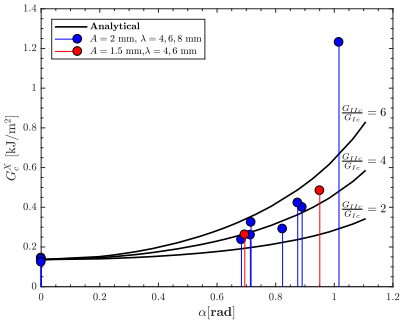

(b) Effective fracture toughness G_c^X versus angle α.

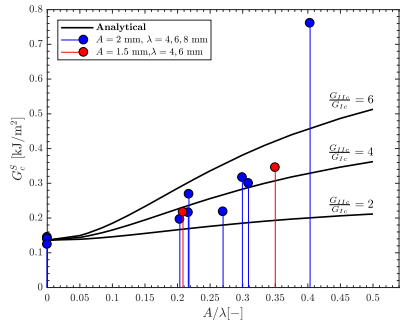

(c) Actual fracture toughness G_c^S versus aspect ratio $\frac{A}{\lambda}$.

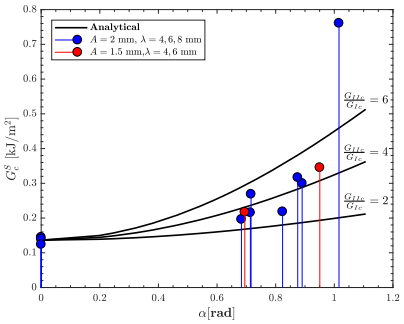

(d) Actual fracture toughness G_c^S versus angle α.

Figure 5.2 Experimental effective and actual fracture toughness, G_c^X and G_c^S, versus aspect ratio $\frac{A}{\lambda}[-]$ and the angle $\alpha[-]$ and SAA with parameters $G_{Ic} = 136.3$ J/m^2, $G_{IIc} = 2,4,6 \cdot G_{Ic}$, linear mixed mode evolution corresponding to $\eta = 1$ in the B-K law and penalty stiffness relation $k_s/k_n = 1$. The markers represent experimental values and the curves correspond to the analytical model.

design tool for the estimation of the prospective increase in the crack resistance properties of a wide range of structured interfaces ranging from trapezoidal to triangular interfaces for moderate A/λ ratios.

However, for each particular interface definition, there is a particular limit value of A/λ from which the analytical model is not able to capture the experimental data with a satisfactory level of agreement. These deviations are mainly attributed to the fact that the modeling assumptions regarding with the fracture conditions at each interface region (inclined and horizontal edges) are not valid any longer. In particular, mixed mode conditions are expected to take place along the complete interface profile, leading to

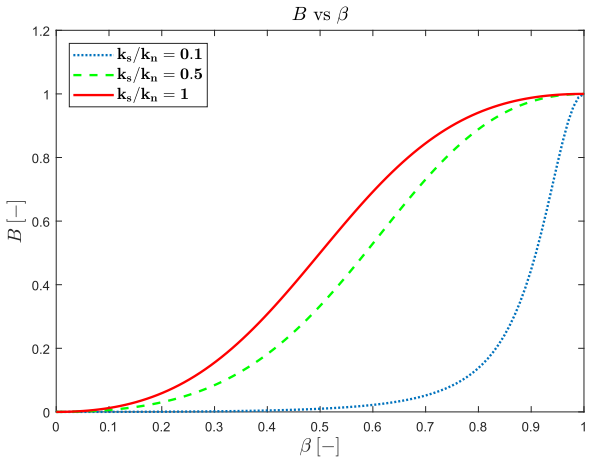

Figure 5.3 Mixed mode value B as a function of mix mode ratio β for $\frac{k_s}{k_n} = 1$ (continuous red line), $\frac{k_s}{k_n} = 0.5$ (dashed green line) and $\frac{k_s}{k_n} = 0.1$ (dotted blue line).

non-uniform strain states at the adhesive layer that might experience notable variations during each step of the test. Further improvements of the present model might also include some aspects of the generalized semi-analytical approach proposed in [253]. These considerations could be analyzed through the use of a numerical model.

5.1.2 Benzeggah-Kenane mixed mode evolution and different values of the stiffness relationship k_s/k_n

The presence of the ratio k_s/k_n in the mixed mode formulation can become a determining factor in the estimation of the energy release rate, that is, an incorrect value of this factor may lead to an inaccurate energy release rate evolution within the range $\beta \in [0,1]$. Usually in the literature, cohesive models set factor $\frac{k_s}{k_n} = 1$ [220, 254]. Nevertheless, this ratio may not reproduce the actual behaviour of the adhesive, both elastic and inelastic parts. Stresses are directly affected by the ratio k_s/k_n through the linear elastic relationship, while the energy-based mixed mode ratio B versus β evolution, Eq. (5.3), is depicted in Fig. 5.3.

As shown in Fig. 5.3, pure Mode I and pure Mode II do not depend on the relation $\frac{k_s}{k_n}$, see Eq. (5.3), leading to $B = 0$ for $\beta = 0$ whereas $B = 1$ for $\beta = 1$, regardless of the $\frac{k_s}{k_n}$ value. However, the mixed mode value B depends on the value of the ratio $\frac{k_s}{k_n}$ in an intermediate scenario and the adhesive behaviour may change considerably. For example, in the range $\beta \in [0,0.2]$, that is, strains close to pure Mode I, mixed mode value B barely varies with parameters $\frac{k_s}{k_n}$ and β. On the other hand, in the range $\beta \in [0.2,1]$ the variation of B strongly depends on the stiffness ratio and mixed mode ratio, so that the global response of the structure will be notable affected by the ratio k_s/k_n. Actually, the critical energy release rate G_c associated with each of the cases considered herein is represented in Fig. 5.4 for the Benzeggah-Kenane criterion (Eq. (3.47)).

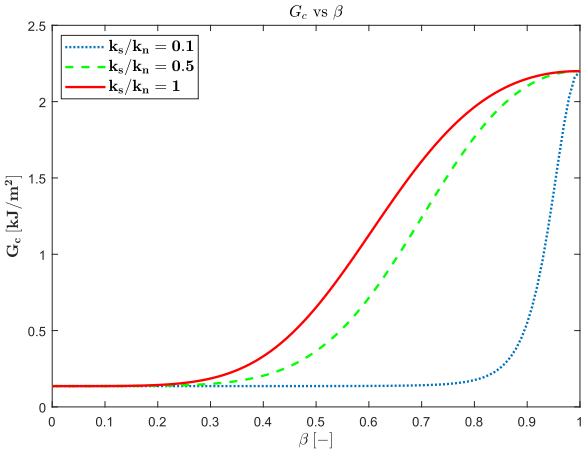

Figure 5.4 Critical energy release rate G_c according to Benzeggah-Kenane criterion as a function of mix mode ratio β for $\frac{k_s}{k_n} = 1$ (continuous red line), $\frac{k_s}{k_n} = 0.5$ (dashed green line) and $\frac{k_s}{k_n} = 0.1$ (dotted blue line). $G_{Ic} = 136.3$ J/m^2, $G_{IIc} = 16 \cdot G_{Ic}$ and $\eta = 2$.

As in the case of B, the influence of ratio $\frac{k_s}{k_n}$ on critical energy release rate G_c is relevant for medium and high values of mixed mode ratio β. In fact, this dependency is increased by the B-K criterion, specially for high ratios of $\frac{G_{IIc}}{G_{Ic}}$. In this way, the ratio $\frac{k_s}{k_n} = 0.1$ releases energy with a value very close to fracture Mode I conditions up to reaching $\beta \approx 0.8$, while critical fracture toughness associated with mixed mode and shear mode is confined to the range $\beta \in [0.8,1]$. This noticeable exponential character of the curve is lost in the case $\frac{k_s}{k_n} = 0.5$, which describes a typical B-K law where mixed mode fracture toughness is enclosed within the range $\beta \in [0.2,1]$. This difference may be crucial in tests presenting a large ratio of mixity, as shown in Section 6.1.2.

An additional remarkable aspect is that the evolution of the critical energy release rate G_c with respect to the mixed mode value of the parameter B is identical for any value of the ratio $\frac{k_s}{k_n}$, as shown in Fig. 5.5. The difference in each of these cases stems from the strain necessary to achieve a certain value of B. That is, to reach a mixity of $B = 0.7$, a ratio of $\beta = 0.94$ is needed for $\frac{k_s}{k_n} = 0.1$, $\beta = 0.69$ for $\frac{k_s}{k_n} = 0.5$ and $\beta = 0.61$ for $\frac{k_s}{k_n} = 1$. Correspondingly, the level of shear deformation to achieve a certain mixed mode value B decreases with the value of the ratio $\frac{k_s}{k_n}$, i.e. the lower stiffness ratio the higher mixed mode ratio β is needed to get the same value of B.

Focusing on the current scope of this Chapter, patterned interfaces present significant mixed mode values B along the crack path because of the interface geometry, which varies with the aspect ratio $\frac{A}{\lambda}$, see [255]. Thus, each of the DCB test with trapezoidal interfaces represents a suitable scenario to analyse the influence of stiffness ratio $\frac{k_s}{k_n}$ on the critical energy release rate. First, we recall the theoretical model in Section 5.1.1, where global fracture toughness, G_c^S and G_c^X, depend on the mixed mode value B and

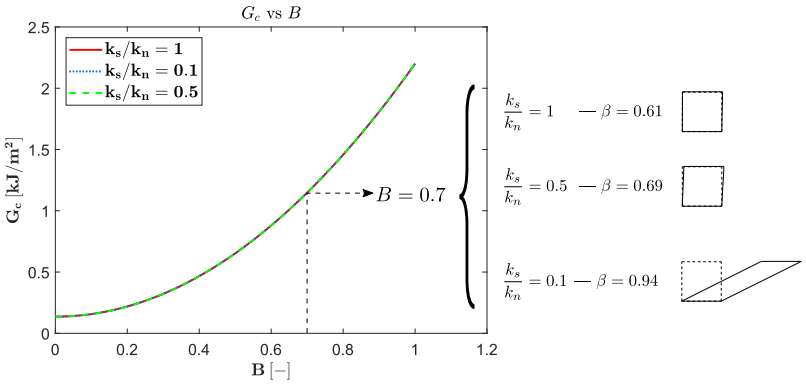

Figure 5.5 Critical energy release rate G_c according to Benzeggah-Kenane criterion as a function B for $\frac{k_s}{k_n} = 1$ (continuous red line), $\frac{k_s}{k_n} = 0.5$ (dashed green line) and $\frac{k_s}{k_n} = 0.1$ (dotted blue line). $G_{Ic} = 136.3$ J/m^2, $G_{IIc} = 16 \cdot G_{Ic}$ and $\eta = 2$.

the length of each section of the trapezium considered separately, l_i and l_h, with respect to the total length $l_t = l_i + l_h$ or the wavelength λ as

$$G_c^S = m_1^S G_{Ic} + m_2^S \left[B^\eta G_{IIc} + (1 - B^\eta) G_{Ic}\right], \tag{5.9}$$

$$G_c^X = m_1^X G_{Ic} + m_2^X \left[B^\eta G_{IIc} + (1 - B^\eta) G_{Ic}\right]. \tag{5.10}$$

With these expressions at hand, it is possible to capture the trend of the evolution of the fracture toughness for different values of $\frac{k_s}{k_n}$ as a function of the interface aspect ratio A/λ, establishing some adhesive parameters such as G_{Ic}, G_{IIc} and η.

The use of a predictive theoretical tool, which is uniquely based on Fracture Mechanics concepts, aims at providing a comprehensive mechanical understanding to the fracture response of the 3D printed DCB specimens under analysis. This study allows to clarify the role of different parameters of the analytical model that govern the mechanical behaviour in the joint.

Fig. 5.6 and Table 5.1 shows the apparent fracture toughness G_c^X and the actual fracture toughness G_c^S as a function of the aspect ratio A/λ for the current experimental tests, as well as the curves corresponding to the SAA presented in Sect. 5.1. Thus, the present theoretical model can be directly compared with empirical values and, particularly, the influence of the $\frac{k_s}{k_n}$ parameter can be verified.

Dotted line in Fig. 5.6 represents a polynomial regression of the experimental points, excluding the value associated with $\frac{A}{\lambda} = 0.412$ (see Chapter 4 for details). This curve has been generated excluding the point associated with $\frac{A}{\lambda} = 0.412$ due to the potential occurrence of several failure mechanisms in the specimen such that shown in Fig. A.2.b that might deviate the regression line previously mentioned. As can be observed, the ratio which fits best with the trend line is $\frac{k_s}{k_n} = 0.5$, while curves associated to

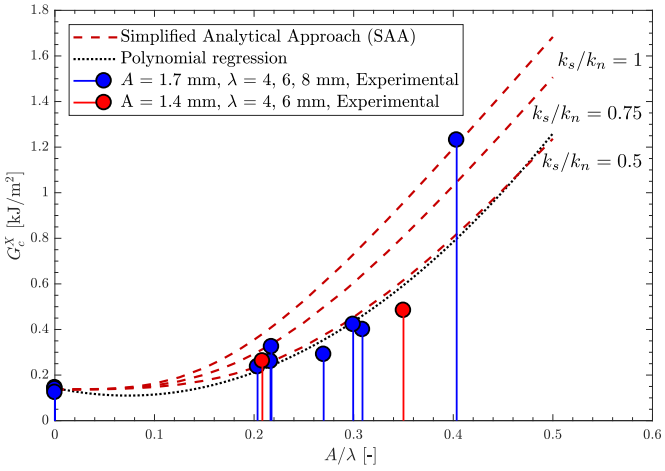

(a) Effective fracture toughness G_c^X versus aspect ratio $\frac{A}{\lambda}$.

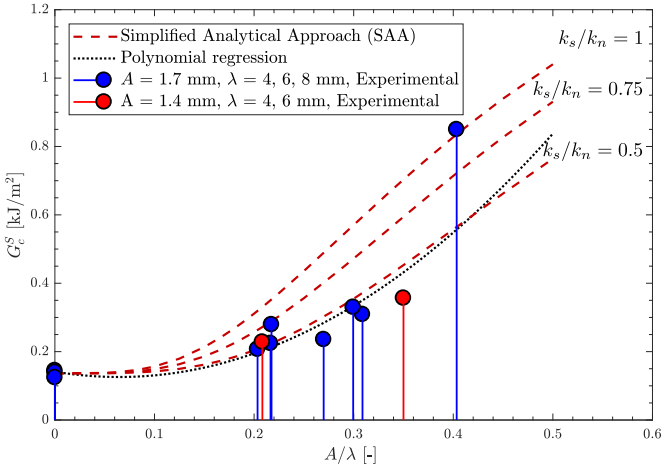

(b) Actual fracture toughness G_c^S versus aspect ratio $\frac{A}{\lambda}$.

Figure 5.6 Experimental effective and actual fracture toughness, G_c^X and G_c^S, versus aspect ratio $\frac{A}{\lambda}[-]$ and analytical model with parameters $G_{Ic} = 136.3$ J/m^2, $G_{IIc} = 16 \cdot G_{Ic}$, nonlinear mixed mode evolution ($\eta = 2$ in the B-K law) and penalty stiffness relation $k_s/k_n = 1, 0.75, 0.5$. The markers represent experimental values.

$\frac{k_s}{k_n} = 0.75$ and $\frac{k_s}{k_n} = 1$ differ considerably from the regression line, being this difference proportional to the stiffness ratio. Moreover, the discrepancies with respect to the empirical points increase with higher values of aspect ratio $\frac{A}{\lambda}$, and the dependency of

Table 5.1 G_c^X and $B_{mean} = \left(\frac{G_c^X - G_{Ic}}{G_{IIc} - G_{Ic}}\right)^{1/\eta}$ calculated from experimental load-displacement curves and theoretically.

	Experimental		SAA $\frac{k_s}{k_n} = 1$		SAA $\frac{k_s}{k_n} = 0.75$		SAA $\frac{k_s}{k_n} = 0.5$	
Configuration	$\mathbf{G_c^X}\left[\frac{\mathrm{J}}{\mathrm{m}^2}\right]$	$B_{mean}[-]$	$\mathbf{G_c^X}\left[\frac{\mathrm{J}}{\mathrm{m}^2}\right]$	$B_{mean}[-]$	$\mathbf{G_c^X}\left[\frac{\mathrm{J}}{\mathrm{m}^2}\right]$	$B_{mean}[-]$	$\mathbf{G_c^X}\left[\frac{\mathrm{J}}{\mathrm{m}^2}\right]$	$B_{mean}[-]$
A1.72λ8.00	273.96 ± 45.30	0.258	395.8	0.3546	323.6	0.3026	252.3	0.2381
A1.76λ6.00	371.13 ± 70.29	0.337	706.9	0.5259	577.9	0.4648	433.7	0.3814
A1.65λ4.00	1231.2 ± 0	0.728	1276.7	0.7434	1046.4	0.6671	818.4	0.5775
A1.25λ6.00	262.1 ± 0	0.247	387.8	0.3491	313.2	0.2941	245.5	0.2310
A1.40λ4.00	484.0 ± 0	0.411	963.7	0.6332	808.3	0.5733	616.2	0.4845

critical energy release rate on stiffness ratio is reduced for low values of $\frac{A}{\lambda}$, that is, for moderate mixed mode values. This outcome is in line with the cohesive-based model and the evolution of G_c described above, see Fig. 5.4. Consequently, relying on the present results it can be stated that the critical fracture toughness hardly varies for low values of mixed mode ratio β, where the joint response is principally characterized by normal strains, whereas for medium and high values of mixed mode ratio β the variation of the critical energy release rate G_c can be notably affected.

Certainly, as the experimental program and the SAA suggested, the enhancement of fracture properties, especially in terms of the fracture toughness, can be attributed to the increment of the mixed-mode ratio in some sections of the pattern and, consequently, to the total energy released. Nevertheless, special attention should be paid to the stiffness in normal and shear modes because the correct characterisation of these parameters in application with high values of mixity is determining.

5.2 Concluding remarks

In this Chapter a simplified analytical approach (SAA) in order to estimate the fracture performance of 3D printed composite DCB specimens exhibiting structured interfaces has been proposed. The developed method enables the prediction of the actual and effective critical energy release rate, G_c^S and G_c^X respectively, by means of the geometrical parameters of the interface profile (amplitude A, wavelength λ, etc) as well as the constitutive behaviour of the joint.

The kinematics of the problem were determined considering some simplifying assumptions, so that the normal and shear displacement within the interface, δ_n and δ_s respectively, only depend upon the slope and the length of each section of the pattern. In this particular case, trapezoidal profiles were analysed. With respect to the stress-displacement relationship, a bilinear cohesive law was considered and two different mixed mode fracture energy evolutions were studied: (i) linear distribution and (ii) Benzeggah-Kenane criterion. Special attention was devoted to the influence of the relation of the penalty stiffness in normal and shear directions $\frac{k_s}{k_n}$ in the critical energy release rate of the pattern.

Finally, the experimental and analytical values corresponding to the DCB tests of the 3D printed composite specimens with trapezoidal interfaces were correlated. The SAA results showed a good agreement with respect to the experimental results for the correct value of the penalty stiffness relationship $\frac{k_s}{k_n}$. In any case, the increasing tendency of the apparent critical fracture toughness G_c^X with respect to the aspect ratio A/λ is achieved regardless the constitutive law.

6 Computational study of structured interfaces - Bilinear Cohesive Zone Model approach

6.1 Analysis of fracture energy in patterned interfaces by means of the correlation of experimental and Finite Element load-displacement curves

One of the potential possibilities for the enhancement of the adhesive joints is the use of architectured materials, whose efficiency has been widely examined and exploited [256] at different scales [257–260], and through multiple applications such as bio-chemical-models [261] or structural models [262–264], among others. Nature offers different methods to strengthen the existing joints between adjacent parts or entities of a particular structure, ranging from human skull [265] to carapace of turtle [266]. These natural fastening techniques share a common feature which enables the enhancement of joints, that is, the presence of a non-flat or structured interface profile.

Thus, the goal of the current Section is triggering the fracture evolution within the bio-inspired specimens by means of the numerical (FE-based) analysis of the DCB coupons tested in Chapter 4, including cohesive capabilities. This fact will provide a profound understanding of the actual fracture conditions at each location at the interface during crack growth. Moreover, these numerical predictions allow the different mechanisms responsible for the fracture toughness amelioration to be identified. Finally, with regard to the numerical analysis, the accuracy of the current simulations is assessed by comparing the predicted load-displacement evolution curves with respect to experimental data, displaying an excellent correlation. Consequently, the present study provides an exhaustive analysis of 3D printed composite DCB specimens with trapezoidal interfaces from the experimental and numerical standpoints in a complementary manner.

This Section is organized as follows. The numerical analysis relying on FE-based

simulations including cohesive interface elements is described in Section 6.1.1. The correlation between the experimental, numerical and theoretical results are presented in Section 6.1.2. Finally, the most important aspects of this study are summarised in Section 6.3.

6.1.1 Finite Element analysis

The principal aspects associated with the current Finite Element computations are discussed herein, emphasizing the material definition and distribution in the specimen, type of elements and characteristics, mesh size and boundary conditions.

The simulations were carried out using the implicit solver of the FE package ABAQUS and large displacements response. Due to the configuration of the experiments, it is plausible to consider plane strain conditions, so that the computations were developed in the 2D setting for the adherent beams as well as the adhesive layer. The only source of nonlinearity in the current models are associated with the fracture events at the joint.

Joint failure was modelled using finite elements relying on the CZM using a finite thickness conception [222,223]. This numerical method has been successfully exploited in the related literature for the simulation of fracture events in composite materials and interfaces, showing a reliable accuracy and a high versatility. In this concern, cohesive elements can be adequately defined to reproduce the behaviour of both flat and trapezoidal interfaces, and allow triggering mixed-mode fracture events at the corresponding locations.

Each DCB beam were discretized using around 130-140k 4-node plane-strain element CPE4 of ABAQUS. Both halves of the DCB coupons were defined according to linear elastic material laws, taking into account the two constituents: (1) glass-fiber composite from $Z = [0 - 2.5\text{mm}]$ (see Fig.6.1 and Fig. A.1) (in accordance with 25 layers), and (2) nylon from $Z = 2.5$mm up to the top, $Z = 4$ mm for the flat case, $Z = 5$ mm for the trapezoidal interface specimen with $A = 2$ mm and $Z = 4.5$ mm for the specimen with $A = 1.5$ mm, according to the nominal value defined in the printing software. The elastic material properties for each of the constituents of the current models are detailed in Table 6.1 [244]. Conforming meshes for the elements in the adhesive zone in terms of spatial discretization and displacement interpolation were employed, leading to the idealization of 120-150 COH2D4 cohesive elements per trapezium.

Table 6.1 Properties of the glass-fiber composite (GFC) and nylon [244].

Material	E_{11} (MPa)	E_{22} (MPa)	E_{33} (MPa)	υ_{12}	υ_{13}	υ_{23}	G_{12} (MPa)
GFC	25863	1221	1221	0.45	0.45	0.45	778
Nylon	384	384	384	0.39	0.39	0.39	-

Small corrections on the nominal value in the trapeziums dimensions were considered in order to reproduce the actual amplitude and wavelength values, as indicated in Table 4.1. Concerning the adhesive layer, initially, the geometric definition of the joints reproduces the ideal geometry of the joint.

The approximate size of the elements, including cohesive and plane strain elements, in comparison with the characteristic wavelength of the pattern corresponded to $l_{coh}/\lambda \sim$

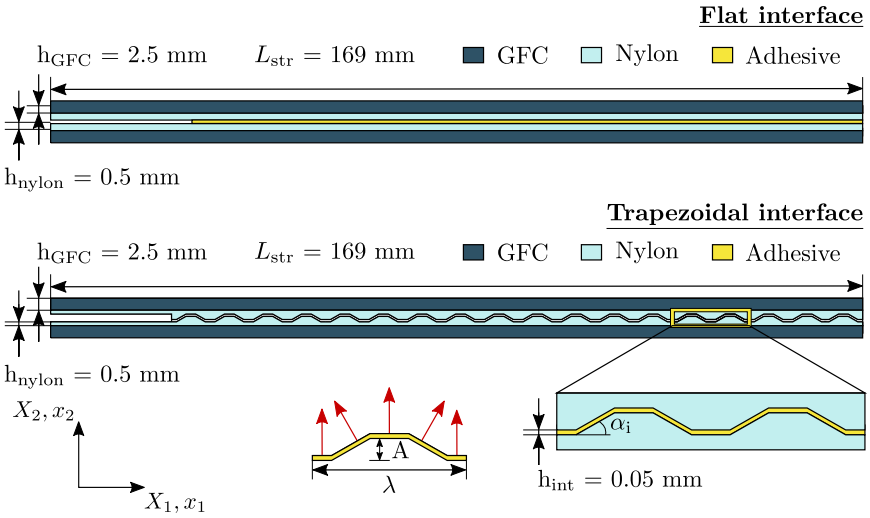

Figure 6.1 Double Cantilever Beam specimen with flat and trapezoidal interface. Materials: glass-fiber composite (GFC), nylon and adhesive. Dimensions: length L_{str}, height of glass-fiber composite h_{GFC}, height of nylon in the bulk part h_{nylon}, amplitude A and wavelength λ of the trapezoidal interface.

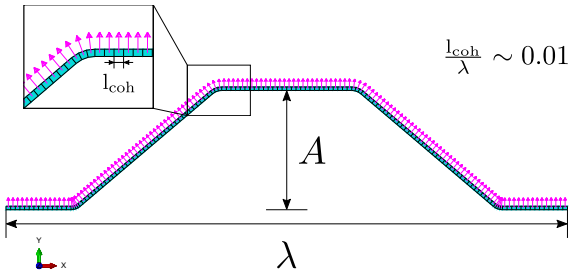

Figure 6.2 Mesh stack orientation of cohesive elements along the interface. The arrows indicate the normal direction in the CZM.

0.01, l_{coh} being the side-length of the finite elements, see Fig 6.2. This size can be considered small enough to get accurate predictions of damage progression along the joint. In addition, the cohesive elements required the definition of an orientation based on a local frame in order to properly identify the contributions of fracture Modes I and II. Thus, the corresponding mesh stack orientation, represented by purple arrows in Fig. 6.2, depicts the normal direction in cohesive elements, whereas the tangential direction is perpendicular to these arrows.

The interface between adherents is modelled by a bilinear cohesive law, governing by the equations presented in Section 3.3.2.

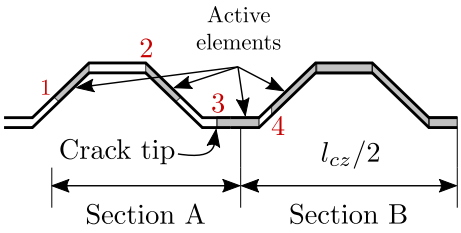

Figure 6.3 Crack tip criteria scheme. l_{cz} represents the cohesive zone length.

With reference to the external loading, a prescribed displacement along the Y-direction at the two external nodes located at $X = -b = -12.75$ mm (see Fig. A.3) was imposed, whereas the displacements along X-direction were also restricted. Specific details with regard to the material definition and the prescribed boundary conditions in the models are given in Appendix A.

Finally, in order to determine the fracture toughness for each configuration, the same process as that described in Appendix A has been followed. However, it is worth mentioning that specific attention was devoted to the identification of the crack tip along the simulations due to the fact that the current simulations estimated the cohesive failure at the joint following a nonuniform manner (which stemmed from the structured interface pattern). Fig. 6.3 is a simplified intermediate situation regarding cohesive failure, where grey areas in the interface represent active elements $(D < 1)$ and white areas represent completely damaged elements $(D = 1)$. Thus, it is possible to get different crack tips along the path (points 1, 2, 3 and 4 in Fig. 6.3). It has been considered that the failure is located in the point belonging to Section A closest to Section B (point 3 in Fig. 6.3) due to the fact that the resistance provided by active elements in Section A is residual. The instabilities of crack propagation in the system generate jumps or abrupt failures along the computations, and therefore the chosen points corresponding to a_{X1} and a_{X2} for the numerically estimated fracture toughness corresponded to the closest possible values to 10 mm and 70 mm, respectively.

6.1.2 Experimental, computational and theoretical correlation: general discussion

An overall discussion of the results derived from the experimental program and the corresponding correlation with the developed computational and analytical modelling tools is presented. The use of predictive tools of diverse character (analytical and numerical), which are based uniquely on fracture mechanics concepts, aims at providing a comprehensive mechanical understanding to the fracture response of the 3D printed DCB specimens under analysis. Moreover, this thorough analysis undoubtedly contributes to shedding light on the identification of the mechanisms that are responsible for the great increment of the fracture toughness in the current prototypes. To this end, FE simulations of every successful DCB test in the experimental campaign have been carried out. Furthermore, additional configurations for different interface profiles were also simulated aiming at obtaining further points in the $G_c - A/\lambda$ diagram, which were employed to visualise the presence of a tendency on the fracture response of the current coupons.

The first stage of the discussion concerns with the analysis of the load-displacement evolution curves of the successful DCB tests in the experimental program, see Fig. 6.4. In these graphs, the predicted numerical results are directly correlated with the measured response from the tests. The square markers in each of these diagram symbolise the points where the crack tip reaches the crack length a_{X1} and a_{X2}, which were needed to calculate the energy released during the corresponding test.

Due to the lack of reliable experimental data concerning the cohesive properties of the adhesive layer, in order to determine a suitable value of normal resistance t_n^0, a parametric study of this parameter was performed with the purpose of adjusting the numerical curve to the experimental evolution for the flat interface cases. Based on our numerical predictions, the value $t_n^0 = 1.84$ MPa fitted with good accuracy the mean values of the experimental peaks in the flat configuration, obtaining 3.21 MPa for the maximum of the numerical curve versus the 3.39 MPa of the mean of the peaks for the experimental curves. The fracture toughness for Mode I of fracture was set equal to $G_{Ic} = 136.3\,\text{J/m}^2$, which was obtained from our experimental flat DCB tests. Regarding k_n, several studies estimated k_n value as a function of the adhesive Young's modulus E_{adh} and thickness h_{adh}, see [226] and references therein. Thus, k_n has been taken as $k_n = \frac{E_{\text{adh}}}{h_{\text{adh}}} = 32$ GPa in the present model.

With the previous values for the cohesive model, the computational simulations were again performed, leading to a very satisfactory agreement along the complete force-displacement evolution of the baseline profile (see Fig. 6.4.a). These FE models for the flat interface cases slightly differed from the experimental data, overestimating the corresponding performance. Thus, for the first crack position $a_{X1} = 10\,\text{mm}$ the experimental imposed displacement and applied force corresponded to $\Delta = 1.45\,\text{mm}$ and $P/W = 1.86\,\text{N/mm}$, respectively, whereas the numerical computations predicted an imposed displacement $\Delta = 1.32\,\text{mm}$ and an applied force $P/W = 2.22\,\text{N/mm}$. In view of these values, the load-displacement evolution, the joint fracture parameters and the crack propagation path the experimental results were considered to had been successfully adjusted.

Moreover, in order to numerically reproduce mixed-mode fracture conditions, the material parameters G_{IIc}, t_s^0 and k_s were also required to be adjusted. These parameters were estimated by performing a numerical parametric study using models including structured interfaces. After that, $G_{IIc} = 2180\,\text{J/m}^2$ and $t_s^0 = 3\,\text{MPa}$ were set. See a summary in Table 6.2.

Table 6.2 Properties of the adhesive modelled as a CZM.

Material	t_n^0 (MPa)	t_s^0 (MPa)	G_{Ic} (kJ/m^2)	G_{IIc} (kJ/m^2)	k_n (MPa)	k_s (MPa)
Adhesive	1.84	3	0.1363	2.18	32162	32162

Notice that, the ratio between Mode II and Mode I fracture energies was equal to $\frac{G_{IIc}}{G_{Ic}} = 16$, which conformed a feasible value for this kind of adhesive layers, as was previously discussed in [37,267,268]. Finally, for the current numerical simulations, the ratio $\frac{k_s}{k_n} = 1$ was set for the penalty stiffness values for Mode II and Mode I, obtaining satisfactory results. We also explore different values of such ratio, especially $\frac{k_s}{k_n} = 0.5$

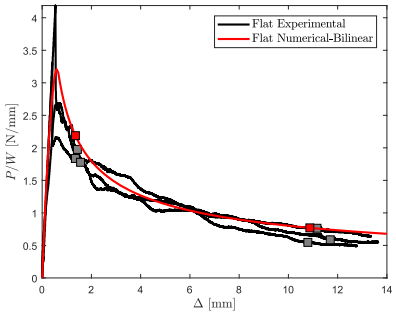

(a) Flat profile.

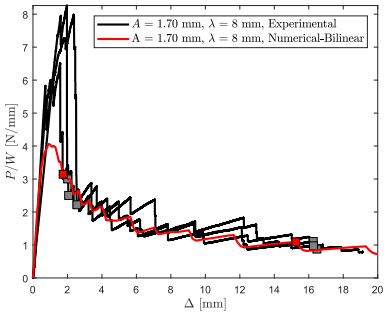

(b) A2.00λ8.00: $A = 1.70$ mm, $\lambda = 8$ mm.

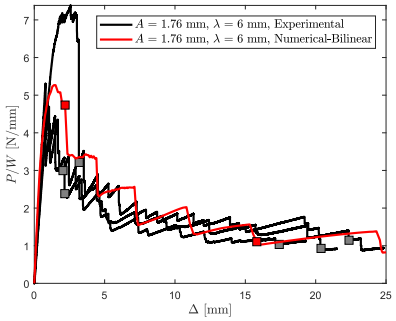

(c) A2.00λ6.00: $A = 1.76$ mm, $\lambda = 6$ mm.

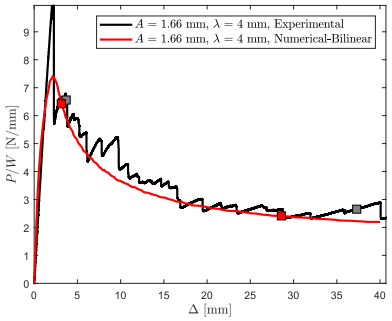

(d) A2.00λ4.00: $A = 1.66$ mm, $\lambda = 4$ mm.

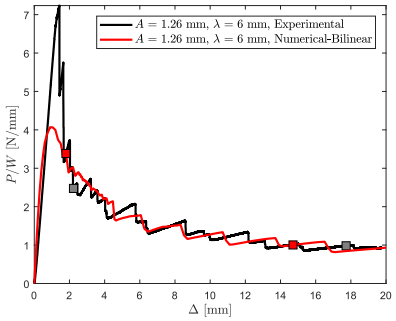

(e) A1.50λ6.00: $A = 1.26$ mm, $\lambda = 6$ mm.

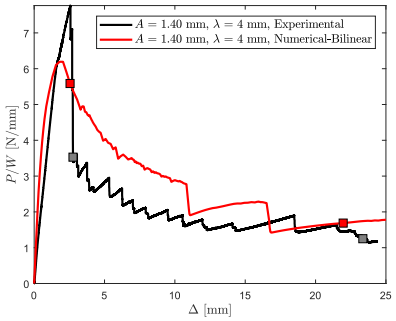

(f) A1.50λ4.00: $A = 1.40$ mm, $\lambda = 4$ mm.

Figure 6.4 Correlation between experimental and numerical load-displacement curves. Square markers represent the point of the curve where crack length reaches a_{X1} and a_{X2}.

which led to the best agreement to the experimental data using the SAA (Fig. 6.5). Unfortunately, nonlinear implicit FE analysis using $\frac{k_s}{k_n} = 0.5$ presented notable convergence difficulties in achieving equilibrium solutions along the simulation, so that the corresponding results are omitted. With the current estimation of the fracture parameters of the adhesive, Fig. 6.4 shows the correlation between load-displacement curves obtained from experimental tests and numerical simulations for the configurations included in the experimental program (see Appendix A). In general, numerical predictions exhibited a very satisfactory accuracy with respect to the experimental data, capturing the linear evolution in the beginning of the test prior damage initiation and the subsequent softening evolution till complete failure.

However, analysing in detail the initial linear elastic range of the evolution, for some specimens, the numerical predictions were deviated from the experimental results, with significant differences in the peak force values. This discrepancy might be caused by the presence of an imperfect termination regarding the adhesive bonding area, specifically, at the commencement of the union. As a result of the potential presence of such imperfection, a higher force was needed for the initiation of adhesive failure during the experimental program.

Progressing along the evolution response, after reaching the highest point in the corresponding curve, crack events were initiated and progressed within the adhesive joint. The occurrence of these inelastic effects produced a notable reduction of the coupon stiffness as a consequence of the degradation of the joint properties. Moreover along this second phase, for every specimen, the experimental data and the numerical predictions display sawtooth-like evolutions, which were associated with the unstable crack propagation at different locations in each trapezium (particularly those located at the local stress concentrators of the interface profile). Note also that the magnitude of these jumps became smaller throughout the test, being almost negligible at the end of the experiment.

Fig. 6.5 shows the apparent and actual fracture toughness, G_c^X and G_c^S respectively, as a function of aspect ratio A/λ for the current experimental tests and numerical simulations, as well as the SAA according to the model presented in Sect. 5.1.2. These graphs contain the DCB configurations that were tested in the present study together with some additional cases, which have been simulated and used to identify the prospective trend of the fracture resistance values. Particularly, the specific aspects of high interest concerns the investigation of the fracture behaviour with identical aspect ratio A/λ and dissimilar values of amplitude and wavelength. Thus, two different samples ($A \simeq 1.70$ and $A \simeq 1.30$) were simulated for a similar value of A/λ. The profiles available in these diagrams correspond to the pairs of values listed in Table 6.3. Likewise, Table 6.4 displays the effective fracture toughness G_c^X and the average mixed mode values B_{mean} represented in Fig. 6.5 for a quantitative comparison between experimental, analytical and computational approaches. Figure 6.5, also includes a trend line corresponding to a polynomial regression of the experimental data.

Focusing on the fracture energy values depicted in Fig. 6.5, it can be observed that an excellent agreement was achieved between computational and experimental points, leading to negligible errors for flat interface cases, and slight discrepancies for structured cases ranging from 1% to 39% in the worst case scenario. On the other hand, an evident

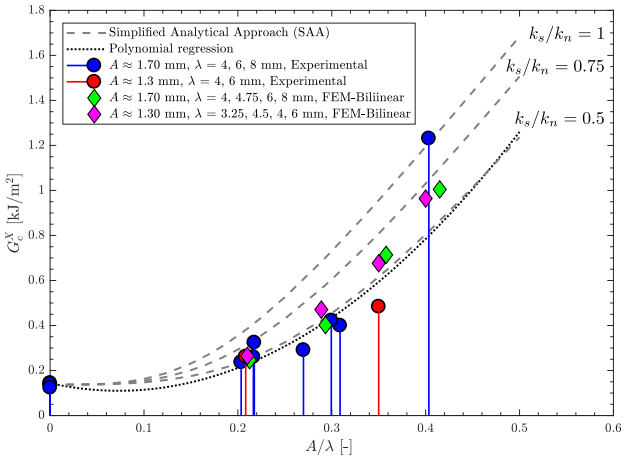

(a) Experimental, analytical (SAA) and numerical effective fracture toughness G_c^X versus aspect ratio A/λ.

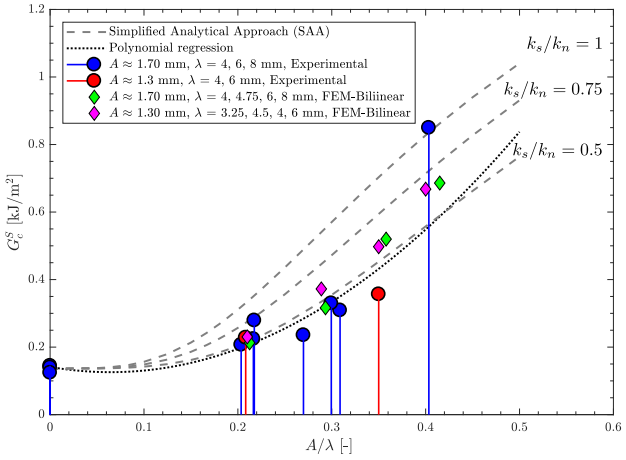

(b) Experimental, analytical (SAA) and numerical actual fracture toughness G_c^S versus aspect ratio A/λ.

Figure 6.5 SAA is set with parameters $G_{Ic} = 136.3$ J/m^2, $G_{IIc} = 16 \cdot G_{Ic}$ and $\eta = 2$. Blue and green markers represent fracture toughness values associated with experimental and numerical specimens, respectively, with $A \approx 1.70$ mm. Red and magenta ones are those corresponding to experimental and numerical specimens, respectively, with $A \approx 1.30$ mm.

Table 6.3 Geometrical parameters of the trapezoidal interface specimens. All the configurations set $r = 1/2$.

Configuration	A[mm]	λ[mm]	$A/\lambda[-]$	Configuration	A[mm]	λ[mm]	$A/\lambda[-]$
A2.00λ8.00	1.70	8.00	0.106	A1.50λ4.00	1.26	6.00	0.104
A2.00λ6.00	1.76	6.00	0.147	A1.50λ4.50	1.30	4.50	0.144
A2.00λ4.75	1.70	4.75	0.179	A1.50λ4.00	1.40	4.00	0.175
A2.00λ4.00	1.66	4.00	0.206	A1.50λ3.25	1.30	3.25	0.200

trend in the numerically and theoretically predictions, which were closely in line with the experiments, can be identified. In this way, Finite Element models support the considerable improvement in fracture toughness using structured interfaces.

In the light of the previous observations, it can be concluded that the numerical predictions using FE methods provided a convincingly global response of the DCB coupons with respect to the experimental tests and can be employed as predictive tools. Due to their satisfactory accuracy, these computational methods can be also remarkably useful for extracting accurate information about CZM, that is, the actual state of the adhesive at different stages of the simulations. Furthermore, as the experimental program and the SAA suggested, the enhancement of fracture properties, especially in terms of the fracture toughness, can be attributed to the increment of the mixed-mode ratio in some sections of the pattern and, consequently, to the total energy released.

Table 6.4 G_c^X and $B_{mean} = \left(\frac{G_c^X - G_{Ic}}{G_{IIc} - G_{Ic}}\right)^{1/\eta}$ calculated from experimental and numerical load-displacement curves as well as by means of SAA ($k_s/k_n = 1$).

	Experimental		Numerical		Analytical	
Configuration	$G_c^X\left[\frac{\text{J}}{\text{m}^2}\right]$	$B_{\text{mean}}[-]$	$G_c^X\left[\frac{\text{J}}{\text{m}^2}\right]$	$B_{\text{mean}}[-]$	$G_c^X\left[\frac{\text{J}}{\text{m}^2}\right]$	$B_{mean}[-]$
A2.00λ8.00	273.96 ± 45.30	0.258	245.9	0.2316	395.8	0.3546
A2.00λ6.00	371.13 ± 70.29	0.337	402.0	0.3606	706.9	0.5259
A2.00λ4.75	—	—	713.8	0.5316	1001.0	0.6473
A2.00λ4.00	1231.2 ± 0	0.728	1004.6	0.6518	1276.7	0.7434
A1.50λ6.00	262.1 ± 0	0.247	265.0	0.2509	387.8	0.3491
A1.50λ4.50	—	—	470.7	0.4045	687.8	0.5170
A1.50λ4.00	484.0 ± 0	0.411	676.5	0.5141	963.7	0.6332
A1.50λ3.25	—	—	963.8	0.6363	1203.4	0.7191

6.2 Fracture energy characterisation of a structured interface by means of a novel J-Integral procedure

Nowadays, it is of crucial relevance the characterization of fracture capacities of bonded joints. The idealization of numerical, theoretical and experimental procedures to this end has been a recurrent research topic in the last decades, as can be shown by the large number of published standards [184, 185, 249, 269, 270], the Double Cantilever

Beam (DCB) being the most extended test so far. On the one hand, at present, most of standards mainly use the applied force and the cross-head displacement together with the measurement of the crack length a during crack propagation to estimate the critical energy release rate, G_c. However, the difficulties to quantify the crack length are well-known and, consequently, some differences may be obtained on the test results [173]. On the other hand, data-reduction methods are based on Euler-Bernoulli or Timoshenko beam theories and the applicability of these approaches is restricted to the assumption of linear elastic behaviour. Moreover, it is accepted that the conception of the DCB test was idealized for: (i) the characterization of pure fracture Mode I conditions throughout the crack progression along the interface, and (ii) stable crack advance. Based on our preliminary results, these two conditions are violated for crack paths following structured interfaces profiles due to the fact that fracture conditions are not preserved constant along the complete path in terms of fracture mixity, and interlaminar crack can propagate unstably at some specific locations of the interface [255]. Nevertheless, a sort of standard method for the characterization of a *nominal fracture toughness* G_c (G_c^X for its apparent value) stemming from the load-displacement curve in a DCB test in line with previous works was initially followed.

With the aim of overcoming the difficulties of the previous techniques, contour integral methods (J-Integral based techniques) widen the range of applicability for material behaviour that does not have to be necessarily linear. The reliability of J-Integral procedures has been proven for various interlaminar tests in the related literature concerning pure Mode I applications [189] , and mixed mode conditions [271, 272]. Hence, this approach can be appropriate to characterise the performance of specimens with structured interfaces made from different materials. Thus, the use of the J-Integral can be employed for the characterization of cohesive laws [157, 252], or viceversa the computation of the J-Integral can be performed extracting the required data from numerical simulations including Cohesive Zone Models (CZMs) for triggering the inelastic response of the interface.

Thus, the first objective concerns with the verification of the procedure for the characterization of the *nominal fracture toughness* G_c (G_c^X for its apparent value) for structured interfaces using J-Integral-based methods. For this purpose, the second salient aspect of the present investigation is the development of a novel J-Integral method for the computation of the *nominal values* of $\bar{J}_c$ and $\bar{J}_c^X$ for structured interfaces [273], but also applicable to any alternative geometric designs. At this point, it is worth mentioning that the estimation of $\bar{J}_c$ is well established in the related literature due to the fact that, by definition, the integration path should follow the crack advance, so that we herewith perform a simple adaptation to structured interfaces. Thus, from the methodological standpoint, the main novelty of the current section is the advent of a new method for the characterization of $\bar{J}_c^X$ along paths that are not necessarily coincident with the crack progression. This new methodology is of especial interest due to the fact that the J-Integral procedures provide the required versatility for the fracture characterization regardless the material law of the constituents.

The organization of this section is as follows. Section 6.2.1 presents a novel J-Integral formulation where a contour integral is used for curved interfaces and the integration path is not necessarily coincident with that followed by the crack, therefore it is possible

to compute $\bar{J}_c$ and $\bar{J}_c^X$. This new method is specialized for the case of composite specimens with trapezoidal interface profiles between the adherents. Section 6.2.2 thoroughly details the post-process flowchart that is required from the corresponding FE analysis in order to compute $\bar{J}_c$ and $\bar{J}_c^X$. Using this novel method, a comparison between the critical energy release rate obtained by means of the load-displacement curves and the current J-Integral formulation is performed in Section 6.2.3. Finally, the convenience of the proposed method is discussed in Section 6.3.

6.2.1 Energy release rate along a crack path: Application for structured interfaces

In this Section, a modified formulation of the so-called J-Integral [189] technique is presented. Although contour integral develop by Rice [189] is suitable for non-straight contours, this modified version enables the evaluation of fracture energy with respect to the effective crack advance a_X, instead of the actual crack length a, see Fig. 6.6. This versatile character permits its usage in cases where the crack is enforced to travel along a certain geometrical profile, e.g. in structured interfaces. Specifically, this approach is useful if the crack measurement direction a_X is not aligned with the crack progression ($\tilde{x}_1$), see Fig. 6.6. Also, this novel procedure allows its generalized application for arbitrary crack paths.

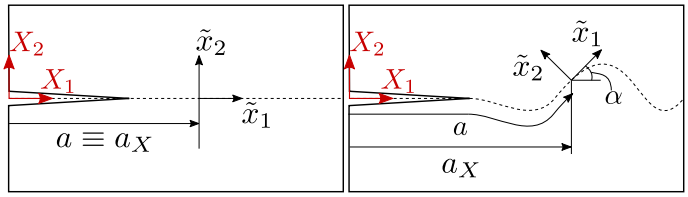

Figure 6.6 Reference axis in flat and structured interfaces. a represents the actual crack length and a_X indicates the effective or apparent crack length.

In the sequel, the main ingredients of the proposed method are outlined. Thus, the fundamentals of line integral analyses are shown in order to identify the basic aspects of the standard formulation that should be modified for its application to effective crack measurement a_X and to provide the physical sense of these changes. Subsequently, the modified J-Integral evaluation is exemplarily applied to a trapezoidal pattern.

6.2.1.1 J-Integral formulation for curved profiles

The J-Integral technique allows the strain energy release rate by means of a path-independent contour integral in fracture applications [189, 219] to be calculated. This method is based on the energy approach of Fracture Mechanics, assuming: an euclidean homogeneous domain with linear or nonlinear elastic behaviour, absence of body forces ($X_i = 0$) and in a state of static equilibrium under the action of external tractions in quasi-static conditions ($\ddot{u}_i \simeq 0$). The boundary conditions associated with this domain are $t_i = \bar{t}_i$ in $\partial\Omega_t$ and $u_i = \bar{u}_i$ in $\partial\Omega_u$, where loads are applied on $\partial\Omega_t$ and displacement conditions are applied on $\partial\Omega_u$. Additionally, no tractions ($\bar{t}_i = 0$) are considered along the crack flanks. In this formulation, equations are referred to the crack tip, and

consequently stress and strain fields are expressed in a reference system which evolves with the crack length a upon crack progression (see Fig. 6.7).

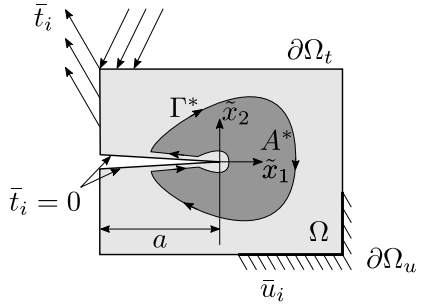

Figure 6.7 Domain (Ω), boundary conditions and reference axis in a body with a crack. $\bar{t}_i$ represents the loads applied over the surface domain $\partial\Omega_t$ and $\bar{u}_i$ symbolises the displacement field applied over the surface domain $\partial\Omega_u$. Flank surfaces are traction free ($\bar{t}_i = 0$). The reference system ($\tilde{x}_1$, $\tilde{x}_2$) moves with the crack growth, defined by the crack length a. Γ^* is an arbitrary closed contour around the crack tip and A^* the area enclosed.

J-Integral has been extensively used to characterise the energy release rate in nonlinear elastic materials. For a physical interpretation, this line integral can be conceived as the rate of potential energy Π with respect to the new area created by a crack A_c as

$$J = -\frac{d\Pi}{dA_c}. \tag{6.1}$$

The potential energy can be expressed as $\Pi = U - W$, where W is the work developed by the external actions ($\bar{t}_i$) and U is the internal elastic energy.

Let consider a crack specimen bounded by the curve Γ^*, whose enclosed area is A^*, see Fig. 6.7. In order to calculate the potential energy in the area, U is integrated in the volume of the domain, while the external work is determined by the corresponding contour integral. Therefore, the total potential can be expressed as

$$\Pi = U - W = \int_{A^*} \omega(\tilde{x}_1,\tilde{x}_2) dA - \int_{\Gamma^*} t_i u_i \, ds, \tag{6.2}$$

where $\omega(\tilde{x}_1,\tilde{x}_2) = \int_0^{\varepsilon_{ij}} \sigma_{ij} d\varepsilon_{ij}$.

The J-Integral is obtained by differentiating Eq. 6.2 with respect to the crack surface (crack length in 2D). Also, a material derivative is employed by taking into account that the reference system ($\tilde{x}_1$, $\tilde{x}_2$) moves with the crack tip, and considering that the crack propagates along the $\tilde{x}_1$ direction [179], the operator reads

$$\frac{d}{da} = \frac{\partial}{\partial a} + \frac{\partial \tilde{x}_1}{\partial a}\frac{\partial}{\partial \tilde{x}_1}. \tag{6.3}$$

In the classical form of the J-Integral, it is assumed that the crack propagates along a fixed direction during the failure process. In most applications, crack travels along a straight line or surface (see Fig. 6.6) and crack measurement direction, a or a_X, coincides on the crack path direction X_1. However, in line with a structured interface concept, the crack tip system will be inclined a certain angle α with respect to an initial reference axis (red axis referenced by capital letters in Fig. 6.6) and crack measurement direction may differ from that reference system. It should be noticed that the path to be followed in such application regarding a patterned interface is known a priori, so that α and the crack tip position can be determined along the entire fracture history. Furthermore, as a result of the moving+rotating axis, the crack length can be defined in two different ways: (i) a representing the actual curved length and (ii) a_X representing the distance travelled along the horizontal axis, i.e. the projection of a over the initial X_1 axis, also called as the effective or apparent crack length. Then, two J-Integral values can be defined: (a) J, that is referred to actual length a and (b) J^X, that is referred to a_X. J is the same for curved interfaces as the one for flat interfaces [189], nevertheless a new expression is needed for J^X.

The main consequences of the moving+rotating reference system over J^X are related to Eq.6.3. For flat interfaces $a = a_X$, so the term $\frac{\partial \tilde{x}_1}{\partial a_X} = -1$, whereas for patterned profiles, it becomes $\frac{\partial \tilde{x}_1}{\partial a_X} = -\frac{1}{cos(\alpha)}$. A detailed description relating both reference systems is available in the next section. Moreover, the flat interface scenario can be taken as a particular case of a curved profile in which $\alpha = 0$ rad. Therefore, Eq. 6.3 can be rewritten as

$$\frac{d}{da_X} = \frac{\partial}{\partial a_X} - \frac{1}{cos(\alpha)} \frac{\partial}{\partial a_X}. \tag{6.4}$$

Following Rice [179, 189] and including the previous modification, the novel expression for the effective J-Integral is obtained according to

$$J^X = -\frac{d\Pi}{da_X} = -\int_{\partial\Gamma} \left(\frac{\omega(\tilde{x}_1,\tilde{x}_2)}{cos(\alpha)} d\tilde{x}_2 - \frac{t_i}{cos(\alpha)} \frac{\partial u_i}{\partial \tilde{x}_1} ds \right). \tag{6.5}$$

The purpose of the new formulation is the same as that corresponding to the original J-integral formulation, i.e. the characterization of the energy release rate in different materials. Therefore, the corresponding hypothesis, advantages and limitations remain unaltered in both standpoints due to the fact that the introduction of angle α does not invalidate the primary assumptions. Nevertheless, effective J-Integral may be used in practical applications, in particular for bonded joints with non-flat profiles.

6.2.1.2 Particular case: trapezoidal pattern

The new perspective of J^X presented in the previous section is herein applied to trapezoidal interfaces. In this particular case, the profile is a piecewise-defined function, but the methodology is suited for any type of continuous profile.

Then, for a given interface geometry it is possible to evaluate α along the entire pattern. Therefore, as long as classical J-Integral can be calculated, the computation of J^X according to Eq. 6.5 can be carried out in a straightforward manner. In particular,

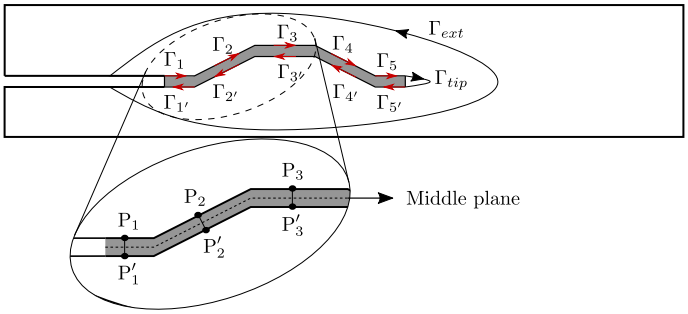

Figure 6.8 Integration paths in a J-Integral along a trapezoidal interface.

in the path along the trapezoidal interface shown in Fig. 6.8, the closed contour of the J-Integral can be decomposed according to the different portions. As a consequence of the path independence character [179] of the contour integral, the J-Integral can be expressed as

$$J = J_{ext} + J_{coh} + J_{tip} = 0, \tag{6.6}$$

where $J_{coh} = J_{\Gamma_1+\Gamma_{1'}} + J_{\Gamma_2+\Gamma_{2'}} + J_{\Gamma_3+\Gamma_{3'}} + J_{\Gamma_4+\Gamma_{4'}} + J_{\Gamma_5+\Gamma_{5'}}$.

J_{coh} can be arranged as a sum of integrals in the different sections and expressed as function of a or a_X (see Fig. 6.8, and Fig. 6.9.a) following

$$J_{coh} = \sum_{k=1}^{n} J_{\Gamma_k+\Gamma_{k'}}(a) = \sum_{k=1}^{n} \int_{\Gamma_k+\Gamma_{k'}} - \left(\omega(\tilde{x}_1,\tilde{x}_2) d\tilde{x}_2 - t_i \frac{\partial u_i}{\partial \tilde{x}_1} ds \right), \tag{6.7}$$

$$J^X_{coh} = \sum_{k=1}^{n} J_{\Gamma_k+\Gamma_{k'}}(a_X) = \sum_{k=1}^{n} \int_{\Gamma_k+\Gamma_{k'}} - \left(\frac{\omega(\tilde{x}_1,\tilde{x}_2)}{\cos\alpha} d\tilde{x}_2 - \frac{t_i}{\cos\alpha} \frac{\partial u_i}{\partial \tilde{x}_1} ds \right). \tag{6.8}$$

Once the fracture process zone is fully developed we end up with $J_{tip} = 0$ and $J_{ext} = J_{coh}$ [179]. Furthermore, in the contour $\Gamma + \Gamma'$ the integration path $ds = d\tilde{x}_1$, so $d\tilde{x}_2 = 0$ [189] and the first term of the integral (Eq. (6.7)-(6.8)), associated with the internal elastic energy ω, is null.

Thus, a correct energy release rate evaluation were performed by starting and ending the contour at a traction free surface, as Rice did with a Barenblatt- Dugdale crack model [189].

In such a way, J-Integral can be written by means of its symmetrical and anti-symmetrical components [274] as

$$J_{coh} = J_{coh,I} + J_{coh,II}, \tag{6.9}$$

$$J^X_{coh} = J^X_{coh,I} + J^X_{coh,II}. \tag{6.10}$$

For the purpose of decomposing the contour integral and considering $ds = d\tilde{x}_1$, J_{coh} can be written in terms of a set of stress tensor components [274] by rearranging the terms according to

$$J_{coh} = \sum_{k=1}^{n} \int_{\Gamma_k+\Gamma_{k'}} t_i \frac{\partial u_i}{\partial \tilde{x}_1} ds = \sum_{k=1}^{n} \int_{\Gamma_k+\Gamma_{k'}} \sigma_{ij} \frac{\partial u_i}{\partial \tilde{x}_1} n_j ds = \sum_{k=1}^{n} \int_{\Gamma_k+\Gamma_{k'}} \left(\sigma_{ij}^{I} \frac{\partial u_i^{I}}{\partial \tilde{x}_1} n_j ds + \sigma_{ij}^{II} \frac{\partial u_i^{II}}{\partial \tilde{x}_1} n_j ds \right), \tag{6.11}$$

$$J_{coh}^{X} = \sum_{k=1}^{n} \int_{\Gamma_k+\Gamma_{k'}} \frac{t_i}{\cos\alpha} \frac{\partial u_i}{\partial \tilde{x}_1} ds = \sum_{k=1}^{n} \int_{\Gamma_k+\Gamma_{k'}} \frac{\sigma_{ij}}{\cos\alpha} \frac{\partial u_i}{\partial \tilde{x}_1} n_j ds = \sum_{k=1}^{n} \int_{\Gamma_k+\Gamma_{k'}} \left(\frac{\sigma_{ij}^{I}}{\cos\alpha} \frac{\partial u_i^{I}}{\partial \tilde{x}_1} n_j ds + \frac{\sigma_{ij}^{II}}{\cos\alpha} \frac{\partial u_i^{II}}{\partial \tilde{x}_1} n_j ds \right). \tag{6.12}$$

Considering symmetric integration paths respect to the middle plane in each section (Fig. 6.8), the decomposed J-Integral [219, 274] can be obtained, where P_i and $P_{i'}$ points are placed on the symmetric paths Γ_k and $\Gamma_{k'}$ according to the middle plane, respectively. Then, symmetric and antisymmetric stress, strain and displacement fields are arranged in the crack front coordinate system ($\tilde{x}_1$, $\tilde{x}_2$ in Fig. 6.9.a) in order to obtain the contributions corresponding to fracture Modes I and II as

$$\begin{aligned}
\sigma_{ij}^{PP'} &= \frac{1}{2}\begin{bmatrix} \sigma_{11}^{P}+\sigma_{11}^{P'} & \sigma_{12}^{P}-\sigma_{12}^{P'} \\ \sigma_{12}^{P}-\sigma_{12}^{P'} & \sigma_{22}^{P}+\sigma_{22}^{P'} \end{bmatrix} + \frac{1}{2}\begin{bmatrix} \sigma_{11}^{P}-\sigma_{11}^{P'} & \sigma_{12}^{P}+\sigma_{12}^{P'} \\ \sigma_{12}^{P}+\sigma_{12}^{P'} & \sigma_{22}^{P}-\sigma_{22}^{P'} \end{bmatrix} = \sigma_{ij}^{PP',I} + \sigma_{ij}^{PP',II}, \\
\varepsilon_{ij}^{PP'} &= \frac{1}{2}\begin{bmatrix} \varepsilon_{11}^{P}+\varepsilon_{11}^{P'} & \varepsilon_{12}^{P}-\varepsilon_{12}^{P'} \\ \varepsilon_{12}^{P}-\varepsilon_{12}^{P'} & \varepsilon_{22}^{P}+\varepsilon_{22}^{P'} \end{bmatrix} + \frac{1}{2}\begin{bmatrix} \varepsilon_{11}^{P}-\varepsilon_{11}^{P'} & \varepsilon_{12}^{P}+\varepsilon_{12}^{P'} \\ \varepsilon_{12}^{P}+\varepsilon_{12}^{P'} & \varepsilon_{22}^{P}-\varepsilon_{22}^{P'} \end{bmatrix} = \varepsilon_{ij}^{PP',I} + \varepsilon_{ij}^{PP',II}, \\
u_i^{PP'} &= \frac{1}{2}\begin{bmatrix} u_1^{P}+u_1^{P'} \\ u_2^{P}-u_2^{P'} \end{bmatrix} + \frac{1}{2}\begin{bmatrix} u_1^{P}-u_1^{P'} \\ u_2^{P}+u_2^{P'} \end{bmatrix} = u_i^{PP',I} + u_i^{PP',II}.
\end{aligned} \tag{6.13}$$

Hence, the J-Integral can be calculated by means of known variables of the cohesive zone, such as normal and tangential tractions, t_n and t_s, and normal and tangential jump displacements, δ_n and δ_s, considering

$$\begin{aligned}
\sigma_{ij}^{PP',I} n_j &= \begin{bmatrix} 0 \\ t_n \end{bmatrix}, \\
\sigma_{ij}^{PP',II} n_j &= \begin{bmatrix} t_s \\ 0 \end{bmatrix},
\end{aligned} \tag{6.14}$$

$$u_i^I = \begin{bmatrix} 0 \\ \delta_n \end{bmatrix}, \qquad u_i^{II} = \begin{bmatrix} \delta_s \\ 0 \end{bmatrix}. \tag{6.15}$$

Moreover, this decomposition allows the integral to be computed along the upper surface Γ only as

$$J_{coh,I} = \sum_{k=1}^{n} J_{I,\Gamma_k+\Gamma_{k'}}(a) = \sum_{k=1}^{n} \int_{\Gamma_k} t_n \frac{\partial \delta_n}{\partial \tilde{x}_1} d\tilde{x}_1, \tag{6.16}$$

$$J_{coh,II} = \sum_{k=1}^{n} J_{II,\Gamma_k+\Gamma_{k'}}(a) = \sum_{k=1}^{n} \int_{\Gamma_k} t_s \frac{\partial \delta_s}{\partial \tilde{x}_1} d\tilde{x}_1, \tag{6.17}$$

$$J^X_{coh,I} = \sum_{k=1}^{n} J_{I,\Gamma_k+\Gamma_{k'}}(a_X) = \sum_{k=1}^{n} \int_{\Gamma_k} \frac{t_n}{\cos\alpha} \frac{\partial \delta_n}{\partial \tilde{x}_1} d\tilde{x}_1, \tag{6.18}$$

$$J^X_{coh,II} = \sum_{k=1}^{n} J_{II,\Gamma_k+\Gamma_{k'}}(a_X) = \sum_{k=1}^{n} \int_{\Gamma_k} \frac{t_s}{\cos\alpha} \frac{\partial \delta_s}{\partial \tilde{x}_1} d\tilde{x}_1. \tag{6.19}$$

Sections I and II in Fig. 6.9.a represent a planar section and a general sloped section with a certain angle α, respectively. Table 6.5 shows the interface coordinates with respect to the global coordinates (X_1,X_2) as a function of the actual crack length a, the effective crack length a_X and local coordinates $(\tilde{x}_1,\tilde{x}_2)$. In this table, a_i and $a_{X,i}$ represent the actual and effective crack length, respectively, at the beginning of the corresponding section. Derivatives of $\tilde{x}_1$ with respect to a and a_X, needed in Eq. 6.3, 6.4, are also included.

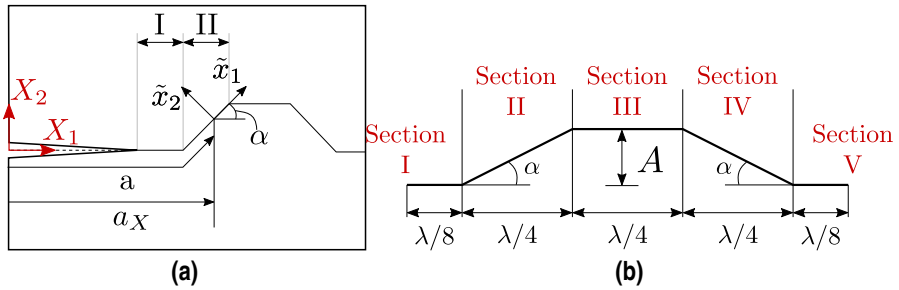

Figure 6.9 (a) Actual crack length a and effective crack length a_X in a trapezoidal interface, angle of the inclined section α, initial coordinate system (X_1,X_2) and crack tip coordinate system $(\tilde{x}_1,\tilde{x}_2)$. (b) Sections in a trapezoidal interface with an amplitude A and a wavelength λ.

Both coordinates $(X(a),Y(a))$ and $(X(a_X),Y(a_X))$ can be obtained from the same crack length measurement, due to the correspondence between a and a_X. For instance,

Table 6.5 X and Y coordinates along the interface as a function of the actual and effective crack lengths, a and a_X, respectively, in a planar and a sloped section. Subscript i represents the state at the beginning of the section.

	Section I	Section II
$X_1(a)$	$X_1(a_i)+(a-a_i)+\tilde{x}_1$	$X_1(a_i)+(a-a_i)\cos(\alpha)+\tilde{x}_1\cdot\cos(\alpha)$
$X_2(a)$	$X_2(a_i)$	$X_2(a_i)+(a-a_i)\sin(\alpha)+\tilde{x}_1\cdot\sin(\alpha)$
$X_1(a_X)$	$X_1(a_{X,i})+(a_X-a_{x,i})+\tilde{x}_1$	$X_1(a_{X,i})+a_X-a_{X,i}+\tilde{x}_1\cdot\cos(\alpha)$
$X_2(a_X)$	$X_2(a_{X,i})$	$X_2(a_{X,i})+(a_X-a_{X,i})\cdot\tan(\alpha)+\tilde{x}_1\cdot\sin(\alpha)$
$\frac{\partial\tilde{x}_1}{\partial a}$	-1	-1
$\frac{\partial\tilde{x}_1}{\partial a_X}$	-1	$\frac{-1}{\cos(\alpha)}$

this relationship in a trapezoidal interface profile for amplitude A and wavelength λ (see Fig. 6.9.b), is detailed in Table 6.6.

Table 6.6 Actual crack length, a, as a function of effective crack length, a_X, in a trapezoidal interface.

Section	$a_X \in$	a
I	$[0,\lambda/8]$	a_X
II	$[\lambda/8,3\lambda/8]$	$\lambda/8+\frac{a_X-\lambda/8}{\cos(\alpha)}$
III	$[3\lambda/8,5\lambda/8]$	$\lambda/8+\frac{\lambda}{4\cdot\cos(\alpha)}+a_X-3\lambda/8$
IV	$[5\lambda/8,7\lambda/8]$	$3\lambda/8+\frac{\lambda}{4\cdot\cos(\alpha)}+\frac{a_X-5\lambda/8}{\cos(\alpha)}$
V	$[7\lambda/8,\lambda]$	$3\lambda/8+\frac{\lambda}{2\cdot\cos(\alpha)}+a_X-7\lambda/8$

6.2.2 Data arrangement of FEM results. Distribution of the strain and stress fields along the path

This Section specifies the steps followed in order to obtain the necessary data for the J-Integral evaluation described in Section 6.2.1. Required data along a fully developed fracture process zone include: (i) tractions, t_n and t_s, (ii) strains ε_n and ε_s, (iii) the damage variable D and (iv) the angle α. The energy release rate evaluation based on a FE model needs an adequate treatment of the results. Therefore, variables involved in this process are arranged according to the position in the fracture process zone and the load step.

The FE model of DCB specimens including trapezoidal interfaces employed to evaluate J and J^X are those described in Section 6.1.1, whose material properties are included in Table 6.1 and Table 6.2 and geometrical parameters and boundary conditions of the test are depicted in Fig. 6.1.

Under the assumption of finite displacements and rotations hypothesis, a geometrically nonlinear analysis is needed. As a result, the usual cohesive law expressions, $t_n=k_n(1-D)\delta_n$ and $t_s=k_s(1-D)\delta_s$, are no longer valid using the initial coordinate system, due to the integration on top and bottom surfaces leads to $\delta_i \neq u_i^{top}-u_i^{bottom}$.

As a constitutive thickness [275] $h = 1$ mm is set by default in Eqs. 6.20-6.23, we obtain $\varepsilon_n = \delta_n/h$ and $\varepsilon_s = \delta_s/h$ [275].

Complying with this hypothesis, cohesive element tractions are directly related to strain components by $t_n = k_n(1-D)h\varepsilon_n$ and $t_s = k_s(1-D)h\varepsilon_s$. Thus, strains can be used in Eqs. 6.20-6.23 in order to adequately evaluate the contribution of each term of the J-Integral (based on Eqs. 6.16-6.19) (avoiding unreal values that may appear due to rigid body rotations if the expression $\delta_i = u_i^{top} - u_i^{bottom}$ are used) as

$$J_{coh,I} = \sum_{k=1}^{n} \int_{\Gamma_k} t_n \frac{\partial \delta_n}{\partial \tilde{x}_1} d\tilde{x}_1 = \sum_{k=1}^{n} \int_{\Gamma_k} t_n \frac{\partial (h\varepsilon_n)}{\partial \tilde{x}_1} d\tilde{x}_1, \tag{6.20}$$

$$J_{coh,II} = \sum_{k=1}^{n} \int_{\Gamma_k} t_s \frac{\partial \delta_s}{\partial \tilde{x}_1} d\tilde{x}_1 = \sum_{k=1}^{n} \int_{\Gamma_k} t_s \frac{\partial (h\varepsilon_s)}{\partial \tilde{x}_1} d\tilde{x}_1, \tag{6.21}$$

$$J^X_{coh,I} = \sum_{k=1}^{n} \int_{\Gamma_k} \frac{t_n}{\cos\alpha} \frac{\partial \delta_n}{\partial \tilde{x}_1} d\tilde{x}_1 = \sum_{k=1}^{n} \int_{\Gamma_k} \frac{t_n}{\cos\alpha} \frac{\partial (h\varepsilon_n)}{\partial \tilde{x}_1} d\tilde{x}_1, \tag{6.22}$$

$$J^X_{coh,II} = \sum_{k=1}^{n} \int_{\Gamma_k} \frac{t_s}{\cos\alpha} \frac{\partial \delta_s}{\partial \tilde{x}_1} d\tilde{x}_1 = \sum_{k=1}^{n} \int_{\Gamma_k} \frac{t_s}{\cos\alpha} \frac{\partial (h\varepsilon_s)}{\partial \tilde{x}_1} d\tilde{x}_1. \tag{6.23}$$

The energy release rate evaluation involves ε_n and ε_s, which are evaluated at integration point level, and then consequently the J-integration path selected should be associated with these entities. Although integration points are inside the elements, their values are directly related to either variables along the top and bottom surfaces because of the quadrature rules of the `COH2D4` element.

In Fig. 6.10.a, the process of data acquisition is detailed, indicating the position of nodes and the integration points in the FE model. These data were collected using a `PYTHON` script to automate the procedure. The matrix M in Fig. 6.10.b contains any variable of interest in the simulation, such as: $\varepsilon_{22} = \varepsilon_n$, $\varepsilon_{12} = \varepsilon_s$, $t_n = \sigma_{22}$, $t_s = \sigma_{12}$, and the damage variable, D. In this matrix, each column represents the integration point in the cohesive elements, where n is the number of total integration points of the cohesive elements, and each row represents the frames or increments of the simulation, where m indicates the total frames of such simulation, see Fig. 6.10.c.

In order to understand the involvement of each term of the matrix (D, t_n, t_s, ε_n, ε_s) in the J-Integral computation, Fig. 6.11 reproduces schematically a conventional DCB test (flat interface).

Fig. 6.11.c and Fig. 6.11.d show the evolution of the damage variable and the normal stresses along a cohesive zone in different frames in the numerical DCB test, see Fig. 6.11.a. The relationship between the damage and normal stresses along the CZM as a function of the loading history are shown in the matrix values included in Fig. 6.11.e and 6.11.f, respectively. On one hand, grey colour indicates pristine elements ($D = 0$), black colour includes damaged elements ($D \in (0,1)$), whereas fully damaged elements ($D = 1$) are not represented, see Fig. 6.11.c. On the other hand, blue elements represent null traction of pristine elements, green ones show tractions in non-damaged elements and red ones represent tractions along damaged elements, see Fig. 6.11.d. Elements in white depict the undeformed shape of the adhesive in both Fig. 6.11.c and Fig. 6.11.d.

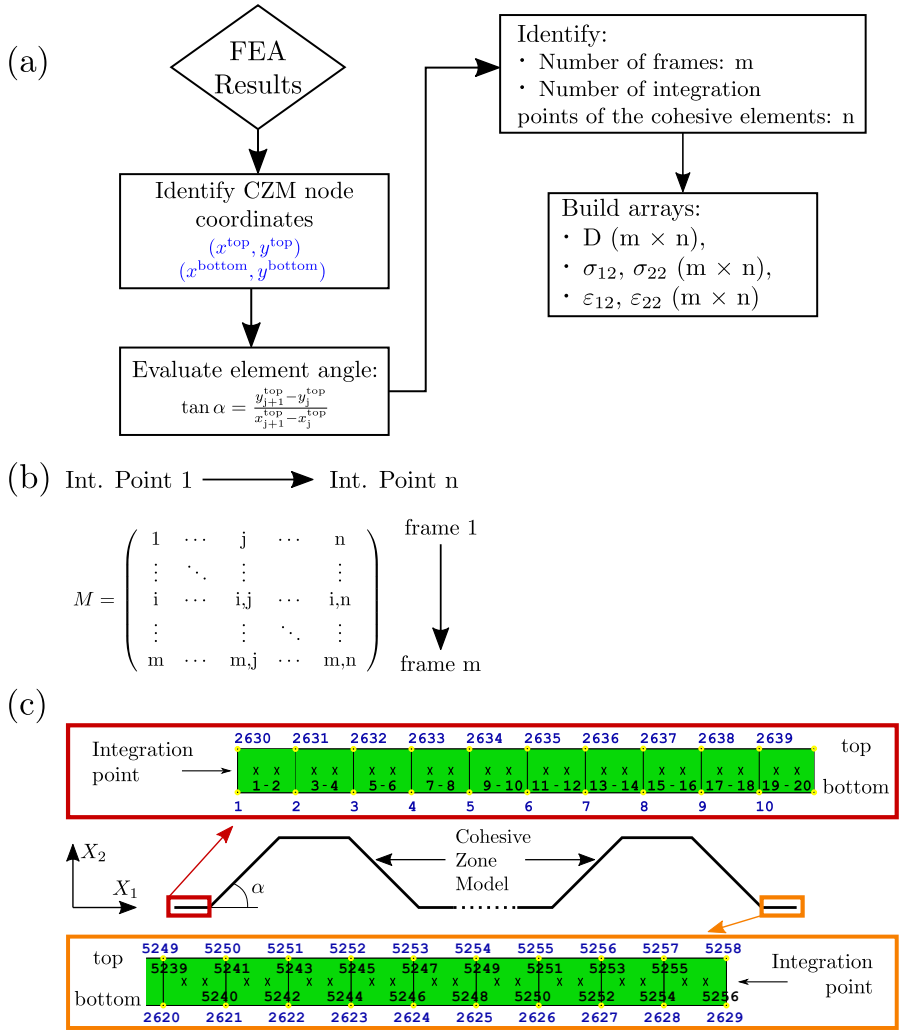

Figure 6.10 (a) Diagram of data acquisition in the FE model, (b) ordered matrix including a variable of interest M, and (c) detail of the used nodes and integrations points along the inteface.

Regarding the traction values in Fig. 6.11.b, t^0 represents the integration point stress at the end of the linear elastic part (prior the damage initiation), that is, the highest stress value in a cohesive element considering a bilinear law. Taking into account the path selected in Section 6.2.1, only tractions and strains in the zone where cohesive model is developed are needed. Then, the integration points used for the J-Integral evaluation (Eqs. 6.20-6.23) are within the range: $D \in (0,1)$.

It is interesting to notice that different scenarios can be found regarding the failure propagation along the crack path. These cases are identified schematically with the

frames 1, i and m in Fig. 6.11.c and Fig. 6.11.d:

- No damage (frame 1): $D = 0$ and $t \in [0, t^0)$. The opening displacements and associated tractions are not large enough to cause damage initiation.
- Damage initiation (frame i): $D \in [0, 1)$ and $t \in [0, t^0] \cup [t^0, 0)$. Failure starts/appears but a fully damaged zone is not achieved.
- Damage propagation (frame m): $D \in [0, 1]$ and $t \in [0, t^0] \cup [t^0, 0]$. Some elements or integration points loose completely their stiffness properties and, consequently, a crack advance is produced, although other elements remain with all their properties intact.

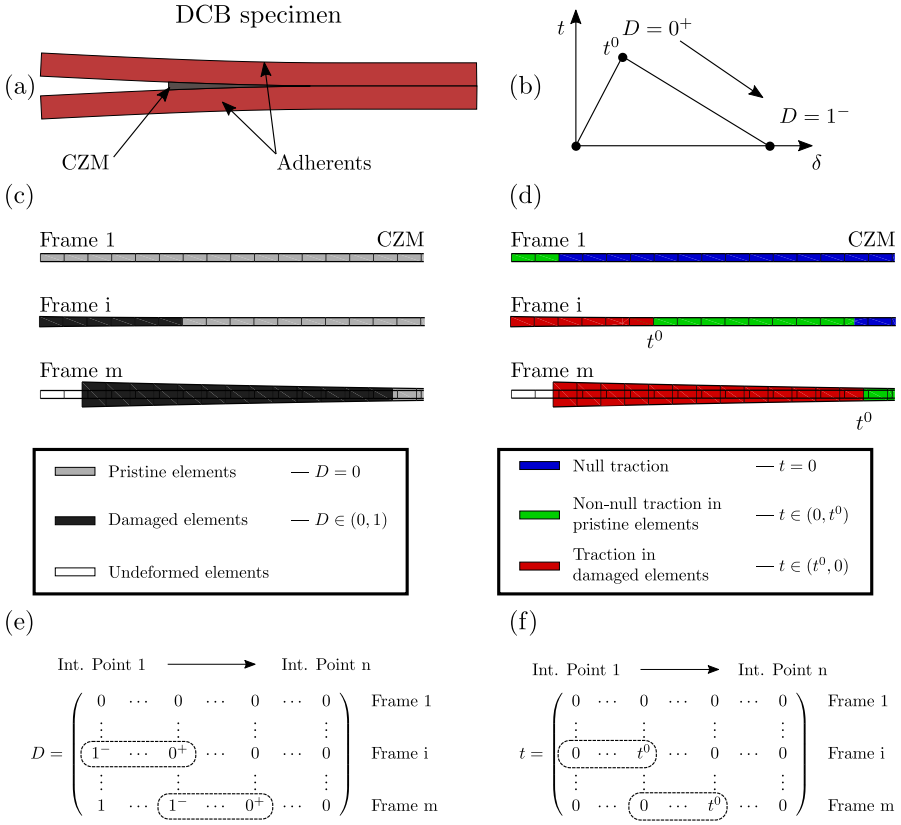

Figure 6.11 Failure progression in CZM of a DCB test. (a) Scheme of a convential DCB test. (b) Bilinear traction-separation response of the cohesive elements. (c) Damage and (d) normal traction along the CZM in different frames of the simulation. The deformed shape is multiplied by a factor of 1. (e) Damage matrix and (f) normal traction matrix in CZM arranged according to the integration point and the frame of the simulation.

Then, J and J^X are calculated using the data from integration points which fulfilled the condition $D \in (0,1)$. Using the previously defined ordered matrix, it is possible to evaluate J and J^X in each frame of the simulation considering separately each row of the array, as shown by the dashed rectangles in the matrices represented in Fig. 6.11.e and Fig. 6.11.f.

However, in DCB specimens including patterned interfaces [255], damage and stress distributions along the crack path are not continuous (i.e. tractions and failure are not monotonically increasing and/or decreasing), as is the case of other conventional tests [173, 219, 220, 276].

The presence of non-flat interfaces leads to irregular stress and strain fields along the interface, see Fig. 6.12.a-d. Then, damage zone is not continuous due to the fact that fracture conditions are not achieved uniformly along the interface, and consequently some elements remain active despite of the presence of fully damaged elements in an intermediate region of the process zone, see Fig. 6.13.

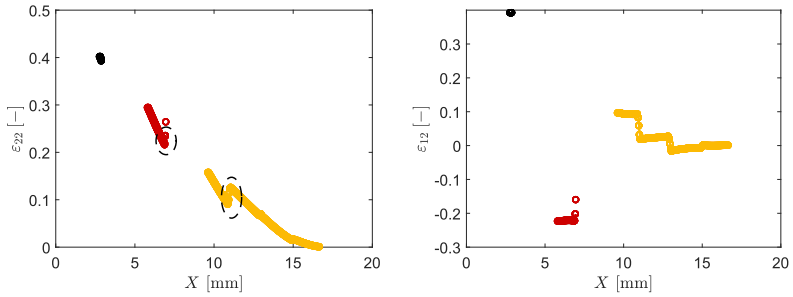

(a) Normal strains ε_{22} along the process zone. **(b)** Tangential strains ε_{12} along the process zone.

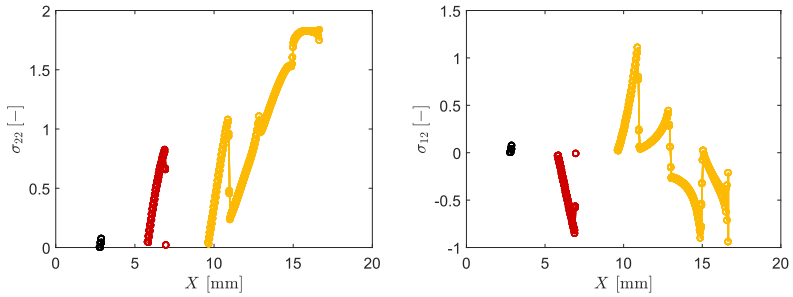

(c) Normal stresses σ_{22} along the process zone. **(d)** Tangential stresses σ_{12} along the process zone.

Figure 6.12 Stress and strain distribution along a structured interface modelled with a CZM.

Furthermore, special attention should be paid to the evaluation of J and J^X due to the

fact that non-uniform stress and strain fields were developed at the joint. Thus, unlike conventional DCB tests, where displacements are decreasing along fracture process zone when approaching to the undamaged zone, patterned interfaces may combine increasing and decreasing displacements along the crack path, see dashed circles in Fig. 6.12.a. Specifically, the derivatives $\frac{\partial \varepsilon_n}{\partial \tilde{x}_1}$ or $\frac{\partial \varepsilon_s}{\partial \tilde{x}_1}$ may change from positive to negative, then following Eqs. 6.20-6.23, the contribution of these regions to the J-Integral evaluation could be negative, see points 2 and 3 of the patterned interface in Fig. 6.13. On the other hand, in flat DCB specimens the derivative $\frac{\partial \varepsilon_n}{\partial \tilde{x}_1}$ remains constant along the whole process zone, see points 1 and 2 over the flat profile in Fig. 6.13. As a consequence, the correct J and J^X evaluation renders

$$J_{coh,I} = \sum_{k=1}^{n} \int_{\Gamma_k} t_n \left| \frac{\partial (h\varepsilon_n)}{\partial \tilde{x}_1} \right| d\tilde{x}_1, \tag{6.24}$$

$$J^X_{coh,I} = \sum_{k=1}^{n} \int_{\Gamma_k} \frac{t_n}{\cos\alpha} \left| \frac{\partial (h\varepsilon_n)}{\partial \tilde{x}_1} \right| d\tilde{x}_1, \tag{6.25}$$

$$J_{coh,II} = \sum_{k=1}^{n} \int_{\Gamma_k} t_s \left| \frac{\partial (h\varepsilon_s)}{\partial \tilde{x}_1} \right| d\tilde{x}_1, \tag{6.26}$$

$$J^X_{coh,II} = \sum_{k=1}^{n} \int_{\Gamma_k} \frac{t_s}{\cos\alpha} \left| \frac{\partial (h\varepsilon_s)}{\partial \tilde{x}_1} \right| d\tilde{x}_1. \tag{6.27}$$

Note that the constitutive thickness in the present model is $h = 1$ mm [275].

Additionally, Eqs. (6.24)-(6.27) should be the sum of the energy release rate of each element due to the distance $d\tilde{x}_1$ between integration points (located at lateral sides of the `COH2D4` elements) of adjacent elements is null. It is interesting to recall that if a self-similar crack growth is obtained during the test (i.e. the fracture process length remain the same in different frames), then, almost identical total released energy values should be obtained for every frame.

6.2.3 Discussion. Comparison of fracture energy obtained from load-displacement curves and J-Integral formulation

In this Section a comparison between two different ways of obtaining the fracture energy in structured interfaces is discussed: load-displacement curves of Section 6.1 and J-Integral developed in Section 6.2. The fracture energy obtained from load-displacement curves considers the average global response of the entire system, while J-Integral method is focused on the behaviour along the interface.

The trapezoidal configurations and geometrical parameters are shown in Fig. 6.14. Overall global dimensions of the used DCB specimens (length, width, thickness, etc.) are those used in the experimental campaign carried out in Chapter 4. Every configuration in Fig. 6.14 was solved using a plane strain model in Abaqus Standard, which includes cohesive elements to model the interface failure. Some convergence issues were encountered to achieve equilibrium solutions, especially for large values of A/λ. A damping factor (stabilization) equal to 1×10^{-4} was used to help the convergence of the

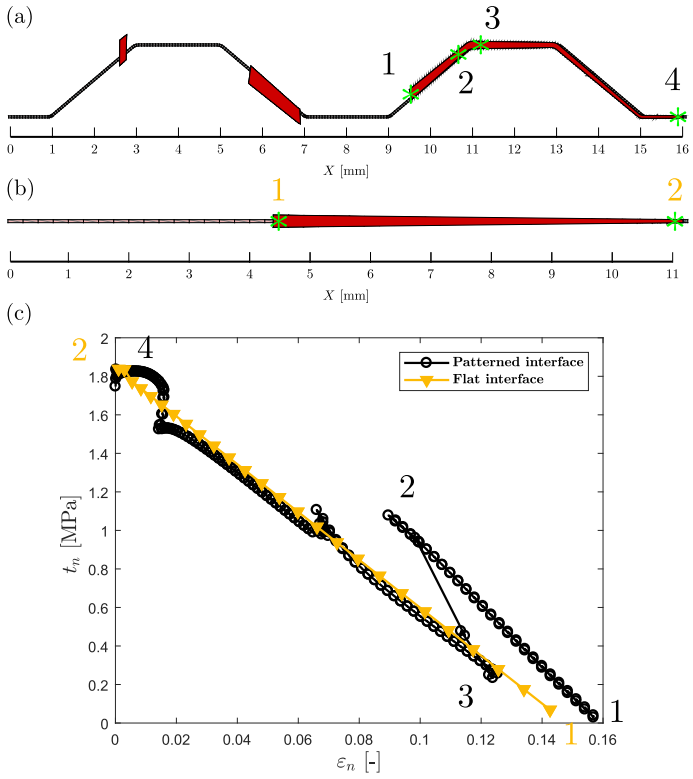

Figure 6.13 Deformed CZM in (a) trapezoidal and (b) flat interface. (c) Normal stress, t_n, evolution versus normal strain, ε_n, along the fracture process zone in flat and patterned interfaces. Numbers in the picture represent the stress-strain state corresponding to the points indicated in the interface deformed shape.

model in configurations C2, C3, C4, C6, C7 and C8. In any case, the static dissipation energy due to the artificial damping for every case under consideration achieved a low rate with respect to other energy measures of the model (always lower than 5.5% of the total internal energy), validating the use of this numerical technique.

Then, following the steps described in Section 6.2.1, J and J^X evolutions with respect to the effective crack length a_X are presented in Fig. 6.15 and 6.16.

J and J^X versus a_X evolution shows peaks during the crack propagation. These peaks are associated with the fact that the crack propagates in an unstable manner up to reaching the next equilibrium state at specific locations of the interface.

Because of inherent unstable behaviour of structured interfaces, critical energy release rate is not achieved in every step of the simulation, that is, $J \neq J_c$ or $J^X \neq J_c^X$. Consequently, the crack does not propagate and the system accumulates energy up to reach the condition $J = J_c$ or $J^X = J_c^X$. In order to calculate a correct mean fracture energy, J and J^X values associated with steps without energy dissipation should be

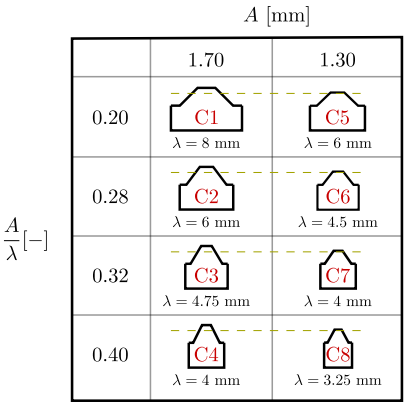

Figure 6.14 Trapezoidal interface configurations employed in the fracture energy evaluation, where A, λ and A/λ represents respectively the amplitude, the wavelength and the aspect ratio of the pattern. Labels C1-C8 identify the different configurations. Discontinuous lines emphasise the differences in amplitude between $A = 1.70$ mm and $A = 1.30$ mm configurations.

removed of the $\bar{J}_c$ and $\bar{J}_c^X$ computation as

$$\bar{J}_c = \frac{1}{a_{X2} - a_{X1}} \int_{a_{X1}}^{a_{X2}} J \, da_X \tag{6.28}$$

$$\bar{J}_c^X = \frac{1}{a_{X2} - a_{X1}} \int_{a_{X1}}^{a_{X2}} J^X \, da_X \tag{6.29}$$

Table 6.7 shows the mean J-Integral value according to Eqs. 6.28 and 6.29. $\bar{J}_c^X$ and $\bar{J}_c$ are evaluated in each case between the effective crack lengths a_{X1} and a_{X2}, so that a direct comparison with G_c and G_c^X results obtained from the load-displacement curves can be performed.

In light of the results, a good agreement can be observed for both actual energy release rate (G_c versus $\bar{J}_c$) and effective energy release rate (G_c^X versus $\bar{J}_c^X$), with a difference ranging from 1.51% (C1) to 17.07% (C4) for $\bar{J}_c$ and ranging from 3.16% (C5) to 5.90% (C1) for $\bar{J}_c^X$.

Table 6.7 show that larger differences are obtained between G_c and $\bar{J}_c$ than between G_c^X and $\bar{J}_c^X$. This fact may be derived from two reasons regarding the conventional methodology to obtain G_c and G_c^X (from load-displacement curves [249,255]). First, the DCB test is conceived for crack propagation in a stable fracture Mode I along a straight interface. These conditions are not achieved in patterned interface DCB tests, where the crack advance occurs unstably and the crack travels in different directions. However, J_c^X calculation involves the distance travelled by the crack along an unidirectional path, as in the case of a conventional DCB test. Second, the energy released and the area associated with new surface generation are determined separately in load-displacement methods, whereas J-Integral allows energy release rate to be calculated in a single

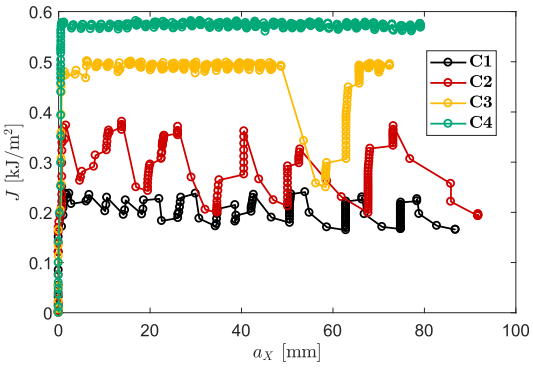

(a) J vs a_X .

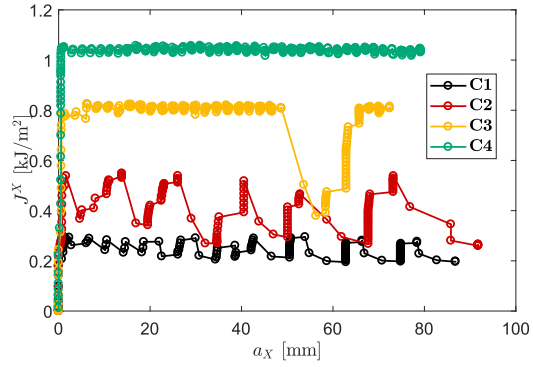

(b) J^X vs a_X.

Figure 6.15 (a) J and (b) J^X versus the apparent crack length a_X in configurations C1, C2, C3 and C4.

operation.

6.3 Concluding remarks

In this Chapter a Finite Element model of the composite 3D printed specimens with trapezoidal interfaces was developed. The numerical simulation of the Double Cantilever beam tests allowed the fracture performance, crack initiation and crack propagation of the structured interfaces to be characterised by means of the Cohesive Zone Model. Particularly, a bilinear cohesive zone law was employed to simulate the adhesive performance, while the adherent was modelled as linear elastic (with the properties of the nylon and glass-fiber composite of the 3D printer).

This computational framework leads to the numerical-experimental correlation between the load-displacement curves of the DCB test presented in Chapter 4, showing

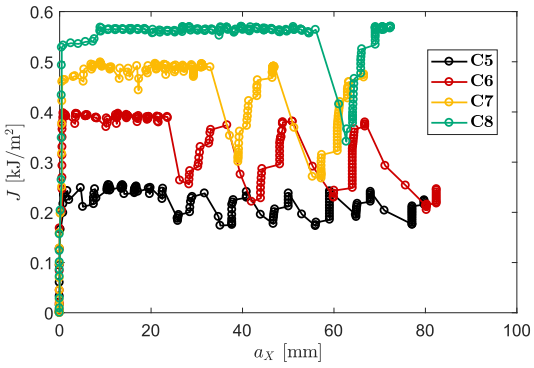

(a) J vs a_X .

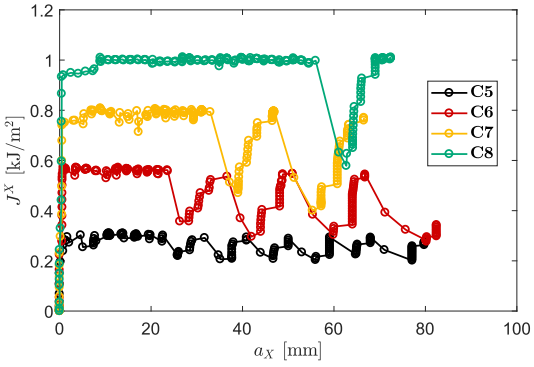

(b) J^X vs a_X .

Figure 6.16 (a) J and (b) J^X versus the apparent crack length a_X in configurations C5, C6, C7 and C8.

a good agreement for the different aspect ratio values A/λ of the profile. Therefore, the increasing tendency of the actual and effective critical energy release rate obtained from the load-displacement curves, G_c^S and G_c^X respectively, with respect to the ratio A/λ is confirmed computationally.

Moreover, the formulation of the J-Integral has been adapted to describe the fracture behaviour of non-straight crack paths. Specifically, J^X was defined as the variation of the potential energy Π with respect the effective crack length a_X, that is, the distance travelled by the crack along the X direction. This standpoint allows the evolution of the energy release rate J with the effective crack propagation a_X to be described. Thus, it can be observed that the unstable crack advancement characteristic in patterned interfaces is associated with the variability of the critical fracture toughness along the crack path.

Table 6.7 G_c, G_c^X $\bar{J}_c$, $\bar{J}_c^X$ calculated from numerical load-displacement curves, and J-Integral formulation.

	Experimental		Load-displacement		J-Integral	
Configuration	$\mathbf{G_c}\left[\frac{\mathrm{J}}{\mathrm{m}^2}\right]$	$\mathbf{G_c^X}\left[\frac{\mathrm{J}}{\mathrm{m}^2}\right]$	$\mathbf{G_c}\left[\frac{\mathrm{J}}{\mathrm{m}^2}\right]$	$\mathbf{G_c^X}\left[\frac{\mathrm{J}}{\mathrm{m}^2}\right]$	$\bar{\mathbf{J}}_\mathbf{c}\left[\frac{\mathrm{J}}{\mathrm{m}^2}\right]$	$\bar{\mathbf{J}}_\mathbf{c}^\mathbf{X}\left[\frac{\mathrm{J}}{\mathrm{m}^2}\right]$
C1	227.0	273.96	198.7	228.9	201.7	242.4
C2	278.1	371.13	287.8	362.7	275.9	385.0
C3	-	-	528.9	778.4	492.5	810.1
C4	760.9	1231.2	692.4	1007.3	574.3	1044.3
C5	217.1	262.1	220.3	253.4	216.2	261.4
C6	-	-	352.3	442.2	324.4	456.7
C7	345.4	484.0	521.6	701.6	460.9	741.1
C8	-	-	671.1	952.2	563.6	998.1

7 Modelling of structured interfaces by means of the Linear Elastic Brittle Interface Model

7.1 A consistent finite displacement and rotation formulation of the Linear Elastic Brittle Interface Model

In the last two decades, CZMs have been extensively employed for failure analysis of weak or imperfect interfaces and thin adhesives between solids whose stiffness is much higher than the stiffness associated with the interface. In this setting, the present investigation is focused on a limit case of a cohesive law devoted to the study of brittle interfaces, that corresponds to the so-called Linear Elastic-Brittle Interface Model (LEBIM). The perfectly brittle approach provides some advantages over other TSL profiles endowing: (i) the simple linear elastic behaviour prior complete and abrupt failure, (ii) the preclusion of the FPZ, since no progressive stiffness deterioration is accounted for in the LEBIM (which relaxes the discretization requirements in comparison with alternative CZMs with nonlinear behaviour), and, as a consequence, (iii) a notable simplification of the numerical implementation tasks. Furthermore, relying on the predictions of the investigations aforementioned, the LEBIM has evidenced high-level characteristics in terms of numerical robustness, simplicity and computational efficiency.

With focus on the numerical implementation of interface failure modelling recalling a non zero-thickness approach, in general terms, despite the existence of different TSLs in the related literature, the procedure to compute the stress and displacement field follows the same scheme regardless the particular profile of the TSL. Basically, the displacements at the interface are calculated according to a local coordinate system

(N_s^c, N_n^c) whose origin is located on the midplane of the interface, see Fig 7.1 for 2D applications, and the particular orientation of the director vectors (N_s^c, N_n^c) characterizes the displacement field contributions associated with the fracture Modes I and II, respectively. Then, the displacements at the crack flanks can be decomposed in their corresponding transverse normal, tangential shear and in-plane or longitudinal shear counterparts, δ_n, δ_s^s and δ_s^l, respectively, and they are used to determine the stress field via the TSL. Nonetheless, usually some assumptions are made to simplify the model and the constitutive equations, as the preclusion of potential material distortions. For instance, in the commercial Finite Element code ABAQUS® [275], for 2D cases, the transverse normal δ_n and tangential shear δ_s^s relative displacements are the specific components that are considered within the cohesive element formulation (COH2D4 for 2D analysis) for the evaluation of the TSL, the in-plane deformation effects being neglected. That is, normal and shear tractions, t_n and t_s, and their conjugated displacements counterparts, δ_n and δ_s^s, are computed within this kind of element topology. Based on these aspects, considerations regarding the in-plane deformation at interfaces cannot be taken into account employing regular elements that are present in most of the commercial FE libraries. Differing from this, recent studies have confirmed the influence of the in-plane effects in the failure response of adhesives [277, 278], which might have a remarkable influence.

In addition to the previous considerations, there are situations in which rigid body translations and rotations become significant, and therefore the nonlinear Continuum Mechanics theory [177] should be taken as underlying modelling framework. In this regard, many of conventional cohesive elements in general purpose FE-codes include an appropriate formulation for geometrically nonlinear analysis, but many TSLs implemented by means of user material subroutine, e.g. UMAT in ABAQUS®, have been mostly developed considering infinitesimal strain theory, as occurred in [226, 279] for the LEBIM. Therefore, the application of the baseline LEBIM requires some modifications in order to consistently account for nonlinear effects via its integration as user-defined material capability (UMAT). Note that alternatively to this modelling option, the authors in [280, 281] proposed the development of interface elements for large deformation analysis for microstructures made of fibrils, whose implementation tasks required the formulation, derivations, and coding of the element kinematics.

Apart from the discrepancies in terms of formulations between small and large displacement theories, it is worth mentioning the different reference systems between general-purpose cohesive and continuum/solid element topologies in their respective local configurations. Thus, on the one hand, the cohesive basis is generally referred to the midplane of the interface, whereas, on the other hand, the solid coordinate system is related to the principal direction of strain (this aspect not being very comprehensively treated in the related literature). Hence, tractions and displacements in the continuum technique need to be expressed in the interface basis for a correct evaluation of the TSL.

In order to address the previous aspects herewith outlined, the main objective of this Section is the development of a computational procedure that enables the robust determination of the displacement field (with potential inclusion of in-plane deformation effects) that is required for the computation of a particular TSL for interface failure modelling using a non-zero thickness interface approach under large displacement

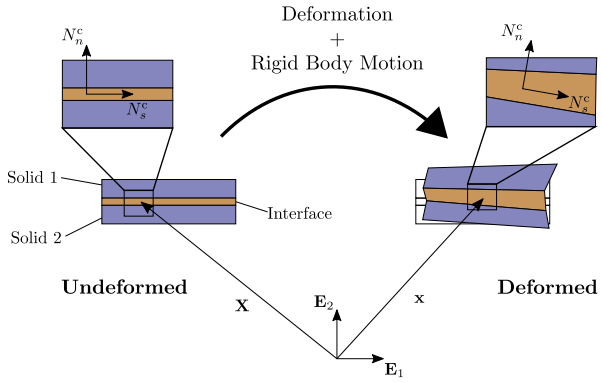

Figure 7.1 Local coordinate system located at the midplane of the interface in undeformed (**X**) and deformed (**x**) situations.

hypotheses. In other words, the principal aim is to overcome the previously listed issues associated with the existence of finite rigid body motion through the development of a formulation suitable for its implementation into general purpose FE packages. A user material subroutine allows transverse normal δ_{n}, tangential shear $\delta_{\mathrm{s}}^{\mathrm{s}}$ and in-plane or longitudinal shear $\delta_{\mathrm{s}}^{\mathrm{l}}$ relative displacements referred to a coordinate system located at the interface midplane to be computed. In particular, this innovative method for determining interface displacements is applied, without loss of generality, to the LEBIM following a nonlinear FE numerical scheme and examined through the prediction of a Horizontal Drum Peel (HDP) test response. Note, as will be recalled in the forthcoming developments, that the current procedure can be employed following two basic approaches, namely, either its incorporation in standard cohesive-like elements or in continuum-like elements, the latter endowing in-plane deformation effects of the interface.

This Section is structured as follows. Section 7.1.1 describes the two basic procedures proposed herein for the reliable computation of interface displacements (relative to the midplane of the interface) in both cohesive and solid elements in ABAQUS. Section 7.1.2 verifies the current methodology through its application of representative benchmark problems. The employment of the developed technique using LEBIM at the interface in the FE simulation of a Horizontal Drum Peel test is shown in Section 7.1.3. Finally, Section 7.1.4 highlights the convenience of the proposed procedure and summarizes the fundamental contributions of this research.

7.1.1 Finite displacement formulation for LEBIM following a continuum-like approach

This Section presents the basic aspects of the two approaches developed herein for the integration of the LEBIM into built-in elements of `ABAQUS`® for large displacements applications. Specifically, an initial thickness of the interface is assumed, and therefore the LEBIM can be integrated into this general purpose package via the user-defined material routine `UMAT`. This fact notably simplifies the required implementation tasks

with respect to alternative formulations as those proposed in [216,222] and the references given therein.

The current nonlinear formulation provides the reliable computation of the displacements field. This field is referred to middle line of the element (dashed line in Fig. 7.2), in order to evaluate adequately any TSL without the need of implementing the kinematic part associated with a geometrically nonlinear interface element.

In order to address this issue, a simple graphical explanation via the analysis of a single element is schematically provided in Fig. 7.2. Thus, in case of small displacement assumptions for the evaluation of the TSL in large displacements scenarios, stresses derived from rigid body rotations arise without the need to deform the element due to clear incoherences, see the first benchmark example in Section 7.1.2. Conversely, the general nonlinear theory allows the relative separation between top and bottom element surfaces to be computed through the evaluation of the current position of the element middle line. This prevents from the appearance of spurious stresses in the corresponding computations. Moreover, large displacement formulations allow the the element mid-line motion to be computed, both α_1 due to a rigid body rotation and α_2 due to a deformation state (see Fig. 7.2).

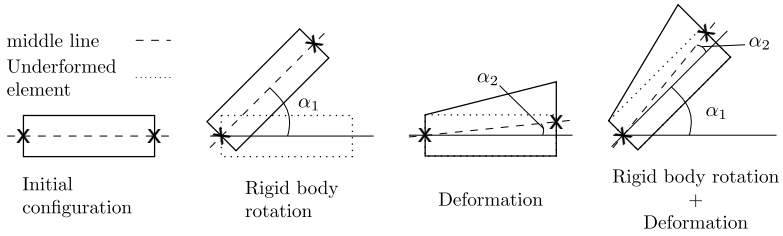

Figure 7.2 Element initial configuration and several possible motions.

In the forthcoming sections, we outline the two approaches proposed herein to deal with this issue for non-zero initial thickness interface models undergoing finite rotations and strains:

- The first methodology corresponds to the integration of the LEBIM into a cohesive element type, specifically the one denominated as `COH2D4` of `ABAQUS`® library (Section 7.1.1.1) which employs the Newton-Cotes quadrature rules. In Fig. 7.3 the *interface-like* approach regarding the relative displacements between top and bottom surfaces and the deformations involved within the bulk are described. In this method, the relative transverse normal and tangential shear displacements, δ_{n} and $\delta_{\mathrm{s}}^{\mathrm{s}}$ respectively, are related to the average transverse normal and shear deformation along the thickness h ($\varepsilon_{\mathrm{nn}}$ and $\varepsilon_{\mathrm{ns}}$ respectively). Such strains are computed at the integration point level, which are located at the midline of the interface whereas the displacement field is derived from the strain field and the interface thickness h. It is worth mentioning that the longitudinal shear strain ε_{ss} is not considered in this approach and, consequently, the relative longitudinal shear displacement or in-plane displacement $\delta_{\mathrm{s}}^{\mathrm{l}}$ is neglected.

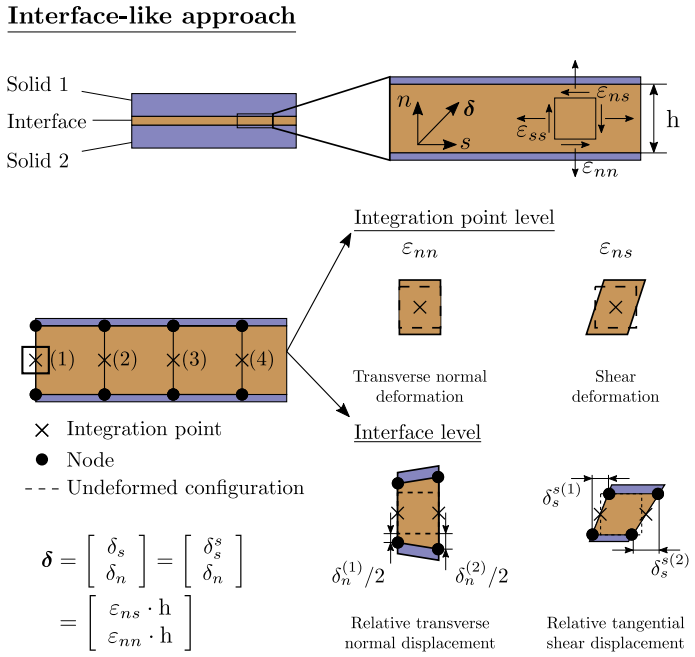

Figure 7.3 *Interface-like* approach, including deformations (transverse normal ε_{nn} and shear ε_{ns}) in the bulk and relative displacements between top and bottom surfaces (relative transverse normal δ_n and relative tangential shear δ_s^s).

- The second approach exploits the use of standard continuum elements, for which we select those denominated as CPE4 elements of ABAQUS® library (Section 7.1.1.2), which employs the standard Gauss quadrature rules. In contrast with the precedent technique, it is important to remark that this second methodology incorporates a new perspective for the evaluation of the TSL at the interface, which additionally includes the potential effect of the in-plane deformation. The *continuum-like* standpoint in Fig. 7.4 allows transverse normal and longitudinal deformation, (ε_{nn} and ε_{ss} respectively), and shear deformation (ε_{ns}) to occur within the interface. This strain state leads to the following *psuedo*-displacement field via the multiplication of the strain tensor by the interface thickness h and the size length L as described in Fig. 7.4: (i) relative transverse normal displacement δ_n, (ii) relative longitudinal shear displacement or in-plane displacement δ_s^l and (iii) relative tangential shear displacement δ_s^s. Hence, the relative shear separation between surfaces δ_s can be produced by shear deformations or by a non-uniform distribution of longitudinal normal deformation along the thickness. For this reason, in these forthcoming applications, it is assumed that both δ_s^s and δ_s^l contribute to the shear component of the constitutive law, that is, $\delta_s = \delta_s^s + \delta_s^l$. Moreover, the *pseudo*-displacements obtained at the integration points (δ_n, δ_s^s, δ_s^l) constitute representative values to evaluate the constitutive law. These values

coincide with the relative separation between top and bottom surfaces in scenarios where the strain field is constant inside the element.

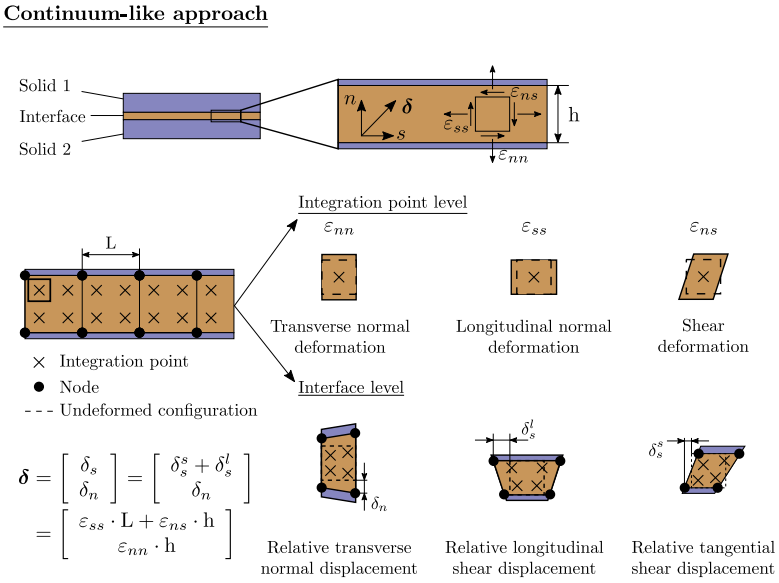

Figure 7.4 *Continuum-like* approach. Transverse normal deformation ε_{nn}, longitudinal normal deformation ε_{ss} and shear deformation ε_{ns} represent the strain state at the integration point level. The relative displacements between top and bottom surfaces (transverse normal δ_n, longitudinal shear or in-plane δ_s^l and tangential shear δ_s^s), serve as a measure of the interface separation and may be variable along the bondline.

Finally, note that both approaches aforementioned have been included into the FE-package ABAQUS® without any loss of generality. Their transfer to any other code with similar user-defined capabilities can be conducted through simple modifications.

7.1.1.1 Interface-like approach

In this Section, the specific procedure for the obtention of the relative displacements (the normal and tangential shear displacements, δ_n and δ_s^s, respectively) that experience a 2D interface element with non-zero thickness is described. This action is of significant importance for the proper evaluation of the TSL under large displacements assumptions, as is the case of the current LEBIM via the employment of user-defined UMAT capability, though its generalization for any other TSL can be carried out in a straightforward manner. In particular, the current scheme is specialized for the built-in cohesive elements COH2D4 of ABAQUS®.

As reported in ABAQUS® documentation [275], the central difference algorithm [282] is employed to compute the strain at the beginning, t, and at the end, $t+\Delta t$, of a certain pseudo-time increment in conjunction with the rigid body rotations that take place

within such increment (the time interval throughout the simulation is denoted as $[0,t]$, where t is the time elapsed that identifies the current body placement). This formulation defines the Euler-Almansi strain tensor as follows

$$\Delta\boldsymbol{\varepsilon} = \frac{\partial \Delta \mathbf{u}}{\partial \mathbf{x}_{t+\Delta t/2}}, \tag{7.1}$$

where $\Delta\boldsymbol{\varepsilon}$ is the strain increment tensor, $\Delta\mathbf{u}$ is the displacement increment and $\mathbf{x}_{t+\Delta t/2} = \frac{1}{2}(\mathbf{x}_t + \mathbf{x}_{t+\Delta t})$ is the vector position at the middle of the time increment $(t+\Delta t/2)$.

The variables of interest in `COH2D4` elements of `ABAQUS`® for the assessment of the particular form of the TSL correspond to the normal and shear strain increments, $\Delta\varepsilon_{nn}$ and $\Delta\varepsilon_{ns}$, respectively. These strain components can be related with the element thickness h, as follows

$$\Delta\varepsilon_{nn} = \frac{\Delta\delta_{\mathrm{n}}}{\frac{1}{2}\left(\mathrm{h}_{t+\Delta t} + \mathrm{h}_t\right)} = \frac{\mathrm{h}_{t+\Delta t} - \mathrm{h}_t}{\frac{1}{2}\left(\mathrm{h}_{t+\Delta t} + \mathrm{h}_t\right)}, \tag{7.2}$$

$$\Delta\varepsilon_{ns} = \frac{\Delta\delta_{\mathrm{s}}^{\mathrm{s}}}{\frac{1}{2}\left(\mathrm{h}_{t+\Delta t} + \mathrm{h}_t\right)}, \tag{7.3}$$

where h_t and $\mathrm{h}_{t+\Delta t}$ are the element thickness at the beginning and at the end of the current pseudo-time increment. Complying with this scheme, the entry variables of the `UMAT` subroutine are expressed in the current configuration, and therefore rigid solid motions are already eliminated from the corresponding strain tensor (this means that no extra computations are required). Thus, the TSL can be directly implemented into the local frame, that is, defined by the normal and tangent vectors of the interface. Subsequently, the rotation of this local TSL to the global system is carried out internally by `ABAQUS`® without the need of the user intervention.

Moreover, due to the fact that some variables are either known from previous time increments, h_t, or computed by the solver and provided as direct entry, $\Delta\varepsilon_{nn}$ and $\Delta\varepsilon_{ns}$, the relative displacement increments $\Delta\delta_{\mathrm{n}} = \mathrm{h}_{t+\Delta t} - \mathrm{h}_t$, and $\Delta\delta_{\mathrm{s}}^{\mathrm{s}}$ can be determined directly through the use of Eqs. (7.2)-(7.3) (constituting a set of two equations with two unknowns that can be directly solved). The scheme provided in Fig. 7.5 summarises the procedure.

This procedure allows the relative displacement between top and bottom surfaces to be applied in any constitutive law, and increases the range of applicability beyond the options implemented in the commercial softwares.

7.1.1.2 Continuum-like approach

This Section introduces an innovative procedure to compute interface flanks separation in a finite element with the purpose of interface failure modelling. For a proper understanding of this novel technique, guidelines of nonlinear Continuum Mechanics in Chapter 2.1 should be reviewed.

1. **Input arguments:**

   $\boldsymbol{\varepsilon}_t$, $\Delta\boldsymbol{\varepsilon}$, $\boldsymbol{\sigma}_t$, h_t

2. **Determine thickness at the end of the increment:**

   $$\mathrm{h}_{t+\Delta t} = \mathrm{h}_t \left(\frac{1 + \frac{1}{2}\Delta\varepsilon_{nn}}{1 - \frac{1}{2}\Delta\varepsilon_{nn}} \right)$$

3. **Determine normal and shear displacement increments:**

   $$\Delta\delta_{\mathrm{n}} = \mathrm{h}_{t+\Delta t} - \mathrm{h}_t$$
   $$\Delta\delta_{\mathrm{s}}^{\mathrm{s}} = \tfrac{1}{2}\left(\mathrm{h}_{t+\Delta t} + \mathrm{h}_t\right)\Delta\varepsilon_{ns}$$
   $$\Delta\boldsymbol{\delta} = \begin{bmatrix} \Delta\delta_{\mathrm{n}} \\ \Delta\delta_{\mathrm{s}}^{\mathrm{s}} \end{bmatrix}$$

4. **Evaluate stress increment and jacobian matrix:**

   $$\Delta\boldsymbol{\sigma} = \mathbb{C}\Delta\boldsymbol{\delta}$$
   $$\mathbb{C} = \begin{bmatrix} k_{\mathrm{n}} & 0 \\ 0 & k_{\mathrm{s}} \end{bmatrix}$$

5. **Output arguments:**

   $$\boldsymbol{\sigma}_{t+\Delta t} = \boldsymbol{\sigma}_t + \Delta\boldsymbol{\sigma}$$
   $\mathbb{C}$, $\mathrm{h}_{t+\Delta t}$

Figure 7.5 Simplified algorithm for displacement-stress estimation in a Traction Separation Law in cohesive elements under finite deformation assumptions.

In most of the commercial FEM codes, in 2D applications, built-in cohesive elements only enable capturing transverse normal and shear deformations whilst the constitutive response of the materials needs to fulfil certain hypothesis regarding the stress and strain fields. In contrast to the standard procedure, the current modelling standpoint offers a wide range of capabilities, such as the calculation of a complete stress and strain state (normal, shear and in-plane deformations) and the advantages of the continuum elements in terms of meshing generation processes.

The differences between governing equations in continuum materials, such as metals or ceramics, among others, with respect to those associated with interface modelling behaviour lead to the development of special-purpose elements. Stress and strain fields in solid materials are generally expressed in principal directions of strain, whereas constitutive laws in cohesive formulations are often referred to the displacements respect to the mid-line of the element (in 2D scenarios).

Hence, the main asset of this method is to determine the transverse normal δ_{n}, tangential shear $\delta_{\mathrm{s}}^{\mathrm{s}}$ and longitudinal shear or in-plane $\delta_{\mathrm{s}}^{\mathrm{l}}$ relative displacements associated with the interface mid-line, as those employed in the cohesive element approach, without the need to formulate a new element.

In this Section the formulation to determine displacements and tractions according to a TSL following a non-zero initial thickness interface assumption is presented. In the sequel, the analysis is restricted to 2D applications.

In a general TSL, the traction vector is a nonlinear function of the displacement field

with respect to the middle line (2D cases) of the element.Fig. 7.6 shows a graphical representation of the basic motions in the interface modelling under constant and variable deformation.

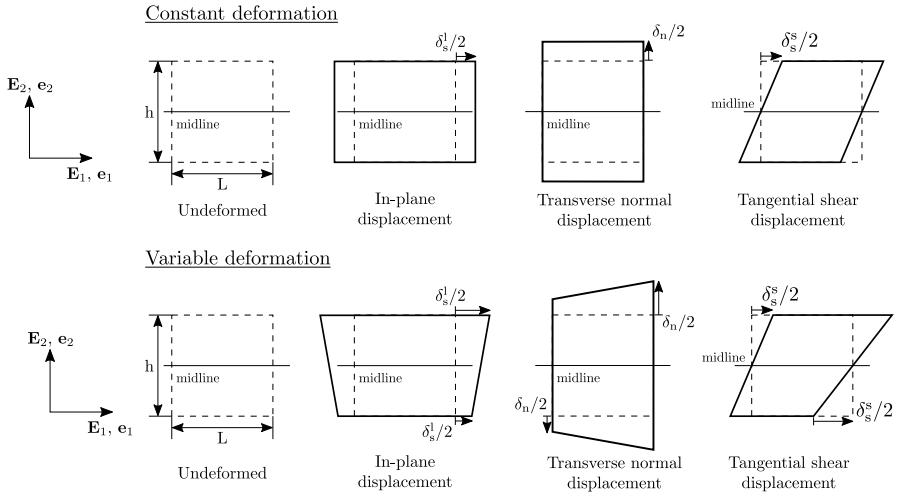

Figure 7.6 Longitudinal shear or in-plane δ_s^l, transverse normal δ_n and tangential shear δ_s^s displacements in a 2D element.

According to the physical interpretation of strain in the previous developments through Eqs. (2.13) and (2.14), a similar approach can be derived for TSLs. In particular, in-plane and normal displacements are the difference between initial and current lengths corresponding to the parallel and perpendicular vectors respect to the element midline. Unlike conventional interface elements, stresses are evaluated from displacements, not from strains, the following expression being used

$$d\mathbf{x} = d\mathbf{X} + d\mathbf{u} \Rightarrow d\mathbf{u} = d\mathbf{x} - d\mathbf{X} = (\mathbf{F} - \mathbf{I})d\mathbf{X}. \tag{7.4}$$

Additionally, considering no superimposed rigid body rotation, pure dilatation parallel and perpendicular to the midline direction and accounting for the polar decomposition can be computed via

$$d\mathbf{u} = (\mathbf{U} - \mathbf{I})d\mathbf{X}, \tag{7.5}$$

where the operator $(\mathbf{U}-\mathbf{I})$ coincides with the Biot strain tensor of the Seth-Hill family $\mathbf{E} = (\mathbf{U} - \mathbf{I})$. Hence, displacements in the case of principal strains can be calculated through employing the following material vectors

$$d\mathbf{u} = (\mathbf{U} - \mathbf{I})\mathbf{N}_h \Rightarrow \begin{bmatrix} 0 \\ \delta_n \end{bmatrix} = \begin{bmatrix} 0 & 0 \\ 0 & U_{22} - 1 \end{bmatrix} \begin{bmatrix} 0 \\ h \end{bmatrix} \Rightarrow \delta_n = (U_{22} - 1)h, \tag{7.6}$$

$$d\mathbf{u} = (\mathbf{U} - \mathbf{I})\mathbf{N}_{\mathrm{L}} \Rightarrow \begin{bmatrix} \delta_{\mathrm{s}}^{\mathrm{l}} \\ 0 \end{bmatrix} = \begin{bmatrix} U_{11} - 1 & 0 \\ 0 & 0 \end{bmatrix} \begin{bmatrix} \mathrm{L} \\ 0 \end{bmatrix} \Rightarrow \delta_{\mathrm{s}}^{\mathrm{l}} = (U_{11} - 1)\mathrm{L}, \quad (7.7)$$

where vector $\mathbf{N}_{\mathrm{h}}$ corresponds to the side perpendicular to the element's midline whereas $\mathbf{N}_{\mathrm{L}}$ stands for the side parallel to the element's midline in Fig. 7.6

According to shear configuration depicted in Fig. 7.6, $\delta_{\mathrm{s}}^{\mathrm{s}}$ could be defined as the displacement of the side perpendicular to the element's midline. In particular, considering simple shear deformation state, this is characterized by the following deformation gradient tensor

$$\mathbf{F} = \begin{bmatrix} 1 & \gamma \\ 0 & 1 \end{bmatrix}, \quad (7.8)$$

where the motion is defined by

$$x_1 = X_1 + \gamma X_2, \quad (7.9)$$

$$x_2 = X_2, \quad (7.10)$$

and the tangential shear displacement in the mentioned case can be determined by means of

$$d\mathbf{u} = (\mathbf{U} - \mathbf{I})\mathbf{N}_{\mathrm{h}} \Rightarrow \begin{bmatrix} \delta_{\mathrm{s}}^{\mathrm{s}} \\ 0 \end{bmatrix} = \begin{bmatrix} 0 & U_{12} \\ 0 & 0 \end{bmatrix} \begin{bmatrix} 0 \\ \mathrm{h} \end{bmatrix} \Rightarrow \delta_{\mathrm{s}}^{\mathrm{s}} = U_{12}\mathrm{h}, \quad (7.11)$$

where it was considered $\mathbf{R} = \mathbf{I}$ due to the fact that the midline does not rotate.

In situations where the midline rotation occurs, the displacements with respect to the midline are required for the proper assessment of the TSL. To do so, a coordinate system coplanar with the mentioned line should be used. To this end, the mid-line direction needs to be tracked during the element motion and the current axis of deformation should be updated. The two-point tensor $\mathbf{F}$ is used to monitor the progress of the direction $\mathbf{T}$, as shown in Fig. 7.7. The angle α between the current vector $\mathbf{t}$ and the initial vector $\mathbf{T}$ is employed to evaluate the rotation tensor $\mathbf{R}$, as

$$\mathbf{R} = \begin{bmatrix} \cos(\alpha) & -\sin(\alpha) \\ \sin(\alpha) & \cos(\alpha) \end{bmatrix}. \quad (7.12)$$

Afterwards, the components of the stretch tensor $\mathbf{U}$ can be determined from Eq. 2.19 as follows

$$\begin{bmatrix} U_{11} & U_{12} \\ U_{21} & U_{22} \end{bmatrix} = \begin{bmatrix} \cos(\alpha)F_{11} + \sin(\alpha)F_{21} & \cos(\alpha)F_{12} + \sin(\alpha)F_{22} \\ -\sin(\alpha)F_{11} + \cos(\alpha)F_{21} & -\sin(\alpha)F_{12} + \cos(\alpha)F_{22} \end{bmatrix}. \quad (7.13)$$

Thus, for cases where the vector $\mathbf{X}_1$ is parallel to the element midline, $\alpha = \alpha_{\mathrm{c}}$ according to Fig. 7.8 and the element midline direction is tracked during the deformation.

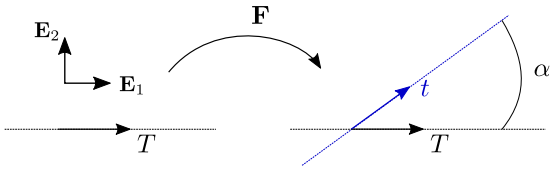

Figure 7.7 Motion of the vector $\mathbf{T}$ after a deformation characterised by $\mathbf{F}$. $\mathbf{T}$ and $\mathbf{t}$ symbolise the vectors in initial and current configurations, respectively, and α stands for the angle between the aforementioned vectors. The basis $\{\mathbf{E}_1, \mathbf{E}_2\}$ indicates the global reference basis.

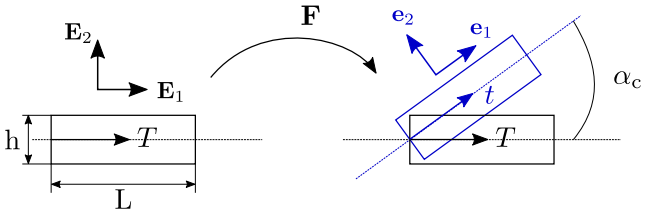

Figure 7.8 Motion of an element (width L and height h) and the corresponding mid-line. $\mathbf{T}$ and $\mathbf{t}$ symbolise the direction of the mid-line in initial and current configurations, respectively, and α_c stands for the angle between the aforementioned vectors. $\{\mathbf{E}_1, \mathbf{E}_2\}$ and $\{\mathbf{e}_1, \mathbf{e}_2\}$ indicates the orthogonal system in current and initial conditions.

The procedure given below shows the criterion to select the components of the vector $\mathbf{T}$ shown in Fig. 7.8, with respect to the global coordinate system $\{\mathbf{E}_1, \mathbf{E}_2\}$. Let $\mathbf{T}$ be a two-dimensional unit vector and $\mathbf{t}$ the current vector after performing the deformation gradient $\mathbf{F}$ as follows

$$\mathbf{t} = \mathbf{F}\mathbf{T} \Rightarrow \begin{bmatrix} t_1 \\ t_2 \end{bmatrix} = \begin{bmatrix} F_{11} & F_{12} \\ F_{21} & F_{22} \end{bmatrix} \begin{bmatrix} T_1 \\ T_2 \end{bmatrix}. \tag{7.14}$$

In order to compute the components of the rotation tensor $\mathbf{R}$ (see Eq. 7.12), $\cos(\alpha_c)$ and $\sin(\alpha_c)$ can be derived from scalar and vectorial products of $\mathbf{t}$ and $\mathbf{T}$, as

$$\cos(\alpha_c) = \frac{\mathbf{T} \cdot \mathbf{t}}{|T||t|} = \frac{F_{11}T_1^2 + (F_{12} + F_{21})T_1T_2 + F_{22}T_2^2}{\sqrt{(F_{11}T_1 + F_{12}T_2)^2 + (F_{21}T_1 + F_{22}T_2)^2}}, \tag{7.15}$$

$$\sin(\alpha_c) = \frac{\mathbf{T} \times \mathbf{t}}{|T||t|} = \frac{(F_{11}T_1 + F_{12}T_2)T_2 - (F_{21}T_1 + F_{22}T_2)T_1}{\sqrt{(F_{11}T_1 + F_{12}T_2)^2 + (F_{21}T_1 + F_{22}T_2)^2}}, \tag{7.16}$$

where $|T| = 1$.

Considering the polar decomposition Eq. 2.19, the material stretch tensor $\mathbf{U}$ can be expressed in terms of the mid-line direction $\mathbf{T}$ as

$$\mathbf{U} = \mathbf{R}^T\mathbf{F} \Rightarrow \begin{bmatrix} U_{11} & U_{12} \\ U_{21} & U_{22} \end{bmatrix} = \begin{bmatrix} \cos(\alpha_c) & \sin(\alpha_c) \\ -\sin(\alpha_c) & \cos(\alpha_c) \end{bmatrix} \begin{bmatrix} F_{11} & F_{12} \\ F_{21} & F_{22} \end{bmatrix}, \tag{7.17}$$

$$\begin{aligned}
U_{11} &= \frac{1}{|T||t|}[(F_{11}^2+F_{21}^2)T_1^2+(F_{11}F_{22}-F_{21}F_{12})T_2^2 \\
&\qquad +[F_{11}(F_{12}+F_{21})+F_{21}(F_{22}-F_{11})]T_1T_2], \\
U_{22} &= \frac{1}{|T||t|}[(F_{22}F_{11}-F_{12}F_{21})T_1^2+(F_{22}^2+F_{12}^2)T_2^2 \\
&\qquad +[F_{22}(F_{12}+F_{21})-F_{12}(F_{22}-F_{11})]T_1T_2], \\
U_{12} &= \frac{1}{|T||t|}[(F_{12}F_{11}+F_{12}F_{22})T_1^2+[F_{12}(F_{12}+F_{21})+F_{22}(F_{22}-F_{11})]T_1T_2], \\
U_{21} &= \frac{1}{|T||t|}[(F_{21}F_{22}+F_{12}F_{11})T_2^2+[F_{21}(F_{12}+F_{21})-F_{11}(F_{22}-F_{11})]T_1T_2].
\end{aligned} \tag{7.18}$$

Thus, if vector $\mathbf{T}$ is coplanar the axis $\mathbf{X}_1$, i.e, $T_1 = 1$ and $T_2 = 0$, the following material stretch tensor is obtained

$$\begin{aligned}
U_{11} &= \frac{(F_{11}^2+F_{21}^2)T_1^2}{\sqrt{(F_{11}T_1)^2+(F_{21}T_1)^2}}, \\
U_{22} &= \frac{(F_{22}F_{11}-F_{12}F_{21})T_1^2}{\sqrt{(F_{11}T_1)^2+(F_{21}T_1)^2}}, \\
U_{12} &= \frac{(F_{12}F_{11}+F_{12}F_{22})T_1^2}{\sqrt{(F_{11}T_1)^2+(F_{21}T_1)^2}}, \\
U_{21} &= 0.
\end{aligned} \tag{7.19}$$

Consequently, for the sake of simplicity, the rotation of the element mid-line can be computed by performing $U_{21} = 0$, see Eq. (7.17) as

$$-\sin(\alpha_c)F_{11}+\cos(\alpha_c)F_{21} \Rightarrow \tan(\alpha_c) = \frac{F_{21}}{F_{11}}. \tag{7.20}$$

Therefore, with a simple calculation of Eq. (7.20) and the polar decomposition in Eq. (2.19) the rotation and the material stretch tensors are computed. Moreover, the tensor $\mathbf{U}$ is characterised by a triangular matrix in which the term U_{21} is equal to zero. Accordingly, interface displacements δ_s^l, δ_n and δ_s^s can be computed through this particular stretch tensor and the material vectors $\mathbf{N}_h$ and $\mathbf{N}_L$, which represent the initial dimension of the quadratic element.

In summary, the procedure to obtain the displacements needed for a TSL from deformation gradient tensor $\mathbf{F}$ under finite deformation hypothesis is the following:

1. Determine the rotation of the element midline through the rotation tensor $\mathbf{R}$ by means of Eq. (7.12), where $\tan(\alpha_c) = \frac{F_{21}}{F_{11}}$.
2. Calculate the material stretch tensor via polar decomposition $\mathbf{U} = \mathbf{R}^T\mathbf{F}$.
3. Compute in-plane δ_s^l, normal δ_n and tangential shear δ_s^s displacements by using the material stretch tensor and $\mathbf{N}_h = \begin{bmatrix} 0 \\ h \end{bmatrix}$ and $\mathbf{N}_L = \begin{bmatrix} L \\ 0 \end{bmatrix}$ vectors as follows

$$\begin{bmatrix} \delta_s^s \\ \delta_n \end{bmatrix} = \begin{bmatrix} U_{11}-1 & U_{21} \\ 0 & U_{22}-1 \end{bmatrix} \begin{bmatrix} 0 \\ h \end{bmatrix}, \tag{7.21}$$

$$\begin{bmatrix} \delta_s^l \\ 0 \end{bmatrix} = \begin{bmatrix} U_{11}-1 & U_{21} \\ 0 & U_{22}-1 \end{bmatrix} \begin{bmatrix} L \\ 0 \end{bmatrix}. \tag{7.22}$$

The elemental motions in an interface model are depicted in Fig. 7.9 along with the coordinate system in lagrangian $\{N_1^{TSL}, N_2^{TSL}\}$ and eulerian $\{n_1^{TSL}, n_2^{TSL}\}$ configurations. It is worth mentioning the absence of rotation under simple shear deformation, where material and spatial basis remain unaltered. This fact contrasts with the conventional elements, where a rotation between initial and current basis can be observed (see Fig. 2.5).

In addition to the previous considerations, the constitutive equations that relate tractions and displacements in a Traction Separation Law should be consistently evaluated. Thus, in contrast with stresses directly derived from strains magnitudes, where a clear distinction can be made between original and current configuration, the displacements in a TSL are not referred to any standpoint, that is, displacements are the same in the material or the spatial frame. Hence, in the present work it is considered that the Cauchy stress tensor in the local basis is defined in Voigt notation by

$$\boldsymbol{\sigma}^{local} = \mathbb{C}\boldsymbol{\delta}, \tag{7.23}$$

where $\boldsymbol{\delta}$ symbolised the pseudo-vector including in-plane, normal and shear displacements and $\mathbb{C}$ is the langrangian elasticity tensor as

$$\begin{bmatrix} \sigma_s^l \\ \sigma_n \\ \sigma_s^s \end{bmatrix} = \begin{bmatrix} k_l & k_{ln} & k_{ls} \\ k_{nl} & k_n & k_{ns} \\ k_{sl} & k_{sn} & k_s \end{bmatrix} \begin{bmatrix} \delta_s^l \\ \delta_n \\ \delta_s^s \end{bmatrix} \tag{7.24}$$

Equations (7.23) and (7.24) associate displacements with stresses in absence of rigid body rotations or in a local frame in the presence of rotations. To perform a proper analysis within the FEM framework, where all the magnitudes are referred to the global

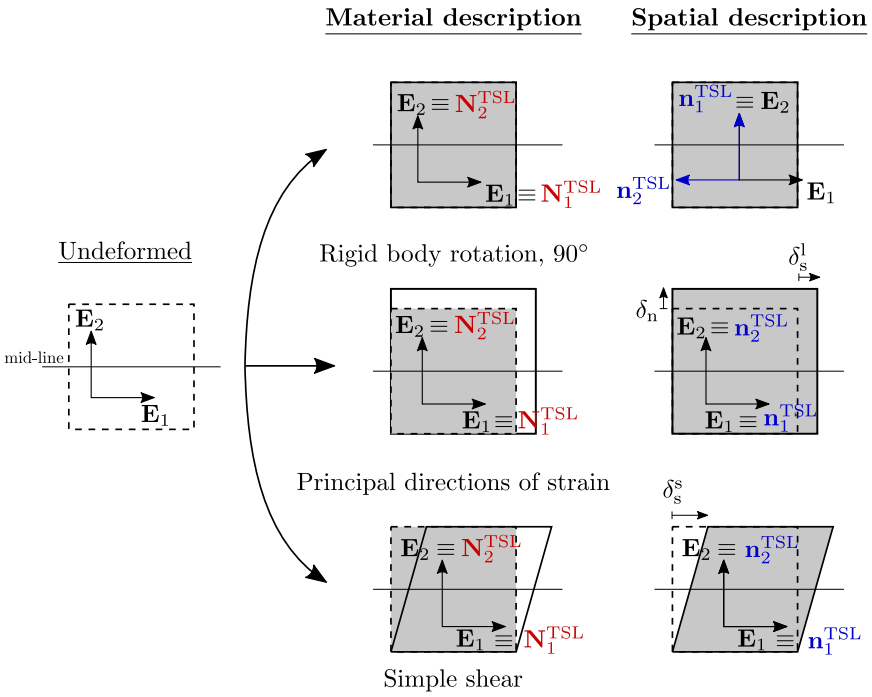

Figure 7.9 Material and spatial coordinate systems under rigid body rotations, principal strain and simple shear.

coordinate axis $\{\mathbf{E}_1,\mathbf{E}_2\}$, an extra rotation is required in order to express stresses and constitutive equations in the correct coordinate basis, as follows

$$\tilde{\mathbb{C}}^{\text{Global}} = \sum_{\substack{i,j,k,l=1\\I,J,K,L=1}}^{3} R_{iI}R_{jJ}R_{kK}R_{lL}\mathbb{C}^{\text{local}}_{IJKL}, \tag{7.25}$$

$$\boldsymbol{\sigma}^{\text{Global}} = \mathbf{R}\boldsymbol{\sigma}^{\text{local}}\mathbf{R}^{\text{T}}. \tag{7.26}$$

7.1.1.3 Algorithms for stress evaluation in conventional and interface elements

In this Section a comparison of the algorithms that can be used to determine stresses in standard continuum elements, characterised by symmetrical deformations (Section 2.2), and the novel interface elements developed in Section 7.1.1.2, characterised by the rotation of the element midline, is outlined. Fig. 7.10 depicts a brief summary of the main differences between the two methods here developed.

The mentioned flowchart highlights the simplicity of the procedure to characterise an interface performance by means of continuum mechanics variables. Furthermore, this approach estimates more accurately the deformation state within the interface in contrast with other conventional methods [216, 222] such as the calculation of the relative displacement between the nodes belonging to the top and bottom surfaces.

Standard continuum element

1. **Input arguments:**
   total strain at the beginning of the increment $\boldsymbol{\varepsilon}_t$, strain increment $\Delta\boldsymbol{\varepsilon}$, deformation gradient at the end of the increment $\mathbf{F}$, rotation matrix $\mathbf{R}$.
2. **Calculate eigenvectors and eigenvalues:**
   $\mathbf{C} = \mathbf{F}^{\mathrm{T}}\mathbf{F} \Rightarrow [\mathbf{N}_1, \mathbf{N}_2, \lambda_1, \lambda_2] = \mathrm{eig}(\mathbf{C})$
3. **Obtain material stretch tensor:**
   $\mathbf{U} = \sum_{\alpha=1}^{3} \lambda_\alpha \mathbf{N}_\alpha \otimes \mathbf{N}_\alpha$
4. **Obtain rotation tensor:**
   $\mathbf{R} = \mathbf{F}\mathbf{U}^{-1}$
5. **Obtain strain tensor:**
   $\mathbf{E}^{(2)} = \sum_{\alpha=1}^{3} \frac{1}{2}\left(\lambda_\alpha^2 - 1\right) \mathbf{N}_\alpha \otimes \mathbf{N}_\alpha$
   $\mathbf{e}^{(-2)} = \sum_{\alpha=1}^{3} \frac{1}{2}\left(1 - \lambda_\alpha^{-2}\right) \mathbf{n}_\alpha \otimes \mathbf{n}_\alpha$
   $\mathbf{E}^{(1)} = \sum_{\alpha=1}^{3} \left(\lambda_\alpha - 1\right) \mathbf{N}_\alpha \otimes \mathbf{N}_\alpha$
   $\mathbf{e}^{(-1)} = \sum_{\alpha=1}^{3} \left(1 - \lambda_\alpha^{-1}\right) \mathbf{n}_\alpha \otimes \mathbf{n}_\alpha$
   $\mathbf{E}^{(0)} = \sum_{\alpha=1}^{3} \ln\left(\lambda_\alpha\right) \mathbf{N}_\alpha \otimes \mathbf{N}_\alpha = \ln\mathbf{U}$
   $\mathbf{e}^{(0)} = \sum_{\alpha=1}^{3} \ln\left(\lambda_\alpha\right) \mathbf{n}_\alpha \otimes \mathbf{n}_\alpha = \ln\mathbf{V}$
6. **Determine stress tensor:**
   $\boldsymbol{S} = \mathbb{C} : \mathbf{E}$
   $\boldsymbol{\sigma} = \tilde{\mathbb{C}} : \mathbf{e}$
7. **Output arguments:**
   $\tilde{\mathbb{C}}$, $\boldsymbol{\sigma}$

Interface element

1. **Input arguments:**
   total strain at the beginning of the increment $\boldsymbol{\varepsilon}_t$, strain increment $\Delta\boldsymbol{\varepsilon}$, deformation gradient at the end of the increment $\mathbf{F}$, element height h, element length L.
2. **Calculate rotation tensor:**
   $\tan\alpha = \dfrac{F_{21}}{F_{11}}$
   $\mathbf{R} = \begin{bmatrix} \cos(\alpha) & -\sin(\alpha) \\ \sin(\alpha) & \cos(\alpha) \end{bmatrix}$
3. **Obtain material stretch tensor:**
   $\mathbf{U} = \mathbf{F}\mathbf{R}^{\mathrm{T}}$
4. **Obtain TSL displacement :**
   $\begin{bmatrix} \delta_{\mathrm{s}}^{\mathrm{s}} \\ \delta_{\mathrm{n}} \end{bmatrix} = (\mathbf{U} - \mathbf{I}) \begin{bmatrix} 0 \\ \mathrm{h} \end{bmatrix}, \begin{bmatrix} \delta_{\mathrm{s}}^{\mathrm{l}} \\ 0 \end{bmatrix} = (\mathbf{U} - \mathbf{I}) \begin{bmatrix} \mathrm{L} \\ 0 \end{bmatrix}, \boldsymbol{\delta} = \begin{bmatrix} \delta_{\mathrm{s}}^{\mathrm{l}} \\ \delta_{\mathrm{n}} \\ \delta_{\mathrm{s}}^{\mathrm{s}} \end{bmatrix}$
5. **Determine stress tensor:**
   $\boldsymbol{\sigma} = \mathbb{C} : \boldsymbol{\delta}$
   $\mathbb{C} = \begin{bmatrix} k_{\mathrm{l}} & k_{\mathrm{ln}} & k_{\mathrm{ls}} \\ k_{\mathrm{nl}} & k_{\mathrm{n}} & k_{\mathrm{ns}} \\ k_{\mathrm{sl}} & k_{\mathrm{sn}} & k_{\mathrm{s}} \end{bmatrix}$
6. **Rotation of tangent matrix $\mathbb{C}$ and $\boldsymbol{\sigma}$ to global Cartesian basis:**
   $\tilde{\mathbb{C}}^{\mathrm{Global}} = \sum_{\substack{i,j,k,l=1 \\ I,J,K,L=1}}^{3} R_{iI} R_{jJ} R_{kK} R_{lL} \mathbb{C}_{IJKL}^{\mathrm{local}}$
   $\boldsymbol{\sigma}^{\mathrm{Global}} = \mathbf{R}\boldsymbol{\sigma}^{\mathrm{local}}\mathbf{R}^{\mathrm{T}}$
7. **Output arguments:**
   $\boldsymbol{\sigma}^{\mathrm{Global}}$, $\tilde{\mathbb{C}}^{\mathrm{Global}}$

Figure 7.10 Simplified algorithms for stress-strain evaluation in a conventional element and stress-displacement estimation for a Traction Separation Law in interface elements under finite deformation assumptions.

7.1.2 Validation of the interface model under large displacement scenarios: benchmark problems in one-element tests

This Section presents a set of benchmark cases in order to verify the current methodology for the displacement evaluation in an interface element. Some deformed configurations within a single element with prescribed displacements are shown. These examples include the basic strain state that an interface finite element could experiment, that is, normal, shear, in-plane deformations and rigid body motions.

For the sake of clarity, the deformations here selected develop an uniform strain state, therefore the deformation gradient $\mathbf{F}$ remains constant inside the element. Fig. 7.11 illustrates the different cases in which normal, shear, in-plane displacements and rigid body rotations are considered separately and coupled:

a) Superimposed rigid body rotation of 90 degrees,

b) Normal displacement,

c) Shear displacement,

d) In-plane displacement,

e) Normal, shear, in-plane displacement and rigid body rotation.

Furthermore, deformation gradient $\mathbf{F}$, mid-line rotation α_c, tensor $(\mathbf{U}-\mathbf{I})$ and relative displacements δ_s^l, δ_n and δ_s^s in the configurations corresponding to Fig. 7.11 are included in Table 7.1.

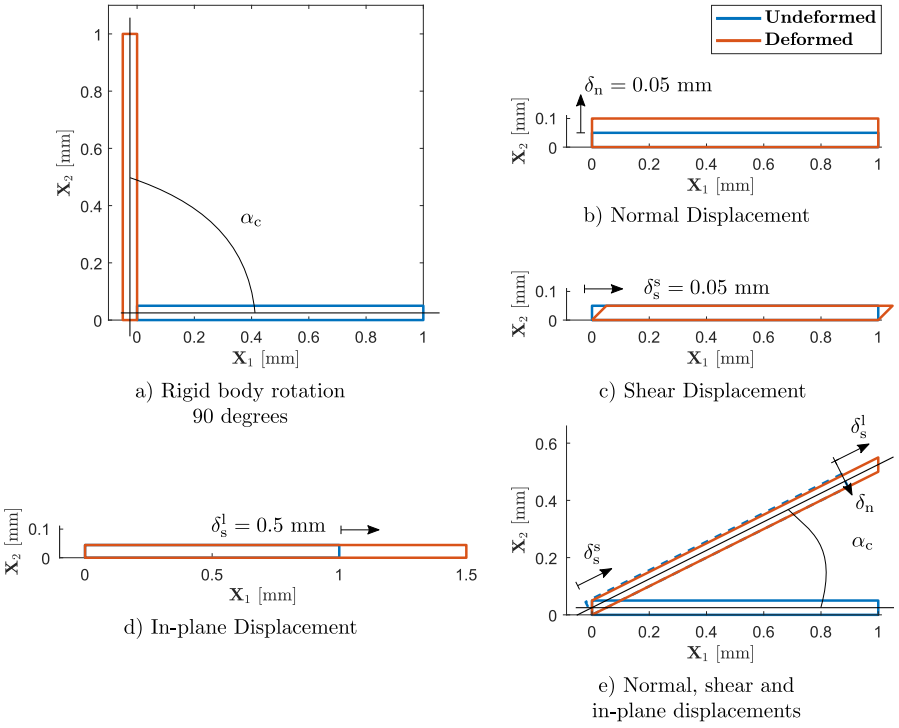

a) Rigid body rotation 90 degrees

b) Normal Displacement

c) Shear Displacement

d) In-plane Displacement

e) Normal, shear and in-plane displacements

Figure 7.11 Validation of the cohesive displacements: a) Rigid body rotation - 90 degrees, b) normal displacement, c) shear displacement, d) in-plane displacement, e) normal, shear and in-plane displacement and rigid body rotation.

The formulation proposed is able to deal with superimposed rigid body rotation α_c (Fig. 7.11.a) due to the fact that the displacements obtained for the TSL evaluation are null. Otherwise, isolated normal δ_n, shear δ_s^s and in-plane δ_s^l displacements (Fig. 7.11.b, Fig. 7.11.c and Fig. 7.11.d, respectively) are captured accurately. Finally, the combination of rigid body motion together with normal, shear and in-plane displacements were accomplished by clamping the left side of the element and prescribing a vertical displacement at the right side of the element in Fig. 7.11.e. In this case, the conventional cohesive formulation neglects the in-plane displacement δ_s^l whereas the novel continuum-like interface methodology enables to calculate such gap. This aspect

Table 7.1 Deformation gradient $\mathbf{F}$, mid-line rotation α_c, tensor $\mathbf{U}-\mathbf{I}$ and interface displacements δ_n, δ_s^s and δ_s^l in the configurations corresponding to Fig. 7.11. Letter I symbolizes the interface-like approach presented in Section 7.1.1.1 and letter C indicates the solid or continuum-like modelling developed in Section 7.1.1.2.

(Continuum-like approach). L = 1 mm and h = 0.05 mm

Case	$\mathbf{F}$ [-]		α_c [°]		$\mathbf{U}-\mathbf{I}$ [-]		δ_n [mm]		δ_s^s [mm]		δ_s^l [mm]	
	I	C	I	C	I	C	I	C	I	C	I	C
a	-	$\begin{bmatrix} 0 & -1 \\ 1 & 0 \end{bmatrix}$	-	90	-	$\begin{bmatrix} 0 & 0 \\ 0 & 0 \end{bmatrix}$	0	0	0	0	-	0
b	-	$\begin{bmatrix} 1 & 0 \\ 0 & 2 \end{bmatrix}$	-	0	-	$\begin{bmatrix} 0 & 0 \\ 0 & 1 \end{bmatrix}$	0.05	0.05	0	0	-	0
c	-	$\begin{bmatrix} 1 & 1 \\ 0 & 1 \end{bmatrix}$	-	0	-	$\begin{bmatrix} 0 & 1 \\ 0 & 0 \end{bmatrix}$	0	0	0.05	0.05	-	0
d	-	$\begin{bmatrix} 1.5 & 0 \\ 0 & 1 \end{bmatrix}$	-	0	-	$\begin{bmatrix} 0.5 & 0 \\ 0 & 0 \end{bmatrix}$	0	0	0	0	-	0.5
e	-	$\begin{bmatrix} 1 & 0 \\ 0.5 & 1 \end{bmatrix}$	-	26.56	-	$\begin{bmatrix} 0.11 & 0.45 \\ 0 & -0.11 \end{bmatrix}$	-0.0053	-0.0053	0.0224	0.0224	-	0.1180

may be relevant in scenarios where the length of the interface varies during the loading application.

These simple calculations are explanatory to understand the outputs of the interface algorithm and they demonstrate the reliability and accuracy needed for its application in problems involving decohesion events.

7.1.3 Application of the novel interface model: Horizontal Drum-Peel test

The suitability of the previous formulation is discussed along this Section. In particular, the novel relative displacement calculation is tested in an engineering application regarding the quality of bonded joints. In practice, the critical fracture toughness or critical energy release rate G_c is a fracture property needed in the design process of many structural elements and the development of numerical tools are valuable for the knowledge of the testing procedure. In this way, Cañas et al. [173] developed a new testing configuration alternative to the DCB test to measure G_c in situ. In this procedure the adhesion properties were evaluated applying a rotation to a drum connected to the specimen made of unidirectional Carbon Fiber Reinforced Plastic (CFRP). A sketch of the test can be observed in Fig. 7.12.

In the experimental campaign, two different behaviours can be appreciated during the test: winding and debonding. In the first step the thin laminate is bent because of the drum rotation and then, in the second step, the adhesive layer commences to peel off, generating a crack growth. These two phases can be clearly distinguished in the torque-displacement curves, where the winding stage is characterised for a constant moment lower than that associated with the delamination stage.

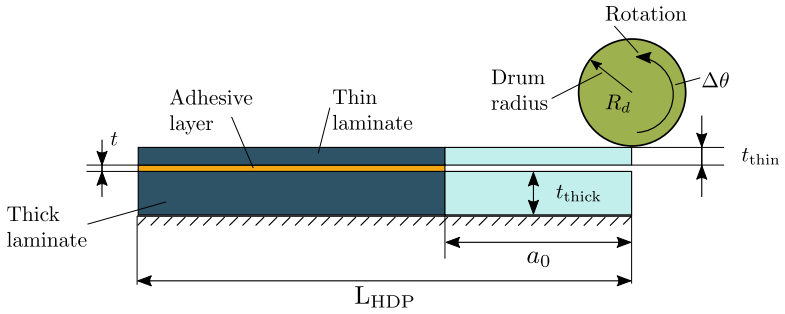

Figure 7.12 Sketch of the Horizontal Drum Peel (HDP) test configuration. t, t_{thin} and t_{thick} represent the adhesive layer, the thin laminate and the thick laminate thickness, respectively. R_d and $\Delta\theta$ correspond to the drum radius and the imposed drum rotation.

To obtain the fracture toughness, the following expression [173] is used

$$G_c = \frac{T_d - T_w}{bR_L}, \tag{7.27}$$

where $R_L = R_d + t_{\text{thin}}/2$, T_w and T_d represent the torque in winding and delamination phases respectively, b is the width of the specimen, R_d stands for the drum radius and t_{thin} is the thin laminate thickness as indicated in Fig. 7.12. See [173] for further details. Thus, only T_d and T_w are needed to be extracted from the Finite Element model to determine the energy release rate of the joint. The rest of the variables involved in the calculation are geometrical parameters (b, t, t_{thin}, R_d). $b = 25$ mm, $R_d = 95$ mm and $t = t_{\text{thin}} = 0.51$ mm for experimental and numerical specimens. The moments T_w and T_d were obtained as the average value between two different peeling lengths in the corresponding phase, winding and delamination respectively.

In this context, the use of Linear Elastic Brittle Interface Model (Section 3.3.3) is justified due to its simplicity and capacity to deal with a large variety of mixity ratios. In this setting, the adhesive layer was modelled employing this technique and, consequently, tractions and relative displacements can be monitored during the simulations.

Based on the work developed in [226], an additional term on the shear stress t_{s} is assumed in the subsequent analysis. In particular, the relative longitudinal shear displacement $\delta_{\text{s}}^{\text{l}}$ contributes to the tangential stress t_{s} and, consequently, to the energy release under fracture Mode II, as follows

$$t_{\text{n}} = \begin{cases} k_{\text{n}}\delta_{\text{n}}, & \text{if } \delta_{\text{n}} \leq \delta_{\text{n}}^{c} \\ 0, & \text{otherwise} \end{cases} \tag{7.28}$$

$$t_{\text{s}} = \begin{cases} k_{\text{s}}\delta_{\text{s}}^{\text{s}} + k_l\delta_{\text{s}}^{\text{l}} = k_{\text{s}}\delta_{\text{s}}, & \text{if } \left|\delta_{\text{s}}^{\text{s}} + \delta_{\text{s}}^{\text{l}}\right| \leq |\delta_{\text{s}}^{\text{s},c}| \\ 0, & \text{otherwise,} \end{cases} \tag{7.29}$$

where t_n and t_s are normal and shear tractions, δ_n, δ_s and are normal and shear relative displacements and k_n and k_s are normal and shear stiffnesses, respectively.

Notwithstanding, as complementary simulations proved (not reported here), the contribution associated with the longitudinal shear component δ_s^l is small in comparison with the tangential shear component δ_s^s. Then, in the Horizontal Drum Peel test the term δ_s^l has a minor role and, in this particular case, the in-plane stiffness is assumed equal to $k_l = 0$.

After interface failure, Eq. (3.50) and (3.51) are assumed to avoid interpenetration between adherents. Note that tractions are limited by a fracture energy criterion: $G \leq G_c$, as shown in Fig. 3.11. Thus, energy release rate stored G and critical fracture toughness G_c are needed to describe the behaviour of the linear-elastic perfectly brittle model. Further details are available in Sect. 3.3.3.

It is also noticeable that, as described above, the use of LEBIM has some advantages, derived from its linear elastic character, over other constitutive laws employed in interface modelling, for example the bilinear or exponential laws within cohesive elements [283]. In particular, the linear elastic behaviour of the LEBIM leads to a constant tangent stiffness tensor $\mathbb{C}$ due to the absence of softening area, characteristic of the mentioned cohesive laws.

Considering the previous aspects, a FE model was carried out using the commercial code ABAQUS®, where the thin and thick laminates ($t_{thin} = 0.51$ mm, $t_{thick} = 15.0$ mm, $L_{HDP} = 297.0$ mm) were discretized with plane strain elements with incompatible modes CPE4I (around 40k elements for both laminates), in order to avoid parasitic shear stresses in the bending behaviour [275]. Additionally, the adhesive layer was meshed employing around 2k CPE4 plane strain elements or COH2D4 cohesive elements, considering a pre-crack length of $a_0 = 60$ mm. It is important to note that the same mesh was employed in the simulations regardless the interface properties, and consequently no mesh effect can be appreciated in the results. Finally, the horizontal drum movement ($R_d = 95$ mm) was simulated as a rigid body rotation making use of analytical surfaces and multi-point constraints (MPC). With respect to the boundary conditions, the bottom surface of the thick laminate was clamped and a rotation in the drum's centre was imposed.

The material properties of the thin and thick laminates and the adhesive layer are presented in Table 7.2 and Table 7.3. In the case of the adhesive, the properties were included by means of UMAT user subroutine. Hence, three interface approaches are compared:

1. Cohesive-Bilinear. Standard bilinear cohesive model (Section 3.3.2).
2. Cohesive-LEBIM. LEBIM using cohesive element formulation (Section 7.1.1.1).
3. Solid-LEBIM. LEBIM formulation for standard continuum elements (Section 7.1.1.2).

It is worth mentioning that in LEBIM cases normal penalty stiffness k_n under compressive strains (k_n^{comp}) must take a high value, so that it was selected equal to that corresponding to the cohesive bilinear case ($k_n^{comp} = 41864 \frac{MPa}{mm}$) as shown in Fig. 7.13. This assumption has been considered because during the winding stage compressions

Table 7.2 Mechanical properties of the thin and thick laminates of the specimen. The CFRP is transversally isotropic.

Material	E_{11} [GPa]	E_{33} [GPa]	G_{12} [GPa]	υ_{12} [-]
Unidirectional	135	10	5	0.3

Table 7.3 Adhesive properties in configurations: Cohesive-Bilinear, Cohesive-LEBIM and Solid-LEBIM.

Configuration	t_n^c [MPa]	t_s^c [MPa]	$k_n \left[\frac{\text{MPa}}{\text{mm}}\right]$	$k_s \left[\frac{\text{MPa}}{\text{mm}}\right]$	$G_{Ic} \left[\frac{\text{J}}{\text{m}^2}\right]$	$G_{IIc} \left[\frac{\text{J}}{\text{m}^2}\right]$
Cohesive-Bilinear	6	40	41864	6976	600	1200
Cohesive-LEBIM	6	40	30	666.6	600	1200
Solid-LEBIM	6	40	30	666.6	600	1200

appear at the initial crack tip and therefore, if the slopes k_n is not stiff enough, the reduction of the element thickness compromises the solution convergence.

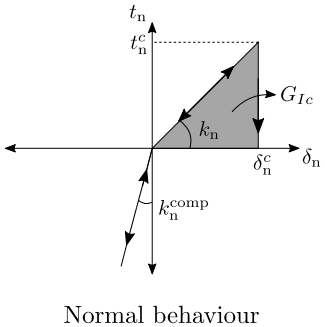

Figure 7.13 Normal penalty stiffness under compressive strains k_n^{comp} in LEBIM.

Fig. 7.14 shows the torque (moment) versus the length travelled by the drum in the three cases aforementioned: Cohesive-Bilinear, Cohesive-LEBIM and Solid-LEBIM, as well as the experimental results (depicted in grey colour).

It can observed that the winding process was captured with excellent agreement in all the configurations because the adhesive failure did not significantly influence the first part of the test, which was ruled by the stiffness of the adherents. Both in transition and delamination phases, a satisfactory agreement was achieved with respect to the experimental curves. Recalling Eq. (7.27), the moment T_w was obtained as the mean value between peeling lengths 10-50 mm in every test whereas T_d was calculated as the mean value between peeling lengths 120-180 mm. The exceptional correspondence between experimental and FE tests regarding the torque evolution can be observed in Table 7.4.

Notice that the fracture toughness only depends on the difference between winding

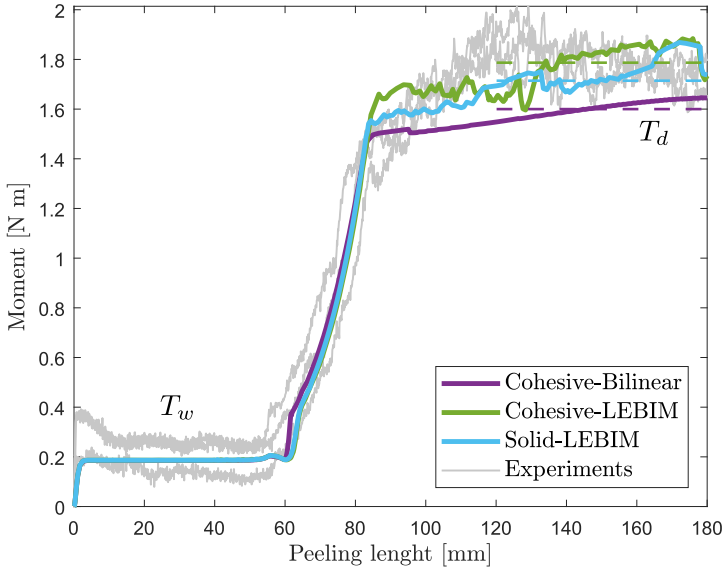

Figure 7.14 Moment vs peeling length for Cohesive-Bilinear (COH2D4 elements), Cohesive-LEBIM (COH2D4 elements) and Solid-LEBIM (CPE4 elements).

Table 7.4 T_d and T_w results in experimental and virtual tests.

Configuration	Exp. 1	Exp. 2	Exp. 3	Cohesive Bilinear	Cohesive-LEBIM	Solid-LEBIM
T_d [N · m]	1.73	1.75	1.84	1.61	1.78	1.73
T_w [N · m]	0.14	0.25	0.26	0.18	0.18	0.18

and delamination moments, so the characteristic decohesion energy was in accordance too, see Table 7.5.

Table 7.5 G_c results in experimental and virtual tests. $G_c|^{\text{Exp}}_{\text{mean}} = 652.5$ [J/m^2] represents the mean critical energy release rate of the experimental tests.

Configuration	Exp. 1	Exp. 2	Exp. 3	Cohesive Bilinear	Cohesive-LEBIM	Solid-LEBIM
G_c [J/m^2]	667.1	627.2	663.3	597.3	668.3	650.8
$G_c/G_c\|^{\text{Exp}}_{\text{mean}}$ [–]	-	-	-	0.89	1.02	0.99

It is important to note that the LEBIM curves show irregularities during the crack growth, being characteristic of the brittle materials. In contrast, in the bilinear curve,

the softening part of the cohesive law tends such irregularities to be relaxed. LEBIM curves, in addition to describe more adequately the fracture progression, allows quicker simulations to be performed. In fact, around 80% of the increments were needed in the Cohesive-LEBIM case and 90% in the Solid-LEBIM case in comparison with the Cohesive-Bilinear simulation. Moreover LEBIM interfaces, both cohesive and solid formulations, provide more accurate predictions with respect to experimental tests (around 1-2% of error) than those associated with bilinear laws (around 10% of difference).

7.1.4 Concluding remarks

This Section outlines the procedure to determine the displacement jumps needed in an interface governed by a Traction Separation Law under finite displacement and rotation assumptions, i.e. transverse normal δ_{n}, tangential shear $\delta_{\mathrm{s}}^{\mathrm{s}}$ and longitudinal shear or in-plane $\delta_{\mathrm{s}}^{\mathrm{l}}$ gaps. The kinematics of this interface modelling has been addressed through the exploitation of two different element methodologies in the software ABAQUS®: (i) 2D cohesive elements (COH2D4) and (ii) 2D regular solid elements (CPE4). Both procedures enable the calculation of the displacements referred to the element midline, which are employed to obtain the traction along the interface.

The effectiveness to model decohesion events of this novel technique were validated with the FE simulation of a Horizontal Drum Peel test and its corresponding experimental-numerical correlation. In such experiment the brittle adhesive behaviour were characterised by a Linear Elastic Brittle Interface Model (LEBIM). In fact, three different approaches for the adhesive performance were reproduced for comparison purposes: (i) the built-in cohesive bilinear law using COH2D4 elements, (ii) user material LEBIM using COH2D4 elements and (iii) user material LEBIM using CPE4 elements.

7.2 Numerical study of mixed-mode interface cracking in hierarchical patterned adhesive joints using a novel geometrically nonlinear Linear Elastic Interface Model

In the present Section, the formulation developed in Section 7.1.1.2 together with the linear elastic-brittle constitutive behaviour governed by Equations (7.28)-(7.29) were employed to characterise the adhesion performance for different test configurations. Additionally, a control algorithm to overcome convergence issues due to the unstable crack propagation and snap-back behaviour that appears in the FE simulations is presented. Within this context, the principal objective of this Section is the comprehensive validation of the geometrically nonlinear LEBIM for mixed-mode loading conditions and for its usage in structured interfaces as in [255, 273].

The organization of the Section is as follows. Section 7.2.1 outlines an overview of the control algorithm. The validation of the current interface model through its assessment for Double Cantilever Beam (DCB), Mixed Mode Bending (MMB) and End Notch Flexure (ENF) tests is detailed in Section 7.2.2, whereas its application to structured interfaces and hierarchical structured interfaces is presented in Section

7.2.3 and Section 7.2.4, respectively. Finally, the concluding remarks of this topic are summarized in Section 7.2.5.

7.2.1 Snap-back control algorithm

From the numerical point of view, in simulations involving damage progression, the nonlinear effects play an important role in the analysis convergence in terms of achieving equilibrium solutions. Usually, in the majority of tests or applications, the boundary conditions are conceived with the aim of either reproducing the experimental gripping conditions in the tests or reflecting the loading conditions of the theoretical analysis. These external solicitations are generally imposed by monotonically increasing/decreasing loads or displacements in specific positions of the specimen with the purpose of obtaining a particular stress, strain or displacement field. However, due to the onset of failure processes and fracture propagation, the linearity of the solution is compromised and the redistribution of the stress field may lead to simultaneous reduction in load and displacement in the external solicitations or, in other words, featuring snap-back behaviours. This fact jeopardizes the convergence of the simulation employing load or displacement controlled boundary conditions. Although there are methods that consider changes in the direction of the load-displacement curves, for instance Riks method [284], other techniques have been developed in order to overcome this kind of instabilities and therefore solving these issues in an efficient manner.

In this setting, Tvergaard [285] proposed an alternative to capture fluctuations in the load-displacement curves by finding a variable that increases monotonically during the simulation. In this way, the control is applied in such variable and the loads and displacements at the boundary are computed as output variables of the Finite Element analysis. This approach allows the Newton–Raphson algorithm to be used without any further modifications, and has been tested in simulations including sphere fracture in composites made up of random distribution of elastic spheres within an elasto-plastic matrix [286] or the investigation of gradient-enhanced dislocation hardening on the mechanics of notch-induced failure [287]. In this sense, the control is applied: (i) to the sum of the opening displacements of some nodes ahead of the crack tip, in presence of a unique interface, or (ii) the relative opening within the interfaces along the loading direction, if more than one interface are involved. In this study, we are focused on the former approach, which is concisely described in the following paragraphs.

Let N_1 and N_2 be the nodes belonging to upper and bottom surfaces of the interface respectively, and $N_{\mathbf{C}}$ a dummy node that can be placed at any point, as depicted in Fig. 7.15. Likewise, $N_{\mathbf{C}}$ will be the control node and N_L the node in which the load or displacement conditions at the boundary are applied. The relative displacement at the interface, corresponding to the global basis $\{X_1, X_2\}$, can be related to the control node $N_{\mathbf{C}}$ by making use of the `AUXILIARY ELEMENT`s as follows

$$\begin{bmatrix} 0 & 0 & 0 \\ 0 & 0 & 0 \\ 1 & -1 & 0 \end{bmatrix} \begin{bmatrix} u_{X_1}^{N_1} \\ u_{X_1}^{N_2} \\ u_{X_1}^{N_{\mathbf{C}}} \end{bmatrix} = \begin{bmatrix} f_{X_1}^{N_1} \\ f_{X_1}^{N_2} \\ f_{X_1}^{N_{\mathbf{C}}} \end{bmatrix}, \tag{7.30}$$

$$\begin{bmatrix} 0 & 0 & 0 \\ 0 & 0 & 0 \\ 1 & -1 & 0 \end{bmatrix} \begin{bmatrix} u_{X_2}^{N_1} \\ u_{X_2}^{N_2} \\ u_{X_2}^{N_C} \end{bmatrix} = \begin{bmatrix} f_{X_2}^{N_1} \\ f_{X_2}^{N_2} \\ f_{X_2}^{N_C} \end{bmatrix}, \tag{7.31}$$

where u_{X_1} and u_{X_2} are nodal displacement in global directions and f_{X_1} and f_{X_2} are the corresponding nodal forces. In the FE analysis the relative displacement at the interface, $\left(u_{X_1}^{N_1} - u_{X_1}^{N_2}\right)$ or $\left(u_{X_2}^{N_1} - u_{X_2}^{N_2}\right)$, is set by prescribing the nodal force of the control node $f_{X_1}^{N_C}$ or $f_{X_2}^{N_C}$. Next, Eq. (7.30) is employed to prescribed the opening displacement along X_1 global direction, whereas Eq. (7.31) is used to set nodal relative displacements along X_2 global direction. A flowchart of the current procedure is given in Fig. 7.15 for the sake of clarity.

Finally, the nodal force at the boundary $f_{X_1}^{N_L}$ or $f_{X_2}^{N_L}$ is equal to the displacement of the control node $u_{X_1}^{N_C}$ or $u_{X_2}^{N_C}$. This relation can be defined through the definition of a new `AUXILIARY ELEMENT` according to

$$\begin{bmatrix} 0 & 1 \\ 0 & 0 \end{bmatrix} \begin{bmatrix} u_{X_2}^{N_L} \\ u_{X_2}^{N_C} \end{bmatrix} = \begin{bmatrix} f_{X_2}^{N_L} \\ f_{X_2}^{N_C} \end{bmatrix}, \tag{7.32}$$

$$\begin{bmatrix} 0 & 0 & 0 & 0 \\ 0 & 0 & 1 & 0 \\ 0 & 0 & 0 & 0 \\ 0 & 0 & 0 & 0 \end{bmatrix} \begin{bmatrix} u_{X_1}^{N_L} \\ u_{X_2}^{N_L} \\ u_{X_1}^{N_C} \\ u_{X_2}^{N_C} \end{bmatrix} = \begin{bmatrix} f_{X_1}^{N_L} \\ f_{X_2}^{N_L} \\ f_{X_1}^{N_C} \\ f_{X_2}^{N_C} \end{bmatrix}, \tag{7.33}$$

where Eq. (7.32) relates the reaction of the normal opening displacement at the interface $u_{X_2}^{N_C}$ to the nodal force in X_2 direction $f_{X_2}^{N_L}$ and Eq. (7.33) associates the reaction of the shear displacement at the interface $u_{X_1}^{N_C}$ to the nodal force in X_2 direction $f_{X_2}^{N_L}$.

Note that in situations where more than one pair of nodes are implied in the process, that is, the `AUXILIARY ELEMENT`s (Eqs. 7.30-7.31) are applied to additional pair of nodes, the nodal force of the control node f^{N_C} represents the sum of the opening displacement of each paired nodes. This scheme may be useful to track the global tendency at the interface instead of focusing in a particular pair of nodes.

These equations are added to the global stiffness matrix of the system in order to compute the unknowns variables, in this case the displacement in the control node u^{N_C} and the displacement of the boundary node u^{N_L}. It is worth to emphasize that u^{N_C}, through the `AUXILIARY ELEMENT` materialised in Eqs. (7.30)-(7.31), corresponds to the reaction force of the boundary node: $u^{N_C} = f^{N_L}$. Therefore, both displacement and force at the boundary, u^{N_L} and f^{N_L} respectively, are calculated as any degree of freedom of the system and they may present non-monotonic behaviour.

As a summary, the control algorithm is outlined in the following scheme:

1. Define a control node N_C anywhere.

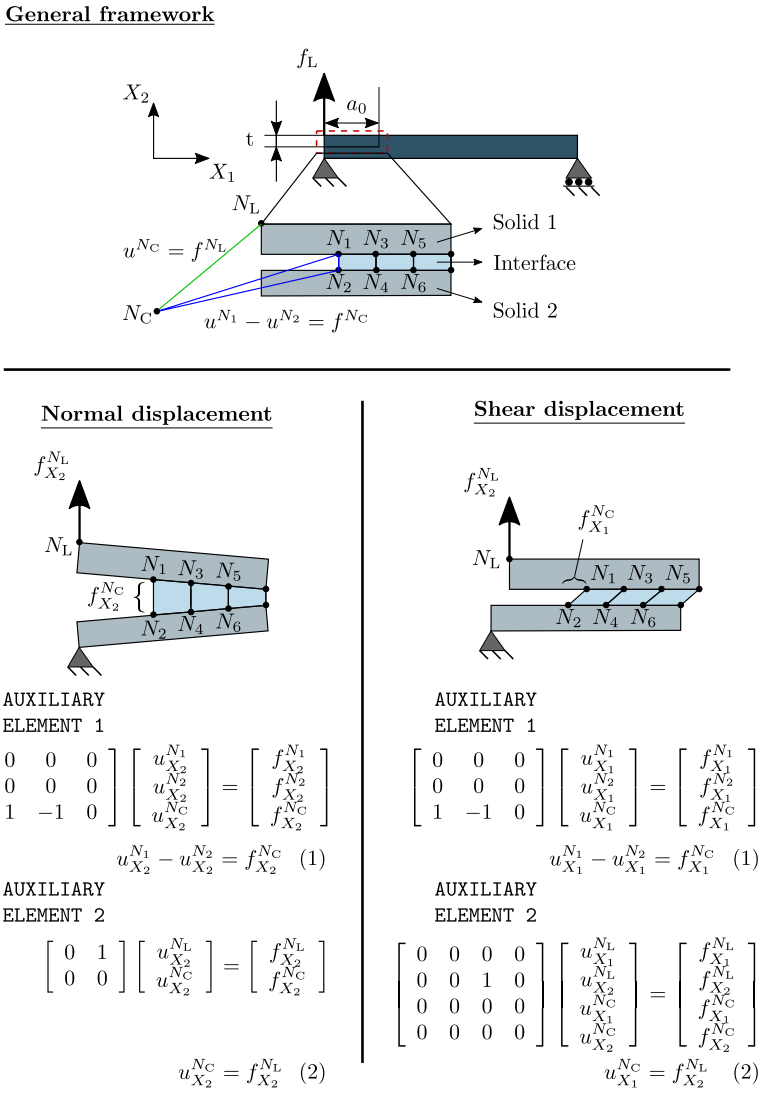

Figure 7.15 Scheme of the control algorithm: N_1-N_6 are interface nodes, $N_\mathbf{C}$ is the control node and N_L is the node where the boundary conditions are established. u and f stand for nodal displacements and nodal forces at the corresponding nodes.

2. Prescribe the opening displacement along the interface by means of the control node f^{N_L} and the `AUXILIARY ELEMENT 1`:
$u^{N_1} - u^{N_2} = f^{N_C}$

3. Relate the displacement of the control node to the nodal force at the boundary through the `AUXILIARY ELEMENT 2`:

$u^{N_C} = f^{N_L}$

4. Include these equations or constraints to the global stiffness matrix.
5. Obtain u^{N_L} and f^{N_L} as part of the FE solution.

7.2.2 Application of the geometrically nonlinear LEBIM to general mixed mode fracture tests DCB, MMB and ENF tests

This Section outlines the validation of the proposed geometrically nonlinear LEBIM for its application to general mixed-mode fracture tests. In particular, we specialize this procedure to obtain numerical-experimental correlations of well established tests: (i) Double Cantilever Beam (DCB) test for fracture Mode I conditions, (ii) Mixed Mode Bending test (MMB) for mixed-mode fracture conditions and End Notch Flexure (ENF) test for fracture Mode II characterization. With the purpose of testing the accuracy of the interface approach presented in Section 7.1.1.2, predictions of such tests, involving delamination events under different loading conditions, are compared with the experimental data extracted from [288]. Note also that other authors [218,289] have previously assessed their corresponding interface decohesion elements and damage propagation with respect to these experiments. It is worth mentioning that, in the following simulations, the in-plane stiffness (k_l in Eq. (7.24)) of the current LEBIM is set equal to zero, neglecting the in-plane deformation effects, with the aim of comparing the performance of the present formulation respect to alternative cohesive elements [216,218,289].

Simulations are carried out using specimens with the following geometric dimensions: 50 mm in length of half-span L_{beam}, 25 mm in width and 1.55 mm half-thickness t. This set up is defined according to the test configuration specified in Fig. 7.16, and it is usually denominated as MMB method that allows different mixed-mode fracture ratios using the same specimen configuration to be assessed. This can be achieved via the definition of a parametric length c, whose value can be accordingly set, ranging from pure fracture Mode I to pure fracture Mode II and covering a wide mixity of ratios. Based on this configuration and recalling standard Bernoulli beam theory, the ratio between the middle and end forces, denoted by P_{M} and P_{E}, respectively, can be related to specific mixed-mode ratios G_{II}/G_T (see [289] for further details).

Additionally to the previous characteristics, an initial crack length a_0 is defined between 30 mm and 40 mm in order to achieve a stable crack propagation, see Fig. 7.16. The corresponding pre-crack lengths a_0, the length of the lever c and the relation between the end and the middle load $P_{\text{M}}/P_{\text{E}}$ for each of the configurations analysed herein are detailed in Table 7.6, emphasizing the mixed-mode fracture ratios. The material properties of the laminates correspond to the AS4/PEEK composite and they are reported in Table 7.7. The specimens are composed of 24 unidirectional plies, employing a Kapton film to induce the initial delamination.

Regarding the characteristics of the numerical models, the adherents are modelled as linear elastic materials, whereas the proposed LEBIM is employed to describe the interface behaviour between the two arms. The baseline numerical model is generated using approximately 5800 2D plane strain elements for the discretization of the entire model, where around 300 of those elements correspond to the interface elements

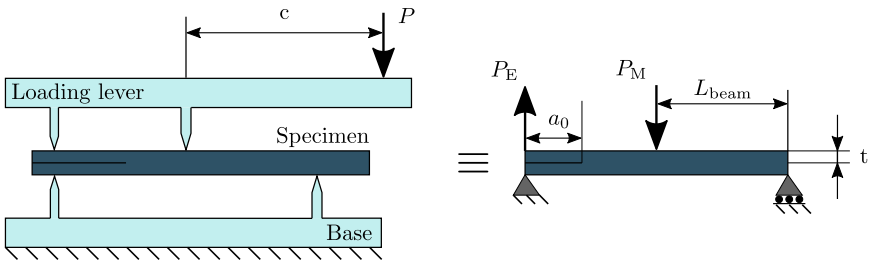

Figure 7.16 Mixed Mode Bending (MMB) test: boundary conditions and specimen dimension. P_E and P_M represent the loads applied at the left end and the middle of the specimen. L_{beam} and t stand for the semi-length and one-arm thick of the coupon, whereas a_0 indicates the length of the initial delamination.

Table 7.6 Initial crack length a_0 length of the lever c and middle-end load P_M/P_E, according to Fig. 7.16, for different mixed-mode ratios G_{II}/G_T.

G_{II}/G_T	0.0 (DCB)	0.2	0.5	0.8	1.0 (ENF)
a_0 [mm]	32.9	33.7	34.1	31.4	39.3
c [mm]	-	97.4	42.2	27.6	-
P_M/P_E [-]	0.0	1.46	2.14	2.79	∞

Table 7.7 AS4/PEEK properties.

E_{11}	E_{22}=E_{33}	G_{12}=G_{13}	G_{23}	ν_{12}=ν_{13}	ν_{23}
129 GPa	10.1 GPa	5.5 GPa	3.7 GPa	0.25	0.45

equipped with LEBIM. The undeformed mesh size at the region of interest is around 0.25 mm in width and 0.05 in height. Table 7.8 shows the input properties for the interface elements [289].

Table 7.8 Linear Elastic Brittle Interface Model properties [289].

t_n^c [MPa]	t_s^c [MPa]	G_{Ic} [kJ/m^2]	G_{IIc} [kJ/m^2]	η [-]
80	100	0.969	1.719	2.284

The control algorithm described in Section 7.2.1 is also applied in the current simulations in order to preclude numerical difficulties for the achievement of converged equilibrium solutions. Such procedure is correspondingly adapted to each configuration (DCB, MMB and ENF) according to the mixed mode of the tests and the relative displacement at the crack tip. Additionally, a new `AUXILIARY ELEMENT` is defined so as to establish the relationship between the forces at the end and at the middle of the

specimen, $f_{X_2}^{N_\mathrm{E}}$ and $f_{X_2}^{N_\mathrm{M}}$ respectively. Note the distinction between beam-theory values P_M and P_E and the finite element values $f_{X_2}^{N_\mathrm{E}}$ and $f_{X_2}^{N_\mathrm{M}}$ to denote the nodal boundary forces. In this way, the relation $P_\mathrm{M}/P_\mathrm{E}$ is constant during the test according to the length of the lever c [289], as shown in Table 7.6, and such relation is imposed in the FE simulation. Fig. 7.17 comprehensively details the procedure to apply normal or shear separation at the crack tip and the way through which the link between the nodal force at the boundary $f_{X_2}^{N_\mathrm{E}}$ and $f_{X_2}^{N_\mathrm{M}}$ with respect to the control node is constructed in order to obtain the desired relation.

The normal displacement depicted in Fig. 7.17 is applied in the DCB and MMB tests. In this regard, with respect to the MMB simulations, we set the ratios $G_{II}/G_T = 0.2$ and $G_{II}/G_T = 0.5$ using this normal displacement. Moreover, in additional computations, the shear displacement in Fig. 7.17 is employed for the simulation of MMB configurations with $G_{II}/G_T = 0.8$ and for the ENF test.

Fig. 7.18 shows the correlation between experimental and numerical results concerning load-displacement curves. In this graph, noticeable snap-back effects throughout the crack propagation in numerical simulations can be identified. This is associated with the boundary conditions imposed in the analysis, in this case an increasing separation (normal or shear) between the crack flanks. Note also that despite the fact that current boundary conditions do not exactly replicate the experimental gripping conditions, numerical predictions are in very close agreement with respect to the tests data, in both the linear elastic and crack growth regions of the evolutions.

Moreover, interestingly, the evaluation of the mixed mode ratio G_{II}/G_T can be performed in a straightforward manner using LEBIM [226], due to only the tractions at the crack tip are required as

$$G_{II}/G_T = \frac{t_s^2/(2k_s)}{\langle t_n\rangle_+^2/(2k_n) + t_s^2/(2k_s)} = \frac{1}{\left(\dfrac{\langle t_n\rangle_+}{t_s}\right)^2 \dfrac{k_s}{k_n} + 1}. \tag{7.34}$$

Fig. 7.19 depicts the evolution of the mixed mode G_{II}/G_T for each configuration according to the expression given in Eq. (7.34) as a function of the crack length. Such curves present a constant value during the crack growth in conjunction with some fluctuations lower than the 10% with respect to their mean values. Table 7.9 reports the qualitative comparison between the experimental and numerical results, where the maximum force F_max and the mixed mode ratio G_{II}/G_T are detailed. In the numerical column, the mean value of the curves in Fig. 7.19 is provided.

Based on the current results, it is possible to state that the current formulation combining continuum elements and Traction Separation Laws relying on the LEBIM enables capturing the initiation and evolution of delamination events under Mode I, Mode II and mixed mode fracture conditions. Furthermore, from a computational perspective, in view of the Fig. 7.18, the control algorithm produces the characteristic snap-back curves during the crack propagation that do not appear in experimental data. This fact stems from differences between the numerical and the experimental loading conditions. Thus, whereas the experimental gripping system did not allowed backward movements at the points where the displacements or forces are applied,

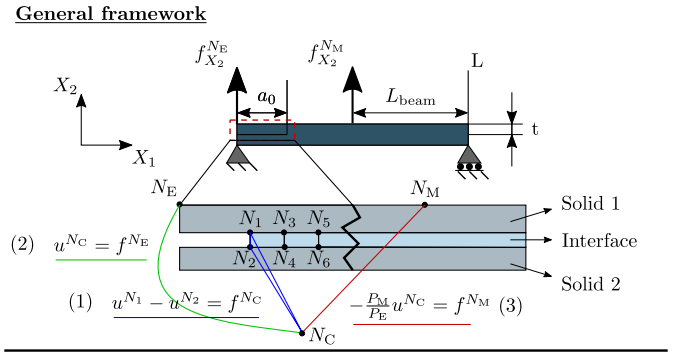

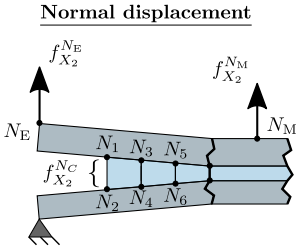

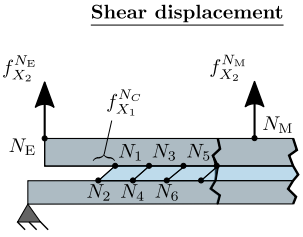

AUXILIARY ELEMENT 1

$$\begin{bmatrix} 0 & 0 & 0 \\ 0 & 0 & 0 \\ 1 & -1 & 0 \end{bmatrix} \begin{bmatrix} u_{X_2}^{N_1} \\ u_{X_2}^{N_2} \\ u_{X_2}^{N_C} \end{bmatrix} = \begin{bmatrix} f_{X_2}^{N_1} \\ f_{X_2}^{N_2} \\ f_{X_2}^{N_C} \end{bmatrix}$$

$$u_{X_2}^{N_1} - u_{X_2}^{N_2} = f_{X_2}^{N_C} \quad (1)$$

AUXILIARY ELEMENT 2

$$\begin{bmatrix} 0 & 1 \\ 0 & 0 \end{bmatrix} \begin{bmatrix} u_{X_2}^{N_E} \\ u_{X_2}^{N_C} \end{bmatrix} = \begin{bmatrix} f_{X_2}^{N_E} \\ f_{X_2}^{N_C} \end{bmatrix}$$

$$u_{X_2}^{N_C} = f_{X_2}^{N_E} \quad (2)$$

AUXILIARY ELEMENT 3

$$\begin{bmatrix} 0 & -\frac{P_M}{P_E} \\ 0 & 0 \end{bmatrix} \begin{bmatrix} u_{X_2}^{N_M} \\ u_{X_2}^{N_C} \end{bmatrix} = \begin{bmatrix} f_{X_2}^{N_M} \\ f_{X_2}^{N_C} \end{bmatrix}$$

$$-\frac{P_M}{P_E} u_{X_2}^{N_C} = f_{X_2}^{N_M} \quad (3)$$

AUXILIARY ELEMENT 1

$$\begin{bmatrix} 0 & 0 & 0 \\ 0 & 0 & 0 \\ 1 & -1 & 0 \end{bmatrix} \begin{bmatrix} u_{X_1}^{N_1} \\ u_{X_1}^{N_2} \\ u_{X_1}^{N_C} \end{bmatrix} = \begin{bmatrix} f_{X_1}^{N_1} \\ f_{X_1}^{N_2} \\ f_{X_1}^{N_C} \end{bmatrix}$$

$$u_{X_1}^{N_1} - u_{X_1}^{N_2} = f_{X_1}^{N_C} \quad (1)$$

AUXILIARY ELEMENT 2

$$\begin{bmatrix} 0 & 0 & 0 & 0 \\ 0 & 0 & 1 & 0 \\ 0 & 0 & 0 & 0 \\ 0 & 0 & 0 & 0 \end{bmatrix} \begin{bmatrix} u_{X_1}^{N_E} \\ u_{X_2}^{N_E} \\ u_{X_1}^{N_C} \\ u_{X_2}^{N_C} \end{bmatrix} = \begin{bmatrix} f_{X_1}^{N_E} \\ f_{X_2}^{N_E} \\ f_{X_1}^{N_C} \\ f_{X_2}^{N_C} \end{bmatrix}$$

$$u_{X_1}^{N_C} = f_{X_2}^{N_E} \quad (2)$$

AUXILIARY ELEMENT 3

$$\begin{bmatrix} 0 & 0 & 0 & 0 \\ 0 & 0 & -\frac{P_M}{P_E} & 0 \\ 0 & 0 & 0 & 0 \\ 0 & 0 & 0 & 0 \end{bmatrix} \begin{bmatrix} u_{X_1}^{N_M} \\ u_{X_2}^{N_M} \\ u_{X_1}^{N_C} \\ u_{X_2}^{N_C} \end{bmatrix} = \begin{bmatrix} f_{X_1}^{N_M} \\ f_{X_2}^{N_M} \\ f_{X_1}^{N_C} \\ f_{X_2}^{N_C} \end{bmatrix}$$

$$-\frac{P_M}{P_E} u_{X_1}^{N_C} = f_{X_2}^{N_M} \quad (3)$$

Figure 7.17 Scheme of the control algorithm for Mixed Mode Bending test: N_1-N_6 are interface nodes, N_C is the control node and N_E and N_M are the nodes where the boundary conditions are established. u and f stand for nodal displacements and nodal forces at the corresponding nodes.

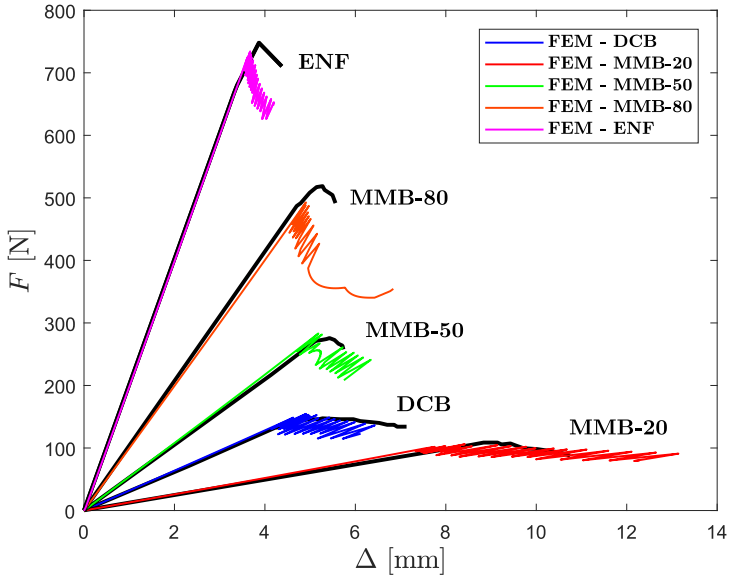

Figure 7.18 Correlation between experimental (black curves) [288] and simulated test corresponding to DCB, MMB and ENF experiments, including mixed mode ratios $G_{II}/G_T = [0.0\ 0.2\ 0.5\ 0.8\ 1.0]$.

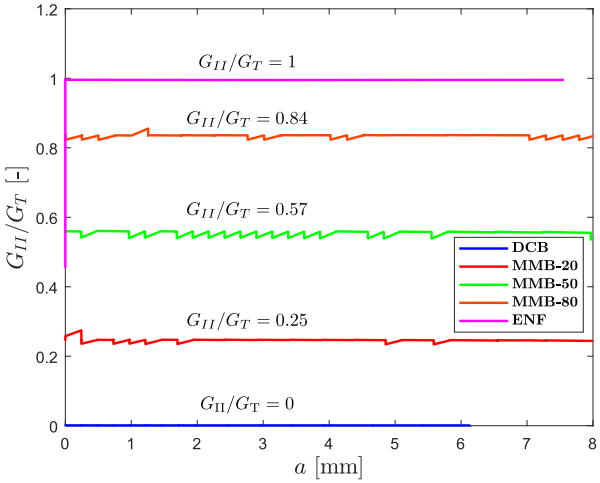

Figure 7.19 Mixed mode evolution G_{II}/G_T at the crack tip according to Eq. (7.34), corresponding to computational models of DCB, MMB and ENF, including beam-theory mixed mode ratios $G_{II}/G_T = [0.0\ 0.2\ 0.5\ 0.8\ 1.0]$ [289].

Table 7.9 Experimental [288] versus numerical results. $F_{\max}$ is the maximum load in the test, experimental G_{II}/G_T is that reported in [288] (based on beam theory) and Eq. 7.34 at the crack tip is employed in numerical G_{II}/G_T.

Experimental		Numerical	
G_{II}/G_T	$F_{\max}$ [N]	G_{II}/G_T	$F_{\max}$ [N]
0.00	147.5	0.00	154.6
0.20	108.7	0.25	106.0
0.50	275.8	0.57	283.1
0.80	518.7	0.84	492.8
1.00	748.0	1.00	734.0

numerical simulations prescribed an opening displacement at the crack tip in pursuit of the computational convergence, even though enabling the snap-back comportment. Note however that, in spite of such discrepancies in terms of the supporting conditions between the experimental and numerical data, the maximum loads for each configuration are in very satisfactory agreement (less than 5% error in the worst case scenario), revealing the accuracy of the proposed LEBIM. Regarding the mixity of the MMB tests, the mixed mode value derived from LEBIM formulation (Eq. 7.34) slightly differs from the predicted value of G_{II}/G_T using the classical Bernoulli beam theory. This small deviation could be attributed to the fact that the current form of such classical theory does not account for geometrically nonlinear effects that are especially relevant for the MMB configuration.

7.2.3 LEBIM validation by means of experimental-numerical correlation of structured interface in DCB tests

This Section addresses the applicability of the proposed geometrically nonlinear LEBIM for the analysis of novel interface profile using structured patterns. In particular, we specialize the manufacturing of trapezoidal interface DCB specimens using Glass Fiber Composite (GFC) and nylon. For validation purposes, the flat specimen and one of the patterned configurations experimentally tested in Chapter 4 were analysed using the interface framework introduced in the present Section. The overall dimensions of the specimens according to the scheme of Fig. 6.1 employed in the FE simulations are:

- Flat interface: $\mathrm{h_{GFC}} = 2.5$ mm, $\mathrm{h_{nylon}} = 1.5$, $\mathrm{h_{int}} = 0.05$ mm, $L_{\mathrm{str}} = 169$ mm.
- Trapezoidal interface: $\mathrm{h_{GFC}} = 2.5$ mm, $\mathrm{h_{nylon}} = 0.5$, $\mathrm{h_{int}} = 0.05$ mm, $L_{\mathrm{str}} = 169$ mm, $A = 1.7$ and $\lambda = 8$ mm.

As the previous case analysed in Section 7.2.2, adherents were simulated using a linear elastic behaviour, no damage emerging then in this part of the specimen, and the interface was represented by LEBIM. The properties used in the interface are specified in Table 7.10 and the GFC and nylon properties are specified in Table 6.1. In the interface region, the penalty stiffness relationship is set so that $k_s/k_n = 1$. The

methodology presented in Section 7.1.1.2 was employed to model the interface in the DCB simulations so as to examine the role of the in-plane deformations.

Table 7.10 Properties of the interface modelled using LEBIM in the experimental-numerical correlation.

Material	t_n^c [MPa]	t_s^c [MPa]	G_{Ic} [J/m^2]	G_{IIc} [J/m^2]
Adhesive	4.0	16.0	136.3	2180

Regarding the FE model, 4-node plane-strain elements (type CPE4 in ABAQUS® library) were employed in the adherents as well as along the interface. In the flat case, around 22k elements constitute the adherents and 576 elements (0.25 mm in length) form the interface region. Conversely, around 140k elements made up the adherents and around 150 interface elements (0.06 mm in length) form each trapezium.

Two different methods were used to evaluate the fracture energy in the patterned interfaces:

- First, the energy release rate G_c, based on the AITM standard [249] and employed previously in [255], is determined as the area under the load-displacement curve with respect to the effective or apparent cracked surface (crack length a_X in a 2D analysis) between two different crack lengths, as

$$G_c^{\mathrm{LD}} = \frac{A^{\mathrm{LD}}}{a_{X2} - a_{X1}}. \tag{7.35}$$

  a_{X1} and a_{X2} included in Fig. 7.22 were employed in the fracture characterisation.

- Second, the effective J-Integral developed in [273], defined as the variation of the potential energy with respect to the horizontal projection of the crack advance (X_1 global axis) according to Eq. (6.5).

  Dividing the last expression into symmetrical and anti-symmetrical counterparts, the fracture energy developed in Mode I and Mode II can be obtained by means of the tractions and displacement along the interface as

$$J_I^X = \sum_{k=1}^{n} J_{I,\Gamma_k+\Gamma_{k'}}(a_X) = \sum_{k=1}^{n} \int_{\Gamma_k} \frac{t_{\mathrm{n}}}{\cos\alpha_i} \frac{\partial \delta_{\mathrm{n}}}{\partial x_1} dx_1, \tag{7.36}$$

$$J_{II}^X = \sum_{k=1}^{n} J_{II,\Gamma_k+\Gamma_{k'}}(a_X) = \sum_{k=1}^{n} \int_{\Gamma_k} \frac{t_{\mathrm{s}}}{\cos\alpha_i} \frac{\partial \delta_{\mathrm{s}}^{\mathrm{s}}}{\partial x_1} dx_1, \tag{7.37}$$

  where α_i is the angle with respect to the horizontal plane (see Fig. 7.25) and it depends on the position along the crack path: $\alpha_i = \alpha_i(X_1)$. Γ_k represents the different sections along the profile. The path selected to perform the J-Integral calculations was the upper and lower surface of the interface, from the crack tip to the point where the normal stress becomes null. Fig.7.23 shows the evolution of the $J^X = J_I^X + J_{II}^X$ with respect to the effective crack length a_X. Additionally,

for comparison purposes, a mean value of the J-Integral is provided by means of Eq. (6.29). This expression allows a direct comparison with G_c, recalling that for elastic materials $J = G$.

Nonetheless, in order to properly exploit the large-displacements procedure pinpointed in Section 7.1 in non-planar interfaces, a pre-process and a slight modification of the `UMAT` are required. Specifically, an initial rotation of the deformation matrix $\mathbf{F}$ is performed to obtain the strain field expressed in a coordinate system in accordance with the initial midplane of the interface. It is worth emphasising that in presence of structured interfaces, the direction of the path α_{i} with respect to the global coordinate system (X_1, X_2) is function of the position. In this way, Eq. 7.39 points out the operator needed to get the appropriate reference system according to

$$\mathbf{F}_{\mathrm{i}} = \mathbf{R}_{\mathrm{i}}^{T} \mathbf{F} \mathbf{R}_{\mathrm{i}}, \tag{7.38}$$

where

$$\mathbf{R}_{\mathrm{i}} = \begin{bmatrix} \cos(\alpha_{\mathrm{i}}) & -\sin(\alpha_{\mathrm{i}}) \\ \sin(\alpha_{\mathrm{i}}) & \cos(\alpha_{\mathrm{i}}) \end{bmatrix}. \tag{7.39}$$

This operation needs to be performed in each integration point with its corresponding α_{i} value. A `PYTHON` script was developed to get the integration point initial slope and it was passed in the `UMAT` as dummy initial state variables by means of the `SDVINI` user subroutine.

It is worth mentioning that, if a local orientation is set during the analysis, stress and strain fields will be expressed in principal directions of deformation and the procedure developed in Section 7.1 is not valid, so no material orientation should be assigned and the output variables of the `UMAT` will be expressed in the global Cartesian basis.

Finally, as variables of the interface elements were expressed in global coordinates, an additional rotation of the stress tensor and Jacobian matrix must be performed. It is worth mentioning that the output variables of the `UMAT` should be expressed in the global Cartesian basis. Hence, a rotation of $-(\alpha + \alpha_{\mathrm{i}})$ radians is carried out for achieving equilibrium and getting convergence. Fig. 7.20 shows the pseudo-code used to calculate the tractions and the Jacobian matrix in curved profiles.

The previous algorithm allows the displacement field along the interface to be computed and, consequently, a comparison between normal, shear and in-plane displacements. Fig. 7.21 displays a drawing of the deformed DCB specimen, together with the corresponding interface region, and the displacement components (δ_{n}, $\delta_{\mathrm{s}}^{\mathrm{s}}$, $\delta_{\mathrm{s}}^{\mathrm{l}}$) along the interface length. It can be observed that δ_{n} represents the highest values in the displacement field, followed by the tangential shear displacement $\delta_{\mathrm{s}}^{\mathrm{s}}$. The in-plane deformations can be considered negligible with respect to δ_{n} or $\delta_{\mathrm{s}}^{\mathrm{s}}$. In fact, the in plane displacements $\delta_{\mathrm{s}}^{\mathrm{l}}$ do not exceed 1×10^{-3} mm during the test, that is, the maximum in-plane displacement represent the 0.5% of the maximum shear displacement and the 0.07% of the maximum normal displacement. Hence, neglecting the in-plane deformation in this scenario is an adequate hypothesis ($k_{\mathrm{l}} = 0$).

Fig. 7.22 shows the experimental-numerical correlation of the load displacement curves corresponding to the DCB tests for flat and trapezoidal interfaces. Fig. 7.23

1. **Input arguments:**
   total strain at the beginning of the increment $\boldsymbol{\varepsilon}_{\mathrm{t}}$, strain increment $\Delta\boldsymbol{\varepsilon}$, deformation gradient at the end of the increment $\mathbf{F}$, element height h, element length L, initial element angle α_{i}.
2. **Express F in a basis coplanar with the initial element midline:**
   $$\mathbf{R}_{\mathrm{i}} = \begin{bmatrix} \cos(\alpha_{\mathrm{i}}) & -\sin(\alpha_{\mathrm{i}}) \\ \sin(\alpha_{\mathrm{i}}) & \cos(\alpha_{\mathrm{i}}) \end{bmatrix}$$
   $$\mathbf{F}_{\mathrm{i}} = \mathbf{R}_{\mathrm{i}}\mathbf{F}\mathbf{R}_{\mathrm{i}}^{\mathrm{T}}$$
3. **Calculate rotation tensor:**
   $$\tan\alpha = \frac{F_{21,\mathrm{i}}}{F_{11,\mathrm{i}}}$$
   $$\mathbf{R} = \begin{bmatrix} \cos(\alpha) & -\sin(\alpha) \\ \sin(\alpha) & \cos(\alpha) \end{bmatrix}$$
4. **Obtain material stretch tensor:**
   $$\mathbf{U} = \mathbf{F}_{\mathrm{i}}\mathbf{R}^{\mathrm{T}}$$
5. **Obtain TSL displacement :**
   $$\begin{bmatrix} \delta_{\mathrm{s}}^{\mathrm{s}} \\ \delta_{\mathrm{n}} \end{bmatrix} = (\mathbf{U}-\mathbf{I})\begin{bmatrix} 0 \\ \mathrm{h} \end{bmatrix}, \quad \begin{bmatrix} \delta_{\mathrm{s}}^{\mathrm{l}} \\ 0 \end{bmatrix} = (\mathbf{U}-\mathbf{I})\begin{bmatrix} \mathrm{L} \\ 0 \end{bmatrix}$$
6. **Determine stress tensor:**
   $$\boldsymbol{\sigma}^{\mathrm{local}} = \mathbb{C}^{\mathrm{local}} : \boldsymbol{\delta},$$
   $$\mathbb{C}^{\mathrm{local}} = \begin{bmatrix} k_{\mathrm{l}} & 0 & 0 \\ 0 & k_{\mathrm{n}} & 0 \\ 0 & 0 & k_{\mathrm{s}} \end{bmatrix}, \boldsymbol{\delta} = \begin{bmatrix} \delta_{\mathrm{s}}^{\mathrm{l}} \\ \delta_{\mathrm{n}} \\ \delta_{\mathrm{s}}^{\mathrm{s}} \end{bmatrix}$$
7. **Rotation of tangent matrix $\mathbb{C}$ and $\boldsymbol{\sigma}$ to global Cartesian basis:**
   $$\alpha_{\mathrm{Global}} = -(\alpha_{\mathrm{i}} + \alpha)$$
   $$\mathbf{R}^{\mathrm{Global}} = \begin{bmatrix} \cos(\alpha_{\mathrm{Global}}) & -\sin(\alpha_{\mathrm{Global}}) \\ \sin(\alpha_{\mathrm{Global}}) & \cos(\alpha_{\mathrm{Global}}) \end{bmatrix}$$
   $$\tilde{\mathbb{C}}^{\mathrm{Global}} = \sum_{\substack{i,j,k,l=1 \\ I,J,K,L=1}}^{3} \mathbf{R}_{iI}^{\mathrm{Global}}\mathbf{R}_{jJ}^{\mathrm{Global}}\mathbf{R}_{kK}^{\mathrm{Global}}\mathbf{R}_{lL}^{\mathrm{Global}}\mathbb{C}_{IJKL}^{\mathrm{local}}$$
   $$\boldsymbol{\sigma}^{\mathrm{Global}} = \mathbf{R}\boldsymbol{\sigma}^{\mathrm{local}}\mathbf{R}^{\mathrm{T}}$$
8. **Output arguments:**
   $$\boldsymbol{\sigma}^{\mathrm{Global}}, \tilde{\mathbb{C}}^{\mathrm{Global}}$$

Figure 7.20 Simplified algorithm for displacement-stress estimation in a Traction Separation Law along a curved crack path for interface elements under finite deformation assumptions.

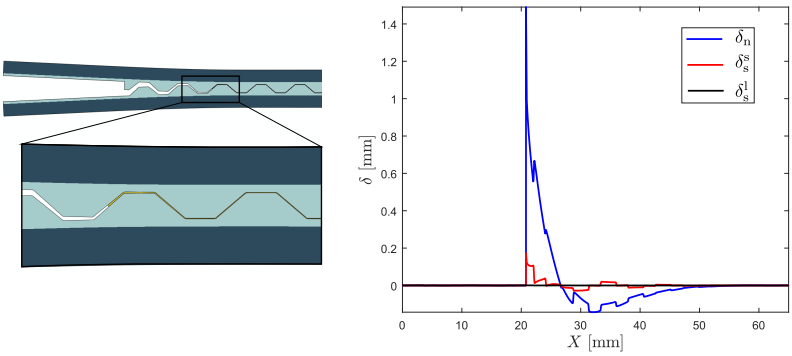

Figure 7.21 Displacement profile (δ_{n}, $\delta_{\mathrm{s}}^{\mathrm{s}}$, $\delta_{\mathrm{s}}^{\mathrm{l}}$) along the interface at $\Delta = 2.4$ mm and $P/W = 2.43$ N/mm in the load-displacement curve.

displays the mixed mode J_{II}^X/J_T^X, where $J_T^X = J_I^X + J_{II}^X$, and J^X evolution with respect to the effective crack length a_X obtained from the FE models.

A good agreement between the curves can be observed in both flat and patterned interfaces. The initial linear-elastic behaviour is appropriately captured as well as the propagation phase, including the unstable crack advance in the trapezoidal case. Furthermore, the prediction of the crack length are in accordance with the experiments. Notwithstanding, the larger differences involving crack length and load-displacement curves occur at the fracture initiation stage. Regarding the fracture mode mixity of the

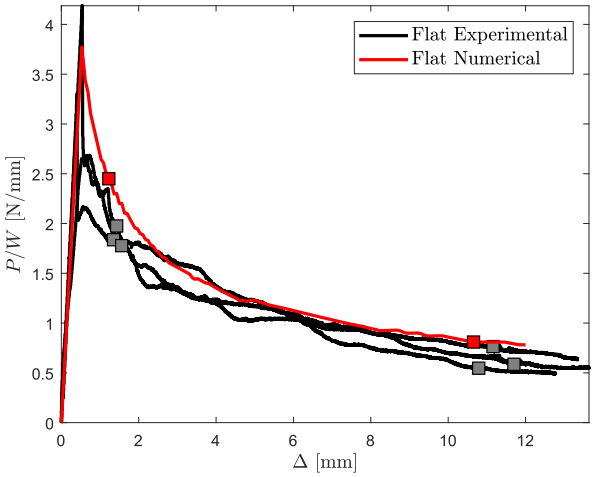

(a) Flat configuration.

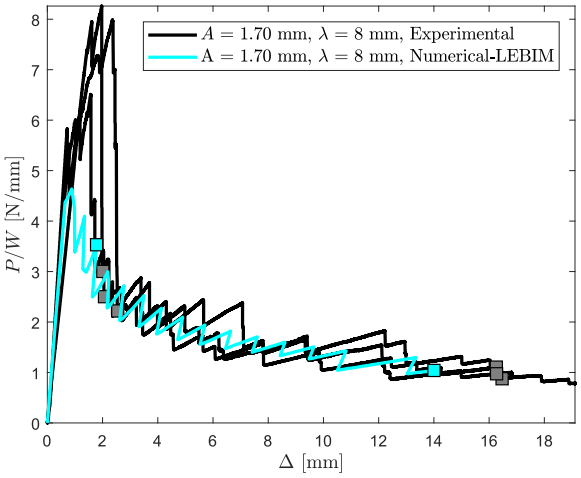

(b) Trapezoidal configuration.

Figure 7.22 Experimental-numerical correlation of the load-displacement curves. Square markers represent the points of the curves where the effective crack length reaches $a_{X1} = 10$ mm and $a_{X2} = 70$ mm.

FE models, the flat configuration led to $B = 0$, as expected, whereas the trapezoidal case presents sharp fluctuations along the virtual test whose maximum values are established around $B = 0.2$. The J-Integral evolution shares the features of the mixed mode distribution and the average effective energy release rate $\bar{J}_c^X$ is almost twice higher in the patterned scenario than in the flat interface ($\bar{J}_c^X = 241.8$ J/m^2 in the

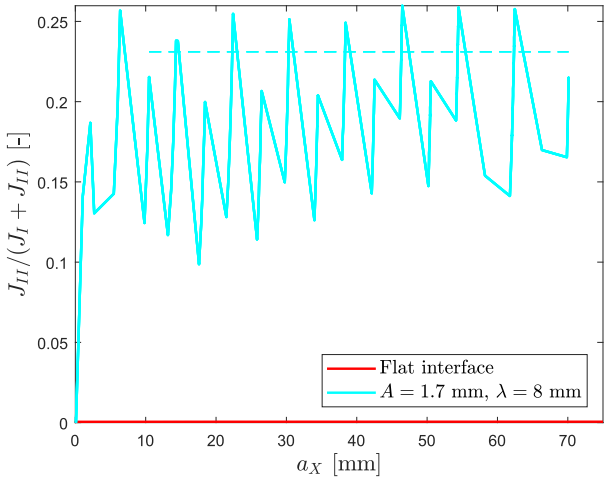

(a) Mixed mode evolution.

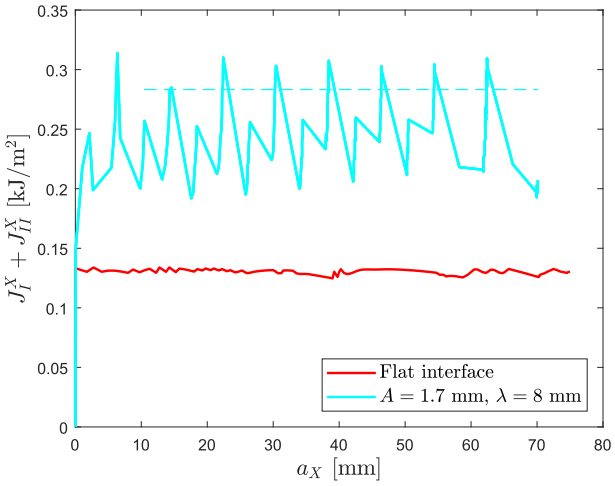

(b) J^X evolution.

Figure 7.23 Numerical evolution of the fracture mixed mode and J^X versus the effective crack length a_X in flat and trapezoidal configurations. Dashed lines represent the average value according to the maximum values or peaks of the curves.

trapezoidal interface and $\bar{J}_c^X = 130.3$ J/m^2 in the reference scenario). A summary of the experimental and numerical analysis is included in Table 7.11.

In view of the results, it is remarkable that the energy release rate obtained from the area of the load-displacement curve G_c^{LD} in the flat case is higher in FE simulations

Table 7.11 Critical energy release rate G_c^{LD} obtained from load-displacement curves (experimental and numerical), mean effective J-Integral $\bar{J}_c^X$ and mean mixed mode of the flat and trapezoidal interfaces in the DCB tests.

Configuration	G_c^{LD} [J/m^2] (Experimental)	G_c^{LD} [J/m^2] (Numerical)	$\bar{J}_c^X$ [J/m^2]	$\frac{J_{II}}{J_T}\|_{\mathrm{mean}}$ [-]
Flat	136.3	148.7	130.3	0.0
Trapezoidal	274.0	257.6	243.3	0.231

than the experimental value $G_{Ic} = 136.3$ kJ/m^2. This discrepancy may emerge from the difference between experimental and computational curves at the beginning of the test. Then, if the crack length a_{X1} was selected so that the corresponding point in the load-displacement curve was located at $\Delta \geq 4$ mm, for example, the discrepancy in the fracture toughness will be reduced. On the contrary, the average value of J^X is lower than G_{Ic}. This reduced value of the pure Mode I energy is associated with the distribution of stresses along the interface. The value of normal traction t_{n} just before the crack propagation is lower than t_{n}^c established in the TSL, as depicted in Fig. 7.24. Hence, the critical energy release rate calculated from the J-Integral, $\bar{J}_c^X$, would be equal to G_{Ic} when the increments of the simulations allow an accurate/perfect traction distribution of the TSL along the interface.

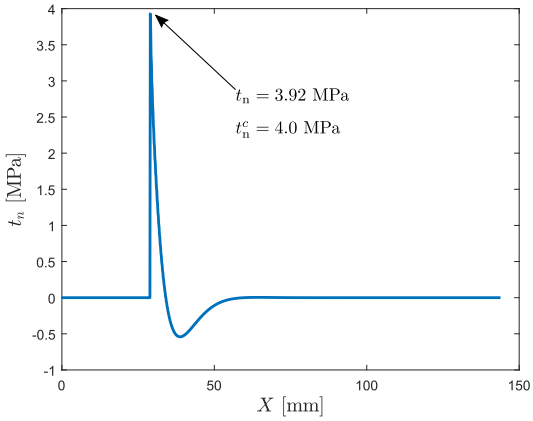

Figure 7.24 Traction distribution along the interface length corresponding to $\Delta = 3.25$ mm and $P/W1.50 =$ N/mm.

Regarding the patterned configuration, the calculation of the effective fracture toughness is in close agreement: less than 7% of difference using the load-displacement curves (G_c^{LD}) and less than 12% using the J-Integral approach ($\bar{J}_c^X$). Moreover, the fracture mixed mode based on Benzeggah-Kenane criterion is highly accurate for energy predictions: $G_c(B = 0.231) = 245.4$ J/m^2, see Eq. (3.47).

7.2.4 Application: hierarchical trapezoidal interfaces

Double Cantilever Beam tests with non flat interfaces between adherents are performed in this Section. This kind of analysis allows to study the fracture energy in presence of mixed mode conditions. In addition, the performance of hierarchical crack paths, involving uni-trapezoidal, bi-trapezoidal and tri-trapezoidal patterns, has been carried out for comparison purposes.

3D printed specimens, depicted in Fig. 7.25, are 160 mm in length L_{hier}, 20 mm in width W and a total height h of 4.9 mm using nylon and glass-fiber composite (GFC) were used. Bulk part of the coupon consists of $h_{GFC} = 1$ mm of GFC and $h_{nylon} = 0.5$ mm of nylon, while the layers that form the trapezoidal interface (A = 1.9 mm, $\lambda = 8$ mm) are made of nylon exclusively.

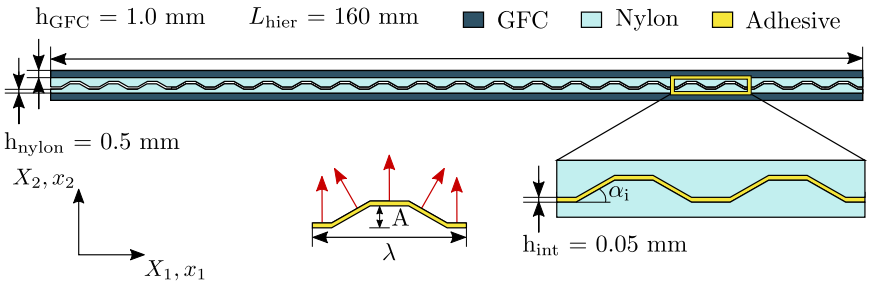

Figure 7.25 Double Cantilever Beam specimen with trapezoidal interface. Materials: glass-fiber composite (GFC), nylon and adhesive. Dimensions: length L_{hier}, height of glass-fiber composite h_{GFC}, height of nylon in the bulk part h_{nylon}, amplitude A and wavelength λ of the trapezoidal interface.

Regarding the hierarchically-based study, three orders of arrangement were investigated: uni-trapezoidal, bi-trapezoidal and tri-trapezoidal pattern. Fig. 7.26 depicts the geometry definition and the differences between shapes. Notice that, elemental features remain constant: amplitude A, wavelength λ, angle α, horizontal length l_h and inclined length l_i. Generally speaking, the height A is reached through one, two or three jumps or steps by travelling the same distance in the horizontal axis. Particular geometrical values of the hierarchic profiles can be observed in Table 7.12.

For the FE analysis, 4-node plane-strain elements (type CPE4 in ABAQUS® library) were used. Material properties are those employed in Table 6.1 and Table 7.10. Around 270k elements were employed to discretize the adherents and approximately 130 interface elements form every trapezium of the adhesive. In Fig. 7.25, red arrows illustrate the normal direction corresponding to each section of the motif.

The same boundary conditions than those used in previous section were applied in this DCB test: a vertical displacement at the upper left end of the specimen while the lower left end is pinned. Likewise, the control algorithm of subsection 7.2.1 is employed in the simulations.

Considering previous aspects, numerical load-displacement curves of the uni-trapezoidal, bi-trapezoidal and tri-trapezoidal interface patterns can be observed in Fig. 7.27.

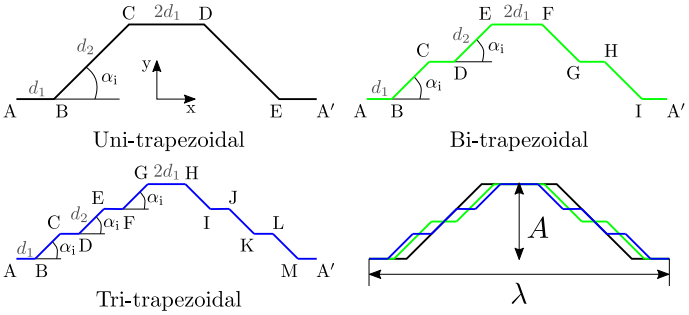

Figure 7.26 Trapezoidal, bi-trapezoidal and tri-trapezoidal shapes contained in the study. d_1 and d_2 represent the flat and inclined section length, respectively. $\alpha_\mathbf{i}$ shows the angle in the inclined sections and A and λ symbolise the amplitude and the wavelength of each configuration.

Table 7.12 Horizontal and inclined section length, d_1 and d_2 respectively, total horizontal and inclined section length, l_h and l_i respectively, and angle of the sloped sections $\alpha_\mathbf{i}$ in trapezoidal, bi-trapezoidal and tri-trapezoidal configurations. d_2^x stands for the horizontal component of the length d_2.

Configuration	d_1[mm]	d_2^x[mm]	$\alpha_\mathbf{i}$[rad]	l_h[mm]	l_i[mm]
Trapezoidal	$\lambda/8$	$\dfrac{A}{\tan\alpha_i}$	$\arctan\frac{4A}{\lambda}$	$\lambda/2$	$2\sqrt{(d_2^x)^2+A^2}$
Bi-Trapezoidal	$\dfrac{\lambda-4d_2^x}{6}$	$\dfrac{A/2}{\tan\alpha_\mathbf{i}}$	$\arctan\frac{4A}{\lambda}$	$\lambda/2$	$4\sqrt{(d_2^x)^2+(A/2)^2}$
Tri-Trapezoidal	$\dfrac{\lambda-6d_2^x}{8}$	$\dfrac{A/3}{\tan\alpha_\mathbf{i}}$	$\arctan\frac{4A}{\lambda}$	$\lambda/2$	$6\sqrt{(d_2^x)^2+(A/3)^2}$

The behaviour of the three configurations is similar: a first linear-elastic stage before damage onset and a region characterised by pronounced snap-back instabilities in the crack advance phase. Notwithstanding, a slight increase in the maximum load of the peaks can be appreciated with the hierarchical level. Additionally, the flattened case presents unstable crack propagation despite of the flat interface, which leads to a saw-tooth force-displacement curve.

Such instabilities can also be appreciated in Fig. 7.28, where the effective J-Integral J^X, according to Eq. (6.5), is represented as a function of the effective crack length a_X. In such figure, it is shown the variability of the energy release rate is noticeable and the increase of the average critical fracture toughness (represented by the dashed lines and calculated by means of the peaks values) with respect to the level of arrangement. In this way, the tri-trapezoidal configuration achieves around 20% of improvement with respect to the uni-trapezoidal interface and around 83% with respect to the flat scenario.

Regarding the obtained fracture mixed mode for the three configurations, we can

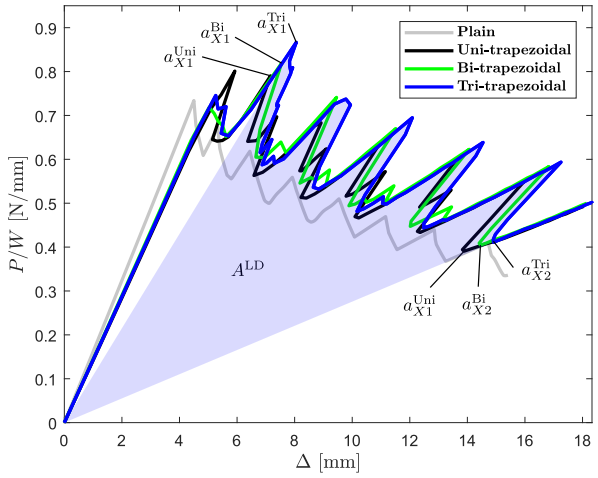

Figure 7.27 Load vs displacement curves of DCB tests with uni-trapezoidal, bi-trapezoidal and tri-trapezoidal interface profiles. a_{X1} and a_{X2} symbolise the initial and final lengths involve in the fracture characterisation and the shaded area A^{LD} represents the area under the load-displacement curve used in Eq. (7.35).

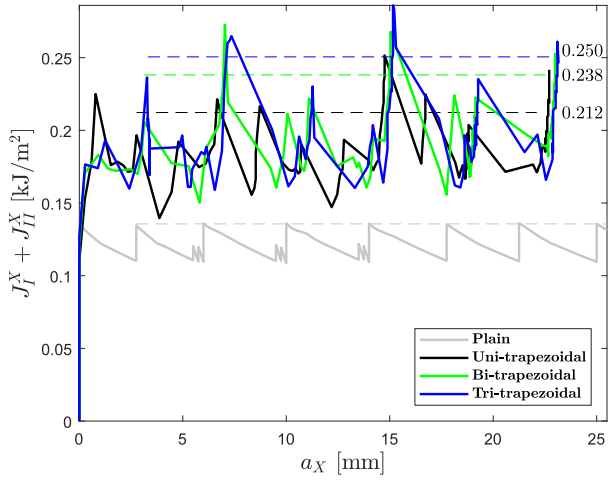

Figure 7.28 Effective J-Integral J^X as a function of the effective crack length a_X corresponding to the Double Cantilever Beam test with uni-, bi- and tri-trapezoidal crack paths.

observe the characteristic variability of the patterned interfaces in Fig 7.29, where the fluctuations become lower with the level of arrangement, that is, the uni-trapezoidal profile presents the highest variation of G_{II}/G_T. Furthermore, a minor increasing tendency of the mean value of the mixed mode during the test can be appreciated: $\frac{G_{II}}{G_T}|^{\text{Uni}}_{\text{mean}} = 0.07$, $\frac{G_{II}}{G_T}|^{\text{Bi}}_{\text{mean}} = 0.10$ and $\frac{G_{II}}{G_T}|^{\text{Tri}}_{\text{mean}} = 0.11$.

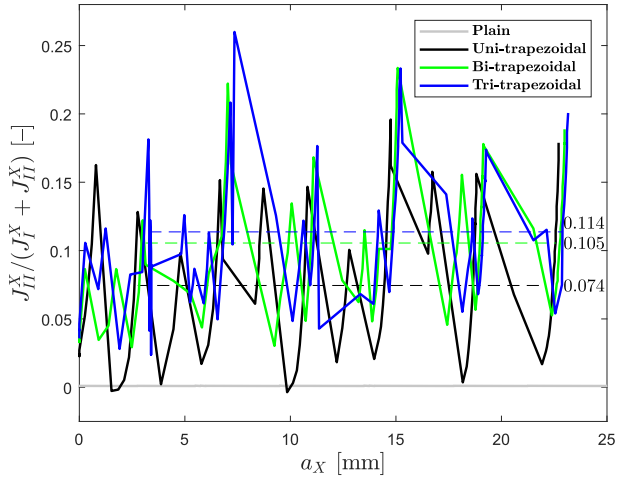

Figure 7.29 Mixed mode evolution J^X_{II}/J^X_T as a function of the effective crack length a_X corresponding to the Double Cantilever Beam test with uni-, bi- and tri-trapezoidal crack paths.

Table 7.13 outlines the principal fracture energy values: G_c^{LD}, $\bar{J}_c^X$ and the mean fracture mixed mode during the DCB test.

Table 7.13 Energy release rate G_c^{LD} obtained from load-displacement curves, mean effective J-Integral $\bar{J}_c^X$ and mean mixed mode of the hierarchical trapezoidal interfaces in the DCB tests.

Configuration	G_c^{LD} [J/m^2]	$\bar{J}_c^X$ [J/m^2]	$\frac{J^X_{II}}{J^X_T}\|_{\text{mean}}$ [-]
Uni-Trapezoidal	195.9	212.3	0.074
Bi-Trapezoidal	205.1	238.1	0.105
Tri-Trapezoidal	210.5	250.5	0.114

The use of LEBIM to characterise the behaviour of structured interfaces facilitates the comparison of the results determined from load-displacement and J-Integral methods. Such values differ between 8.4% and 17.2%. This difference arises from the energy calculation procedure: on the one hand, the area method implicitly implies an average of every point of the load-displacement curve (between the two crack lengths selected

a_{X1} and a_{X2}); on the other hand, the J-Integral average value is performed involving the peaks of the curve in Fig. 7.28. As the mixed mode tendency aforementioned, the mean critical energy release rate (G_c^{LD} or $\bar{J}_c^X$) increases with the level of arrangement, although such increment is small in comparison with the presence of the actual patterned interface. That is, with respect to the reference scenario (DCB test with straight interface, G_{Ic}), the simplest trapezoidal pattern implies an increment of the fracture toughness around the 56%, whereas the trapezoidal profile with the highest level of arrangement (tri-trapezoidal), involves an increase of 84%. Despite of the impact of the hierarchical arrangement is lower than the overall dimensions of the pattern (amplitude and wavelength) in the fracture properties, the growing tendency suggests that high levels of the arrangement of the geometry may be an interesting strategy to enhance the resistance of adhesively bonded joints.

7.2.5 Concluding remarks

In this Section a computational framework for interface modelling based on two fundamental aspects has been summarised: (i) calculation of displacement jumps or interface gaps under large displacement conditions and (ii) snap-back control algorithm to overcome instabilities.

This FE approach enabled the characterization of mixed mode fracture events, as those occurred in Double Cantilever Beam (DCB), Mixed Mode Bending (MMB) and End Notch Flexure (ENF) tests. The validity of the current numerical methodology was verified with experimental DCB, MMB and ENF tests, as well as with structured-interface DCB specimens. Moreover, a hierarchical trapezoidal-like crack path was examined in order to investigate the effect of the level of arrangement (uni-, bi- and tri-trapezoidal profiles) in the energy dissipated during the crack propagation, resulting in an increase of the fracture toughness.

8 Conclusions and future work

8.1 Conclusions

In the present Thesis, an experimental, analytical and numerical study of structured or patterned interfaces in adhesively bonded joints of 3D printed composite specimens was performed. Geometrical modification of the bondline have demonstrated to be an efficient strategy to increase the strength and the crack resistance in this kind of joints. The main conclusions are divided into the three approaches herein developed.

Experimental standpoint

Regarding the empirical perspective addressed in Chapter 4, an experimental analysis of the crack resistance of adhesive joints in DCB specimens with structured patterns at the interface using ALM production techniques has been performed. In particular, the current analysis has been focused on the crack resistance performance of trapezoidal interface profiles with different aspect ratios A/λ (A = amplitude, λ = wavelength).

The experimental analysis has concerned a preliminary stage that regarded the assessment of available ALM production capabilities at the Elasticity and Strength of Materials laboratory at the University de Seville (Spain). Due to the existing practical limitations, DCBs with structured patterns were produced from nylon–glass-fibre reinforced composites, guaranteeing the repeatability and reliability of the geometrical definition for the subsequent experimental program.

The influence of the interface aspect ratio A/λ on the fracture toughness has been investigated. According to the experimental data and in line with [92], the higher A/λ ratio, the higher improvements on the apparent fracture resistance G_c^X and the actual fracture resistance G_c^S with respect to the flat configuration. These results revealed the increasing contribution of fracture Mode II at the local crack tip for higher values of A/λ. From a qualitative standpoint, in comparison to reference flat DCB values, the current experimental results showed an increase of the effective critical energy release rate around 99% for the most unfavourable interface pattern, whereas this increment

can achieve an improvement of 803% for the best configuration under analysis. These promising data clearly manifest the potential benefits arising from the production of bonded joints with patterned trapezoidal interfaces.

These new interface definitions can be remarkably promoted by the advent of new ALM or 3D printing production techniques, which would endow the optimization of such concepts. Finally, the comprehensive investigation of these new prototypes using composite materials would have a strong impact on the production of highly efficient structural systems in different engineering sectors.

Analytical standpoint

In the simplified theoretical analysis of Chapter 5, the fracture performance of 3D printed composite DCB coupons with structured patterns has been investigated. Particularly, trapezoidal interfaces with different aspect ratios A/λ were analysed.

Considering the linear evolution of the energy release rate G_c with the mixed mode B and a relation of $k_s/k_n = 1$ in Sect. 5.1.1, the mixed-mode fracture conditions at the trapezoidal interfaces has been estimated by means of a novel theoretical model. This simple analysis tool enabled the prediction of the critical energy release rate in trapezoidal interfaces within the range $A/\lambda = [0-0.30]$ with a very satisfactory level of accuracy. For higher values for A/λ, the developed tool deviated from the experimental results due to the limitations stemming from the modeling assumptions. Nevertheless, the proposed model can be seen as a valuable preliminary design tool for the estimation of the prospective increase in the crack resistance properties for structured interfaces for moderate A/λ ratios.

The main objective of the model in Sect. 5.1.2 was devoted to enhance the simplified theoretical tool proposed in Sect. 5.1.1 in order to capture the evolution of critical energy release rate G_c for a wider range of mixed-mode fracture conditions. For this purpose, the stiffness ratio between shear and normal directions $\frac{k_s}{k_n}$ and a nonlinear evolution of the critical energy release rate through the B-K law were introduced in the model formulation, improving the accuracy of the simplified cohesive-based approach predictions.

In conclusion, considering the results obtained in Fig. 5.6 and Table 5.1, the fracture response trend of DCB specimens with trapezoidal patterns can be efficiently predicted in advance by means of the proposed Simplified Analytical Approach (SAA) and this model endows a new design tool for adhesive joints. Derived from the current results, it can be seen that the use of Additive Manufacturing techniques together with optimisation tasks in interface definitions can lead to the production of modern lightweight composite structures with outstanding interlaminar fracture capacities through the exploitation of patterned interfaces.

Numerical results by means of a Bilinear Cohesive Zone Model

In Chapter 6, the fracture performance of 3D printed composite DCB coupons with structured patterns has been investigated from a computational point of view. In partic-

ular, the interface profiles under analysis concerned with trapezoidal definitions, which endowed a good compromise between fracture resistance capabilities and geometrical termination, using the Cohesive Zone Model and a bilinear cohesive law to represent the adhesive performance.

On the one hand, regarding the approach associated with the load-displacement curves, the use of CZM has been exploited in order to reproduce experimental results triggering fracture events at the joint. FEM simulations concerned four different aspect ratios $A/\lambda \approx 0.20, 0.28, 0.32, 0.40$ and two different amplitudes $A \approx 1.30, 1.70$ mm. Numerical load-displacement curves satisfactorily agreed with the experimental evolutions, capturing both linear evolution prior failure initiation and the subsequent softening branch. The computational models were able to reproduce the characteristic peaks of trapezoidal interface curves, leading to slight deviations regarding the estimation of the fracture toughness within the range 1-39% with respect to the measured values. Moreover, the current FEM simulations supported the significant improvements in the fracture energy of trapezoidal interfaces, justifying this increase throughout the mixed-mode distribution during the test.

Relying on the results reported (Table 6.4), non-conventional or structured patterns can be considered as an excellent design alternative for the achievement of outstanding increments of the bond resistance of adhesive joints.

On the other hand, regarding the novel J-Integral procedure, a new definition of the J-Integral procedure for its application to non-uniform crack paths has been developed. This technique allows the determination of the energy release rate under any preferential direction, that is not necessarily aligned with the actual crack path. The interest of such a methodology is its application in engineering structures and concepts which include structured patterns, whereby the apparent fracture energy is of interest, among many other potential cases.

The applicability of the current approach has been assessed for the particular case of Double Cantilever Beam specimens with different trapezoidal interface configurations, varying the wavelength λ and the amplitude A of the pattern between the different configurations under analysis. These coupons were modelled using nonlinear geometrically Finite Element models and the cohesive zone model. The post-process of the results derived from the FE analysis has been presented together with the characteristic stress and strain fields along the cohesive zone. Besides, some numerical considerations were taken into account for an accurate J-Integral evaluation, concerning finite displacements and rotations.

The energy release rate evolution G_c with respect to the effective crack length a_X has been presented. Due to the presence of the patterned interfaces, the fracture process zone was not continuous during the crack advance in an individual coupon and, consequently, discontinuous jumps were produced in the fracture energy evolution, which could vary from 40% to 75% of its mean value, depending on the configuration.

Both energy release rates associated with the current contour integral expression and the load-displacement curve were compared. Differences achieved were below 17% in the most unfavourable configuration, validating the proposed methodology for the computation of J-Integral for the estimation of the apparent fracture energy against alternative procedures. Such differences may be derived from dissimilar fracture

conditions in flat and patterned interface specimens. On one hand, conventional DCB test is established for stable crack growth and straight crack propagation. Furthermore, load-displacement methods determine energy released and created area individually. On the other hand, patterned interfaces induce unstable failure progression and the crack direction varies along the path. Additionally, contour integral methods compute the energy release rate in a straightforward manner.

Numerical results by means of a Linear Elastic Brittle Interface Model

In Chapter 7 a novel consistent procedure to compute the displacements needed in a traction-separation law (TSL) suitable for Finite Element codes has been developed, in the framework of finite displacements hypothesis and applied into the software ABAQUS®. Two different methods have been carried out in this 2D analysis: i) an approach based upon cohesive element technology and ii) an approach founded on nonlinear continuum mechanics. In the former case normal and shear displacements δ_n and δ_s are determined by means of the strain field and the central difference algorithm. In the latter case, polar decomposition and a proper definition of the rigid body rotation allow the computation of a complete interface displacement field (transverse normal δ_n, tangential shear δ_s^s and longitudinal normal δ_s^l displacements) from the deformation gradient matrix $\mathbf{F}$.

Additionally, representative benchmark problems including 1-element tests with prescribed node displacements, such as rotations, normal shear and in-plane deformations, served as validation process of the two approaches, achieving accurate results. Both interface-like and continuum-like large displacement formulations together with a Linear Elastic Brittle Interface model has been compared with the so-called bi-linear cohesive law in a Horizontal Drum Peel. These experiments show a good agreement with respect to the fracture toughness G_c and the moment vs. peeling length curves. The capacity of the proposed techniques to deal with surface separations under large displacement conditions has been verified. Remarkably, relative displacements using continuum elements in a FE package were calculated by means of a user material subroutine without requiring the formulation of a special-purpose element.

Although the solid element conception has been used to get normal and shear displacements δ_n and δ_s^s (comparable with cohesive element utilities), the truly potential of this kind of approach will be achieved in models where in-plane deformation plays a crucial role ($\delta_s^l \neq 0$).

Moreover, a comprehensive framework of computational interface modelling has been presented. The following three techniques have been summarised with the aim to overwhelm difficulties during the analysis of interfaces with complex geometry: (i) an innovative versatile model to calculate interface gaps under large displacement conditions, (ii) the Linear Elastic Brittle Interface Model able to describe the abrupt failure phenomena present in some joints, (iii) and a control algorithm to deal with snap-back instabilities result from the fracture mixed-mode variability along non-straight interface patterns. The first two methods have been embedded in a material user-subroutine UMAT of the software package ABAQUS® whereas the latter one was performed by linking boundary conditions and crack tip opening employing auxiliary elements.

Aforementioned scheme was applied to delamination of composite laminates in a large range of mixed-mode fracture conditions: Double Cantilever Beam (DCB), Mixed Mode Bending (MMB) and End Notch Flexure (ENF) tests. Numerical outcomes obtained from the Finite Element analysis were compared with experimental test available in the literature. The numerical-experimental correlation exhibits an excellent agreement and the employment of this interface modelling in structures involving a large variety of mixed-mode fracture conditions is justified.

Finally, the strategy proposed were exploited in Double Cantilever Beam Finite Element tests including structured interfaces with different orders of hierarchical organization. In particular, uni-trapezoidal, bi-trapezoidal and tri-trapezoidal profiles were examined in the simulations. The load-displacement curves present analogous behaviours, developing a linear-elastic phase before damage appearance and consecutive snap-back responses during the crack propagation. It is worth mentioning that the higher order of the arrangement in the pattern the slightly larger fluctuations and higher maximum peak values are obtained. As load-displacement curves anticipate, energy release rate does not increase considerably with the hierarchical order considering the situations and the geometrical parameter suggested in this work. So, a high level of hierarchical arrangement may be needed to achieve a noticeable improvement in the interface fracture properties. Lastly, the shape and overall dimensions of the pattern may have more influence than the arrangement level.

Considerations about structured interfaces

The biomimicking or the bio-inspired models aim to be efficient methods to optimise engineering structures. There are some aspects in the manufacturing or design processes in which the geometry or the arrangement of the elements in a structure have a great impact. Specifically, in the field of adhesive joints, the anodizing technique in metals and the peel ply method in composites parts constitute two well-established surface treatments to improve the performance of adhesively bonded joints. Both approaches alter the geometry of the surface and promote higher energy dissipation rates with respect to the reference scenario, which leaded to their implementation at the industrial scale. Notwithstanding, considering a particular pair of adherent-adhesive, the optimisation of the crack resistance properties as a consequence of the geometry of the bondline is limited to the micro scale. That is, the modification of the interface topology at the macro level is not yet contemplated in the design of adhesive joints. The advent of the 3D printing methodologies may overwhelm some of the difficulties that emerge in the application of bio-inspired interface designs during the manufacturing process, for instance, the absence of tooling and moulds needed in conventional methods to manufacture intricate shapes.

8.2 Future work

Experimental

Future research activities would concern the comparison between different interface patterns under tensile and other different loading conditions. These activities would also include the complete characterization of the adhesive properties by means of specific experimental campaigns. Additionally, optimization procedures regarding the interface geometry could be performed in order to take advantage of adhesive fracture properties.

These novel designs could be carried out using the standard tests for adhesively bonded joints:

- Mixed Mode Bending test,
- End Notch Flexure test,
- Single Lap Joint test,
- Double Lap Joint test,
- Butt Joints,
- Runout panels.

Such configurations can be efficiently manufactured using Additive Layer Manufacturing techniques, thanks to the easiness to accomplish intricate patterns, either in 3D printed fibre-reinforced polymers or metals. In this line, it would be interesting the manufacturing of structured interfaces employing conventional composite laminates so as to analyse the viability of patterned crack paths in industrial components.

Moreover, it would be interesting to study the fatigue life and the response under impacts of the wavy interfaces.

Theoretical

The simplified analytical model proposed can be further enhanced by combining the cohesive-based approach, in which the energy dissipated relies on the geometry of the interface pattern, and strength of material models, where the continuum properties of the adherents are accounted for determining the deformed shape of the beam. This mixed method could be materialised by spring foundation beam-theory models with non-straight interfaces.

Numerical

The development of numerical methods that can reproduce the fracture conditions at every location throughout the geometrical pattern would represent a powerful optimization tool. The Finite Element simulations could define the principal guidelines to calculate the best interface geometry as a function of the test configuration and boundary conditions. In fact, the numerical tools described herein for 2D structured interface

in Double Cantilever Beam tests under plain strain conditions could be employed to predict the fracture response of the aforementioned adhesively bonded joints (Mixed Mode Bending, Single Lap Shear, etc).

The Linear Elastic Brittle Interface Model under large displacement hypothesis can be extended to 3D configurations in order to investigate the effect of a finite width of the specimens or 3D structures.

Finally, the introduction of damage models within the adherents will clarify the migration of the crack from the interface to the bulk material, so that we will know the influence of the interface in the specimen and some critical features as the Stress Intensity Factor induced by the curvature. The Phase Field approach together with the Cohesive Zone Model could be a convenient framework to completely characterise the fracture behaviour of adhesively bonded joints in layered materials.

Appendix A
Summary of the experimental program: basic definitions

In this Appendix, the experimental program of the current 3D printed glass-fiber–nylon composite specimens with structured interfaces is briefly discussed, see Chapter 4 for further details. Particularly, special attention is devoted to the specification of: (1) the geometrical dimensions and material distribution of the coupons, (2) the main particularities of the manufacturing process and the production of structured interfaces obeying trapezoidal profiles, (3) the definition of the test set-up, and (4) the interpretation of the experimental results.

Due to its versatility and strong potential to generate composite specimens with intricate geometrical definitions, the production of the current coupons was conducted using the ALM technology integrated into the 3D printer MarkOne®. General features of the production system and material properties can be found in [244], whilst the preliminary steps to achieve the coupons with the suitable geometrical and surface terminations are available in [255]. The employed layer-by-layer deposition technique permitted the manufacturing of structured interfaces without the need of any additional preparation or conforming process, so that the samples were manufactured in-situ in a single operation. Through this technique, specimens with flat and non-conventional interfaces following an hybrid configuration made from nylon and glass-fibre reinforced composite materials were produced, and therefore a direct comparison of the corresponding fracture performances was done.

Among different geometrical definitions, trapezoidal profiles were chosen to accomplish the structured patterns due to the fact that they have some advantages over other possible configurations (triangular, rectangular, etc), especially in terms of the accuracy in the geometric terminations. In this regard, through the production preliminary 3D printing samples, we observed that the minimal dimension that the printer was able to produce was around the thickness of a tow of the material supplied for the use of the printer and, as a consequence of this production constraint, the sharp zones of the pattern may present significant deviations from the nominal dimensions. Thus, trapezoidal patterns led to a good compromise between reliable geometric terminations and

potential gain in fracture resistance using the current ALM technique. This fact allows the required repeatability along the experimental program to be guaranteed [255].

Both flat and structured interface specimens were produced with the same overall dimensions and printing direction and consequently the unique difference between flat and patterned cases regarded to the configuration of the top layers, which conformed the actual interface profile. The thickness of each sample was oriented along the Z-direction of the printer, see Fig. A.1, whereas length L = 169 mm and width W = 20 mm corresponded to the $X-Y$ plane. Thus, three different categories for the designs under study can be distinguished in the DCB coupon production:

- Flat specimens: total thickness $\frac{h_{\text{total}}}{2} = h_{\text{GFC}} + h_{\text{nylon}}$ = 4 mm, consisting of 25 layers with 0.1 mm in thickness of glass-fibre reinforced composite (yellow lines), h_{GFC}, and 15 nylon layers (grey lines) with 0.1 mm in thickness $\left(h_{\text{nylon}} = 1.5\,\text{mm}\right)$.
- Trapezoidal specimens with $A = 2\,\text{mm}$: total thickness $\frac{h_{\text{total}}}{2} = h_{\text{GFC}} + h_{\text{nylon}} + A$ = 5 mm, consisting of 25 layers with 0.1 mm in thickness of glass-fibre reinforced composite (yellow lines), h_{GFC}, and 25 nylon layers (grey lines) with 0.1 mm in thickness ($h_{\text{nylon}} = 0.5$ mm, $A = 2$ mm).
- Trapezoidal specimens with $A = 1.5\,\text{mm}$: total thickness $\frac{h_{\text{total}}}{2} = h_{\text{GFC}} + h_{\text{nylon}} + A$ = 4.5 mm, consisting of 25 layers with 0.1 mm in thickness of glass-fibre reinforced composite (yellow lines), h_{GFC}, and 20 nylon layers (grey lines) with 0.1 mm in thickness ($h_{\text{nylon}} = 0.5$ mm, $A = 1.5$ mm).

Thus, total thickness is h_{total} = 8 mm for flat and structured interface specimens with $A = 2\,\text{mm}$ and h_{total} =7.5 mm for structured interface specimens with $A = 1.5\,\text{mm}$. Consequently, a difference of 0.5 mm in the total thickness represents a variation of 25% in the amplitude value of the interface (from $A = 2$ mm to $A = 1.5$ mm), which 5 of the nylon layers are not part of the trapezoidal region.

The material properties for each constituent corresponded to: $E_{11} = 25.84\,\text{GPa}$, $E_{22} = 1.13\,\text{GPa}$, $G_{12} = 0.88\,\text{GPa}$ and $\nu_{12} = 0.45$ for glass-fibre reinforced composite, $E = 0.384\,\text{GPa}$ and $\nu = 0.39$ for nylon [244], and $E = 4.231\,\text{GPa}$, $G = 1.461\,\text{GPa}$ for the adhesive layer [267].

For each configuration, combining $\lambda = 4, 6, 8$ mm, $A = 1.5, 2$ mm and $r = \frac{2\bar{a}}{\lambda} = 1/2$ ($2\bar{a}$ being the horizontal length of a trapezium), three samples were produced, which were identified according to Table A.1, where A_{nom} and λ_{nom} refer to nominal values and A_{act} and λ_{act} refer to actual values.

Ideally, crack should propagate along the profile during the tests, as shown Fig. A.2.a. However, some DCB samples led to invalid results due to the fact that the crack growth was not confined to the interface, migrating towards adjacent regions of the specimen, see Fig. A.2.b. This undesirable response was attributed to the presence of defects during the printing process, and therefore only coupons performed a valid propagation were included in the present study. The number of successful specimens in each configuration are indicated in brackets in Table A.1.

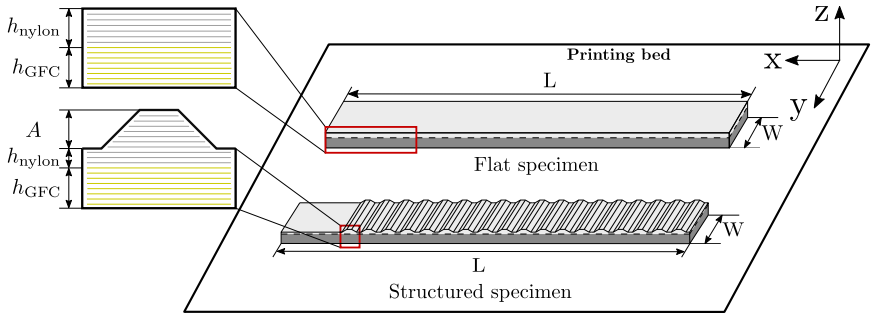

Figure A.1 Reference axes in the printing process and specimen disposal in the printing bed. Yellow lines represent GFC layers and grey lines symbolize nylon layers.

Table A.1 Geometrical parameters of the trapezoidal interface specimens, where A_{nom} and A_{act} represent the nominal and actual mean amplitude values, respectively, and λ_{nom} and λ_{act} represent the nominal and actual mean wavelength values, respectively. All the configurations set $r = 1/2$. The number of successful specimens in each configuration are indicated in brackets.

Configuration	A_{nom} [mm]	λ_{nom} [mm]	A_{act} [mm]	λ_{act} [mm]
A2.00λ8.00 (3)	2	8	1.70	8
A2.00λ6.00 (3)	2	6	1.76	6
A2.00λ4.00 (1)	2	4	1.66	4
A1.50λ8.00 (0)	1.5	8	-	-
A1.50λ6.00 (1)	1.5	6	1.26	6
A1.50λ4.00 (1)	1.5	4	1.40	4

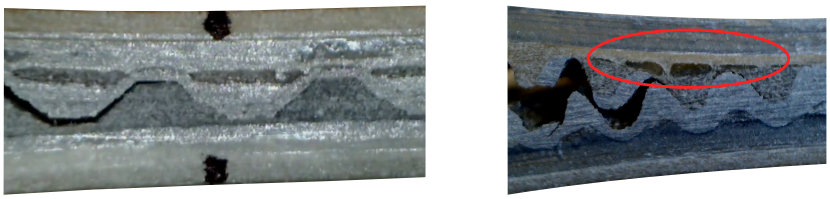

Figure A.2 (a) Appropriate and (b) wrong crack propagation, due to coupon fracture, in a trapezoidal interface.

Fig. A.3 shows the rig corresponding to the DCB tests, where a_0 identifies the pre-crack length, b is the distance between the beginning of the beam and the applied displacement point, and $\Delta = 2u$ stands for the total displacement of the testing machine.

The tests were performed according to the specifications outlined in [249], so that the

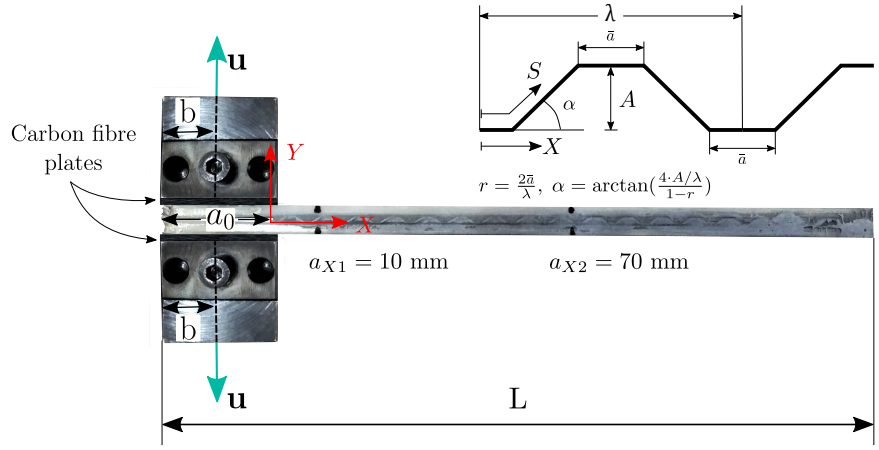

Figure A.3 Trapezoidal interface definition for the DCB specimen with trapezoidal interface and parameters $A = 2$ mm and $\lambda = 8$ mm with load blocks and boundary conditions in the test. Auxiliary carbon fibre reinforced plates were used to set the DCB specimens to the gripping fixture.

supporting conditions and the applied loading corresponded to: a vertical cross-head displacement Δ applied at $x = -a_0 + b$, while the right-side border placed at $x = L - a_0$ was not restricted, see Fig. A.3. The universal testing machine INSTRON 4482 recorded the cross-head displacement along the Y-direction and the corresponding force value applied. These data are necessary to plot the load-displacement curve, from which the energy released can be computed.

Assuming that the unique source of energy dissipation is the joint failure and the DCB beams follow a linear elastic response, it is fundamental to define a variable that make comparable the energy released from the load-displacement curve in both types of configurations, i.e. coupons with flat and structured interface patterns. Consequently, two different critical energy release rate are henceforth defined:

- Effective critical energy release rate, G_c^X. This magnitude is identified with the energy dissipated during the crack propagation taking X-direction as reference (Fig. A.3). Then, the crack length is identified by a_X, and the computation of the critical energy release rate reads:

$$G_c^X = -\frac{\partial \Pi_f(a_X)}{\partial (W \cdot a_X)}, \tag{A.1}$$

  where $\mathrm{d}\Pi_f(a_X)$ is the energy dissipated during the crack propagation when the crack grows an area $\mathrm{d}A_f = W \mathrm{d}a_X$.

- Actual critical energy release rate, G_c^s. It corresponds to the energy dissipated during the crack propagation, taking S-direction as reference (Fig. A.3), which is

identified with a curvilinear axis that follows the actual interface profile:

$$G_c^S = -\frac{\partial \Pi_f(a_S)}{\partial (W \cdot a_S)}, \tag{A.2}$$

where $\mathrm{d}\Pi_f(a_S)$ stands for the energy dissipated during the crack propagation when the crack grows an area $\mathrm{d}A_f = W\mathrm{d}a_S$.

The current coupons were tested without any previous loading history, monitoring the crack growth during data recording. DCB tests were conducted using a displacement rate equal to $\dot{\Delta} = 0.5$ mm/min, assuming quasi-static loading conditions. According to [249], $\partial\Pi_f$ can be experimentally determined using the load-displacement evolution curve for each test. Specifically, two reference points were used for this purpose, which corresponded to the crack lengths $a_{X1} = 10$ mm and $a_{X2} = 70$ mm. Accordingly, the effective critical energy release rate, G_c^X, can be computed through dividing the energy released during the test by the projection of the area created on the horizontal plane ($W \cdot a_X = W \cdot (a_{X2} - a_{X1})$). Differing from the previous fracture calculation, the actual critical energy release rate, G_c^S, can be obtained by considering the actual area created during the crack propagation ($W \cdot a_S = W \cdot (a_{S2} - a_{S1})$), where $a_S = a_S(a_X, A, \lambda)$.

Table A.2 lists the effective (G_c^X) and actual (G_c^S) critical energy release rates for the current DCB coupons. For the reported DCB cases, crack patterns were confined to the adhesive layers between both parts of the DCB system. Analysing these data, it can be clearly observed the outstanding increment in the fracture resistance of the current 3D printed specimens with patterned interfaces with respect to the corresponding values to the flat profiles. This gain is more pronounced for larger values of the ratio A/λ leading to an increase of around 900%, which are in line with the findings of [92], and showing the strong potential and the very attractive capabilities of the current designs. Moreover, it is noticeable that trapezoidal interfaces only provided mechanical benefits in terms of fracture resistance properties for all the values A/λ herein considered.

Table A.2 Effective fracture toughness G_c^X, actual fracture toughness G_c^s, effective and actual fracture toughness ratio $\frac{G_c^X}{G_c^S}$ and projected area in horizontal plane and actual area created ratio $\frac{A_S}{A_X}$ in each configuration tested.

Configuration	A_{act} [mm]	λ_{act} [mm]	A_{act}/λ_{act} [−]	$G_c^X \left[\frac{\mathrm{J}}{\mathrm{m}^2}\right]$	$G_c^S \left[\frac{\mathrm{J}}{\mathrm{m}^2}\right]$	G_c^X/G_c^S[−]	A_S/A_X[−]
A0.00λ0.00	-	-	0	136.3	136.3	1	1
A2.00λ8.00	1.70	8	0.212	274.0	236.8	1.15	1.15
A1.50λ6.00	1.26	6	0.210	262.1	228.2	1.15	1.15
A2.00λ6.00	1.76	6	0.294	371.2	291.5	1.27	1.27
A1.50λ4.00	1.40	4	0.350	484.0	345.4	1.36	1.36
A2.00λ4.00	1.66	4	0.404	1231.2	760.9	1.45	1.45

List of Contributions

The following international and national publications have been originated during the work in the present Thesis.

International Peer-Review Publications

1. J. Justo, L. Távara, L. García-Guzmán, F. París. Characterization of 3D printed long fibre reinforced composites. *Composite Structures*, 185:537 - 548, 2018.

2. L. García-Guzmán, L. Távara, J. Reinoso, J. Justo, F. París. Fracture resistance of 3D printed adhesively bonded DCB composite specimens using structured interfaces: Experimental and theoretical study, *Composite Structures*, 188: 173:184, 2018.

3. L. García-Guzmán, L. Távara, J. Reinoso, F. París. Fracture energy characterisation of a structured interface by means of a novel J-Integral procedure, *The Journal of Strain Analysis for Engineering Design*, Special Issue Article, 2019.

4. L. García-Guzmán, L. Távara, J. Reinoso, F. París. Analysis of 3D Printed Trapezoidal Interfaces by Means of a Novel Cohesive-Based Analytical Approach, *Journal of Multiscale Modelling*, 10(3):1842001, 2019.

5. L. García-Guzmán, J. Reinoso, L. Távara, F. París. A consistent finite displacement and rotation formulation of the Linear Elastic Brittle Interface Model for triggering interlaminar damage in fibre-reinforced composites, *Composites Part B: Engineering*, sent.

6. L. García-Guzmán, J. Reinoso, A. Valverde, E. Martínez-Pañeda, L. Távara. Numerical study of interface cracking in composite structures using a novel geometrically nonlinear Linear Elastic Interface Model, *Composite Structures*, sent.

Articles in International Conference Proceedings

1. L. García-Guzmán, L. Távara, J. Reinoso, F. París. Analysis of 3D printed trapezoidal interfaces by means of a novel cohesive-based analytical approach. *17th International Conference on Fracture and Damage Mechanics*, September 4th - 6th, Seville 2018.

Articles in National Conference Proceedings

1. L. García-Guzmán, L. Távara, J. Reinoso, A. Valverde, F. París. Cálculo de la tenacidad a fractura efectiva J^X: Integral-J aplicada a interfases estructuradas. *Congreso del Grupo Español de Fractura 2019*, April 3rd - 5th, Sevilla 2019.

2. L. García-Guzmán, L. Távara, J. Reinoso, A. Valverde, F. París. Influencia de las interfases estructuradas en la tenacidad a fractura de uniones adhesivas en especímenes DCB fabricados mediante impresión 3D: estudio experimental y analítico. *35 Encuentro del Grupo Español de Fractura 2019*, March 14th - 16th, Málaga 2019.

3. L. García-Guzmán, L. Távara, J. Reinoso, J. Justo, F. París. Estudio experimental de interfases no convencionales con patrones trapezoidales. *XII Congreso Nacional de Materiales Compuestos - MATCOMP 2017*, June 21st - 23rd, San Sebastián 2017.

List of Figures

List of Tables

Bibliography

[1] B. D. Agarwal, L. J. Broutman and K. Chandrashekhara. *Analysis and performance of fiber composites*. John Wiley & Sons, 2017.

[2] R. M. Jones. *Mechanics of composite materials*. CRC press, 2014.

[3] S. W. Tsai and E. M. Wu. A general theory of strength for anisotropic materials. *Journal of Composite Materials*, 5(1):58 – 80, 1971.

[4] Z. Hashin. Analysis of composite materials—a survey. *Journal of Applied Mechanics*, 50(3):481–505, 1983.

[5] S. W. Tsai. Strength characteristics of composite materials. Technical report, Philco Corp Newport Beach CA, 1965.

[6] V. D. Azzi and S. W. Tsai. Anisotropic strength of composites. *Experimental Mechanics*, 5(9):283 – 288, 1965.

[7] O. Hoffman. The brittle strength of orthotropic materials. *Journal of Composite Materials*, 1(2):200 – 206, 1967.

[8] C. C. Chamis. Failure criteria for filamentary composites. *Composite Materials: Testing and Design. ASTM International*, pages 336 – 351, 1969.

[9] R. L. Whistler. History and future expectation of starch use. *Starch: Chemistry and Technology*, pages 1–9, 1984.

[10] I. Skeist. *Handbook of adhesives*. Springer Science & Business Media, 2012.

[11] R. H. Bogue. *The chemistry and technology of gelatin and glue*. McGraw-Hill, 1922.

[12] A . G. Ward. The present position in gelatin and glue research. *The Journal of Photographic Science*, 9(1):56 – 66, 1961.

[13] A. Baker. *Bonded repair of aircraft structures*, volume 7. Springer Science & Business Media, 2012.

[14] L. J. Hart-Smith. Analysis and design of advanced composite bounded joints. *NASA Technical Report*, 1974.

[15] L. J. Hart-Smith. Bonded-bolted composite joints. *Journal of Aircraft*, 22(11):993 – 1000, 1985.

[16] A. Kinloch. *Adhesion and Adhesives: Science and Technology*. Springer Science & Business Media, 1987.

[17] L.F.M. Silva, A. Öchsner and R. Adams. *Handbook of Adhesion Technology*. Springer Science & Business Media, 2011.

[18] J. W. McBain and D. G. Hopkins. On adhesives and adhesive action. *The Journal of Physical Chemistry*, 29(2):188 – 204, 1925.

[19] J. J. Bikerman. *The science of adhesive joints*. Elsevier, 2013.

[20] B. W. Malpass, D. E. Packham and K. Bright. A study of the adhesion of polyethylene to porous alumina films using the scanning electron microscope. *Journal of Applied Polymer Science*, 18(11):3249 – 3258, 1974.

[21] D. E. Packham, K. Bright and B. W. Malpass. Mechanical factors in the adhesion of polyethylene to aluminium. *Journal of applied polymer science*, 18(11):3237 – 3247, 1974.

[22] S. Tavakoli. Surface preparation: power beams clean up. *Assembly Automation*, 14(4):36 – 38, 1994.

[23] H. Zhang, W. Wen and H. Cui. Study on the strength prediction model of Comeld composites joints. *Composites Part B: Engineering*, 43(8):3310 – 3317, 2012.

[24] W. Tu, P.H. Wen and F.J. Guild. Multi-region mesh free method for Comeld™ joints. *Computational Materials Science*, 48(3):481 – 489, 2010.

[25] W. Tu, P.H. Wen, P.J. Hogg and F.J. Guild. Optimisation of the protrusion geometry in Comeld™ joints. *Composites Science and Technology*, 71(6):868 – 876, 2011.

[26] N. Li, P.H. Chen, X.Y. Liu, W. Ma and X.C. Wang. A micro-macro finite element model for failure prediction of Comeld™ joints. *Composites Science and Technology*, 117:334 – 341, 2015.

[27] J. Mohan, A. Ivanković and N. Murphy. Mode I fracture toughness of co-cured and secondary bonded composite joints. *International Journal of Adhesion and Adhesives*, 51:13 – 22, 2014.

[28] J. Mohan, A. Ivanković and N. Murphy. Mixed-mode fracture toughness of co-cured and secondary bonded composite joints. *Engineering Fracture Mechanics*, 134:148 – 167, 2015.

[29] L. F. M. da Silva, R. J. C. Carbas, G. W. Critchlow, M. A. V. Figueiredo and K. Brown. Effect of material, geometry, surface treatment and environment on the shear strength of single lap joints. *International Journal of Adhesion and Adhesives*, 29(6):621 – 632, 2009. Special Issue on Durability of Adhesive Joints.

[30] M. S. Islam, L. Tong and P. J. Falzon. Influence of metal surface preparation on its surface profile, contact angle, surface energy and adhesion with glass fibre prepreg. *International Journal of Adhesion and Adhesives*, 51:32 – 41, 2014.

[31] H. M. S. Iqbal, S. Bhowmik and R. Benedictus. Surface modification of high performance polymers by atmospheric pressure plasma and failure mechanism of adhesive bonded joints. *International Journal of Adhesion and Adhesives*, 30(6):418 – 424, 2010.

[32] M. Kanerva and O. Saarela. The peel ply surface treatment for adhesive bonding of composites: A review. *International Journal of Adhesion and Adhesives*, 43:60 – 69, 2013.

[33] M. Kanerva, E. Sarlin, M. Hoikkanen, K. Rämö, O. Saarela and J. Vuorinen. Interface modification of glass fibre–polyester composite–composite joints using peel plies. *International Journal of Adhesion and Adhesives*, 59:40 – 52, 2015.

[34] C. Buchmann, S. Langer, J. Filsinger and K. Drechsler. Analysis of the removal of peel ply from CFRP surfaces. *Composites Part B: Engineering*, 89:352 – 361, 2016.

[35] S. Marzi, A. Biel and U. Stigh. On experimental methods to investigate the effect of layer thickness on the fracture behavior of adhesively bonded joints. *International Journal of Adhesion and Adhesives*, 31(8):840 – 850, 2011.

[36] K. Naito, M. Onta and Y. Kogo. The effect of adhesive thickness on tensile and shear strength of polyimide adhesive. *International Journal of Adhesion and Adhesives*, 36:77 – 85, 2012.

[37] L. F. M. da Silva, F. A. C. R. G. de Magalhães, F. J. P. Chaves and M. F. S. F. de Moura. Mode II fracture toughness of a brittle and a ductile adhesive as a function of the adhesive thickness. *The Journal of Adhesion*, 86(9):891–905, 2010.

[38] L. Liao, C. Huang and T. Sawa. Effect of adhesive thickness, adhesive type and scarf angle on the mechanical properties of scarf adhesive joints. *International Journal of Solids and Structures*, 50(25):4333 – 4340, 2013.

[39] A. Lousdad, A. Megueni and A.S. Bouchikhi. Geometric edge shape based optimization for interfacial shear stress reduction in fiber reinforced polymer plate retrofitted concrete beams. *Computational Materials Science*, 47(4):911 – 918, 2010.

[40] J. A. B. P. Neto, R. D. S. G. Campilho and L. F. M. da Silva. Parametric study of adhesive joints with composites. *International Journal of Adhesion and Adhesives*, 37:96 – 101, 2012.

[41] M. D. Banea, L. F. M. da Silva, R. J. C. Carbas and S. de Barros. Debonding on command of multi-material adhesive joints. *The Journal of Adhesion*, 93(10):756 – 770, 2017.

[42] Y. Lu, J. Broughton and P. Winfield. A review of innovations in disbonding techniques for repair and recycling of automotive vehicles. *International Journal of Adhesion and Adhesives*, 50:119 – 127, 2014.

[43] M. D. Bartlett and A. J. Crosby. High capacity, easy release adhesives from renewable materials. *Advanced Materials*, 26(21):3405 – 3409, 2014.

[44] M. D. Banea, L. F. M. da Silva, R. D. S. G. Campilho and C. Sato. Smart adhesive joints: An overview of recent developments. *The Journal of Adhesion*, 90(1):16–40, 2014.

[45] S. Budhe, M. D. Banea, S. de Barros and L. F. M. da Silva. An updated review of adhesively bonded joints in composite materials. *International Journal of Adhesion and Adhesives*, 72:30 – 42, 2017.

[46] M. D. Banea and L. F. M. da Silva. Adhesively bonded joints in composite materials: An overview. *Proceedings of the Institution of Mechanical Engineers, Part L: Journal of Materials: Design and Applications*, 223(1):1–18, 2009.

[47] J. M. Harkness. A Lifetime of Connections: Otto Herbert Schmitt, 1913 - 1998. *Physics in Perspective*, 4(4):456–490, 2002.

[48] Velcro S. A. Improvements in or relating to a method and a device for producing a velvet type fabric. *Patent No. 721 338 Switzerland*, 1955.

[49] J. F. V. Vincent, O. A. Bogatyreva, N. R. Bogatyrev, A. Bowyer and A. K. Pahl. Biomimetics: its practice and theory. *Journal of The Royal Society Interface*, 3(9):471–482, 2006.

[50] G. S. Altshuller. *The innovation algorithm: TRIZ, systematic innovation and technical creativity*. Technical Innovation Center, Inc., 1999.

[51] N. R. Bogatyrev. A “living” machine. *Journal of Bionic Engineering*, 1(3):79 – 87, 2004.

[52] J. Vincent and L. M. Darrell. Systematic technology transfer from biology to engineering. *Philosophical transactions. Series A, Mathematical, physical, and engineering sciences*, 360:159 – 73, 2002.

[53] F. Barthelat. Biomimetics for next generation materials. *Philosophical transactions. Series A, Mathematical, physical, and engineering sciences*, 365:2907 – 2919, 2008.

[54] F. Barthelat, Z. Yin and M. J. Buehler. Structure and mechanics of interfaces in biological materials. *Nature Reviews Materials*, 1:1–16, 2016.

[55] U. G. K. Wegst and M. F. Ashby. The mechanical efficiency of natural materials. *Philosophical Magazine*, 84(21):2167 – 2186, 2004.

[56] S. E. Naleway, M. M. Porter, J. McKittrick and M. A. Meyers. Structural design elements in biological materials: Application to bioinspiration. *Advanced Materials*, 27(37):5455 – 5476, 2015.

[57] J. A. Kluge, O. Rabotyagova, G. G. Leisk and D. L. Kaplan. Spider silks and their applications. *Trends in Biotechnology*, 26(5):244 – 251, 2008.

[58] D. S. Fudge, K. H. Gardner, V. T. Forsyth, C. Riekel and J. M. Gosline. The mechanical properties of hydrated intermediate filaments: Insights from hagfish slime threads. *Biophysical Journal*, 85(3):2015 – 2027, 2003.

[59] J. C. Weaver, G. W. Milliron, A. Miserez, K. Evans-Lutterodt, S. Herrera, I. Gallana, W. J. Mershon, B. Swanson, P. Zavattieri, E. DiMasi and D. Kisailus. The stomatopod dactyl club: A formidable damage-tolerant biological hammer. *Science*, 336(6086):1275 – 1280, 2012.

[60] A. Khayer Dastjerdi and F. Barthelat. Teleost fish scales amongst the toughest collagenous materials. *Journal of the Mechanical Behavior of Biomedical Materials*, 52:95 – 107, 2015.

[61] B. W. Cribb, A. Rathmell, R. Charters, R. Rasch, H. Huang and I. R. Tibbetts. Structure, composition and properties of naturally occurring non-calcified crustacean cuticle. *Arthropod Structure & Development*, 38(3):173 – 178, 2009.

[62] J. F. B. Bruet, J. Song, M. C. Boyce and C. Ortiz. Materials design principles of ancient fish armour. *Nature Materials*, 7:748 – 756, 2008.

[63] R. Menig, M.H. Meyers, M.A. Meyers and K.S. Vecchio. Quasi-static and dynamic mechanical response of haliotis rufescens (abalone) shells. *Acta Materialia*, 48(9):2383 – 2398, 2000.

[64] R. Menig, M. H Meyers, M. A Meyers and K.S Vecchio. Quasi-static and dynamic mechanical response of strombus gigas (conch) shells. *Materials Science and Engineering: A*, 297(1):203 – 211, 2001.

[65] M. A. Kasapi and J. M. Gosline. Design complexity and fracture control in the equine hoof wall. *Journal of Experimental Biology*, 200(11):1639 – 1659, 1997.

[66] L. Tombolato, E. E. Novitskaya, P. Y. Chen, F. A. Sheppard and J. McKittrick. Microstructure, elastic properties and deformation mechanisms of horn keratin. *Acta Biomaterialia*, 6(2):319 – 330, 2010.

[67] H. Rhee, M.F. Horstemeyer, Y. Hwang, H. Lim, H. El Kadiri and W. Trim. A study on the structure and mechanical behavior of the terrapene carolina carapace: A pathway to design bio-inspired synthetic composites. *Materials Science and Engineering: C*, 29(8):2333 – 2339, 2009.

[68] P. Y. Chen, J. McKittrick and M. A. Meyers. Biological materials: Functional adaptations and bioinspired designs. *Progress in Materials Science*, 57(8):1492 – 1704, 2012.

[69] S. Krauss, E. Monsonego-Ornan, E. Zelzer, P. Fratzl and R. Shahar. Mechanical function of a complex three-dimensional suture joining the bony elements in the shell of the red-eared slider turtle. *Advanced Materials*, 21(4):407 – 412, 2009.

[70] I. C. Gebeshuber, J. H. Kindt, J. B. Thompson, Y. Del Amo, H. Stachelberger, M. A. Brzezinski, G. D. Stucky, D. E. Morse and P. K. Hansma. Atomic force microscopy study of living diatoms in ambient conditions. *Journal of Microscopy*, 212(3):292 – 299, 2003.

[71] W. Yang, I. H. Chen, B. Gludovatz, E. A. Zimmermann, R. O. Ritchie and M. A. Meyers. Natural flexible dermal armor. *Advanced Materials*, 25(1):31 – 48, 2013.

[72] M. J. Connors, H. Ehrlich, M. Hog, C. Godeffroy, S. Araya, I. Kallai, D. Gazit, M. Boyce and C. Ortiz. Three-dimensional structure of the shell plate assembly of the chiton tonicella marmorea and its biomechanical consequences. *Journal of Structural Biology*, 177(2):314 – 328, 2012.

[73] F. Barthelat, H. Tang, P.D. Zavattieri, C.M. Li and H.D. Espinosa. On the mechanics of mother-of-pearl: A key feature in the material hierarchical structure. *Journal of the Mechanics and Physics of Solids*, 55(2):306 – 337, 2007.

[74] H. Tang, F. Barthelat and H.D. Espinosa. An elasto-viscoplastic interface model for investigating the constitutive behavior of nacre. *Journal of the Mechanics and Physics of Solids*, 55(7):1410 – 1438, 2007.

[75] H. D. Espinosa, J. E. Rim, F. Barthelat and M. J. Buehler. Merger of structure and material in nacre and bone – perspectives on de novo biomimetic materials. *Progress in Materials Science*, 54(8):1059 – 1100, 2009.

[76] R. Rabiei, S. Bekah and F. Barthelat. Failure mode transition in nacre and bone-like materials. *Acta Biomaterialia*, 6(10):4081 – 4089, 2010.

[77] F. Barthelat and R. Rabiei. Toughness amplification in natural composites. *Journal of the Mechanics and Physics of Solids*, 59(4):829 – 840, 2011.

[78] F. Barthelat. Designing nacre-like materials for simultaneous stiffness, strength and toughness: Optimum materials, composition, microstructure and size. *Journal of the Mechanics and Physics of Solids*, 73:22 – 37, 2014.

[79] F. Barthelat. Architectured materials in engineering and biology: fabrication, structure, mechanics and performance. *International Materials Reviews*, 60(8):413 – 430, 2015.

[80] J. W. C. Dunlop, R. Weinkamer and P. Fratzl. Artful interfaces within biological materials. *Materials Today*, 14(3):70 – 78, 2011.

[81] R. K. Chintapalli, S. Breton, A. Khayer Dastjerdi and F. Barthelat. Strain rate hardening: A hidden but critical mechanism for biological composites? *Acta Biomaterialia*, 10(12):5064 – 5073, 2014.

[82] M. Mirkhalaf, A. Khayer Dastjerdi and F. Barthelat. Overcoming the brittleness of glass through bio-inspiration and micro-architecture. *Nature communications*, 5:3166, 2014.

[83] M. Mirkhalaf and F. Barthelat. Design, 3D printing and testing of architectured materials with bistable interlocks. *Extreme Mechanics Letters*, 11:1 – 7, 2017.

[84] I.A. Malik, M. Mirkhalaf and F. Barthelat. Bio-inspired "jigsaw"-like interlocking sutures: Modeling, optimization, 3D printing and testing. *Journal of the Mechanics and Physics of Solids*, 102:224 – 238, 2017.

[85] Z. Qin, L. Dimas, D. Adler, G. Bratzel and M. J. Buehler. Biological materials by design. *Journal of Physics: Condensed Matter*, 26(7):073101, 2014.

[86] Y. Li, C. Ortiz and M. C. Boyce. A generalized mechanical model for suture interfaces of arbitrary geometry. *Journal of the Mechanics and Physics of Solids*, 61(4):1144 – 1167, 2013.

[87] Y. Li, C. Ortiz and M. C. Boyce. Bioinspired, mechanical, deterministic fractal model for hierarchical suture joints. *Physical Review E: Statistical, nonlinear, and soft matter physics*, 85:031901, 2012.

[88] Y. Li, C. Ortiz and M. C. Boyce. Stiffness and strength of suture joints in nature. *Physical Review E: Statistical, nonlinear, and soft matter physics*, 84:062904, 2011.

[89] E. Lin, Y. Li, J. Weaver, C. Ortiz and M. C. Boyce. Tunability and enhancement of mechanical behavior with additively manufactured bio-inspired hierarchical suture interfaces. *Journal of Materials Research*, 29:1867 – 1875, 2014.

[90] E. Lin, Y. Li, C. Ortiz and M. C. Boyce. 3D printed, bio-inspired prototypes and analytical models for structured suture interfaces with geometrically-tuned deformation and failure behavior. *Journal of the Mechanics and Physics of Solids*, 73:166 – 182, 2014.

[91] F. A. Cordisco, P. D. Zavattieri, L. G. Hector and A. F. Bower. Toughness of a patterned interface between two elastically dissimilar solids. *Engineering Fracture Mechanics*, 96:192 – 208, 2012.

[92] F. A. Cordisco, P. D. Zavattieri, L. G. Hector and B. E. Carlson. Mode I fracture along adhesively bonded sinusoidal interfaces. *International Journal of Solids and Structures*, 83:45 – 64, 2016.

[93] N. Suksangpanya, N. A. Yaraghi, D. Kisailus and P. Zavattieri. Twisting cracks in Bouligand structures. *Journal of the Mechanical Behavior of Biomedical Materials*, 76:38 – 57, 2017.

[94] N. Suksangpanya, N. A. Yaraghi, R. B. Pipes, D. Kisailus and P. Zavattieri. Crack twisting and toughening strategies in Bouligand architectures. *International Journal of Solids and Structures*, 150:83 – 106, 2018.

[95] M. S. Hosseini, F. A. Cordisco and P. D. Zavattieri. Analysis of bioinspired non-interlocking geometrically patterned interfaces under predominant mode I loading. *Journal of the Mechanical Behavior of Biomedical Materials*, 96:244 – 260, 2019.

[96] M. A. Meyers, P. Y. Chen, A. Y. M. Lin and Y. Seki. Biological materials: Structure and mechanical properties. *Progress in Materials Science*, 53(1):1 – 206, 2008.

[97] N. Lee, M.F. Horstemeyer, H. Rhee, B. Nabors, J. Liao and N.L. Williams. Hierarchical multiscale structure–property relationships of the red-bellied woodpecker (melanerpes carolinus) beak. *Journal of the Royal Society Interface*, 11(96):014009, 2014.

[98] J. Cray Jr, M. P. Mooney and M. I. Siegel. Timing of ectocranial suture activity in pan troglodytes as related to cranial volume and dental eruption. *The Anatomical Record*, 293(8):1289 – 1296, 2010.

[99] C. W. Hull. Apparatus for production of three-dimensional objects by stereolithography. *US Patent 4575330*, 1986.

[100] B. Bhushan and M. Caspers. An overview of additive manufacturing (3D printing) for microfabrication. *Microsystem Technologies*, 23(4):1117 – 1124, 2017.

[101] N. van de Werken, J. Hurley, P. Khanbolouki, A. N. Sarvestani, A. Y. Tamijani and M. Tehrani. Design considerations and modeling of fiber reinforced 3D printed parts. *Composites Part B: Engineering*, 160:684 – 692, 2019.

[102] B. Utela, D. Storti, R. Anderson and M. Ganter. A review of process development steps for new material systems in three dimensional printing (3DP). *Journal of Manufacturing Processes*, 10(2):96 – 104, 2008.

[103] H. Lee, C. H. J. Lim, M. J. Low, N. Tham, V. M. Murukeshan and Y. J. Kim. Lasers in additive manufacturing: A review. *International Journal of Precision Engineering and Manufacturing-Green Technology*, 4(3):307 – 322, 2017.

[104] N. Travitzky, A. Bonet, B. Dermeik, T. Fey, I. Filbert-Demut, L. Schlier, T. Schlordt and P. Greil. Additive manufacturing of ceramic-based materials. *Advanced Engineering Materials*, 16(6):729 – 754, 2014.

[105] Y. Bai and C. Williams. An exploration of binder jetting of copper. *Rapid Prototyping Journal*, 21:177 – 185, 03 2015.

[106] A. Sova, S. Grigoriev, A. Okunkova and I. Smurov. Potential of cold gas dynamic spray as additive manufacturing technology. *The International Journal of Advanced Manufacturing Technology*, 69(9):2269 – 2278, 2013.

[107] W. Chen, L. Thornley, H. G. Coe, S. J. Tonneslan, J. J. Vericella, C. Zhu, E. B. Duoss, Ryan M. Hunt, M. J. Wight, D. Apelian, A. J. Pascall, J. D. Kuntz and C. M. Spadaccini. Direct metal writing: Controlling the rheology through microstructure. *Applied Physics Letters*, 110(9):094104, 2017.

[108] X. Wang, M. Jiang, Z. Zhou, J. Gou and D. Hui. 3D printing of polymer matrix composites: A review and prospective. *Composites Part B: Engineering*, 110:442 – 458, 2017.

[109] A. Takezawa and M. Kobashi. Design methodology for porous composites with tunable thermal expansion produced by multi-material topology optimization and additive manufacturing. *Composites Part B: Engineering*, 131:21 – 29, 2017.

[110] P. Parandoush and D. Lin. A review on additive manufacturing of polymer-fiber composites. *Composite Structures*, 182:36 – 53, 2017.

[111] F.S. Senatov, K.V. Niaza, A.A. Stepashkin and S.D. Kaloshkin. Low-cycle fatigue behavior of 3d-printed pla-based porous scaffolds. *Composites Part B: Engineering*, 97:193 – 200, 2016.

[112] S. Dul, L. Fambri and A. Pegoretti. Fused deposition modelling with abs–graphene nanocomposites. *Composites Part A: Applied Science and Manufacturing*, 85:181 – 191, 2016.

[113] K.S. Boparai, R. Singh, F. Fabbrocino and F. Fraternali. Thermal characterization of recycled polymer for additive manufacturing applications. *Composites Part B: Engineering*, 106:42 – 47, 2016.

[114] X. Li, M. Gao and Y. Jiang. Microstructure and mechanical properties of porous alumina ceramic prepared by a combination of 3–D printing and sintering. *Ceramics International*, 42(10):12531 – 12535, 2016.

[115] J. Maurath and N. Willenbacher. 3D printing of open-porous cellular ceramics with high specific strength. *Journal of the European Ceramic Society*, 37(15):4833 – 4842, 2017.

[116] B. Khoshnevis. Automated construction by contour crafting—related robotics and information technologies. *Automation in Construction*, 13(1):5 – 19, 2004.

[117] A. A. Hassen, R. Springfield, J. Lindahl, B. Post, L. Love, C. Duty, U. Vaidya, R. B. Pipes and V. Kunc. The durability of large-scale additive manufacturing composite molds. *CAMX 2016 Conference*, 2016.

[118] V. Kunc, J. Lindahl, R. Dinwiddie, B. Post, L. Love, C. Duty, M. Matlack, R. Fahey Jr and A. A. Hassen. Investigation of in-autoclave additive manufacturing composite tooling. *CAMX 2016 Conference*, 2016.

[119] A. Roschli, K. T. Gaul, A. M. Boulger, B. K. Post, P. C. Chesser, L. J. Love, F. Blue and M. Borish. Designing for big area additive manufacturing. *Additive Manufacturing*, 25:275 – 285, 2019.

[120] Thermwood announces vertical layer printing. *Reinforced Plastics*, 63(1):20, 2019.

[121] L. J. Love, V. Kunc, O. Rios, C. E. Duty, A. M. Elliott, B. K. Post, R. J. Smith and C. A. Blue. The importance of carbon fiber to polymer additive manufacturing. *Journal of Materials Research*, 29(17):1893 – 1898, 2014.

[122] W. Zhong, F. Li, Z. Zhang, L. Song and Z. Li. Short fiber reinforced composites for fused deposition modeling. *Materials Science and Engineering: A*, 301(2):125 – 130, 2001.

[123] M.L. Shofner, K. Lozano, F.J. Rodríguez-Macías and E.V. Barrera. Nanofiber-reinforced polymers prepared by fused deposition modeling. *Journal of Applied Polymer Science*, 89(11):3081 – 3090, 2003.

[124] J. Gardner, G. Sauti, J. W. Kim, R. Cano, R. Wincheski, C. Stelter, B. Grimsley, D. Working and E. Siochi. 3-D printing of multifunctional carbon nanotube yarn reinforced components. *Additive Manufacturing*, 12:38 – 44, 2016.

[125] R. Matsuzaki, M. Ueda, M. Namiki, J. Tae-Kun, H. Asahara, K. Horiguchi, T. Nakamura, A. Todoroki and Y. Hirano. Three-dimensional printing of continuous-fiber composites by in-nozzle impregnation. *Scientific Reports*, 6:23058, 2016.

[126] F. van der Klift, Y. Koga, A. Todoroki, M. Ueda, Y. Hirano and R. Matsuzaki. 3D printing of Continuous Carbon Fibre Reinforced Thermo-Plastic (CFRTP) tensile test specimens. *Open Journal of Composite Materials*, 06:18 – 27, 2016.

[127] G. W. Melenka, B. K.O. Cheung, J. S. Schofield, M. R. Dawson and J. P. Carey. Evaluation and prediction of the tensile properties of continuous fiber-reinforced 3D printed structures. *Composite Structures*, 153:866 – 875, 2016.

[128] B. Brenken, E. Barocio, A. Favaloro, V. Kunc and R. B. Pipes. Fused filament fabrication of fiber-reinforced polymers: A review. *Additive Manufacturing*, 21:1 – 16, 2018.

[129] Z. X. Khoo, J. E. M. Teoh, Y. Liu, C. K. Chua, S. Yang, J. An, K. F. Leong and W. Y. Yeong. 3D printing of smart materials: A review on recent progresses in 4D printing. *Virtual and Physical Prototyping*, 10(3):103 – 122, 2015.

[130] H.Z. Lu, C. Yang, X. Luo, H.W. Ma, B. Song, Y.Y. Li and L.C. Zhang. Ultrahigh-performance TiNi shape memory alloy by 4D printing. *Materials Science and Engineering: A*, 763:138166, 2019.

[131] M. P. Caputo, A. E. Berkowitz, A. Armstrong, P. Müllner and C. V. Solomon. 4D printing of net shape parts made from Ni-Mn-Ga magnetic shape-memory alloys. *Additive Manufacturing*, 21:579 – 588, 2018.

[132] Y. Y. C. Choong, S. Maleksaeedi, H. Eng, J. Wei and P. C. Su. 4D printing of high performance shape memory polymer using stereolithography. *Materials & Design*, 126:219 – 225, 2017.

[133] B. Hao, Y. Li, X. Xiao, W. Dai, H. Chen and S. Chen. A facile photo-polymerization method for reconfigurable shape memory polymers. *Materials Letters*, 254:214 – 217, 2019.

[134] Y. S. Lui, W. T. Sow, L. P. Tan, Y. Wu, Y. Lai and H. Li. 4D printing and stimuli-responsive materials in biomedical aspects. *Acta Biomaterialia*, 92:19 – 36, 2019.

[135] Y. Liu, W. Zhang, F. Zhang, X. Lan, J. Leng, S. Liu, X. Jia, C. Cotton, B. Sun, B. Gu and T. W. Chou. Shape memory behavior and recovery force of 4D printed laminated miura-origami structures subjected to compressive loading. *Composites Part B: Engineering*, 153:233 – 242, 2018.

[136] O. Volkersen. Die niektraftverteilung in zugbeanspruchten mit konstanten laschenquerschritten. *Luftfahrtforschung*, 15:41 – 47, 1938.

[137] L.J. Hart-Smith. Adhesive-bonded single-lap joints. Technical report, National Aeronautics and Space Administration, 1973.

[138] S. Srinivas. Analysis of bonded joints. Technical report, National Aeronautics and Space Administration, 1975.

[139] C. Yang and S. S. Pang. Stress-strain analysis of adhesive-bonded single-lap composite joints under cylindrical bending. *Composites Engineering*, 3(11):1051 – 1063, 1993.

[140] L. Tong. An assessment of failure criteria to predict the strength of adhesively bonded composite double lap joints. *Journal of Reinforced Plastics and Composites*, 16(8):698 – 713, 1997.

[141] Y. Frostig, O. T. Thomsen and F. Mortensen. Analysis of adhesive-bonded joints, square-end, and spew-fillet—high-order theory approach. *Journal of Engineering Mechanics*, 125(11):1298 – 1307, 1999.

[142] P. J. C. das Neves, L.F.M. Silva and R. Adams. Analysis of mixed adhesive bonded joints Part I: Theoretical formulation. *Journal of Adhesion Science and Technology*, 23:1 – 34, 2009.

[143] F. Mortensen and O.T. Thomsen. Analysis of adhesive bonded joints: a unified approach. *Composites Science and Technology*, 62(7):1011 – 1031, 2002.

[144] C. Yang, H. Huang, J. S. Tomblin and W. Sun. Elastic-plastic model of adhesive-bonded single-lap composite joints. *Journal of Composite Materials*, 38(4):293 – 309, 2004.

[145] B. Bednarcyk, Y. Bansal, C. S. Collier, M. J. Pindera and J. Zhang. Analysis tools for adhesively bonded composite joints, Part 1: Higher-order theory. *AIAA Journal*, 44:171 – 180, 2006.

[146] J. Zhang, B. Bednarcyk, C. S. Collier, P. Yarrington, Y. Bansal and M. J. Pindera. Analysis tools for adhesively bonded composite joints, Part 2: Unified analytical theory. *AIAA Journal*, 44:1709 – 1719, 2006.

[147] J.A. Harris and R.A. Adams. Strength prediction of bonded single lap joints by non-linear finite element methods. *International Journal of Adhesion and Adhesives*, 4(2):65 – 78, 1984.

[148] R. D. Adams, R. W. Atkins, J. A. Harris and A. J. Kinloch. Stress analysis and failure properties of carbon-fibre-reinforced-plastic/steel double-lap joints. *The Journal of Adhesion*, 20(1):29–53, 1986.

[149] R.D. Adams and J.A. Harris. The influence of local geometry on the strength of adhesive joints. *International Journal of Adhesion and Adhesives*, 7(2):69 – 80, 1987.

[150] J.W. Hutchinson and Z. Suo. Mixed mode cracking in layered materials. *Advances in Applied Mechanics*, 29:63 – 191, 1991.

[151] J. Q. Xu, Y. H. Liu and X. G. Wang. Numerical methods for the determination of multiple stress singularities and related stress intensity coefficients. *Engineering Fracture Mechanics*, 63(6):775 – 790, 1999.

[152] H.L. Groth. Stress singularities and fracture at interface corners in bonded joints. *International Journal of Adhesion and Adhesives*, 8(2):107 – 113, 1988.

[153] A. Barroso, V. Mantič and F. París. Singularity analysis of anisotropic multimaterial corners. *International Journal of Fracture*, 119(1):1 – 23, 2003.

[154] A. Barroso, V. Mantič and F. París. Singularity parameter determination in adhesively bonded lap joints for use in failure criteria. *Composites Science and Technology*, 68(13):2671 – 2677, 2008.

[155] A. Barroso, V. Mantič and F. París. Computing stress singularities in transversely isotropic multimaterial corners by means of explicit expressions of the orthonormalized Stroh-eigenvectors. *Engineering Fracture Mechanics*, 76(2):250 – 268, 2009.

[156] T. Ungsuwarungsri and W. G. Knauss. The role of damage-softened material behavior in the fracture of composites and adhesives. *International Journal of Fracture*, 35(3):221 – 241, 1987.

[157] B. F. Sørensen and T. K. Jacobsen. Determination of cohesive laws by the J-integral approach. *Engineering Fracture Mechanics*, 70(14):1841 – 1858, 2003.

[158] S. Li, M. D. Thouless, A. M. Waas, J. A. Schroeder and P. D. Zavattieri. Use of mode-I cohesive-zone models to describe the fracture of an adhesively-bonded polymer-matrix composite. *Composites Science and Technology*, 65(2):281 – 293, 2005.

[159] S. Li, M. D. Thouless, A. M. Waas, J. A. Schroeder and P. D. Zavattieri. Use of a cohesive-zone model to analyze the fracture of a fiber-reinforced polymer–matrix composite. *Composites Science and Technology*, 65(3):537 – 549, 2005.

[160] S. Li, M. D. Thouless, A. M. Waas, J. A. Schroeder and P. D. Zavattieri. Competing failure mechanisms in mixed-mode fracture of an adhesively bonded polymer-matrix composite. *International Journal of Adhesion and Adhesives*, 26(8):609 – 616, 2006.

[161] S. Li, M. D. Thouless, A. M. Waas, J. A. Schroeder and P. D. Zavattieri. Mixed-mode cohesive-zone models for fracture of an adhesively bonded polymer–matrix composite. *Engineering Fracture Mechanics*, 73(1):64 – 78, 2006.

[162] B. Ren and S. Li. Multiscale modeling and prediction of bonded joint failure by using an adhesive process zone model. *Theoretical and Applied Fracture Mechanics*, 72:76 – 88, 2014.

[163] D. C. O'Mahoney, K. B. Katnam, N. P. O'Dowd, C. T. McCarthy and T. M. Young. Taguchi analysis of bonded composite single-lap joints using a combined interface–adhesive damage model. *International Journal of Adhesion and Adhesives*, 40:168 – 178, 2013.

[164] R. D. S. G. Campilho, M. D. Banea, A. M. G. Pinto, L. F. M. da Silva and A. M. P. de Jesus. Strength prediction of single- and double-lap joints by standard and extended finite element modelling. *International Journal of Adhesion and Adhesives*, 31(5):363 – 372, 2011.

[165] S. Sugiman, A.D. Crocombe and I.A. Aschroft. Modelling the static response of unaged adhesively bonded structures. *Engineering Fracture Mechanics*, 98:296 – 314, 2013.

[166] R.D.S.G. Campilho, M.D. Banea, J.A.B.P. Neto and L.F.M. da Silva. Modelling adhesive joints with cohesive zone models: effect of the cohesive law shape of the adhesive layer. *International Journal of Adhesion and Adhesives*, 44:48 – 56, 2013.

[167] M.D. Banea, L.F.M. da Silva and R.D.S.G. Campilho. Mode I fracture toughness of adhesively bonded joints as a function of temperature: Experimental and numerical study. *International Journal of Adhesion and Adhesives*, 31(5):273 – 279, 2011.

[168] A. P. Vassilopoulos. *Fatigue and fracture of adhesively-bonded composite joints*. Elsevier, 2014.

[169] D. Álvarez, B.R.K. Blackman, F.J. Guild and A.J. Kinloch. Mode I fracture in adhesively-bonded joints: A mesh-size independent modelling approach using cohesive elements. *Engineering Fracture Mechanics*, 115:73 – 95, 2014.

[170] I. Guiamatsia, J.K. Ankersen, G.A.O. Davies and L. Iannucci. Decohesion finite element with enriched basis functions for delamination. *Composites Science and Technology*, 69(15):2616 – 2624, 2009.

[171] C.L. Tsai, Y.L. Guan, D.C. Ohanehi, J.G. Dillard, D.A. Dillard and R.C. Batra. Analysis of cohesive failure in adhesively bonded joints with the SSPH meshless method. *International Journal of Adhesion and Adhesives*, 51:67 – 80, 2014.

[172] Y. T. Kim, M. J. Lee and B. C. Lee. Simulation of adhesive joints using the superimposed finite element method and a cohesive zone model. *International Journal of Adhesion and Adhesives*, 31(5):357 – 362, 2011.

[173] J. Cañas, L. Távara, A. Blázquez, A. Estefani and G. Santacruz. A new in situ peeling test for the characterisation of composite bonded joints. *Composites Part A: Applied Science and Manufacturing*, 113:298 – 310, 2018.

[174] M. Muñoz-Reja, L. Távara, V. Mantič and P. Cornetti. Crack onset and propagation in composite materials using finite fracture mechanics on elastic interfaces. *Procedia Materials Science*, 3:1365 – 1370, 2014.

[175] L. Távara, V. Mantič, E. Graciani and F. París. Modelling interfacial debonds in unidirectional fibre-reinforced composites under biaxial transverse loads. *Composite Structures*, 136:305 – 312, 2016.

[176] J. E. Marsden and T. Hughes. *Mathematical foundations of elasticity*. Courier Corporation, 1994.

[177] J. Bonet and R. D. Wood. *Nonlinear Continuum Mechanics for Finite Element Analysis*. Cambridge University Press, 2 edition, 2008.

[178] O. C. Zienkiewicz, R. L. Taylor and J. Z. Zhu. *The finite element method: its basis and fundamentals*. Elsevier, 2005.

[179] T. L. Anderson. *Fracture mechanics: fundamentals and applications*. CRC press, 2017.

[180] A. A. Griffith. The phenomena of rupture and flow in solids. *Philosophical Transactions of the Royal Society of London. Series A, containing papers of a mathematical or physical character*, 221:163 – 198, 1921.

[181] G.R. Irwin. Analysis of stresses and strains near the end of a crack traversing a plate. *Journal of Applied Mechanics*, 24:361 – 364, 1957.

[182] E.G. Kirsch. Die theorie der elastizität und die bedürfnisse der festigkeitslehre. *Zeitschrift des Vereines deutscher Ingenieure*, 42:797 – 807, 1898.

[183] C. E. Inglis. Stresses in plates due to the presence of cracks and sharp corners. *Transactions of the Institute of Naval Architects*, 55:219 – 241, 1913.

[184] ISO 15024:2001 fibre-reinforced plastic composites – determination of mode I interlaminar fracture toughness, GIC, for unidirectionally reinforced materials. Technical report, 2001.

[185] ASTM D5528-13, Standard Test Method for Mode I Interlaminar Fracture Toughness of Unidirectional Fiber-Reinforced Polymer Matrix Composites. Technical report, 2013.

[186] H. M. Westergaard. Bearing pressures and cracks. *Journal of Applied Mechanics*, 6:49 – 53, 1939.

[187] I. N. Sneddon. The distribution of stress in the neighbourhood of a crack in an elastic solid. *Proceedings of the Royal Society of London A: Mathematical, Physical and Engineering Sciences*, 187(1009):229 – 260, 1946.

[188] M. L. Williams. On the stress distribution at the base of a stationary crack. *Journal of Applied Mechanics*, 24:109 – 114, 1957.

[189] J. Rice. A path independent integral and the approximate analysis of strain concentration by notched and cracks. *Journal of Applied Mechanics*, 35:379 – 386, 1968.

[190] J.R. Rice and G.F. Rosengren. Plane strain deformation near a crack tip in a power-law hardening material. *Journal of the Mechanics and Physics of Solids*, 16(1):1 – 12, 1968.

[191] M. L. Williams. The stresses around a fault or crack in dissimilar media. *Bulletin of the Seismological Society of America*, 49(2):199 – 204, 1959.

[192] G. C. Sih and J. Rice. The bending of plates of dissimilar materials with cracks. *Journal of Applied Mechanics*, 31(3):477 – 482, 1964.

[193] A. H. England. A crack between dissimilar media. *Journal of Applied Mechanics*, 32(2):400 – 402, 1965.

[194] F. Erdogan. Stress distribution in bonded dissimilar materials with cracks. *Journal of Applied Mechanics*, 32(2):403 – 410, 1965.

[195] J. Rice and G. C. Sih. Plane problems of cracks in dissimilar media. *Journal of Applied Mechanics*, 32(2):418 – 423, 1965.

[196] M. Comninou. The interface crack. *Journal of Applied Mechanics*, 44(4):631 – 636, 1977.

[197] M. Comninou. The interface crack in a shear field. *Journal of Applied Mechanics*, 45(2):287 – 290, 1978.

[198] J. W. Hutchinson, M. E. Mear and J. Rice. Crack paralleling an interface between dissimilar materials. *Journal of Applied Mechanics*, 54(4):828 – 832, 1987.

[199] H.C. Cao and A.G. Evans. An experimental study of the fracture resistance of bimaterial interfaces. *Mechanics of Materials*, 7(4):295 – 304, 1989.

[200] J. S. Wang and Z. Suo. Experimental determination of interfacial toughness curves using brazil-nut-sandwiches. *Acta Metallurgica et Materialia*, 38(7):1279 – 1290, 1990.

[201] J. S. Wang. Interfacial fracture toughness of a copper/alumina system and the effect of the loading phase angle. *Mechanics of Materials*, 20(3):251 – 259, 1995.

[202] T. Ikeda, N. Miyazaki and T. Soda. Mixed mode fracture criterion of interface crack between dissimilar materials. *Engineering Fracture Mechanics*, 59(6):725 – 735, 1998.

[203] L. Banks-Sills, N. Travitzky, D. Ashkenazi and R. Eliasi. A methodology for measuring interface fracture toughness of composite materials. *International Journal of Fracture*, 99:143 – 161, 1999.

[204] L. Banks-Sills, N. Travitzky and D. Ashkenazi. Interface fracture properties of a bimaterial ceramic composite. *Mechanics of Materials*, 32(12):711 – 722, 2000.

[205] L. Banks-Sills. Interface fracture mechanics: theory and experiment. *International Journal of Fracture*, 191(1):131 – 146, 2015.

[206] G.I Barenblatt. The formation of equilibrium cracks during brittle fracture. General ideas and hypotheses. Axially-symmetric cracks. *Journal of Applied Mathematics and Mechanics*, 23(3):622 – 636, 1959.

[207] G.I. Barenblatt. The mathematical theory of equilibrium cracks in brittle fracture. *Advances in Applied Mechanics*, 7:55 – 129, 1962.

[208] D.S. Dugdale. Yielding of steel sheets containing slits. *Journal of the Mechanics and Physics of Solids*, 8(2):100 – 104, 1960.

[209] A. Needleman. A continuum model for void nucleation by inclusion debonding. *Journal of Applied Mechanics*, 54:525 – 532, 1987.

[210] A. Needleman. An analysis of tensile decohesion along an interface. *Journal of the Mechanics and Physics of Solids*, 38(3):289 – 324, 1990.

[211] A. Needleman. An analysis of decohesion along an imperfect interface. *International Journal of Fracture*, 42:21 – 40, 1990.

[212] J. R. Rice and J. S. Wang. Embrittlement of interfaces by solute segregation. *Materials Science and Engineering: A*, 107:23 – 40, 1989.

[213] V. Tvergaard and J. W. Hutchinson. The relation between crack growth resistance and fracture process parameters in elastic-plastic solids. *Journal of the Mechanics and Physics of Solids*, 40(6):1377 – 1397, 1992.

[214] G.T. Camacho and M. Ortiz. Computational modelling of impact damage in brittle materials. *International Journal of Solids and Structures*, 33(20):2899 – 2938, 1996.

[215] P. H. Geubelle and J. S. Baylor. Impact-induced delamination of composites: a 2D simulation. *Composites Part B: Engineering*, 29(5):589 – 602, 1998.

[216] J. Reinoso and M. Paggi. A consistent interface element formulation for geometrical and material nonlinearities. *Computational Mechanics*, 54(6):1569 – 1581, 2014.

[217] M. Paggi and J. Reinoso. Revisiting the problem of a crack impinging on an interface: a modeling framework for the interaction between the phase field approach for brittle fracture and the interface cohesive zone model. *Computer Methods in Applied Mechanics and Engineering*, 321:145 – 172, 2017.

[218] A. Turon, P.P. Camanho, J. Costa and C.G. Dávila. A damage model for the simulation of delamination in advanced composites under variable-mode loading. *Mechanics of Materials*, 38(11):1072 – 1089, 2006.

[219] C. Sarrado, A. Turon, J. Renart and I. Urresti. Assessment of energy dissipation during mixed-mode delamination growth using cohesive zone models. *Composites Part A: Applied Science and Manufacturing*, 43(11):2128 – 2136, 2012.

[220] A. Turon, P.P. Camanho, J. Costa and J. Renart. Accurate simulation of delamination growth under mixed-mode loading using cohesive elements: Definition of interlaminar strengths and elastic stiffness. *Composite Structures*, 92(8):1857 – 1864, 2010.

[221] P.D. Zavattieri, L.G. Hector Jr and A.F. Bower. Cohesive zone simulations of crack growth along a rough interface between two elastic-plastic solids. *Engineering Fracture Mechanics*, 75:4309 – 4332, 2008.

[222] J. Reinoso, M. Paggi and A. Blázquez. A nonlinear finite thickness cohesive interface element for modeling delamination in fibre-reinforced composite laminates. *Composites Part B: Engineering*, 109:116 – 128, 2017.

[223] C. Sarrado, F. A. Leone and A. Turon. Finite-thickness cohesive elements for modeling thick adhesives. *Engineering Fracture Mechanics*, 168:105 – 113, 2016.

[224] W.C. Cui, M.R. Wisnom and M. Jones. A comparison of failure criteria to predict delamination of unidirectional glass/epoxy specimens waisted through the thickness. *Composites*, 23(3):158 – 166, 1992.

[225] M.L. Benzeggagh and M. Kenane. Measurement of mixed-mode delamination fracture toughness of unidirectional glass/epoxy composites with mixed-mode bending apparatus. *Composites Science and Technology*, 56(4):439 – 449, 1996.

[226] V. Mantič, L. Távara, A. Blázquez, E. Graciani and F. París. A linear elastic-brittle interface model: application for the onset and propagation of a fibre-matrix interface crack under biaxial transverse loads. *International Journal of Fracture*, 195(1-2):15 – 38, 2015.

[227] S. Lenci. Analysis of a crack at a weak interface. *International Journal of Fracture*, 108(3):275 – 290, 2001.

[228] Z. Hashin. Thin interphase/imperfect interface in elasticity with application to coated fiber composites. *Journal of the Mechanics and Physics of Solids*, 50(12):2509 – 2537, 2002.

[229] A. Carpinteri, P. Cornetti and N. Pugno. Edge debonding in FRP strengthened beams: Stress versus energy failure criteria. *Engineering Structures*, 31(10):2436 – 2447, 2009.

[230] L. Távara, V. Mantič, E. Graciani, J. Cañas and F. París. Analysis of a crack in a thin adhesive layer between orthotropic materials. An application to composite interlaminar fracture toughness test. *Computer Modeling in Engineering and Sciences*, 58(3):247 – 270, 2010.

[231] L. Prandtl and W. G. Knauss. A thought model for the fracture of brittle solids. *International Journal of Fracture*, 171(2):105 – 109, 2011.

[232] N. F. Mott. Fracture of metals: theoretical considerations. *Engineering*, 165(14):16 – 18, 1948.

[233] L. Távara, V. Mantič, E. Graciani and F. París. BEM analysis of crack onset and propagation along fiber–matrix interface under transverse tension using a linear elastic–brittle interface model. *Engineering Analysis with Boundary Elements*, 35(2):207 – 222, 2011.

[234] L. Škec, G. Alfano and G. Jelenić. On Gc, Jc and the characterisation of the mode-I fracture resistance in delamination or adhesive debonding. *International Journal of Solids and Structures*, 144:100 – 122, 2018.

[235] K. Bertoldi, D. Bigoni and W. J. Drugan. Structural interfaces in linear elasticity. Part I: Nonlocality and gradient approximations. *Journal of the Mechanics and Physics of Solids*, 55(1):1 – 34, 2007.

[236] K. Bertoldi, D. Bigoni and W. J. Drugan. Structural interfaces in linear elasticity. Part II: Effective properties and neutrality. *Journal of the Mechanics and Physics of Solids*, 55(1):35 – 63, 2007.

[237] K. Bertoldi, D. Bigoni and W. J. Drugan. A discrete-fibers model for bridged cracks and reinforced elliptical voids. *Journal of The Mechanics and Physics of Solids*, 55:1016 – 1035, 2007.

[238] M. Paggi and P. Wriggers. Stiffness and strength of hierarchical polycrystalline materials with imperfect interfaces. *Journal of the Mechanics and Physics of Solids*, 60(4):557–572, 2012.

[239] M. Paggi. Crack propagation in honeycomb cellular materials: A computational approach. *Metals*, 2:65 – 78, 2012.

[240] Y. Zhang, H. Yao, C. Ortiz, J. Xu and M. Dao. Bio-inspired interfacial strengthening strategy through geometrically interlocking designs. *Journal of the Mechanical Behavior of Biomedical Materials*, 15:70 – 77, 2012.

[241] H. A. Bruck, G. Fowler, S. K. Gupta and T. M Valentine. Using geometric complexity to enhance the interfacial strength of heterogeneous structures fabricated in a multi-stage, multi-piece molding process. *Experimental Mechanics*, 44:261 – 271, 2012.

[242] N. Mohan, P. Senthil, S. Vinodh and N. Jayanth. A review on composite materials and process parameters optimisation for the fused deposition modelling process. *Virtual and Physical Prototyping*, 12(1):47 – 59, 2017.

[243] H. Prüß and T. Vietor. Design for fiber-reinforced additive manufacturing. *Journal of Mechanical Design*, 137(11):111409, 2015.

[244] J. Justo, L. Távara, L. García-Guzmán and F. París. Characterization of 3D printed long fibre reinforced composites. *Composite Structures*, 185:537 – 548, 2018.

[245] X. Tian, T. Liu, C. Yang, Q. Wang and D. Li. Interface and performance of 3D printed continuous carbon fiber reinforced PLA composites. *Composites: Part A*, 88:198 – 205, 2016.

[246] N. Li, Y. Li and S. Liu. Rapid prototyping of continuous carbon fiber reinforced polylacticacid composites by 3D printing. *Journal of Materials Processing Technology*, 238:218 – 225, 2016.

[247] F. Ning, W. Cong, J. Qiu, J. Wei and S. Wang. Additive manufacturing of carbon fiber reinforced thermoplastic composites using fused deposition modeling. *Composites Part B: Engineering*, 80:369 – 378, 2015.

[248] R. H. Sanatgara, C. Campagne and V. Nierstrasza. Investigation of the adhesion properties of direct 3D printing of polymers and nanocomposites on textiles: Effect of FDM printing process parameters. *Applied Surface Science*, 403:551 – 563, 2017.

[249] AITM 1-0053 - Carbon Fibre Reinforced Plastics. Determination of fracture toughness energy of bonded joints. Mode I. G1C. Issue 1. Technical report, Airbus, 2009.

[250] G. Bresson, J. Jumel, M. E. R Shanahan and P. Serin. Statistical aspects of the mechanical behaviour a paste adhesive. *International Journal of Adhesion & Adhesives*, 40:70 – 79, 2013.

[251] A. Srivastava, S. Osovski and A. Needleman. Engineering the crack path by controlling the microstructure. *Journal of the Mechanics and Physics of Solids*, 100:1 – 20, 2017.

[252] K. Maloney and N. Fleck. Damage tolerance of an architected adhesive joint. *International Journal of Solids and Structures*, 132:9 – 19, 2018.

[253] A. Carpinteri, M. Paggi and G. Zavarise. The effect of contact on the decohesion of laminated beams with multiple microcracks. *International Journal of Solids and Structures*, 45(1):129 – 143, 2008.

[254] P. P. Camanho and C. G. Dávila. Mixed-mode decohesion finite elements for the simulation of delamination in composite materials. *NASA Technical Report*, NASA/TM-2002–211737:1 – 37, 2002.

[255] L. García-Guzmán, L. Távara, J. Reinoso, J. Justo and F. París. Fracture resistance of 3D printed adhesively bonded DCB composite specimens using structured interfaces: Experimental and theoretical study. *Composite Structures*, 188:173 – 184, 2018.

[256] N. A. Fleck, V. S. Deshpande and M. F. Ashby. Micro-architectured materials: past, present and future. *Proceedings of the Royal Society of London A: Mathematical, Physical and Engineering Sciences*, 466(2121):2495 – 2516, 2010.

[257] S. Wu, X. Liu, K. W. K. Yeung, H. Guo, P. Li, T. Hu, C. Y. Chung and P. K. Chu. Surface nano-architectures and their effects on the mechanical properties and corrosion behavior of Ti-based orthopedic implants. *Surface and Coatings Technology*, 233:13 – 26, 2013.

[258] Y. An, J. Han, X. Zhang, W. Han, Y. Cheng, P. Hu and G. Zhao. Bioinspired high toughness graphene/zrb2 hybrid composites with hierarchical architectures spanning several length scales. *Carbon*, 107:209 – 216, 2016.

[259] N. Liang, J. Liu, S. Lin, Y. Wang, J. T. Wang, Y. Zhao and Y. Zhu. A multiscale architectured CuCrZr alloy with high strength, electrical conductivity and thermal stability. *Journal of Alloys and Compounds*, 735:1389 – 1394, 2018.

[260] J. W. C. Dunlop and P. Fratzl. Multilevel architectures in natural materials. *Scripta Materialia*, 68(1):8 – 12, 2013.

[261] A. Vigliotti, R. M. McMeeking and V. S. Deshpande. Simulation of the cytoskeletal response of cells on grooved or patterned substrates. *Journal of The Royal Society Interface*, 12(105):20141320, 2015.

[262] M. R. O'Masta, L. Dong, L. St-Pierre, H. N. G. Wadley and V. S. Deshpande. The fracture toughness of octet-truss lattices. *Journal of the Mechanics and Physics of Solids*, 98:271 – 289, 2017.

[263] F. Côtè, V. S. Deshpande, N. A. Fleck and A. G. Evans. The compressive and shear responses of corrugated and diamond lattice materials. *International Journal of Solids and Structures*, 43(20):6220 – 6242, 2006.

[264] Q. Wu, Y. Gao, X. Wei, D. Mousanezhad, L. Ma, A. Vaziri and J. Xiong. Mechanical properties and failure mechanisms of sandwich panels with ultra-lightweight three-dimensional hierarchical lattice cores. *International Journal of Solids and Structures*, 132:171 – 187, 2018.

[265] T. Miura, C. A. Perlyn, M. Kinboshi, N. Ogihara, M. Kobayasi-Miura, G. M. Morris-Kay and K. Shiota. Mechanism of skull suture maintenance and interdigitation. *Journal of Anatomy*, 215(6):642 – 655, 2009.

[266] W. Zhang, C. Wu, C. Zhang and Z. Chen. Microstructure and mechanical property of turtle shell. *Theoretical and Applied Mechanics Letters*, 2(1):014009, 2012.

[267] T. R. Guess, E. D. Reedy and M. E. Stavig. Mechanical properties of Hysol EA-9394 structural adhesive. Technical report, Sandia National Laboratories, 1995.

[268] R. D. S. G. Campilho, M. F. S. F. de Moura, D. A. Ramantani, J. J. L. Morais and J. J. M. S. Domingues. Tensile behaviour of three-dimensional carbon-epoxy adhesively bonded single- and double-strap repairs. *International Journal of Adhesion and Adhesives*, 29(6):678 – 686, 2009.

[269] ASTM D3433-99, Standard test method for fracture strength in cleavage of adhesives in bonded metal joints. Technical report, ASTM International, 2012.

[270] ISO 25217:2009, Adhesives – Determination of the mode 1 adhesive fracture energy of structural adhesive joints using double cantilever beam and tapered double cantilever beam specimens. Technical report, 2009.

[271] C. Sarrado, A. Turon, J. Renart and J. Costa. An experimental data reduction method for the mixed mode bending test based on the J-integral approach. *Composites Science and Technology*, 117:85 – 91, 2015.

[272] J. L. Högberg, B. F. Sørensen and U. Stigh. Constitutive behaviour of mixed mode loaded adhesive layer. *International Journal of Solids and Structures*, 44(25):8335 – 8354, 2007.

[273] L. García-Guzmán, L. Távara, J. Reinoso and F. París. Fracture energy characterisation of a structured interface by means of a novel J-Integral procedure. *The Journal of Strain Analysis for Engineering Design*, Special Issue Article, 2019.

[274] R. H. Rigby and M. H. Aliabadi. Decomposition of the mixed-mode J-integral—revisited. *International Journal of Solids and Structures*, 35(17):2073 – 2099, 1998.

[275] *ABAQUS/Standard User's Manual, Version 6.14*. Simulia, 2014.

[276] M. Conroy, A. J. Kinloch, J. G. Williams and A. Ivankovic. Mixed mode partitioning of beam-like geometries: A damage dependent solution. *Engineering Fracture Mechanics*, 149:351 – 367, 2015.

[277] A. M. Aragón, S. Soghrati and P. H. Geubelle. Effect of in-plane deformation on the cohesive failure of heterogeneous adhesives. *Journal of the Mechanics and Physics of Solids*, 61(7):1600 – 1611, 2013.

[278] A. McBride, J. Mergheim, A. Javili, P. Steinmann and S. Bargmann. Micro-to-macro transitions for heterogeneous material layers accounting for in-plane stretch. *Journal of the Mechanics and Physics of Solids*, 60(6):1221 – 1239, 2012.

[279] L. Távara, J. Reinoso, A. Blázquez and V. Mantič. On the 3D extension of failure models for adhesive joints under mixed-mode fracture conditions: LEBIM and CZM. *Theoretical and Applied Fracture Mechanics*, 100:362 – 376, 2019.

[280] M. Paggi and J. Reinoso. An anisotropic large displacement cohesive zone model for fibrillar and crazing interfaces. *International Journal of Solids and Structures*, 69-70:106 – 120, 2015.

[281] J. Reinoso, G. Catalanotti, A. Blázquez, P. Areias, P. P. Camanho and F. París. A consistent anisotropic damage model for laminated fiber-reinforced composites using the 3D-version of the Puck failure criterion. *International Journal of Solids and Structures*, 126-127:37 – 53, 2017.

[282] T. J. R. Hughes and J. Winget. Finite rotation effects in numerical integration of rate constitutive equations arising in large-deformation analysis. *International Journal for Numerical Methods in Engineering*, 15(12):1862 – 1867, 1980.

[283] K. Park and G. Paulino. Cohesive zone models: A critical review of traction-separation relationships across fracture surfaces. *Applied Mechanics Reviews*, 64(6), 2011.

[284] E. Riks. An incremental approach to the solution of snapping and buckling problems. *International Journal of Solids and Structures*, 15(7):529 – 551, 1979.

[285] V. Tvergaard. Effect of thickness inhomogeneities in internally pressurized elastic-plastic spherical shells. *Journal of the Mechanics and Physics of Solids*, 24(5):291 – 304, 1976.

[286] J. Segurado and J. LLorca. A new three-dimensional interface finite element to simulate fracture in composites. *International Journal of Solids and Structures*, 41(11):2977 – 2993, 2004.

[287] E. Martínez-Pañeda, S. del Busto and C. Betegón. Non-local plasticity effects on notch fracture mechanics. *Theoretical and Applied Fracture Mechanics*, 92:276 – 287, 2017.

[288] J. R. Reeder and J. H. Rews. Mixed-mode bending method for delamination testing. *AIAA Journal*, 28(7):1270 – 1276, 1990.

[289] G. G. Camanho, C. G. Dávila and M. F. de Moura. Numerical simulation of mixed-mode progressive delamination in composite materials. *Journal of Composite Materials*, 37:1415 – 1438, 2003.